Quantifying Thermal Infrared Emission from Active Lava Surfaces to Improve Models of Effusive Volcanism

by

James Oliver Thompson

Bachelor of Science in Geology, University of Southampton (U.K.), 2014

Masters of Science in Volcanology, University of Bristol (U.K.), 2015

Submitted to the Graduate Faculty of

the Kenneth P. Dietrich School of Arts and Sciences in partial fulfillment

of the requirements for the degree of

Doctor of Philosophy

University of Pittsburgh

2020

UNIVERSITY OF PITTSBURGH

KENNETH P. DIETRICH SCHOOL OF ARTS AND SCIENCES

This dissertation was presented

by

James Oliver Thompson

It was defended on

May 18, 2020

and approved by

Michael S. Ramsey, Professor, Geology and Environmental Science

William Harbert, Professor, Geology and Environmental Science

Brian Stewart, Associate Professor, Geology and Environmental Science

Eitan Shelef, Assistant Professor, Geology and Environmental Science

Andrew Harris, Professor, Le Laboratoire Magmas et Volcans, Université Blaise Pascal (France)

Dissertation Director: Michael S. Ramsey, Professor, Geology and Environmental Science

Quantifying Thermal Infrared Emission from Active Lava Surfaces to Improve Models of Effusive Volcanism

James Oliver Thompson, PhD

University of Pittsburgh, 2020

Thermal infrared data of active lava surfaces provides important information including temperature and emissivity, as well as derived volcanological properties such as composition, particle size, heat budgets, and vesicularity. These data are routinely acquired at active volcanoes from the ground, air, and space, but most are saturated or limited in spatial and spectral resolution. To resolve these limitations and expand the utility of these observations, a new portable, ground-based, high-resolution system known as the Miniature Multispectral Thermal infrared Camera (MMT-Cam) was developed to investigate active volcanic processes. In 2017 and 2018, the MMT-Cam was deployed at Kīlauea volcano (Hawai'i) to acquire thermal infrared data of the Halema'uma'u Crater lava lake and Pu'u 'Ō'ō lava flows. The MMT-Cam data provided a unique opportunity to determine the relationship between the emitted radiance from high-temperature surfaces and the derived emissivity and temperature, all fundamental to flow propagation thermo-rheological models. In addition to the camera data, spaceborne and airborne thermal infrared data were simultaneously acquired by NASA. The combination of these datasets enabled the relationship between derived thermal properties at different spatial and spectral resolutions and the accuracy of those measurements to be quantified. The MMT-Cam data analysis revealed that the primary emissivity absorption of basalts shift to higher wavelengths and shallows as the lava cools and forms a crust. During this transition, emissivity increased by ∼14%, producing a decrease in total radiance and increase in temperature. The effect of varying emissivity during lava propagation and cooling was evaluated using the PyFLOWGO thermo-rheological model with a new temperature-dependent variable emissivity module. The results using the new module were validated using ground measurements of heat flux and channel width, with a strong correlation observed to both of these attributes. Comparing the results using this new module to those using the original constant emissivity module revealed that the heat flux decreases by at least 30% and the final runout distance increased by a least 5%. Acquiring this new high-resolution ground-based data has improved flow propagation modeling and reduced the uncertainties in downflow hazards assessments, thereby potentially lowering future risks posed to local populations.

Table of Contents

List of Tables

List of Figures

Preface

I would like to thank and acknowledge my entire doctoral committee: Michael Ramsey, William Harbert, Brian Stewart, Eitan Shelf, and Andrew Harris for their advice and guidance through my journey to achieve this doctoral degree. I would especially like to thank my supervisor Michael Ramsey for the incredible opportunities he has provided me with and his patient guidance through my development as a researcher. I would like to thank the Machine and Electronics Shops of the Kenneth P. Dietrich School of Arts and Sciences at the University of Pittsburgh for their dedicated work fabricating the MMT-Cam components. I would like to thank Jeff Hall, David Tratt, Glynn Hulley, and Alan Gillespie for their assistance calibrating the MMT-Cam and modifying the TES algorithm for the MMT-Cam. Thanks to the Syracuse University Lava Project Team for scheduling and performing a lava pour experiment. I would like to thank the USGS HVO for their assistance in conducting the field campaigns, especially Matt Patrick, Greg Vaughan, and Tina Neal. Additional thanks to the NASA HyspIRI Preparatory Campaign Group (especially Ben Phillips), the NASA ground and flight teams, the ASTER science team, and Hawai'i Volcanoes National Park for facilitating the field campaigns in 2017 and 2018. Additional thanks to Andrew Harris and Oryaëlle Chevrel for their assistance with FLOWGO and PyFLOWGO modeling.

Thank you to the past and present IVIS laboratory members who I have worked closely with over the past 4 years to investigate thermal properties of geological surfaces at all resolutions, it has been fun if a challenge at times. I am thankful to my fellow Geology and Environmental Science graduate students, especially my cohort (Angela, Aster, Becky, Becky, Ben, Javiera, Marja, and Sandy), who we have shared this journey with together. I am grateful for all the support and guidance through thick and fine from all my family and friends, both far and wide. I am mostly thankful for the love and advice from my parents (Mark and Steph) and brother (Sam), without them I would not be where I am today or the man I hoped to be. Most of all, I dedicate this work to my wife (Christine) who has been with me through all and driven me to achieve my goals, no matter how hard they may have seemed at the time. You taught me to be strong and never stop believing in dreams, without you I would not have accomplished what I have today and I hope for many more achievements together in the future. Thank you.

1.0 Introduction

Thermal infrared (TIR) remote sensing of active volcanoes has been used for over 40 years to understand the thermal outputs of eruptions and provide insights into the physical processes (Spampinato et al., 2011; Harris, 2013; Ramsey and Harris, 2013). In effusive eruptions, radiant, convective, and conductive heat fluxes can be derived from TIR remote sensing datasets to quantify the total thermal output of lava surfaces. TIR remote sensing has become pivotal in the volcanology discipline, especially for lava flow propagation modeling because critical thermal properties can be provided to aid in the simulations. Thermal emissions from active lava surfaces vary over numerous spatial (millimeters to meters) and temporal (seconds to minutes) scales, causing issues in quantifying and representing the complete thermal variability of the surface. Ground-based TIR measurements have the potential to improve spatial, temporal, and spectral resolution analyses of lava surfaces, provided the instruments can accurately measure the thermal properties of lava surfaces over eruption temperatures (1100-1500 K).

A new portable, ground-based imaging system was developed to investigate the thermal properties of volcanic processes during lava propagation and cooling, although it is potentially applicable to any dynamic geologic process. The Miniature Multispectral Thermal infrared Camera (MMT-Cam) is an imaging system that acquires data at six TIR wavelength bands between 8 and 12 μm nearly simultaneously. The spatial and temporal resolutions of the camera system are high at 640 $\times$ 512 pixels and 1 second, respectively. The imaging system was calibrated using full-aperture blackbody experiments at a range of temperatures from 283 to 1023 K to account for all instrumental, optical, and transmission effects. In addition, the baseline drift due to changing internal camera temperature was measured and removed to accomplish a full calibration. As a result, accurate multispectral TIR data can be acquired from dynamic surfaces such as propagating and cooling lava flow surfaces at the critical temporal (seconds) and thermal (initial rapid cooling) scales. These improved acquisition parameters provide valuable data for compositional, thermal, and textural spatiotemporal variability analyses of these volcanic surfaces. Furthermore, the MMT-Cam specifications are designed to be comparable to current and proposed Earth-orbiting TIR instruments to better evaluate the potential for future TIR datasets to deliver similar results.

Using TIR data from multiple instruments and platforms for analysis of an entire active volcanic system is becoming more common with the increasing availability of new data (Cashman et al.,

2013; Ramsey and Harris, 2013; Worden et al., 2014). However, the accuracy and uncertainty associated with these combined datasets are poorly constrained over the full range of eruption temperatures and possible volcanic processes (e.g., breakout and overturning). In this study, four TIR datasets acquired over active lava surfaces are compared to quantify the uncertainty, accuracy, and variability in derived surface radiance, emissivity, and kinetic temperature. These data were acquired at Kīlauea volcano in Hawai'i, USA, in January - February 2017 and 2018. The analysis reveals that decreasing spatial resolution strongly limits the accuracy of the derived surface thermal properties, resulting in values that are significantly below those expected for molten basaltic lava at liquidus temperatures (Putirka, 1997; Lee et al., 2009, 2013). The surface radiance was ∼2400% underestimated in the spaceborne data compared to only ∼200% in ground-based data based on the radiance emitted by a surface at the liquidus temperature of a typical Hawaiian basalt. As a result, the surface emissivity was overestimated and the kinetic temperature was underestimated by at least 30% and 200%, respectively, in the airborne and spaceborne datasets. A thermal mixed pixel separation analysis was conducted to extract only the molten fraction within each pixel in an attempt to mitigate this complicating factor. This improved the spaceborne and airborne surface radiance values to within 15% of the expected values and the derived emissivity and kinetic temperature within 8% and 12%, respectively (Abtahi et al., 2002; Lee et al., 2013). It is, therefore, possible to use moderate spatial resolution TIR data to derive accurate and reliable emissivity and kinetic temperatures of a molten lava surface that are comparable to the higher resolution data from airborne and ground instruments. This approach, resulting in more accurate kinetic temperature and emissivity of the active surfaces, can improve estimates of flow hazards by greatly improving lava flow propagation models that rely on these eruption data.

The third study uses the MMT-Cam high-spatiotemporal data of active lava surfaces acquired at Kīlauea volcano in 2018. Active lava surfaces produced through effusive eruptions are typically observed in the form of lava flows, lakes, or domes. There are numerous volcanoes on Earth that regularly produce active lava including Kīlauea volcano in Hawai'i, which had a continuous lava lake and extensive lava flow field until the end of the last eruptive phase in 2018 (Orr et al., 2013; Patrick et al., 2013, 2018). The goal was to quantify the short-term variability of thermal outputs (e.g., kinetic temperature and heat flux) of molten lava during cooling and propagation with concurrent *in situ* multispectral emissivity measurements. As expected, there was a strong correlation between kinetic temperature, fraction of melt, heat flux, and inverse emissivity for the cooling lava surfaces immediately following emplacement. The temporal results reveal low- and

high-frequency variations in thermal outputs, up to 25% and 5% variability, respectively. The spatial analysis provided insights into emplacement dynamics and activity potential through the interpretation of the refined heat flux measurements. For example, these highlighted lava lake overturning, subsurface supply pathways, and lava flow breakout zones. Additionally, the emissivity measurements indicated a lower efficiency of radiant heat flux from molten lava surfaces prior to a viscoelastic crust forming, which results in lower calculated heat fluxes than previous estimates. This could imply that prior heat budget calculations and lava flow propagation models overestimate heat flux by at least 20% from the molten lava prior to cooling and crust formation (Harris, 2013). Therefore, if the results of this study are used to more accurately calibrate these calculations and models, higher quality and more reliable values would be derived (up to 30%), reducing the uncertainty in hazard models reliant on these values.

The ability to accurately model active lava flow propagation is critically important for determining the potential hazards a lava eruption can pose to local populations and infrastructure. Emissivity is an important surface property that describes how efficiently a surface radiates energy and is used in both heat flux and cooling rate calculations to help predict the propagation of lava flows. Typically, emissivity is treated as a constant in these models, but in reality it varies with temperature and other crystalline variations (Harris and Rowland, 2001; Harris, 2013; Chevrel et al., 2018; Ramsey et al., 2019).

In the final study, high resolution multispectral TIR data acquired of a small tumulus lava flow were used to determine the temperature dependency on emissivity during a lava flow (Orr et al., 2013). This relationship was used to develop a variable emissivity radiative heat flux module to integrate with PyFLOWGO, a well defined thermo-rheological lava flow model (Harris and Rowland, 2001, 2015; Chevrel et al., 2018). Integration of the module was validated using MMT-Cam and visual ground measurements of the thermal properties and physical dimensions of the lava flow. Compared with the original PyFLOWGO results, the modified PyFLOWGO simulated a $\sim$5% increase in runout distance and up to 75% less heat flux over the final 20% of propagation. After refinement and validation, the modified PyFLOWGO model simulated the 2018 Lower East Rift Zone fissure 8 emplaced channelized lava flow between May 27 and June 3, 2018 to evaluate the scalability of the new variable emissivity module (Neal et al., 2019; Patrick et al., 2019). The results revealed a decrease in heat flux by $\sim$30%, which caused a $\sim$7% increase in final runout distance, compared to results using the original PyFLOWGO model. This represents the importance of accounting for the variability in emissivity during lava flow propagation to achieve an accurate

estimation of the lava flow, especially for longer flows where an increase of 830 meters for a 12.47 kilometer flow was observed. This overall change of 5-7% in final runout distance could be critically important in hazard assessments to help reduce the risk lava flows pose to local populations and infrastructure.

2.0 MMT-Cam: A New Miniature Multispectral Thermal Infrared Camera System for Capturing Dynamic Earth Processes

2.1 Introduction

The TIR region of the infrared spectrum is used to investigate the thermal properties of a variety of volcanic processes and products, such as fumarole activity, ash cloud dynamics, and lava flow propagation (Harris et al., 2005; Prata and Bernardo, 2009; Spampinato et al., 2011). Previous TIR spectroscopy studies of lava flows include the investigation of emissivity dependence, cooling rates, surface textures, and compositions (e.g., Spampinato et al. 2011; Ramsey and Harris 2013; Ramsey et al. 2016). Specific studies on lava flow propagation range from measuring effusion rates and heat flux using Landsat Enhanced Thematic Mapper (ETM) data, thermal image chronometry, Light Detection and Ranging (LiDAR) measurements, and handheld broadband thermal cameras (Gaddis et al., 1990; Flynn and Mouginis-Mark, 1994; Lombardo and Buongiorno, 2006). However, a majority of these studies use a constant assumed maximum emissivity or attempt to derive a broadband emissivity from prior laboratory or image data in thermal calculations (Ramsey and Harris, 2013). More recent studies suggest that emissivity varies with temperature and wavelength, directly affecting the calculation of temperature and implying the need for an improved method of efficiently deriving emissivity data (Ball and Pinkerton, 2006; Ramsey and Wessels, 2007; Ramsey et al., 2016). Furthermore, the accuracy of the derived brightness temperature and wavelength-dependent emissivity of an object is improved with increased spectral resolution (Realmuto, 1990; Gillespie et al., 1998). Once determined, well-constrained emissivity can later be used with approaches such as linear spectral deconvolution modeling to quantitatively determine possible mineralogical, textural, and thermal endmembers within the image scene (Ramsey and Christensen, 1998; Ramsey and Fink, 1999; Carter et al., 2009; Rose et al., 2014). However, the thermo-temporal dependence of emissivity required to accurately derive these parameters must be better understood, accurately calibrated, and well constrained (Lombardo and Buongiorno, 2006).

To accomplish these goals *in situ*, I developed a new portable ground-based system capable of capturing dynamic geologic processes, called the Miniature Multispectral Thermal infrared Camera (MMT-Cam). The MMT-Cam contains six wavelength bands that span from 8 to 12 μm (Figure 2.1) plus one broadband (unfiltered 8 to 12 μm) band, which are all acquired nearly si-

multaneously. The imaging system was developed primarily to determine the thermal properties of active volcanic surfaces and provide the validation data for future spaceborne TIR instrument concepts. The primary scientific goal of the MMT-Cam is to constrain both the thermal history and spatiotemporal/thermo-rheological evolution of active lava surfaces. Previous ground-based studies on lava flows have identified eruption vents, active flow emplacement, flow progression, the morphologies of lava surfaces as well as postemplacement processes such as flow inflation (Calvari et al., 2005; Harris et al., 2005, 2007; Lodato et al., 2007; Spampinato et al., 2011). For example, during the 2002/2003 Stromboli volcano eruption, handheld TIR cameras measured temperature variability along the lava flow field from ∼300 to ∼1150 K that quantitatively identified active lava channels and vent locations (Calvari et al., 2005; Lodato et al., 2007). Studies have also investigated the spatial and temporal distributions of heat fluxes and the rates of spreading and crustal growth at both active lava lakes and flows (Harris et al., 2007; Calkins et al., 2008; Spampinato et al., 2008). TIR studies of the lava lake at Erebus volcano calculated temporal fluctuations in the average flux of ∼8% daily and spatial variability up to 20% across the lava lake surface (Calkins et al., 2008). The majority of past studies calculate the temperature from TIR radiance data using a single assumed maximum emissivity or attempt to derive a broadband emissivity or temperature, which are oversimplifications (Ramsey and Harris, 2013). This camera system attempts to improve upon existing ground-based TIR technologies by retrieving accurate temperatures and multispectral emissivity values in a compact, portable form factor. The multispectral adaptation made possible with the MMT-Cam provides calibrated, ground-based *in situ* emissivity data that can later be used for thermal calculations in flow modeling or to constrain the composition and micrometer-scale surface texture, neither of which have been achieved previously (Ramsey and Harris, 2013). The wavelength bands were selected to be comparable to both existing Earth-orbiting TIR sensors and proposed future sensors (Figure 2.1) (Abrams, 2000; Abrams and Hook, 2013; Hulley et al., 2017). Ultimately, the MMT-Cam provides instrument testing and data analysis important for possible future NASA TIR mission concepts (National Academies of Sciences and Medicine, 2018).

2.2 Design and Development

The MMT-Cam concept development was motivated by balancing physical specifications (size, weight, and portability) together with lower cost and comparability to current and future satellite-

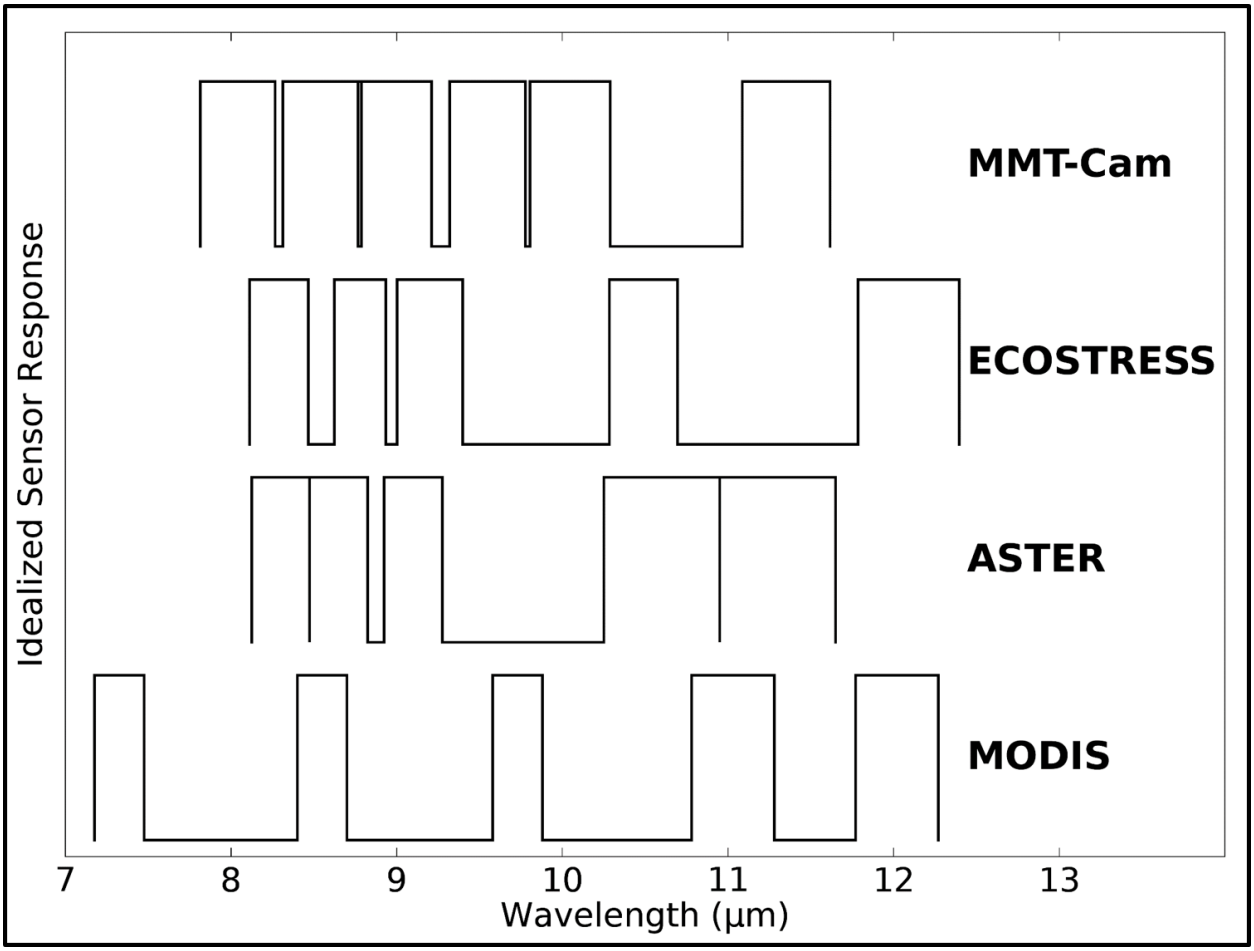

Figure 2.1: Comparison of the idealized wavelength bands [full-width at half-maximum (FWHM)] of the MMT-Cam and current spaceborne TIR instruments.

based TIR datasets (Figure 2.1) (Abrams, 2000; Hulley et al., 2017). The main objective of developing this imaging system is to acquire datasets of active volcanic processes that will potentially improve understanding of the dynamics of lava cooling and eventually lava hazard forecasting. This was an important objective highlighted in the recently published decadal survey for earth science and applications from space (National Academies of Sciences and Medicine, 2018).

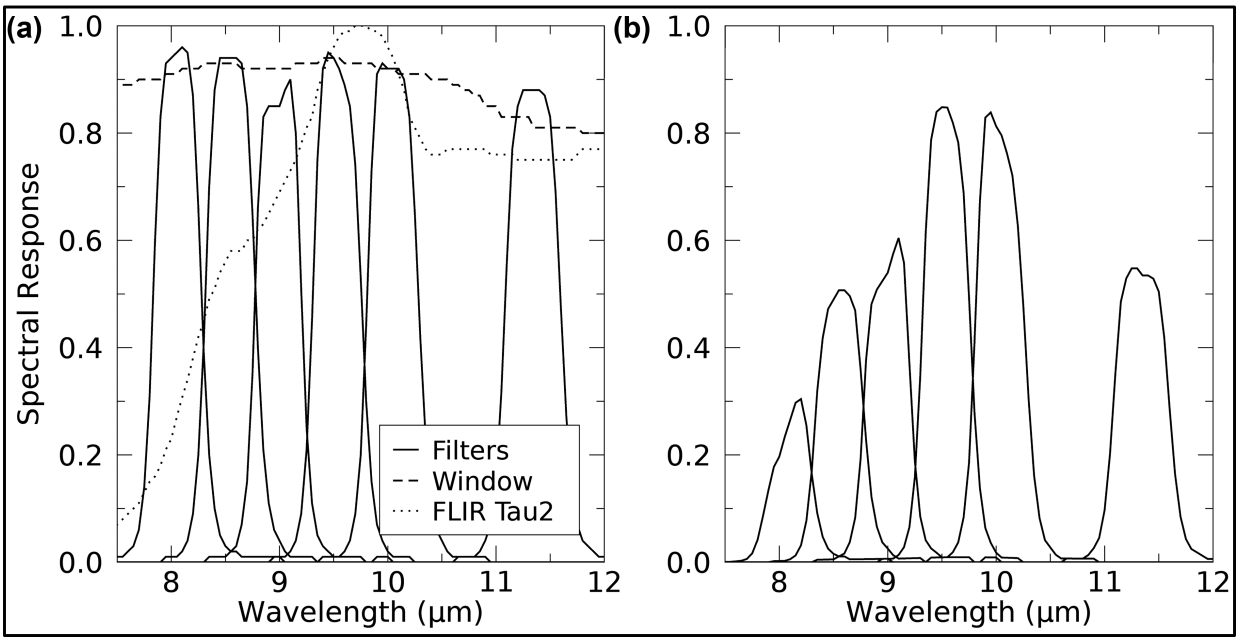

Figure 2.2: Spectral response curves of the MMT-Cam system. (a) Individual spectral response of each filter (Andover Corporation, 2017), that of the germanium window, and the FLIR Tau2 (combined response of the microbolometer detector and camera lens) (FLIR Systems, 2014). (b) Final convolved spectral response for each wavelength band.

To acquire unsaturated TIR data of hot materials (volcanic processes) and gasses, a sensor with a radiometric range up to 800 K, high accuracy (<0.5 K), and high sensitivity (noise equivalent delta temperature (NEΔT) <0.2 K) are required (Spampinato et al., 2008). In addition, the high spatial and temporal resolutions of the MMT-Cam (Table 2.1) enable more accurate measurements of higher frequency processes. With this capability, critically important changes in the temporal (first several seconds following emplacement) and thermal (the initial 200 K degrees of cooling) scales are potentially captured. For example, a lava surface can rapidly cool, crystallize, and form a glassy crust or remobilize and extrude molten lava. It is over these scales where active lava surfaces are the most complex mixture of molten rock plus a cooling viscoelastic glassy surface, and where

the emissivity is changing rapidly (Byrnes et al., 2004). These processes are also observed at various spatial scales from submillimeter to tens of meters, depending on the investigation and distance from the camera to the target. These data can then be incorporated into lava flow propagation models that require accurate temperatures for cooling calculations. Improvement in the models overall accuracy would potentially improve future hazard forecasting.

Table 2.1: MMT-Cam system specifications.

Parameter	Specification
Sensor	FLIR A65 (2nd generation)
Core	FLIR Tau2
Field of View (FOV)	$45^o \times 37^o$ (13 millimeter lens)
Spatial Resolution	40 millimeters (IFOV at 10 meters)
Response Time	12 milliseconds
Frame Rate	30 Hertz
Temporal resolution	1 second
Radiometric Range (Gain Mode)	248 K to 408 K (high) / 233 K to 823 K (low)
Radiometric Accuracy	±5%
Radiometric Resolution	14-bit
Spectral Range	7.5 - 13 μm
Filter Wheel	7 port - 6 IR filters + broadband (open port)
Calibration	Full-aperture blackbody

The MMT-Cam system uses a FLIR A65 TIR camera with a Tau2 core (FLIR Systems, 2014). The Tau2 is an uncooled Vanadium oxide (VOX) microbolometer detector with a spectral range of 7.5–13 μm (Figure 2.2), a 17-μm pitch focal plane array (FPA) of 640 × 512 pixels. Data are acquired at 30 Hz (FLIR Systems, 2014). The detector operates in one of two radiometric ranges of 233–823 K (low gain) and 248–408 K (high gain), with a broadband thermal infrared sensitivity (NEΔT) of approximately 50 mK (Table 2.1) (FLIR Systems, 2014). The camera lens has a diameter of 16 millimeters with a focal length of 13 millimeters and a field of view of 45° × 37°. A seven-port filter wheel assembly was added in front of the lens that contains six TIR bandpass filters (plus one open position for broadband measurements), controlled by a high-precision stepper

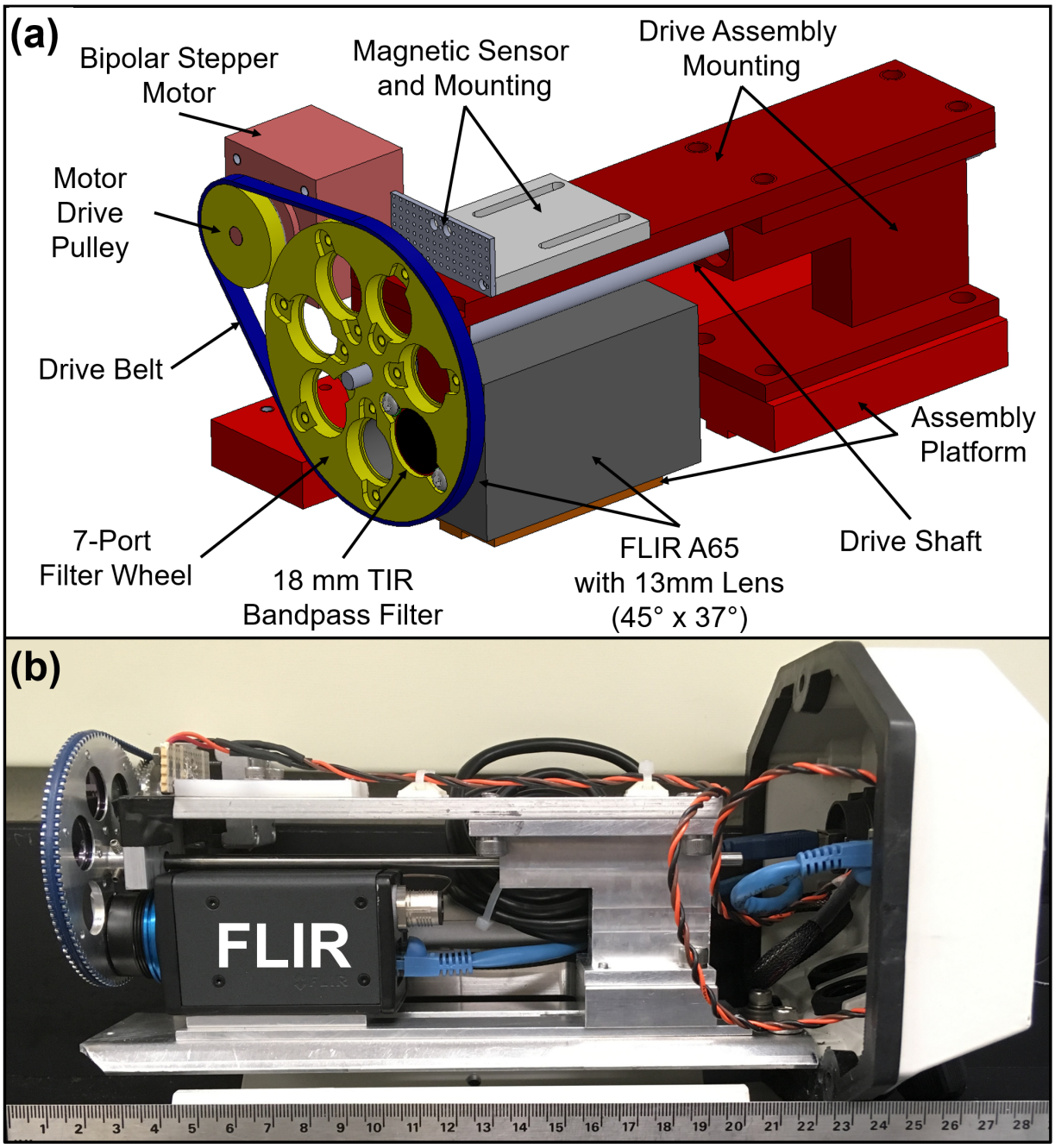

Figure 2.3: MMT-Cam system. (a) CAD assembly model. (b) Completed assembly inside the weatherproof enclosure, showing the location of FLIR A65 camera core and filter wheel (photograph taken by J.O. Thompson). A thermocouple is also attached to outside of the FLIR A65 body to monitor its temperature, which is used in the calibration procedure.

motor (Figure 2.3). The entire assembly was fabricated at the University of Pittsburgh. The filters are secured into the filter wheel using lock screws, preventing any movement of the filters within the wheel housing. Andover optics manufactured the 18 millimeter-diameter TIR filters with bands centered at 8.04, 8.55, 8.99, 9.55, 10.04, and 11.35 μm, each having an average bandwidth of 0.5 μm and minimum transmission of 85% (Figure 2.2). The TIR filters are manufactured from a germanium substrate with a nonradioactive dielectric multilayer coating, reducing any TIR reflections from 36% to 1% (Andover Corporation, 2017). These particular wavelengths are chosen for comparability with current/future spaceborne and airborne multispectral TIR data. The entire assembly is housed inside an environmental enclosure with a germanium antireflective-coated window port. The germanium window is chosen for its durability and high TIR transmission properties. In order to identify any detector temperature change or drift between collections, an ambient blackbody was added in front of the germanium window as well as an internal thermocouple. The aluminum blackbody plate is coated with high temperature, high-emissivity (blackbody) paint. The blackbody plate is mounted using attachment screws that hold the plate directly against the outside of the window, preventing any external radiant sources reaching the detector. It is imaged both before and after any data acquisition. All blackbody images are compared to identify any anomalies. The detector/camera temperature is continually monitored with the internal thermocouple mounted on the camera itself.

The complete MMT-Cam system (Figure 2.3) is operated from a small computer housed within a ruggedized, weather-proof case. The computer controls the camera, operates the filter wheel, and stores the acquired data. The entire camera system is powered by three 12-volt Lithium-ion batteries that enable over 5 hours of data collection in the field or unlimited collection with a direct connection to a power source if available. The long battery life allows the acquisition of high temporal, high volume datasets, so the entire thermal evolution of a lava flow surface is captured. The MMT-Cam weighs 3.5 kg and is $30 \times 15 \times 15$ cm in volume (Figure 2.3). The computer/power case weighs an additional 11 kg and is $50 \times 35 \times 20$ cm in size. Together with a tripod, this system is easily portable by one person.

The MMT-Cam acquires the data continuously as the filter wheel rotates in front of the camera lens, at approximately one revolution every second. Individual images for each filter are only extracted from the data file where the filters are perfectly aligned with the camera lens. This results in one data packet (six multispectral images plus one broadband image) being produced for each filter wheel rotation. The data extraction is achieved using software developed in-house

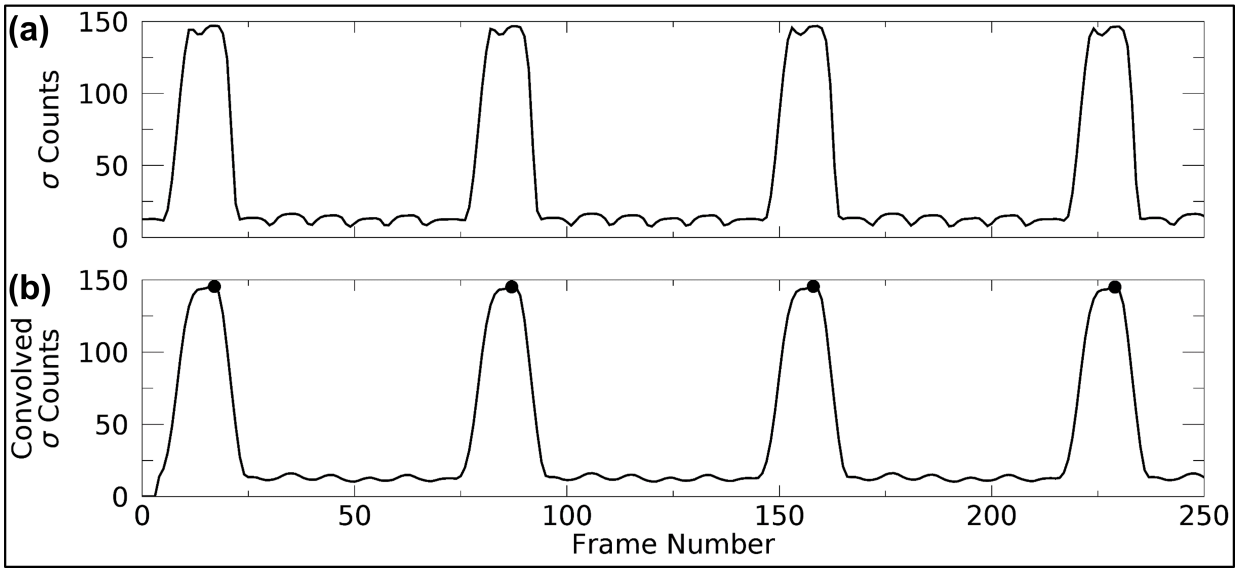

Figure 2.4: Plot illustrating the frame alignment and extraction process. (a) Frame number versus the standard deviation (σ) of raw counts across the FPA. The highest peaks correspond to the open port in the filter wheel (broadband) aligning with the camera lens. (b) Frame number versus the box-car convolved standard deviation (σ) of the raw counts shown in (a). The box-car convolution running average reduces the noise, improving the accuracy of the frame location algorithm. The black points are calculated using a peak location algorithm and denote the frame number(s) extracted from the raw data.

(Appendix C) that first, convolves the standard deviation of the raw counts in each frame with a box-car signal to exaggerate major and smooth minor variability in the data (Figure 2.4). This reduces the noise and improves the accuracy of data extraction. Following this step, a peak locator algorithm is applied to the convolved standard deviation data to locate the broadband image that coincides with each signal peak (where $dy/dx = 0$). It is at these points where the camera and filters are perfectly aligned and the broadband image for each filter wheel rotation is identified. The image data for each for the subsequent six filters are extracted based on the known rotation rate of the filter wheel and the acquisition frequency of the camera. The high-precision stepper motor precisely controls the filter wheel rotation and momentarily dwells rotation at each filter alignment position. Thus, guaranteeing each pixel in the FPA is collocated with the same area on each filter for every rotation. The convolved data are only used to locate the aligned frames, with the corresponding scientific data frames extracted from the raw counts (Figure 2.4). From that raw count's file, two frames are extracted per wavelength band per filter wheel rotation, which are then averaged to improve the signal-to-noise ratio (SNR) and reduce systematic errors.

2.3 Calibration

A detailed calibration of the MMT-Cam was performed to correct for camera temperature drift, any optical attenuation caused by both the germanium window and bandpass filters, as well as the geometric and self-reflectance effects arising from having the filters in front of the optics. The calibration was achieved through a two-stage process (Figure 2.5). The data from this calibration also allowed the effective noise floor through each filter to be determined.

The first stage of the calibration process involved long duration experiments to determine the effect of camera temperature drift on the reported raw counts during data collection of a constant temperature blackbody (Figure 2.5c). The MMT-Cam detector is uncooled and increases in temperature over time. Therefore, the effect of changing detector temperature on the raw measurements must be well constrained to achieve the most accurate calibration. The long duration experiments allowed a temperature-dependent drift correction to be calculated for each filter (Figure 2.6 and Appendix A). These experiments highlight the potential target temperature error that can arise from even a small camera temperature change. For example, in the low gain of the MMT-Cam, the raw count difference caused by a $\sim$5 K drift in camera temperature is equivalent to a $\sim$25 K

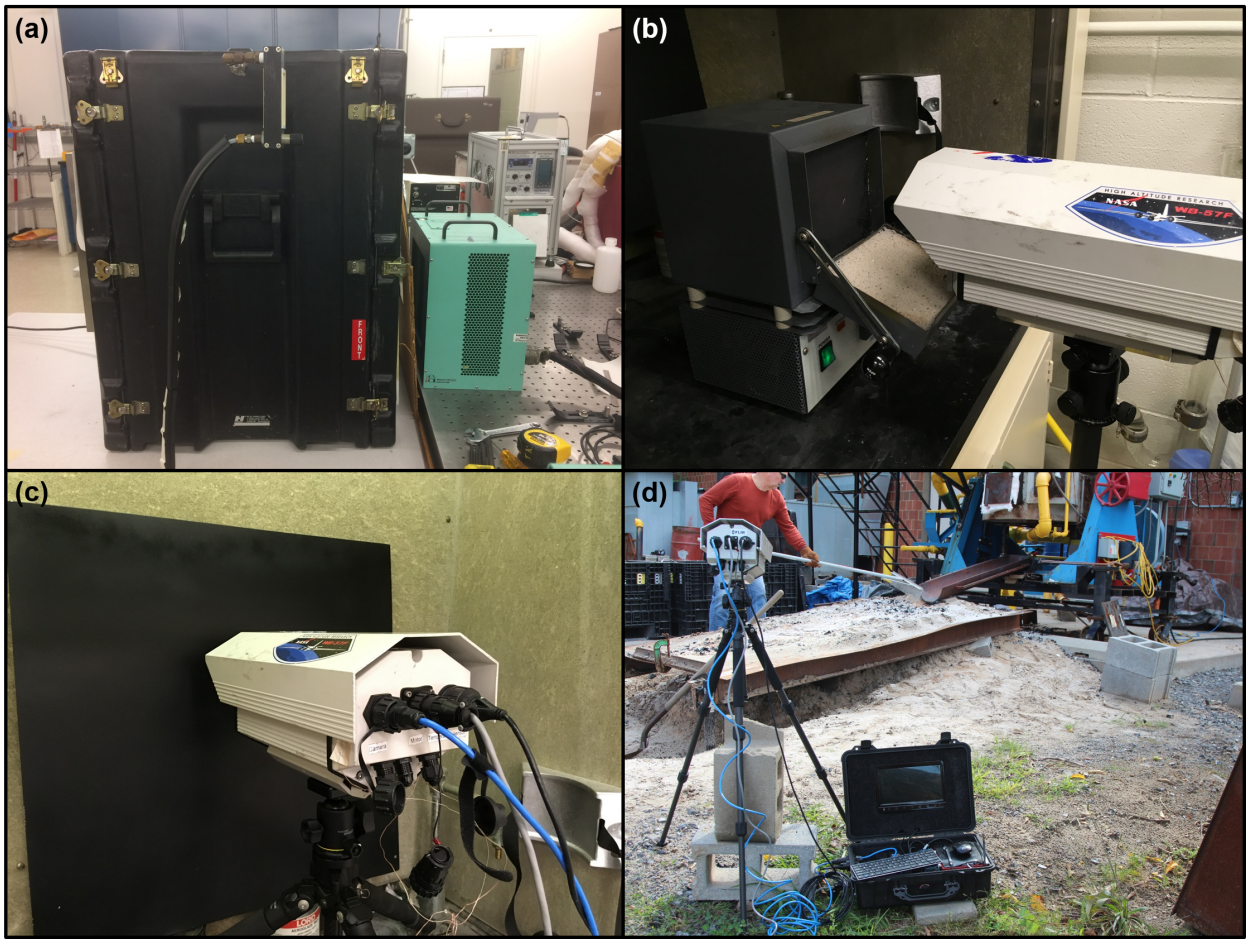

Figure 2.5: Images of the MMT-Cam during the calibration process. (a) The MMT-Cam in the environmental control chamber viewing a variable aperture blackbody at Aerospace Corporation. (b) The MMT-Cam viewing the high-temperature aperture blackbody at the University of Pittsburgh. (c) The MMT-Cam viewing the constant aperture blackbody at the University of Pittsburgh used in the long duration calibration experiments. (d) The MMT-Cam deployed at the Syracuse University Lava Project during the low gain validation testing. Photographs taken by J.O. Thompson.

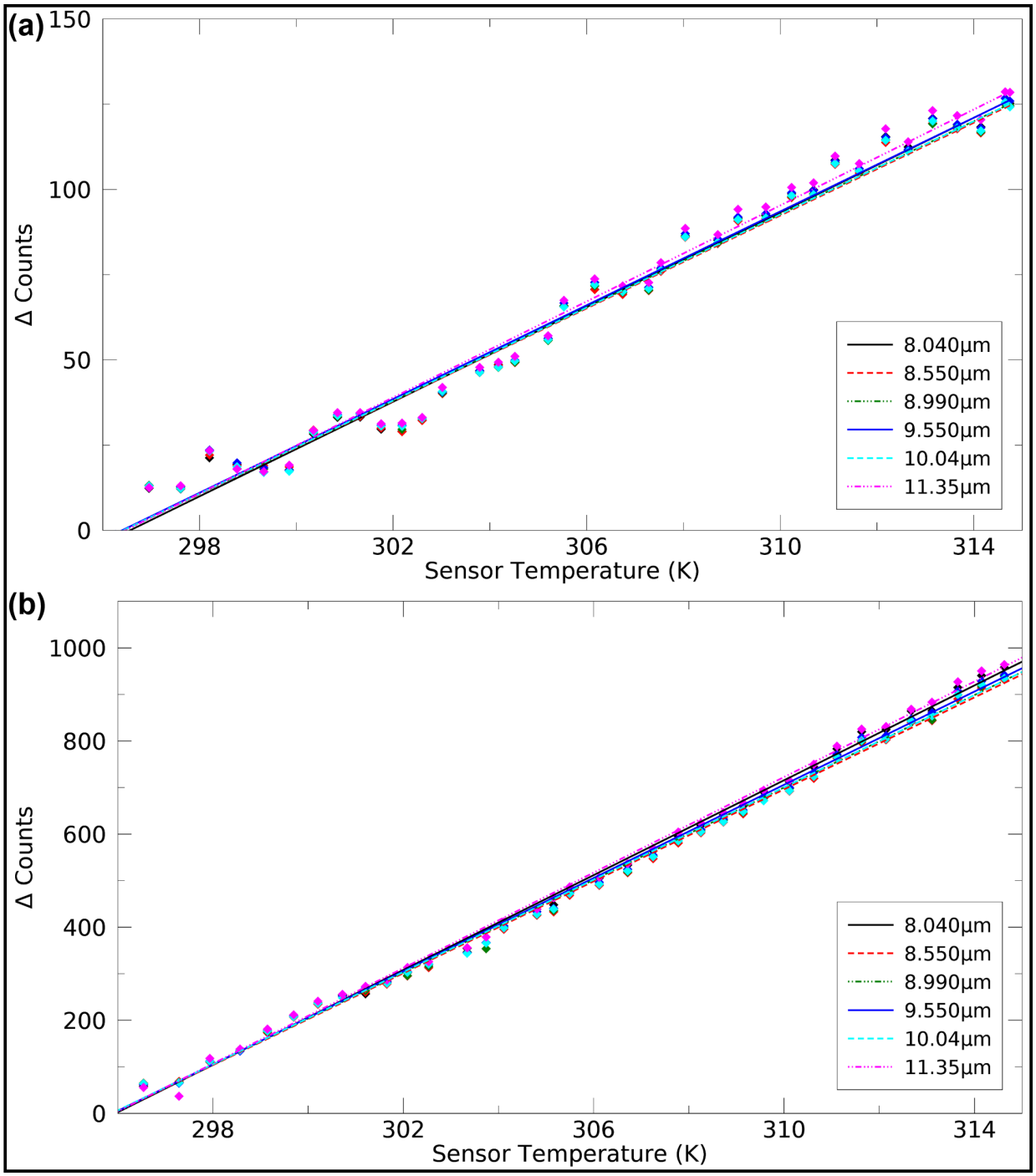

Figure 2.6: Mean change in counts (Δ counts) over the entire FPA versus camera temperature for each wavelength band. (a) Low-gain mode and (b) high-gain mode. During these drift measurement experiments, the camera viewed a blackbody plate maintained at a constant temperature of 293 K, in both low- and high-gain modes.

change in target temperature at 293 K (Figure 2.6). Data from any similar camera design, therefore, should be treated as highly suspect unless these corrections are first made. The cause of this increase in raw counts arises primarily from the increase in self-emission from the warming camera reflecting off the filters (which effectively act as mirrors at all wavelengths except over the filter wavelengths) as well as a component emitted by the warming filters themselves. The long duration drift measurement experiments are periodically repeated (once a year or before a field campaign) to check for any change.

The second stage of the instrument calibration was conducted at the TIR optical sensor laboratory at The Aerospace Corporation, El Segundo, CA, USA (Figure 2.5a). Full-aperture blackbody observations using a temperature-controlled microgroove blackbody at a range of temperatures between 283 and 473 K were performed. A similar set of observations for higher temperatures were then conducted at the University of Pittsburgh, USA, using a blackbody plate heated by a box furnace to temperatures ranging from 473 to 1023 K (Figure 2.5b). The derived spectral radiance of the microgroove blackbody and the box furnace blackbody are calculated using the Planck equation with temperatures derived from a high-accuracy broadband radiometer (Planck, 1901). The per-pixel raw data (in "*counts*") measured at the FPA are compared to the actual broadband and in-band blackbody spectral radiance values to quantify these effects (Figure 2.7 and Appendix B), after the temperature drift correction was applied (Figure 2.6). During the calibration, the internal temperature of the MMT-Cam varied from 303.7 to 315.7 K. The temperature drift correction was used to calculate the contribution of the internal temperature on the measurements during acquisition, which was then subtracted from the raw measurements before the second calibration was computed. The relationship between counts and target spectral radiance was slightly nonlinear for most of the filters (Figure 2.7 and Appendix B).

Therefore, a second-order polynomial model was calculated for every pixel in the FPA for each of the six wavelength bands, producing 1966080 unique calibration models for each gain mode (Appendix B). Equation (2.1) shows this polynomial model relating the difference between the raw data measured by the detector [counts (CNT)] to the actual spectral radiance emitted by the blackbody (L_ε, λ) (Figure 2.7 and Appendix C). A unique set of three constants ($P[0 \rightarrow 2]$) are produced for every pixel in the FPA at both gain modes and for each wavelength, an example is given in Table 2.2.

$$L_{\varepsilon,\lambda} = P[0] + P[1] \cdot CNT + P[2] \cdot CNT^2 \tag{2.1}$$

During field data acquisition, the ambient temperature blackbody and internal thermocouple

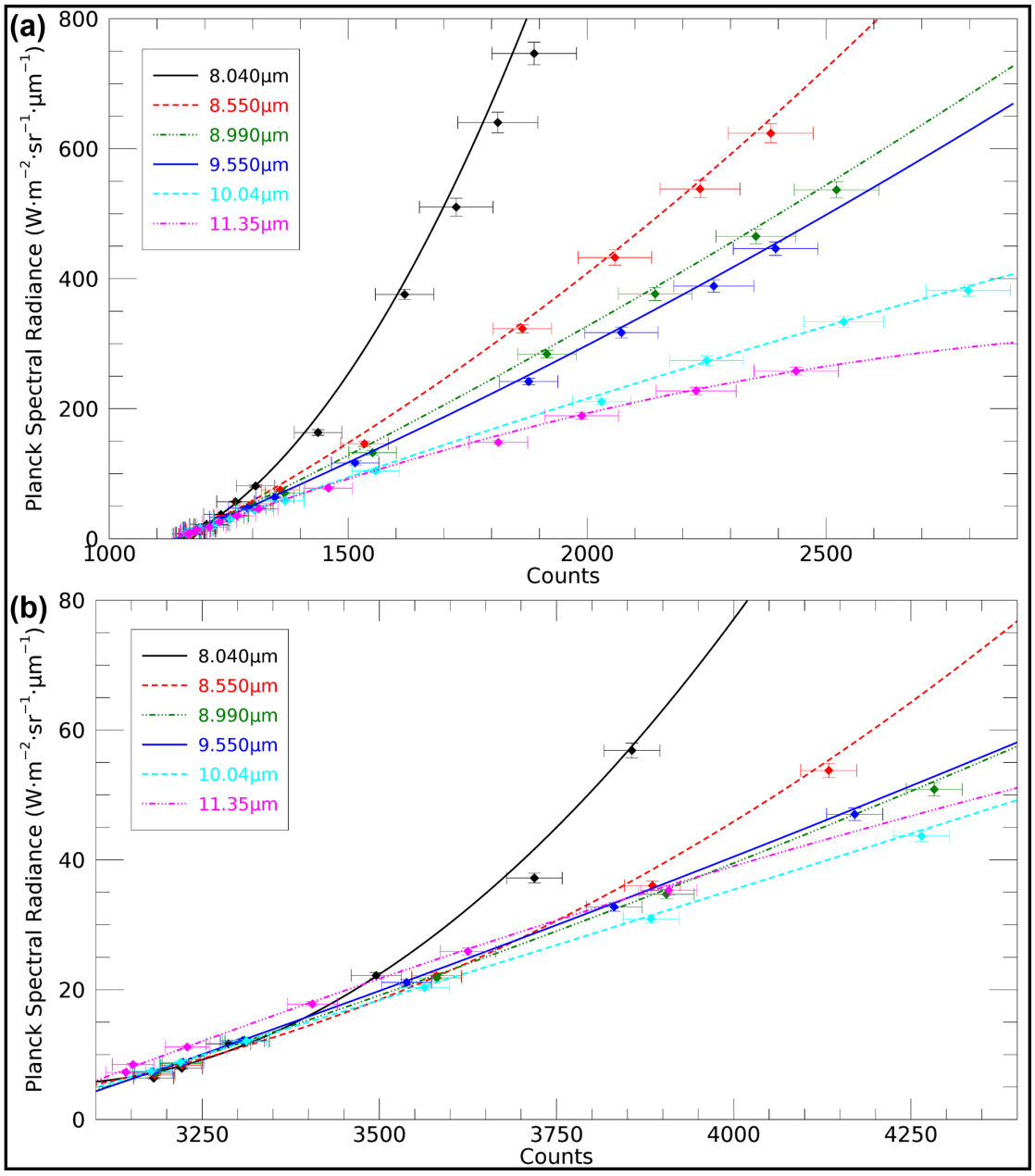

Figure 2.7: Planck spectral radiance versus the measured FLIR counts. (a) Low-gain mode and (b) high-gain mode. Plots show the fit of the instrument calibration algorithm to the raw data (corrected for camera temperature drift) versus spectral radiance for each band from 283 to 1023 K, correcting for instrument optical and transmission effects. The calibration uses a second order polynomial model with three discrete constants, with each band and each pixel in the FPA having unique constants. The data shown are the mean values for the entire FPA at each band and the error bars represent the range of values across the entire FPA.

Table 2.2: Example of the constants used in equation 2.1.

	Constants (low gain)			Constants (high gain)		
Band	**P[0]**	**P[1]**	**P[2]**	**P[0]**	**P[1]**	**P[2]**
1	914.16	-1.96	0.00102	697.95	-0.46	0.000076
2	-307.19	0.14	0.00011	172.86	-0.13	0.000025
3	-355.48	0.27	0.00004	-58.30	0.01	0.000005
4	-302.16	0.22	0.00004	-83.08	0.02	0.000003
5	-327.33	0.31	-0.00002	-94.97	0.03	-0.000005
6	-382.96	0.40	-0.00006	-171.29	0.07	0.000005

[1]An example of the constants used in Equation 2.1 for all wavelength bands in low and high gain mode of the MMT-Cam

measurements are used to detect and correct for any detector drift that may occur during long operational periods under changing environmental conditions.

The MMT-Cam noise equivalent delta radiance (NEΔL) was determined for each pixel in the FPA at every wavelength band by multiplying the spectral radiance noise over time measured for each blackbody temperature by the rate of change in spectral radiance per count at the corresponding spectral radiance (Table 2.3) using the following equation:

$$NE\Delta L = \sum_{x=0}^{M-1} \sum_{y=0}^{N-1} \sigma_0^{50}[f(x,y)] \cdot f'(x,y) \tag{2.2}$$

where $\sigma_0^{50}[f(x,y)]$ represents the temporal noise of each pixel in the FPA acquired at every target spectral radiance from 4 to 746 $\mathrm{W \cdot m^{-2} \cdot sr^{-1} \cdot \mu m^{-1}}$. The temporal noise was calculated from the standard deviation of counts over 50 sequential frames for each pixel and band. $f'(x,y)$ denotes the rate of change in spectral radiance per count at every target spectral radiance. The rate of change was calculated from the differential of (1) $(P[1] + [2 \cdot P[2] \cdot CNT])$, with CNT representing the mean counts value over 50 subsequent frames. M and N are the pixel number in the x- and y- axes of the FPA. The mean NEΔL values are all below 0.3 $\mathrm{W \cdot m^{-2} \cdot sr^{-1} \cdot \mu m^{-1}}$ with little variability, which implies the imaging system is not strongly background limited (Table 2.3). There

Table 2.3: Mean NEΔL, NEΔT, SNR, and combined errors of the MMT-Cam data averaged over the entire FPA and over all bands with increasing object temperatures.

Target Temperature (K)	**NEΔL**	**SNR**	**NEΔT**	**SNR**	**Total Errors (%)**
283	0.082 (0.004)	85 (4)	0.441 (0.081)	687 (22)	2.04
293	0.082 (0.003)	98 (5)	0.442 (0.074)	705 (22)	1.94
313	0.104 (0.014)	145 (7)	0.447 (0.081)	714 (25)	2.15
352	0.084 (0.004)	173 (9)	0.446 (0.0823)	796 (16)	2.25
392	0.085 (0.005)	264 (13)	0.447 (0.078)	874 (18)	2.28
431	0.088 (0.007)	390 (20)	0.447 (0.099)	958 (22)	2.29
471	0.093 (0.009)	537 (27)	0.459 (0.101)	1025 (22)	2.30
573	0.099 (0.009)	733 (37)	0.466 (0.131)	1115 (31)	3.47
663	0.112 (0.018)	1317 (66)	0.466 (0.144)	1237 (39)	2.64
763	0.156 (0.032)	2023 (102)	0.589 (0.151)	1271 (42)	2.14
863	0.195 (0.041)	2196 (110)	0.675 (0.211)	1309 (65)	2.64
958	0.223 (0.045)	2375 (119)	0.739 (0.153)	1409 (53)	2.28

[2]The standard deviation values are represented by the values in brackets. The SNR correspond to the noise values calculated in the prior column.

is less than a factor of two variability in NEΔL values both across the FPA and between wavelength bands, with maximum two-sigma (95%) NEΔL confidence of 0.22 and 0.45 $\mathrm{W \cdot m^{-2} \cdot sr^{-1} \cdot \mu m^{-1}}$ calculated, respectively. The MMT-Cam SNR was also computed at various blackbody spectral radiances (Table 2.3) using the following equation:

$$SNR_{rad} = \left[\sum_{x=0}^{M-1} \sum_{y=0}^{N-1} \frac{\hat{f}^T(x,y)^2}{NE\Delta L(x,y)^2} \right]^{1/2} \tag{2.3}$$

where $\hat{f}^T(x,y)$ denotes the fully calibrated mean spectral radiance over 50 sequential frames for each pixel at every target spectral radiance. $NE\Delta L(x,y)$ represents the NEΔL value for each

pixel in the FPA at each target spectral radiance. The mean SNR values are greater than 80 (in spectral radiance space) at all bands and spectral radiances (and above 500 at higher scene spectral radiance values), which allows subtle variations in surface thermal properties to be detected. NEΔT and SNR were also calculated in temperature (Kelvin) for comparison to other TIR systems on various platforms. For example, the NEΔT of the Advanced Spaceborne Thermal Emission and Reflectance Radiometer (ASTER), Hyperspectral Thermal Emission Spectrometer (HyTES), and MMT-Cam at 300 K are $\sim$0.3, $\sim$0.2, and $\sim$0.4 K, respectively. The ASTER and HyTES detectors are expected to have better NEΔT values as the detectors are cryogenically cooled, compared to the NEΔT values of the uncooled detector in the MMT-Cam. Finally, the total combined spectral radiance errors were calculated for the entire calibration procedure resulting in a maximum error of $\sim$3.5% and a mean error of $\sim$2.4% (Table 2.3).

2.4 Band-to-Band Registration

During data acquisition there is a potential for bands to misalign from each other during a cycle (Figure 2.8). This is caused by instrument jitter induced by vibrations within the deployment environment and exaggerated when insufficient demobilizing techniques are implemented. A solution to remove this band-to-band registration error is to post-process the data using a fast Fourier transform based algorithm (Appendix D). Band-to-band registration transforms one band with respect to a reference band, to ensure the elements of an object being observed are aligned by the same coordinate pair in all the bands (Averbuch and Keller, 2002). Numerous methods have been developed to tackle this issue, however, a fast Fourier transform (FFT) algorithm approach has had the most success when used on TIR datasets as it does not rely on edge or feature detection and matching (which can be difficult in TIR data to discern precisely). Instead the FFT algorithm approach utilizes a two dimensional frequency map to align bands (Averbuch and Keller, 2002). The FFT algorithm is used with a centroid approach to align central frequency features between bands. This method is used to register each band with the first band in each filter wheel rotation cycle (Figure 2.8 and Appendix D). Typically, the band-to-band registration improved the average band misalignment from 5.4$\pm$2.15 to 1.09$\pm$0.92 (Figure 2.8).

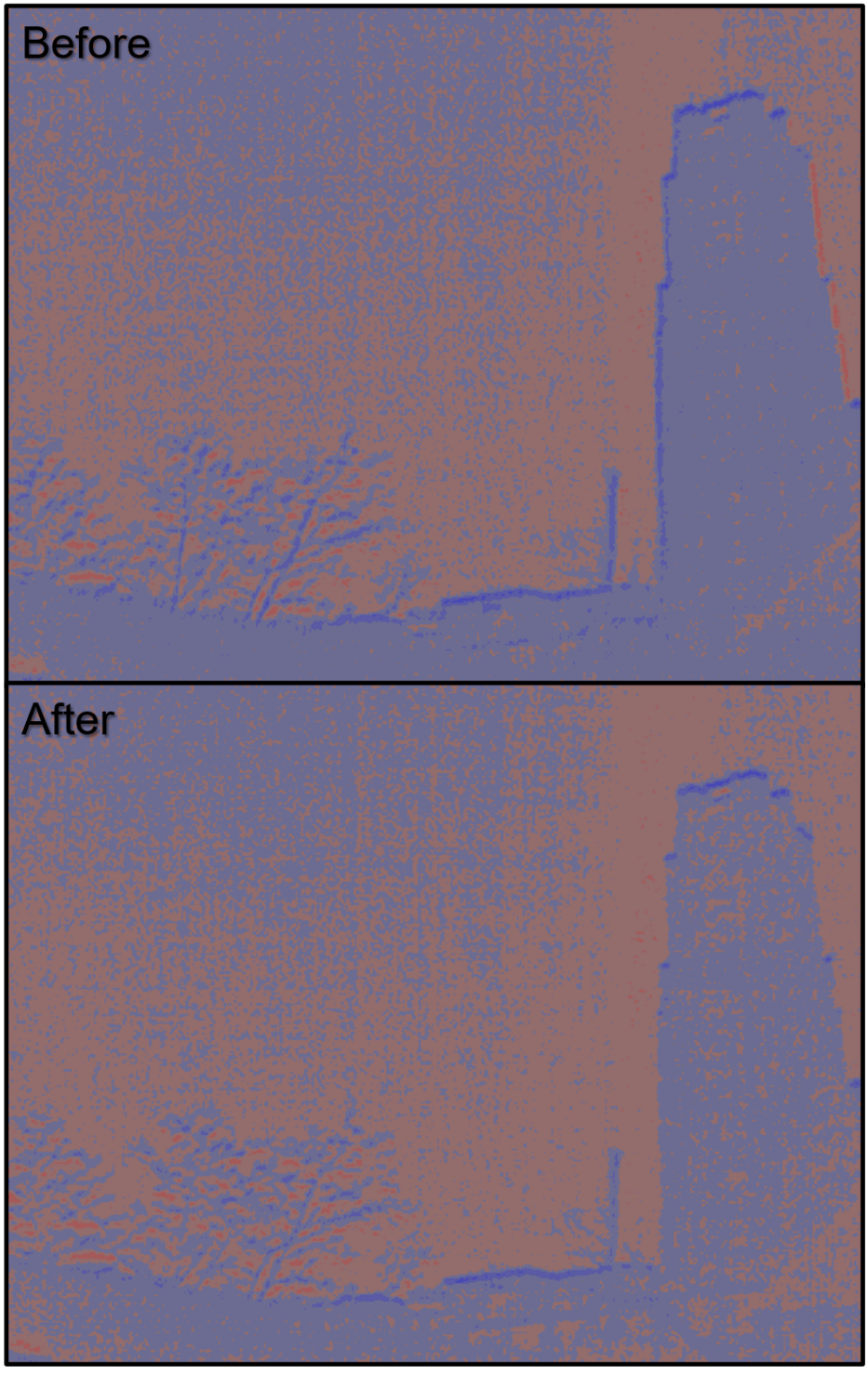

Figure 2.8: Change detection between bands 5 (10.04 μm) and 2 (8.55 μm) (top) before and (bottom) after band-to-band registration

2.5 Atmospheric Correction and TES Algorithm

Atmospheric correction of the MMT-Cam calibrated spectral radiance data accounts for the atmospheric transmission and emission along the path length, from the target surface to the detector, as well as the atmospheric downwelling radiance. The atmospheric transmission and emission contributions are modeled using the SpectralCalc simulator with the HITRAN 2012 database (Rothman et al., 2013; GATS, 2019) and downwelling radiance contributions are determined through full-aperture clear-sky reflection measurements (Appendix D). The temperature and emissivity are derived from the calibrated and atmospherically corrected spectral radiance data through the application of the ASTER temperature and emissivity separation (TES) algorithm (Gillespie et al., 1998). It has been slightly modified here for the specifications of the MMT-Cam data (Appendix D). This modification uses a scaling factor to preserve the deep spectral contrast of low emissivity surfaces such as those of pure minerals. The original TES algorithm does not incorporate low emissivity values of minerals (<0.6) into its regression (Gillespie et al., 1998). The updated TES algorithm uses this regression analysis to correct for the downwelling radiance on the target surface to produce more accurate derived temperatures and emissivity (Appendix D). The major effects of the atmospheric correction and TES algorithm are more pronounced at shorter wavelengths and on surfaces with high spectral contrast.

2.6 Testing

The initial testing of the MMT-Cam system following the calibration procedure and atmospheric correction was conducted outside the IVIS laboratory at the University of Pittsburgh under clear sky conditions, at an atmospheric air temperature of 300 K and relative humidity of 50%. High-gain mode MMT-Cam multispectral TIR data were acquired of three hand samples heated to approximately 373 K, from a distance of 0.4 meters and at a normal incidence angle. The three samples measured were quartz and obsidian (samples used as spectral standards in the IVIS laboratory at the University of Pittsburgh) as well as a basalt sample from Hawai'i (Figure 2.10). All the sample surfaces are rough at the submillimeter scale. The maximum sample temperatures derived from the calibrated/atmospherically corrected multispectral radiance data are given in Table 2.4 and are consistent with concurrent broadband TIR brightness temperatures acquired using

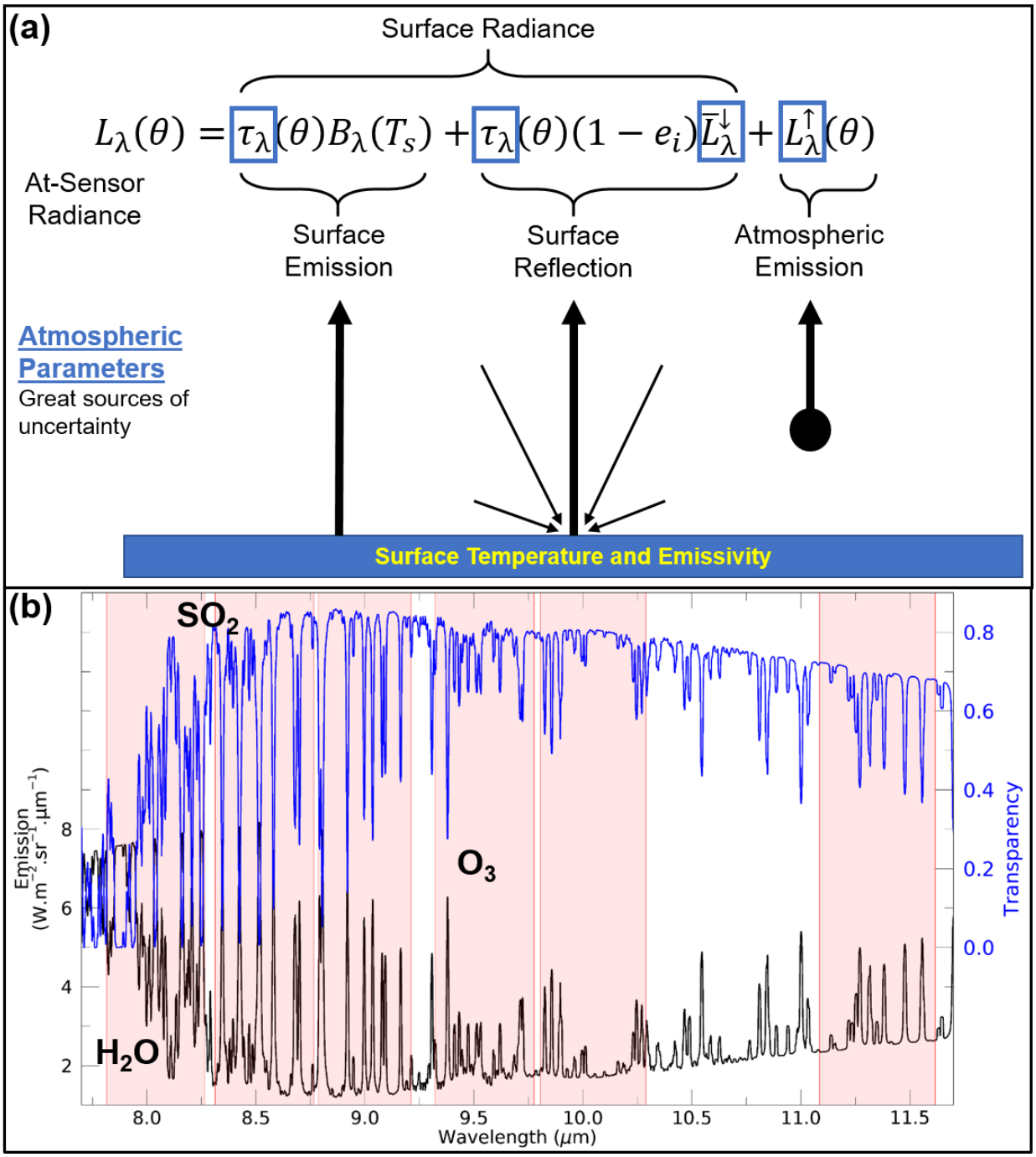

Figure 2.9: (a) A schematic of the atmospheric contributions to the radiance detected at the sensor, including reflections and emissions. (b) The typical horizontal emission and transparency of the atmosphere at a path length of 1 kilometer.

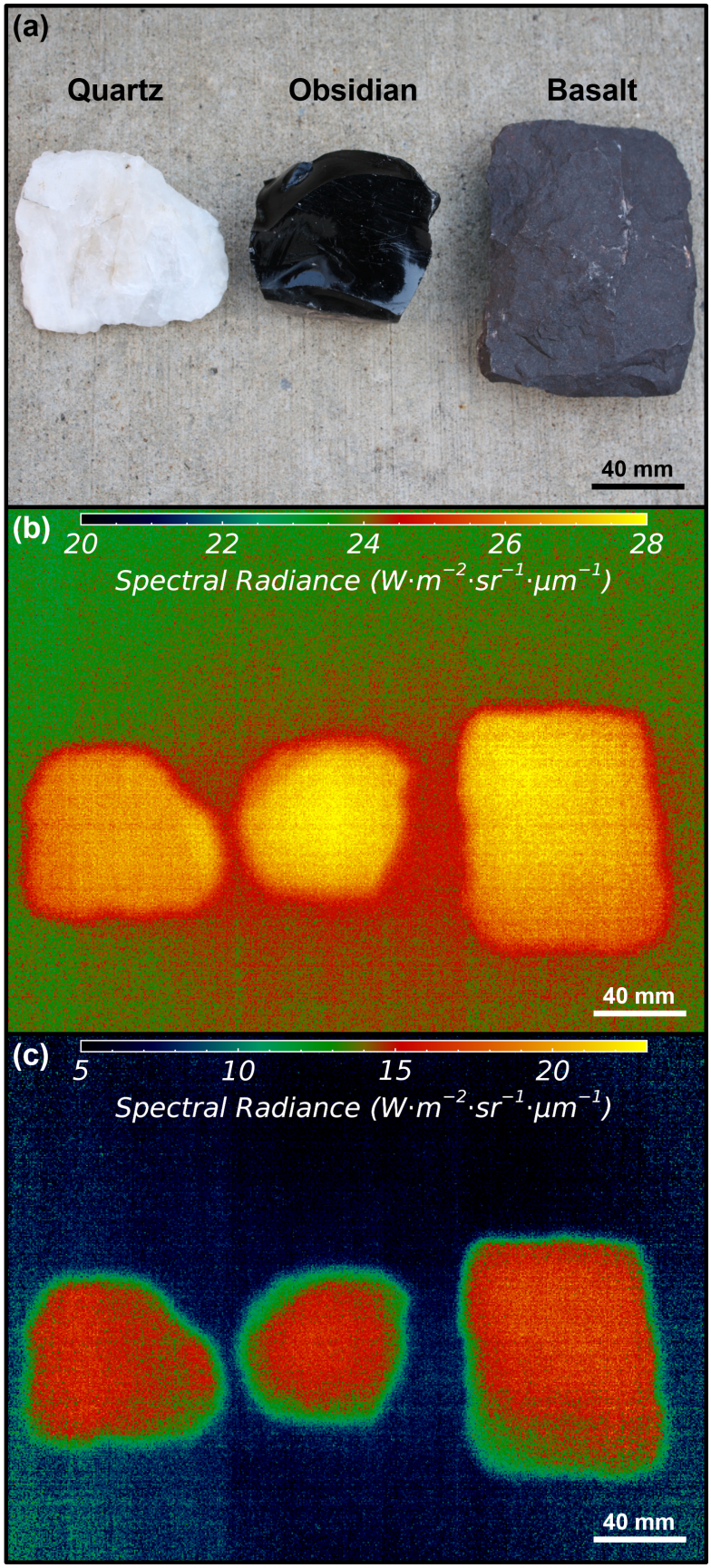

Figure 2.10: Three samples used for the MMT-Cam high-gain mode testing: (left to right) quartz, obsidian, and basalt. (a) Visible image with sample labels. (b and c) MMT-Cam image data of the hand samples heated to approximately 373 K in an oven and then transported outdoors. Data were acquired from a distance of 0.4 meters and orientated at a normal incidence angle to the sample surfaces. (b) Uncalibrated spectral radiance data stretched to emphasize the full dynamic range. (c) Fully calibrated and corrected spectral radiance data. Note the improvement in errors associated with the transmission effects (seen as an overall higher scene radiance) and geometry effects (seen as a higher radiance in the scene center) caused by the instrument design.

a Raytek Raynger MX radiometer (Table 2.4). The radiometer derived sample temperatures are lower than the 373 K temperature because of cooling during transportation from the oven to the outside testing location. Therefore, for validation, the radiometer derived temperatures are more directly comparable with the MMT-Cam derived temperatures (Table 2.4).

Table 2.4: Comparison between the sample temperatures derived from the MMT-Cam radiance data at different stages along the calibration and atmospheric correction process.

	Sample Temperature (K)		
	Quartz	**Obsidian**	**Basalt**
Raytek Broadband Radiometer	358±3.6	363±3.6	368±3.7
Un-Calibrated	1125	1100	1080
No Detector Temperature Correction	355±5.5	345±5.4	345±5.4
Full Calibration	361±9.2	365±9.3	370±9.4
Calibration + Atmospheric Correction	359±6.6	364±6.1	368±7.9

[3]The samples were heated in an oven to ∼373 K prior to being moved outside for testing. The radiometer derived temperatures report the brightness temperature of the samples at the time of the MMT-Cam acquisition and are used to validate the MMT-Cam derived temperatures. Plus/minus represent the total combined errors associated to the accuracy of the MMT-Cam during acquisition as determined by the calibration process.

The fully calibrated/atmospherically corrected MMT-Cam emissivity spectra are compared with those from the high-resolution IVIS Laboratory Fourier-transform infrared (FTIR) spectrometer, which are degraded to the MMT-Cam spectral resolution (Figure 2.11). The spectral morphology of the MMT-Cam data compares well to the laboratory FTIR data (Figure 2.11). However, small discrepancies between the FTIR and MMT-Cam derived spectra are seen (Figure 2.11). Most significant is the difference in spectral depth caused by the atmospheric effects on the samples measured by the MMT-Cam. The laboratory measurements follow the same method described in Ruff et al. (1997), whereby the sample is placed inside a blackbody chamber under a constant temperature with a zero percent relative humidity (Ruff et al., 1997). Therefore, the atmospheric

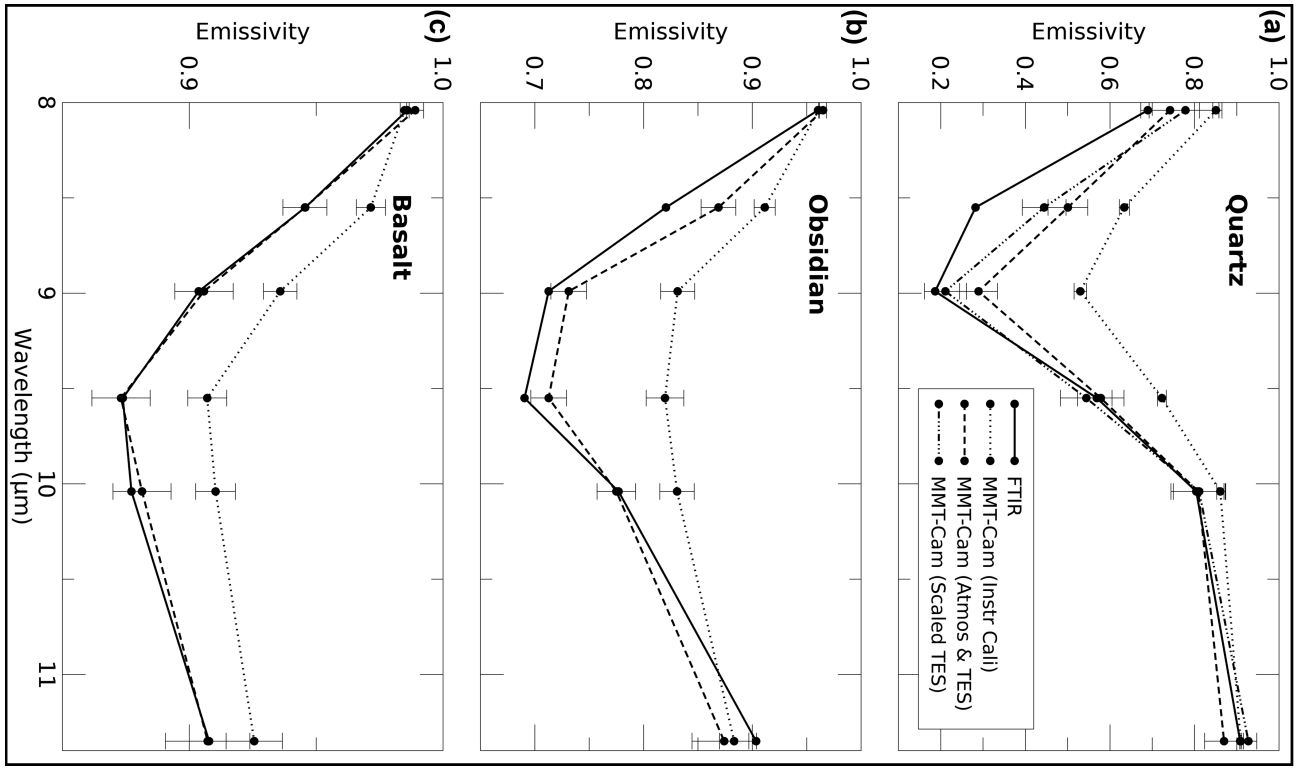

Figure 2.11: Comparison between the calibrated MMT-Cam derived (non-atmospherically corrected) emissivity spectra (dotted line), the MMT-Cam atmospherically corrected and TES derived emissivity spectra (dashed line), and the FTIR spectrometer derived spectra (spectrally degraded to the MMT-Cam resolution) (solid line) of three hand samples. In addition, the MMT-Cam scaled TES derived emissivity spectrum (dashed-dotted line) is shown for the quartz spectrum because of its deep spectral contrast. (a) Quartz, (b) obsidian, and (c) basalt hand samples were heated to approximately 373 K prior to MMT-Cam and FTIR data acquisition, with the actual temperatures reported in Table 2.4. The MMT-Cam was in high-gain mode during acquisition.

affects are dramatically limited. Other minor differences between the laboratory and MMT-Cam spectra arise from the difference in spectral resolutions (0.01 μm for the laboratory spectrometer versus 0.5 μm for the MMT-Cam). The mean difference between the final MMT-Cam and the FTIR derived emissivity of the quartz, obsidian, and basalt are 11.1%, 2.6%, and 0.2%, respectively.

Testing of the MMT-Cam in the low-gain mode of a dynamic source was completed by acquiring multispectral TIR data of a synthetic lava flow performed at the lava pour experimental facility run by the Syracuse University Lava Project team (Figure 2.5d) (Karson and Wysocki, 2012). At the facility, basaltic rock fragments are melted in a large furnace and poured onto a sand substrate to produce a small-scale lava pour about 3 meters long and 0.1 meters thick (Figure 2.12). During the lava pour, the MMT-Cam was orientated at $\sim$25° from the normal incidence angle of the pour surface at a distance of 1.5 meters. The multispectral TIR data show a distinct change in the emissivity of the basaltic lava surface as it cools (Figure 2.12). During emplacement at 1410 $\pm$ 32 K and subsequent cooling to 920 $\pm$ 22 K, the emissivity spectral contrast decreases and a distinct absorption feature appears in band 4 (9.55 μm) likely due to the presence of a forming glassy crust. The mean emissivity from 8 to 12 μm increases from 0.762 $\pm$ 0.02 to 0.883 $\pm$ 0.03, a change of 15.9% (Figure 2.12c).

Multispectral data acquired from surfaces hotter than the maximum radiometric limit of the detector (823 K) are not saturated because the bandpass filters significantly reduce the flux to the detector by up to 70%. The reduction in flux to the detector, however, caused by the germanium window of the enclosure is only $\sim$10%. This is insignificant to prevent the broadband data from saturating at the maximum radiometric limit of the detector. A neutral density filter may be considered in the future for the broadband port to mitigate this saturation. The derived temperature and emissivity values are similar to the known values of molten basalts and other laboratory emissivity values of cooling basaltic melts, acquired under comparable experimental conditions (Abtahi et al., 2002; Lee et al., 2013). Furthermore, the temperature variations observed across the lava pour are consistent with the variability measured using ground-based broadband TIR cameras at Erta 'Ale volcano between the molten (<1300 K) and crustal (>950K) regions of the lava lake (Spampinato et al., 2008).

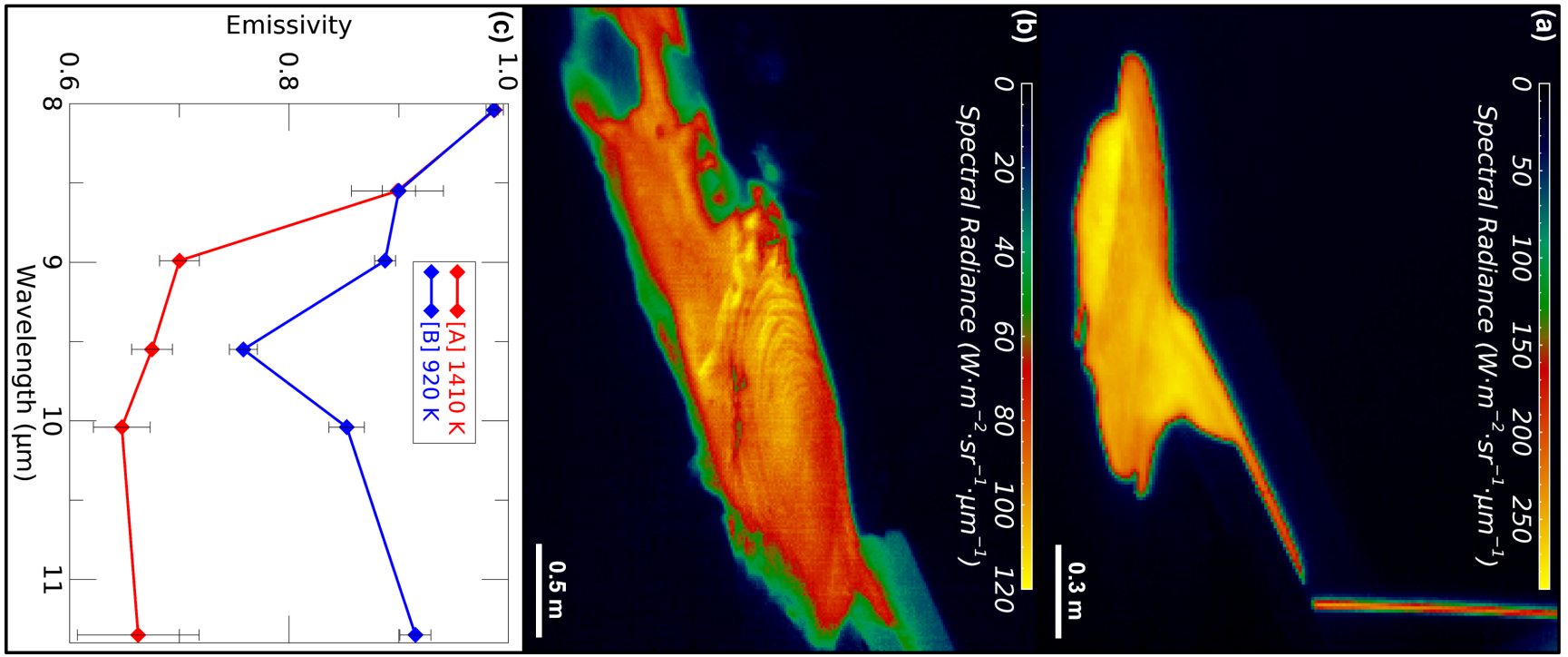

Figure 2.12: Fully calibrated TIR spectral radiance 11.35-μm image data and the emissivity spectra acquired during camera testing at a basaltic lava pour. (a) Initial phase of the pour. (b) Final extent of the pour. (c) Mean emissivity spectra and temperature derived from the spectral radiance data, with the error bars indicating the normalized standard deviation of the lava extent. The mean emissivity is 0.762 $\pm$ 0.02 for the initial phase at 1410 $\pm$ 32 K and 0.883 $\pm$ 0.03 for the final extent at 920 $\pm$ 22 K, a 15.9% increase in emissivity over 490 K of cooling. The multispectral data were unsaturated because the MMT-Cam was in low-gain mode and more importantly, the bandpass filters significantly reduce the flux to the detector. However, the broadband data were saturated. The MMT-Cam was orientated at $\sim$25° from the normal incidence angle of the pour surface at a distance of 1.5 meters.

2.7 Conclusions

A new portable, inexpensive, ground-based multispectral TIR imaging system was developed to measure the emissivity and temperature of natural dynamic surfaces. The well-calibrated MMT-Cam has six wavelength bands between 8 and 12 μm as well as one broadband temperature band. On the other hand, the MMT-Cam is well-suited for measuring the emitted spectral radiance from any static geologic surface/sample, and the instrument is designed specifically for highly dynamic processes. The data acquired by this camera system are primarily used to observe the changes in molten lava surfaces during cooling and the formation of a glassy, semiamorphous crust (Figure 2.12). The data are also providing valuable information on the ability of current satellite-based sensors to detect similar changes in emissivity of thermally mixed surfaces. These same data will form the performance metrics for future mission proposals based on similar uncooled, inexpensive microbolometer instruments. The spatial, temporal, and spectral resolutions of the MMT-Cam make it ideally suited for these assessments.

The detailed calibration of this system is critical for extracting geologically meaningful emission spectra. Similar systems or attempts to filter TIR broadband cameras without this level of detailed calibration procedures will result in inaccurate data that cannot be directly compared to spectral libraries or data from spaceborne sensors. The initial testing of the MMT-Cam validated the instrument calibration procedure using a robust and rigorous procedure that corrects the filter transmissivities and instrument effects. As a result, not only is a pixel-based calibration required but also the knowledge of the detector/camera temperature drift is vital for removing all image and spectral artifacts. The MMT-Cam was tested on both low temperature stationary samples and dynamic high-temperature molten surfaces to evaluate the performance and reliability of the data acquired. This testing validated that the imaging system accurately retrieves temperatures and emissivity values of a wide range of surface states, from solid to molten, at a range of temperatures and compositions. The MMT-Cam system is a reliable tool for acquiring accurate multispectral TIR data of a variety of geological surfaces, at a wide range of temperatures and a variety of dynamic processes.

3.0 Uncertainty Analysis of Remotely-Acquired Thermal Infrared Data to Extract the Thermal Properties of Active Lava Surfaces

3.1 Introduction

Using remote sensing data to monitor volcanic eruptions have improved our understanding of the precursory activity, eruptions dynamics, and eruptive products (Spampinato et al., 2011; Cashman et al., 2013). TIR data between a spectral range of 8 to 12 μm have been utilized since the early 1960s, with major developments in spaceborne, airborne, and ground-based TIR technologies occurring over this time. These systems provide new data that are important for modeling volcanic activity over a variety of spatial, spectral, and temporal scales (e.g., Ramsey and Harris 2013). For example, the data have improved the accuracy, reliability, and duration of precursory evaluations, constrained eruption dynamics, and improved both magma rheological and thermal models of all volcanic products (Calvari et al., 2010; Spampinato et al., 2011; Murphy et al., 2013).

Multi-instrument, multi-platform TIR data of an entire volcanic system must be properly integrated and cross-calibrated to understand the entire thermal regime of a system. An orbiting instrument such as ASTER acquiring moderate spatial (90 meters) and spectral (5 TIR bands) resolution data will provide lower temporal frequency observations ($\sim$16 days) of the larger volcanic system and the ongoing eruption (Yamaguchi et al., 1998). Typically, these systems miss the detailed spatial and spectral observations of low-level smaller-scale thermal anomalies and processes unless specific methods are adapted to directly detect and characterize these, and/or coincident mid-infrared data are exploited (Flynn et al., 2001; Murphy et al., 2013). Airborne and ground-based instruments can observe smaller anomalies at the required spatial, spectral, and radiometric resolutions, but they are unable to provide data over extended time periods and may miss the synoptic coverage. Hence, there is a need for instrument and data synergy to improve observations from an individual source as well as the scientific interpretation of the volcanic system. This synergy requires accuracy and uncertainty quantification to improve analysis confidence. This issue has been investigated over many scenarios (Handcock et al., 2006; Roberts et al., 2012; Western et al., 2015; Guanter et al., 2019) but not for observations of active molten lava surfaces where rapid changes in thermal properties occur both spatially and temporally at very high surface temperatures ($<$1450 K), as seen in the recent basaltic eruptions in Hawai'i, USA.

Basaltic volcanism is the most common form of extrusive volcanism on Earth, occurring at every tectonic setting (Walker, 1993). Recent significant basaltic eruptions have occurred at Piton de la Fournaise (Reunion Island); Yasur (Vanuatu); Tolbachik (Russia); and Kīlauea (Hawai'i), emphasizing the hazards that these eruptions pose. For example, in 2018 the lava flows from the Lower East Rift Zone (LERZ) of Kīlauea volcano threatened lives and property in the Puna District of the Island of Hawai'i, USA (Global Volcanism Program, 2018). During the 4-month long eruption, 23 fissures opened emplacing over 750 m^3 of lava that covered the populated Leilani Estates and destroyed 716 dwellings (Neal et al., 2019). Near-daily broadband helicopter-based TIR camera data were acquired to produce lava inundation maps, but limited thermal lava flow propagation forecasts were calculated, mostly due to the lack of an available robust and reliable modeling approach.

With these recent large flow-producing eruptions, there is an increasing need to develop rapidly implementable lava flow propagation models to aid in volcanic hazard response. Developing these models requires improvements in the accuracy of estimating lava flow pathways and velocity to reduce the hazard risk to proximal communities. Volcanic eruption flow flow modeling relies on factors including but not limited to effusion rates, flow dynamics, viscosity, cooling rate, in addition to continuously-updated topography (Harris and Rowland, 2001; Crisci et al., 2004; Negro et al., 2008). Typically, these models use data from TIR instruments to measure cooling and model viscosity. Therefore, improvements in the accuracy and constraint of uncertainty in the measured surface radiance, kinetic temperature, and emissivity from these instruments will improve our ability to model downslope lava surface dynamics, rheological changes, flow propagation, and hazard assessments (e.g., Ramsey and Harris 2013; Ramsey et al. 2019).

TIR data for this study were acquired during the 2017 and 2018 NASA Hawai'i airborne campaigns and were utilized to determine the spatial and spectral resolution influence on the derived kinetic temperature and emissivity of the active lava surfaces as they cool. Simultaneous TIR data were acquired using the ground-based MMT-Cam imaging system (Thompson et al., 2019), the airborne HyTES (Johnson et al., 2011), and the MODIS/ASTER (MASTER) airborne simulator (Hook et al., 2001), as well as, the spaceborne ASTER instrument (Yamaguchi et al., 1998), with increasingly lower spatial resolutions, respectively. A primary goal was to constrain the relationship between the acquired surface radiance and derived emissivity to increase the accuracy of the surface temperatures from TIR data (Spampinato et al., 2011; Ramsey and Harris, 2013).

3.2 Background

The TIR spectral region is primarily used in volcanology to determine the eruption temperature, with later multispectral systems being able to also derive surface emissivity (Spampinato et al., 2011). Previous TIR spectroscopy studies investigated emissivity, cooling rates, surface textures, and compositions (e.g., Spampinato et al. 2011; Ramsey and Harris 2013; Ramsey et al. 2016). However, the extreme thermal heterogeneity of active volcanic surfaces can easily lead to misclassification or oversimplification of the true thermal fractions (Wright and Flynn, 2003). This is made worse by the currently available low spatial resolution (>500 m) TIR datasets that are not able to accurately resolve the maximum temperature or representative emissivity spectrum. There are relatively few studies (e.g., Wright and Flynn 2003) that have investigated the influence of spatial and spectral resolution on these calculations over temperatures where a molten lava surface cools (<1450 K). Therefore, simply deconvolving the molten fraction with the maximum temperature within each pixel will improve the accuracy and uncertainty of the emissivity, kinetic temperature, and radiant flux.

Measuring accurate thermal properties of a molten lava surface is also critical to lava flow propagation models (Harris and Rowland, 2001; Favalli et al., 2005). With the increasing number of spectral bands in more recent TIR imagers (e.g., HyTES (Johnson et al., 2011) and the Mineral and Gas Identifier (MAGI) (Hall et al., 2015)), the radiative temperature and emissivity of an object's surface can be extracted with increasing accuracy (Realmuto, 1990; Planck, 1901; Gillespie et al., 1998). A well-constrained emissivity can then be used with approaches such as linear spectral deconvolution modeling to quantitatively determine possible spectral endmembers that defines the mineralogical, textural, and thermal fractions (Ramsey and Christensen, 1998; Ramsey and Fink, 1999; Carter et al., 2009; Rose et al., 2014). Additionally, kinetic temperature (and to a lesser degree, emissivity) is required to determine the runout distance and hazard potential using radiant heat flux in lava flow propagation models (Favalli et al., 2005; Harris et al., 2011). However, the accuracy of these derived properties over the cooling temperature range of typical lavas is poorly constrained at the various spatial resolutions of current TIR instruments. Therefore, improving the accuracy of the kinetic temperature and emissivity of the previously-determined molten fraction should then reduce the uncertainty in flow model analyses that directly rely on these thermal properties.

3.3 Data

3.3.1 Study Area

This study was conducted during two field campaigns at Kīlauea volcano in Hawai'i, USA, in January - February 2017 and 2018, a period when both the summit lava lake and coastal plain surface lava flows were active. The activity was focused primarily at the lava lake in the Halema'uma'u Crater and propagating lava flows from the Pu'u 'Ō'ō vent (Figure 3.1). Kīlauea is a basaltic shield volcano that has been erupting nearly continuously for the past 500 years (Holcomb, 1987). The lava surfaces are produced during long sustained eruptions where pāhoehoe (tube- and surface-fed) and 'a'ā flows are emplaced (Holcomb, 1987). The lava lake in the Halema'uma'u Crater observed during this study was active from 2008 until 2018 and varied in size with maximum dimensions of 160 meters wide and 225 meters long (Figure 3.1) (Patrick et al., 2013). During this period, there were fluctuations in lava lake activity with continuous gas plumes and irregular small explosions, finally ending with the summit collapse in May 2018 (Patrick et al., 2013; Neal et al., 2019). At the time of the field campaigns, the lava lake level was relatively high but not overflowing, approximately 100–130 meters below the Halema'uma'u Crater rim. It was continuously circulating with fresh lava upwelling in the north that migrated to the south, cooled and formed plates of cooler solidified lava. The lava then sank in the south, distinguished by the occurrence of strong spattering and degassing (Patrick et al., 2018). The lava flows from the Pu'u 'Ō'ō vent were active for ∼30 years erupting in many locations over numerous eruptive episodes, producing mostly pāhoehoe lava flows with the occasional 'a'ā lava flow (Holcomb, 1987; Orr et al., 2013). This long eruption finally ended in 2018 with the cessation of the LERZ fissure eruption in the Leilani Estates (Neal et al., 2019). The lava flows observed during the 2017–2018 study were part of the 61g episode that erupted from the east flank of Pu'u 'Ō'ō. These flows propagated down the Pulama pali and entered the Pacific Ocean at Kamokuna as a series of pāhoehoe surface lava flow and lava tubes (Figure 3.1) (Orr et al., 2013). The majority of the flows observed were tube-fed pāhoehoe, both sheet-like and ropey in texture. Previous remote sensing studies of the pre-2018 Kīlauea eruption have investigated lava discharge rates (Poland, 2014), lava flow emplacement tracking (Dietterich et al., 2012), and lava pathway mechanisms (Koeppen et al., 2013) all of which could potentially be improved with more accurate thermal measurements. The areas for this study were chosen for the high probability of observing molten lava surfaces combined with the availability of a variety

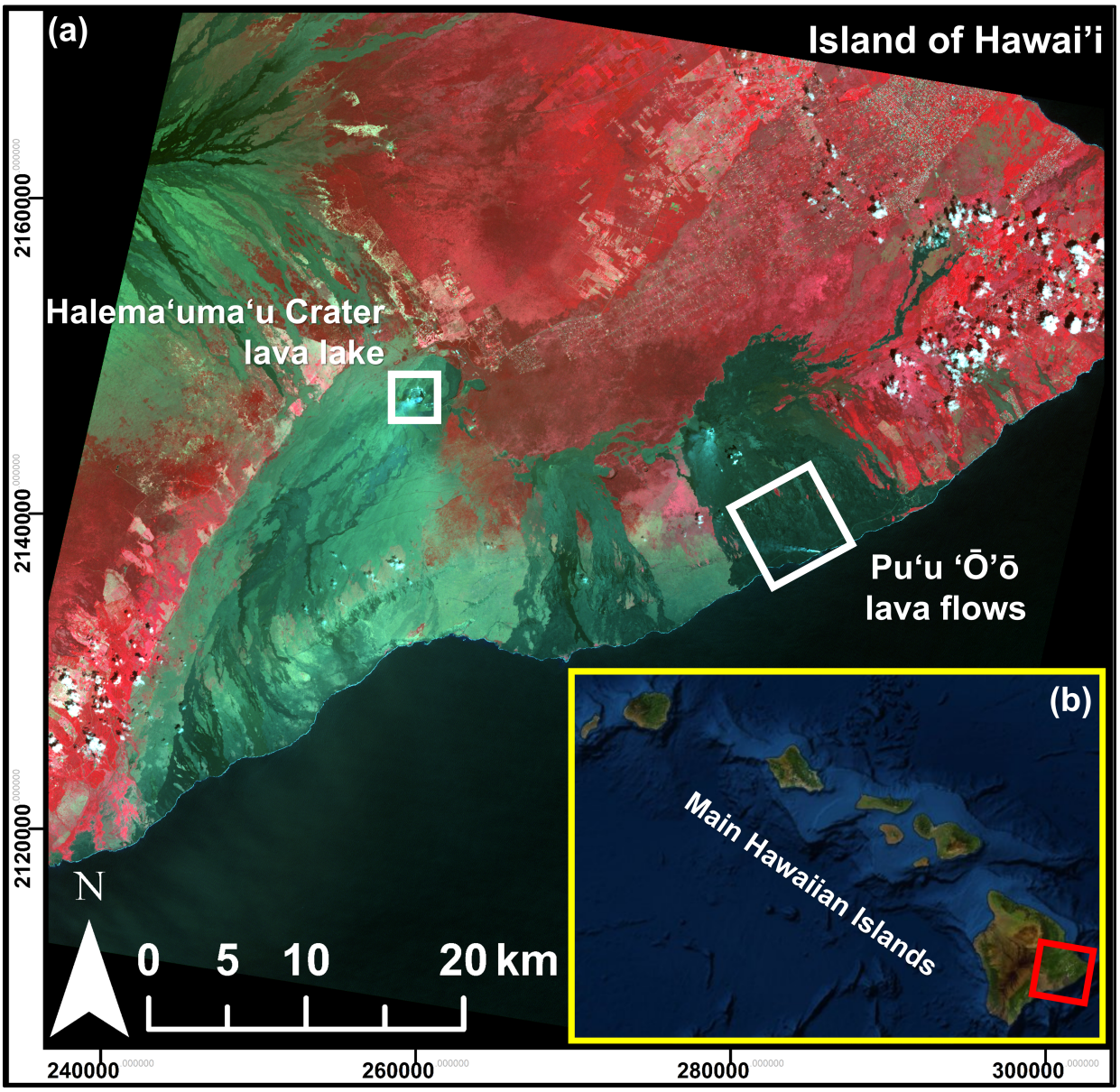

Figure 3.1: (a) Advanced Spaceborne Thermal Emission and Reflection Radiometer (ASTER) visible false-color image (RBG: 0.81 μm, 0.65 μm, and 0.56 μm) of the southeastern region of the Island of Hawai'i, showing the analysis locations of the Halema'uma'u Crater lava lake and Pu'u 'Ō'ō lava flows at Kīlauea volcano (white boxes). The ASTER data were acquired on March 7, 2017, at 20:06:02 UTC (Yamaguchi et al., 1998). (b) Insert shows the entire state of the Hawaiian island chain in the central Pacific Ocean, the red box indicating the area of the ASTER image shown. (Source: ESRI and DigitalGlobe)

of remote sensing TIR datasets.

3.3.2 Remote Sensing Data

3.3.2.1 Instruments

During the field campaigns, TIR data were acquired of the volcanic targets on 22 separate occasions. Of these, simultaneous data from all the instruments were acquired three times (Table 3.1). These included data from ground and airborne instruments made possible by two NASA-sponsored airborne campaigns to Hawai'i in support of a proposed satellite mission data collection/analysis effort. The spaceborne data were acquired by the ASTER instrument, which has been in orbit aboard the Terra satellite since December 1999 (Yamaguchi et al., 1998). Following the failure of the shortwave infrared (SWIR) system in 2008, ASTER is now a two-subsystem instrument with eight bands between 0.52 and 11.65 μm and a spatial resolution between 15 and 90 meters (Yamaguchi et al., 1998). For this study, only the five TIR bands between 8.125 and 11.65 μm with a spatial resolution of 90 meters were used (Table 3.2). The airborne MASTER and HyTES instruments were mounted on a NASA ER-2 aircraft that flew at an altitude of $\sim$20 kilometers. MASTER is a 50-bands instrument that detects radiance between 0.4 and 13.0 μm, with a FOV of 85.92° resulting in a ground spatial resolution of $\sim$50 meters from the flight altitude (Hook et al., 2001). In this study, the seven TIR bands were used between 8.0 and 13 μm (Table 3.2). HyTES is a hyperspectral TIR instrument with 256 bands that detects radiance between 7.5 and 12 μm, with a FOV of 50° resulting in a ground spatial resolution of $\sim$35 meters at an altitude of $\sim$20 kilometers (Johnson et al., 2011). In this study, 128 HyTES bands between 8.3 and 11.6 μm were used due to an instrument calibration resampling (Table 3.2). Finally, the MMT-Cam ground-based system acquired data in six spectral bands plus a broadband temperature band between 8.0 and 11.5 μm, with a FOV of 45° x 37° (Table 3.2) (Thompson et al., 2019).

3.3.2.2 Data Calibration

Before extracting the surface kinetic temperature and emissivity from the various datasets, the raw radiance data were calibrated and corrected for instrumentation and atmospheric effects (Figure 3.2). The ASTER instrument data were radiometrically calibrated by viewing an internal constant temperature blackbody and cold space. Occasionally, the internal blackbody is heated and cooled to provide a multi-temperature radiometric calibration (Yamaguchi et al., 1998). The MASTER

Table 3.1: Atmospheric conditions and target locations during each acquisition data.

Acquisition Data	**Time (UTC)**	**No Data**	**Temperature (Kelvin)**	**Humidity (%)**	**Target**
01/19/2017	6:32	HyTES	301.1	59.8	Lava Lake
01/26/2017	20:59	HyTES	290.5	82.4	Lava Lake
01/30/2018	20:59	-	313.2	25.3	Lava Flow
02/06/2018	21:06	-	301.7	47.9	Lava Lake
02/08/2018	08:42	-	299.6	49.8	Lava Flow

Table 3.2: Instrument specifications.

	MMT-Cam (ground)	**MASTER TIR (airborne)**	**HyTES (airborne)**	**ASTER TIR (spaceborne)**
Detector	VOX microbolometer	HgCdTe photoconductive	QWIP	HgCdTe photoconductive
Field of View	45^o x 37^o	85.92^o	50^o	
Spatial Resolution	0.04 / 0.3 meters	50 meters	35 meters	90 meters
Spectral Resolution	6	9(7)	186	5
Temporal Resolution	1 second	Daily during campaign	Daily during campaign	5-15 days
Radiometric Range	233 to 832 K	245 to 480 K	240 to 455 K	200 to 370 K
Radiometric Accuracy	5%	<5%	<1%	<3%

and HyTES data were corrected for aircraft motion and orthorectified using digital terrain models (Hook et al., 2001; Johnson et al., 2011). The MASTER instrument is spectrally and radiometrically calibrated in the laboratory using two blackbodies pre- and post-campaign, with a cold blackbody used during the data acquisition (Hook et al., 2001). In the laboratory, the HyTES instrument is spectrally calibrated using narrowband interference filters and radiometrically calibrated using a blackbody between 277 and 313 K (Johnson et al., 2011). Finally, the MMT-Cam instrument is spectrally and radiometrically calibrated in the laboratory using a blackbody between 293 and 1073 K (Appendices A - C) (Thompson et al., 2019).

The ASTER, MASTER, HyTES, and MMT-Cam radiometrically calibrated at-sensor TIR radiance data were all atmospherically corrected to derive the at-surface radiance (Figure 3.2). The MASTER and ASTER data were corrected using the MODTRAN radiative transfer model with the water vapor scaling method to optimize the atmospheric correction (Tonooka, 2001). The HyTES data were corrected using the in-scene atmospheric correction method (Young et al., 2002). The MMT-Cam spectral bands were co-registered using a fast Fourier transform algorithm with centroid matching and then atmospherically corrected using the SpectralCalc simulator (Appendix D) (Thompson et al., 2019).

3.4 Methodology

3.4.1 Kinetic Temperature and Emissivity

Kinetic temperature and emissivity were derived from the calibrated surface radiance data using the TES algorithm (Figure 3.2), first developed for ASTER data (Gillespie et al., 1998). The algorithm first assumes a brightness temperature using a maximum scene emissivity and the spectral morphology of each pixel is derived. An emissivity calibration curve relating spectral contrast to the minimum emissivity was then used to constrain the true emissivity values from band ratios. The calibration curve was empirically determined for each instrument separately using data from a laboratory spectral library. Finally, the kinetic temperature was then calculated from the maximum derived emissivity using the inverse Planck function (Gillespie et al., 1998).

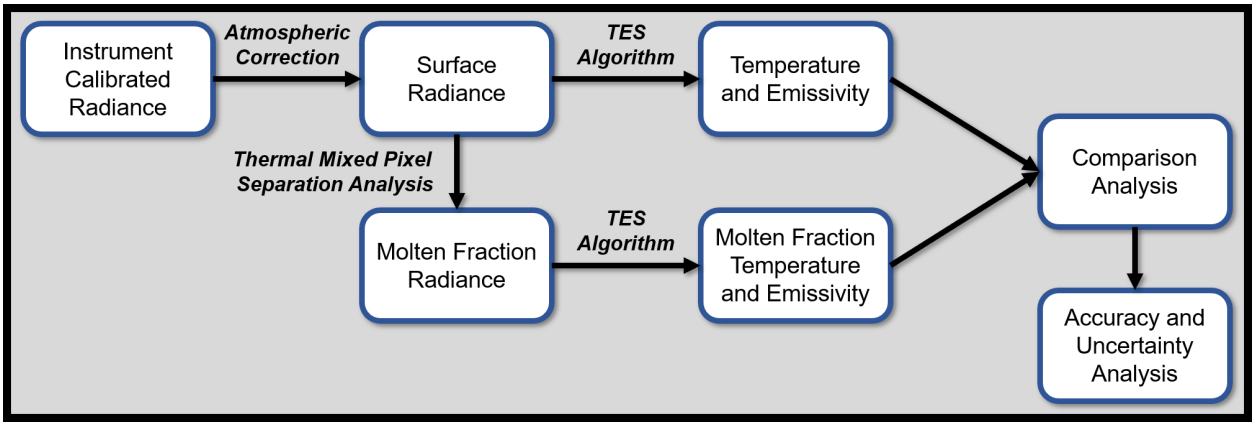

Figure 3.2: A flowchart illustrating the methods used in this study.

3.4.2 Thermally-Mixed Pixel (TMP) Separation Analysis

In most TIR remote sensing data of active volcanic thermal anomalies, a pixel contains multiple surface fractions (or endmembers) that can include temperature, composition, and texture. The spectrum of a mixed pixel composed of two or more fractions represents the areal-weighted averages of those endmembers rather than being dominated by any one (Ramsey and Christensen, 1998). This problem increases in complexity with lower spatial resolution data and the increased mixing of potentially more surface fractions (Harris, 2013). However, the endmembers within any given pixel can be deciphered with knowledge of radiance theory, a well-developed spectral deconvolution model, and an understanding of the spectral signatures of the endmembers (e.g., an endmember spectral library).

A straightforward solution to the thermally-mixed pixel problem was originally developed by Dozier (Dozier, 1981) using a dual-band approach to define the two thermal fractions within a pixel (Figure 3.2). The method uses surface radiance values from two spectral bands to derive the unique combination of each fraction, both the value and proportion:

$$M_{(\lambda_n,T_{int})} = p \cdot M_{(\lambda_n,T_h)} + (1-p) \cdot M_{(\lambda_n,T_b)} \tag{3.1}$$

where $M_{(\lambda_n,T_{int})}$ is the mixed surface radiance in band n for the mixed temperature (T_{int}). $M_{(\lambda_n,T_h)}$ and $M_{(\lambda_n,T_b)}$ are the surface radiances contributed by the hot temperature fraction and background temperature fraction, respectively; and p is the proportion of the hot fraction within the pixel area (Dozier, 1981; Matson and Dozier, 1981). Equation (3.1) was solved with two simultaneous

equations at two different wavelength bands, each containing two unknown variables. This approach provides a unique solution for the radiance of one fraction (either molten lava or the background) and its fractional proportion after assuming or knowing the value for the other radiance value.

In this study, the surface radiance values were unmixed within each pixel for each dataset using a band at 8.5 μm and 11.0 μm. The background fraction applied to the analysis was the average value of the non-active regions for each scene and each band in the dataset. After the thermal mixed pixel (TMP) separation analysis was applied, the molten fraction datasets were integrated into the TES algorithm in order to only derive kinetic temperature and emissivity of the molten fractions (Figure 3.2). These values for each pixel were then compared to the results from the same pixels prior to the unmixing analysis. Finally, the variability within each dataset was quantified to evaluate the effect of spatial and spectral resolution on the discrepancies and uniqueness.

3.4.3 Accuracy and Uncertainty Assessment

The accuracy and degree of variability of the measured surface radiance as well as the derived kinetic temperature and emissivity for each TIR dataset were quantified through comparative analysis (Figure 3.2). The TMP separation analysis approach was held as constant as possible to evaluate only the influence of spatial resolution. After spatial resolution, the largest variability between the datasets was the spectral resolution, which has less of an effect because the band locations are commonly within 0.5 μm of each other. The hyperspectral resolution of the HyTES data increases the level of complexity for the comparative analysis to the multispectral resolution datasets. All analyses on the HyTES data were computed at full resolution, however, these results were then spectrally degraded to perform the later comparison. The HyTES data also provide a spectral resolution comparison with the MASTER data acquired at the same time and at a similar spatial resolution, which allows the influence of spectral resolution to be quantified. Finally, the sensitivity of spatial resolution on the derived kinetic temperature and emissivity was determined to quantify constraints on the degree of uncertainty with spatial resolution change.

3.5 Results

3.5.1 ASTER Data

Two regions of interest (ROI) of cooling lava surfaces (the lava lake at the Halema'uma'u Crater and the lava flows from Pu'u 'Ō'ō on the coastal plain) were chosen to evaluate the retrieval of surface radiance, kinetic temperature, and emissivity from the ASTER data. Within these ROIs, mixtures of both the cool crust and molten lava surfaces were represented in most pixels (Figure 3.3).

The ASTER surface radiance of the active lava was lower than expected for molten basalt (Figure 3.4) with an average of 19.7 $W \cdot m^{-2} \cdot sr^{-1} \cdot \mu m^{-1}$ and a variability of 5.9 $W \cdot m^{-2} \cdot sr^{-1} \cdot \mu m^{-1}$. The emissivity spectra had an absorption feature at 8.63 μm and higher spectral contrast in the lava lake data. The average pixel-integrated emissivity was 0.898 with a variability of 0.077 (Figure 3.4), whereas the average pixel-integrated kinetic temperature was 354 K with a variability of 24 K; both of which were significantly lower than expected for molten basaltic lavas (Abtahi et al., 2002; Lee et al., 2009; Harris, 2013).

3.5.2 MASTER and HyTES Data

The same two ROIs were selected in the MASTER and HyTES data; however, the number of pixels that constitute each of these were higher by a factor of approximately three compared to the ASTER analysis (Figure 3.3).

The MASTER surface radiance was also lower than expected for the temperatures of molten basalt (Figure 3.4) with an average of 25.8 $W \cdot m^{-2} \cdot sr^{-1} \cdot \mu m^{-1}$ and variability of 8.9 $W \cdot m^{-2} \cdot sr^{-1} \cdot \mu m^{-1}$. The pixel-integrated emissivity spectra had a narrow absorption feature at 8.63 μm and a broader absorption feature around 10.63 μm (Figure 3.4). The average emissivity was 0.723 with a variability of 0.130. The average pixel-integrated kinetic temperature was 425 K with a variability of 64 K.

The HyTES surface radiance data were lower than those extracted from MASTER over the lava flows but greater over the lava lake (Figure 3.4). The average surface radiance was 34.8 $W \cdot m^{-2} \cdot sr^{-1} \cdot \mu m^{-1}$ with a variability of 13.8 $W \cdot m^{-2} \cdot sr^{-1} \cdot \mu m^{-1}$. The emissivity spectra had an absorption feature at $\sim$9.48 μm (Figure 3.4). The average pixel-integrated emissivity was 0.805 with a variability of 0.114, and lower values were derived from the lava lake; whereas the average

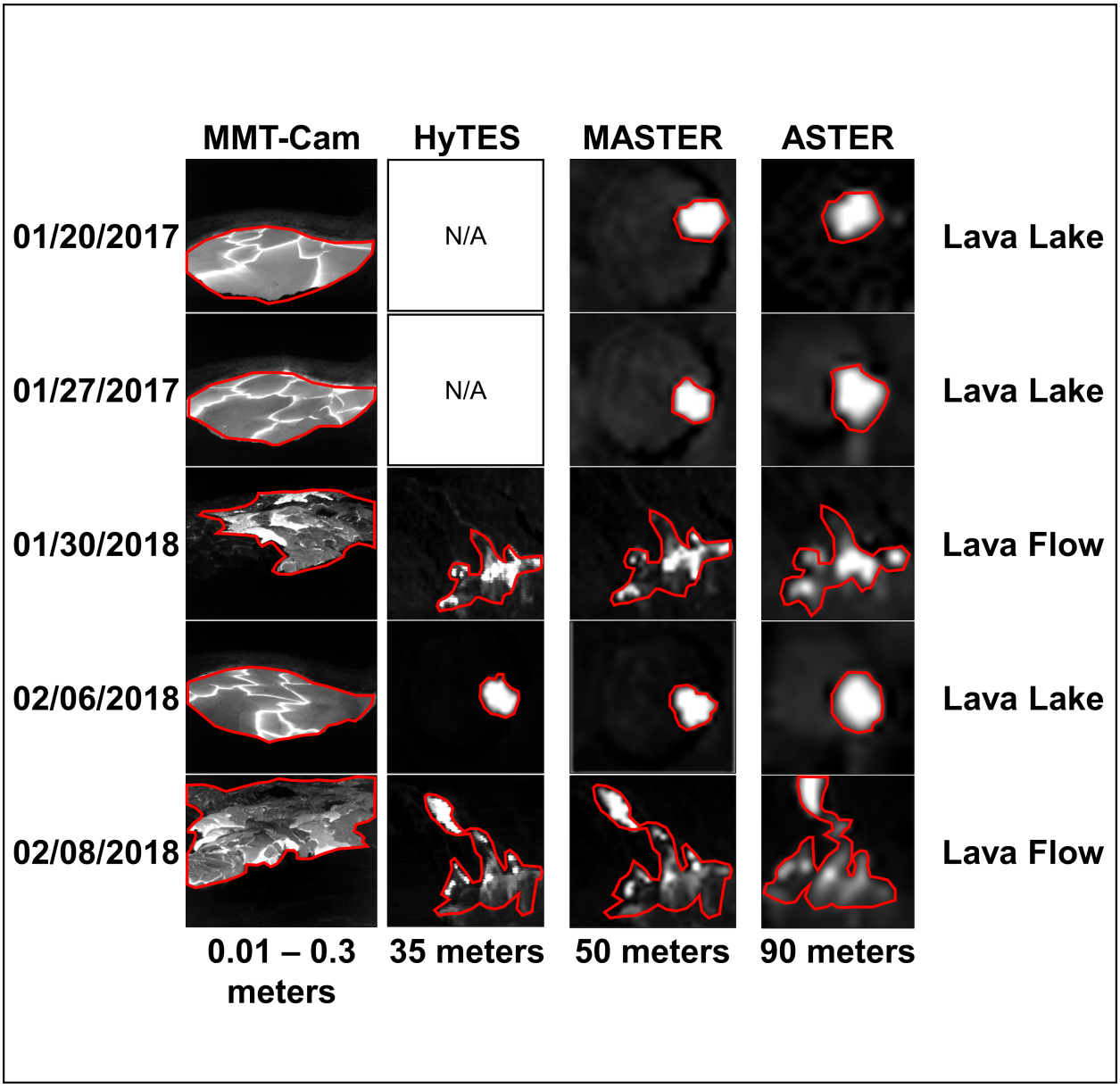

Figure 3.3: Examples of the TIR surface radiance data acquired of the Halema'uma'u Crater lava lake and Pu'u 'Ō'ō lava flows from the different datasets at ∼11.3 μm. Data from 01/20/2017, 01/30/2018, and 02/06/2018 were acquired during the day (∼20:00 UTC) and data from 01/20/2017 and 02/08/2018 were acquired during the night (∼07:45 UTC). The HyTES instrument was not flown in 2017. The red polygons represent the ROIs used in the analysis.

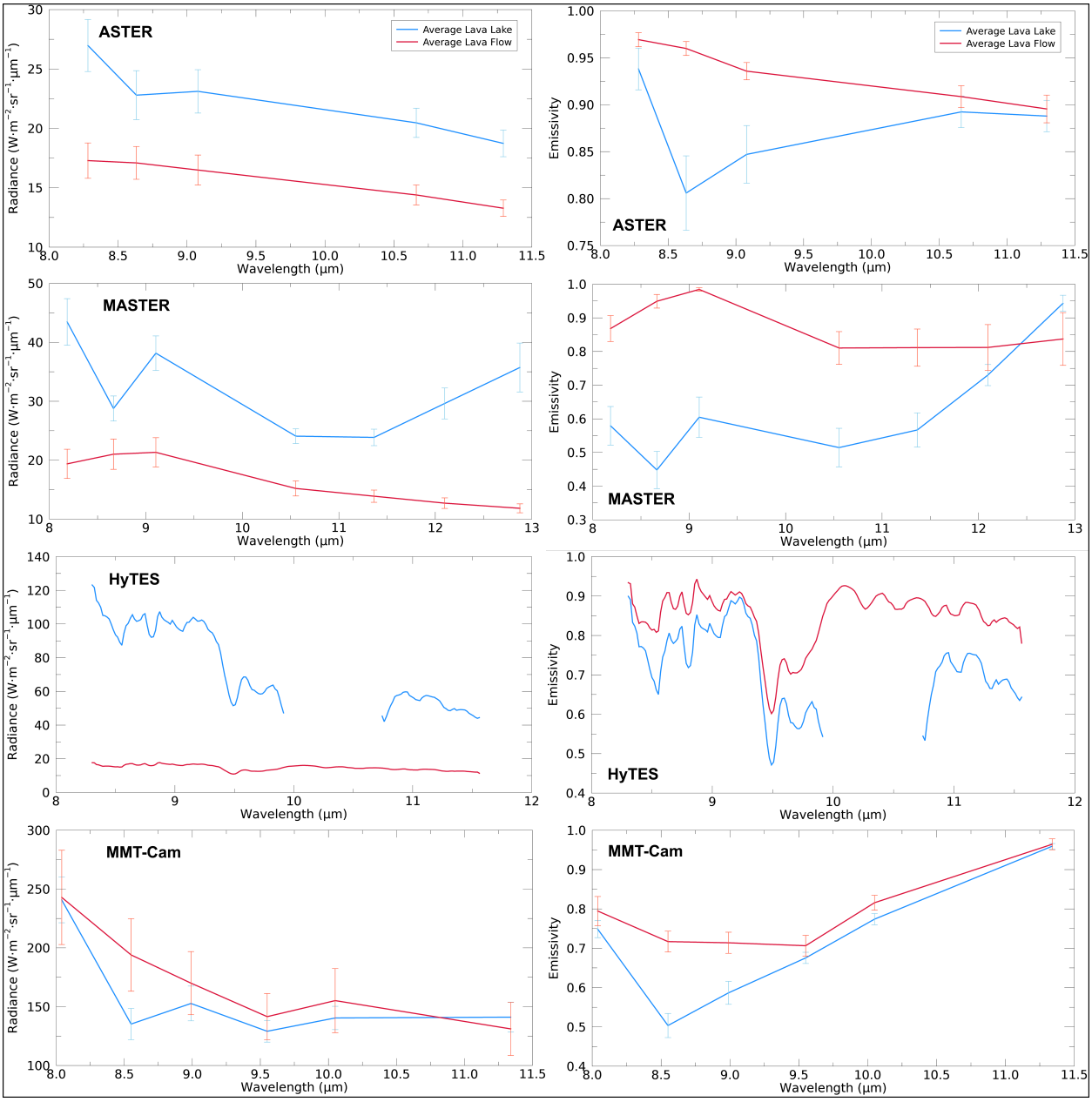

Figure 3.4: (left column) Average mixed pixel surface radiance and (right column) emissivity spectra acquired at the Halema'uma'u Crater lava lake (blue) and Pu'u 'Ō'ō lava flows (red) derived from ASTER TIR, MASTER TIR, HyTES, and MMT-Cam data. The error bars represent the standard deviation variation in the ROIs. Note there were no HyTES data between 9.92 and 10.75 μm on 02/08/2018 so these data were not included in the lava lake plots.

pixel-integrated kinetic temperature was 408 K with a variability of 33 K. These values were also lower than the MASTER-derived temperatures, but at a lower variability.

3.5.3 MMT-Cam Data

The MMT-Cam data presented here were extracted from ROIs covering similar activity as the airborne and spaceborne data ROIs, especially at the lava lake (Figure 3.3). The lava flow ROIs, however, were significantly smaller but more spatial details were observed in these data due to the high spatial resolution (<0.1 meters). The radiance and kinetic temperatures derived from the MMT-Cam data were higher than the other datasets analyzed in the study, as expected.

The radiance derived from the MMT-Cam ROIs was closer to the values for molten basalt at the wavelengths and bandwidths of the MMT-Cam instrument (Figure 3.4). The average was 162.9 $W \cdot m^{-2} \cdot sr^{-1} \cdot \mu m^{-1}$ with a variability of 76.3 $W \cdot m^{-2} \cdot sr^{-1} \cdot \mu m^{-1}$. The emissivity spectra show a strong absorption between 8.55 and 9.55 μm, with both a single broad feature and two narrow features (Figure 3.4). The average pixel-integrated emissivity was 0.739 with a variability of 0.087, and the average pixel-integrated kinetic temperature was 736 K with a variability of 163 K.

3.5.4 Mixed Pixel Derivation

All the TIR datasets were next subjected to TMP separation analysis to extract the values associated with the maximum thermal fraction within each pixel (e.g., molten lava). This step evaluates the ability to measure an accurate molten fraction (if one was present) regardless of spatial scale within a given pixel and the radiance values associated with it. The background radiance values applied to this analysis were calculated from the average values of pixels at the background temperature for each band of each dataset and observation. The largest difference between the original data and the unmixed counterparts was observed in the ASTER data and the smallest was seen in the MMT-Cam data, as might be expected based on pixel sizes.

Following the mixed pixel derivations using an average background radiance of 8.2 $W \cdot m^{-2} \cdot sr^{-1} \cdot \mu m^{-1}$, the average ASTER surface radiance for the molten fraction increased to 493.2 $W \cdot m^{-2} \cdot sr^{-1} \cdot \mu m^{-1}$ as did the variability to 191.6 $W \cdot m^{-2} \cdot sr^{-1} \cdot \mu m^{-1}$ (Figure 3.5). The emissivity spectra had an absorption feature at 8.63 μm (except in one lava flow dataset) with a strong decrease in emissivity at shorter wavelengths (Figure 3.5). The absorption feature observed at 8.5-9.0 μm was associated with a molten Si-O absorption and was likely absent in the ASTER lava flow data due

to the very low molten fractions (<0.05) observed with pixels at this target. The average molten fraction emissivity was 0.752 with a variability of 0.099; whereas the average molten fraction kinetic temperature was 1242 K with a variability of 337 K.

For the unmixed MASTER data using an average background radiance of 8.4 $W \cdot m^{-2} \cdot sr^{-1} \cdot \mu m^{-1}$, the average surface radiance derived for the maximum thermal fraction was 300.6 $W \cdot m^{-2} \cdot sr^{-1} \cdot \mu m^{-1}$ with a variability of 111.5 $W \cdot m^{-2} \cdot sr^{-1} \cdot \mu m^{-1}$ (Figure 3.5). The emissivity spectra from the lava lake show an absorption feature at 8.63 μm and the lava flow ROIs show a broad absorption feature at 10.63 μm with a decrease at wavelengths shorter than 9.09 μm (Figure 3.5). The average molten fraction emissivity was 0.584 with a variability of 0.141; whereas the average molten fraction kinetic temperature was 1128 K with a variability of 408 K.

Using an average calculated background radiance of 8.0 $W \cdot m^{-2} \cdot sr^{-1} \cdot \mu m^{-1}$, the average HyTES surface radiance derived for the molten fraction was 402.6 $W \cdot m^{-2} \cdot sr^{-1} \cdot \mu m^{-1}$ with a variability of 146.7 $W \cdot m^{-2} \cdot sr^{-1} \cdot \mu m^{-1}$. The emissivity spectra show an absorption feature at around 9.5 μm and a broader feature centered at 9.75 μm, with a decrease in overall emissivity at shorter wavelengths (Figure 3.5). The average molten fraction emissivity and kinetic temperature values were 0.604 and 1266 K with variabilities of 0.260 and 404 K, respectively.

Lastly, using an average background radiance of 15.3 $W \cdot m^{-2} \cdot sr^{-1} \cdot \mu m^{-1}$, the average molten surface radiance derived from the MMT-Cam data was 454.3 $W \cdot m^{-2} \cdot sr^{-1} \cdot \mu m^{-1}$ with a variability of 158.1 $W \cdot m^{-2} \cdot sr^{-1} \cdot \mu m^{-1}$. The derived lava lake emissivity spectra show a single absorption feature between 8.55 and 8.99 μm or a doublet feature at 8.55 and 9.55 μm (Figure 3.5). The lava flow emissivity decreased at less than 10.05 μm and was centered at 8.55 μm (Figure 3.5). The average molten fraction emissivity and kinetic temperature values were 0.711 and 1226 K with variabilities of 0.078 and 330 K, respectively.

3.5.5 Comparisons and Trends

Qualitatively, significant variations were observed between the four datasets as a consequence of differences in spatial resolutions (Figure 3.3). The lower spatial resolution ASTER data provide the least lava surface detail, whereas the high-resolution MMT-Cam data provide the greatest details. For example, crustal plates and molten spreading margins at the lava lake were observed in the MMT-Cam data but not in the ASTER data (Figure 3.3). However, the entire lava flow field was underrepresented in the MMT-Cam data due to the proximity of the instrument to the

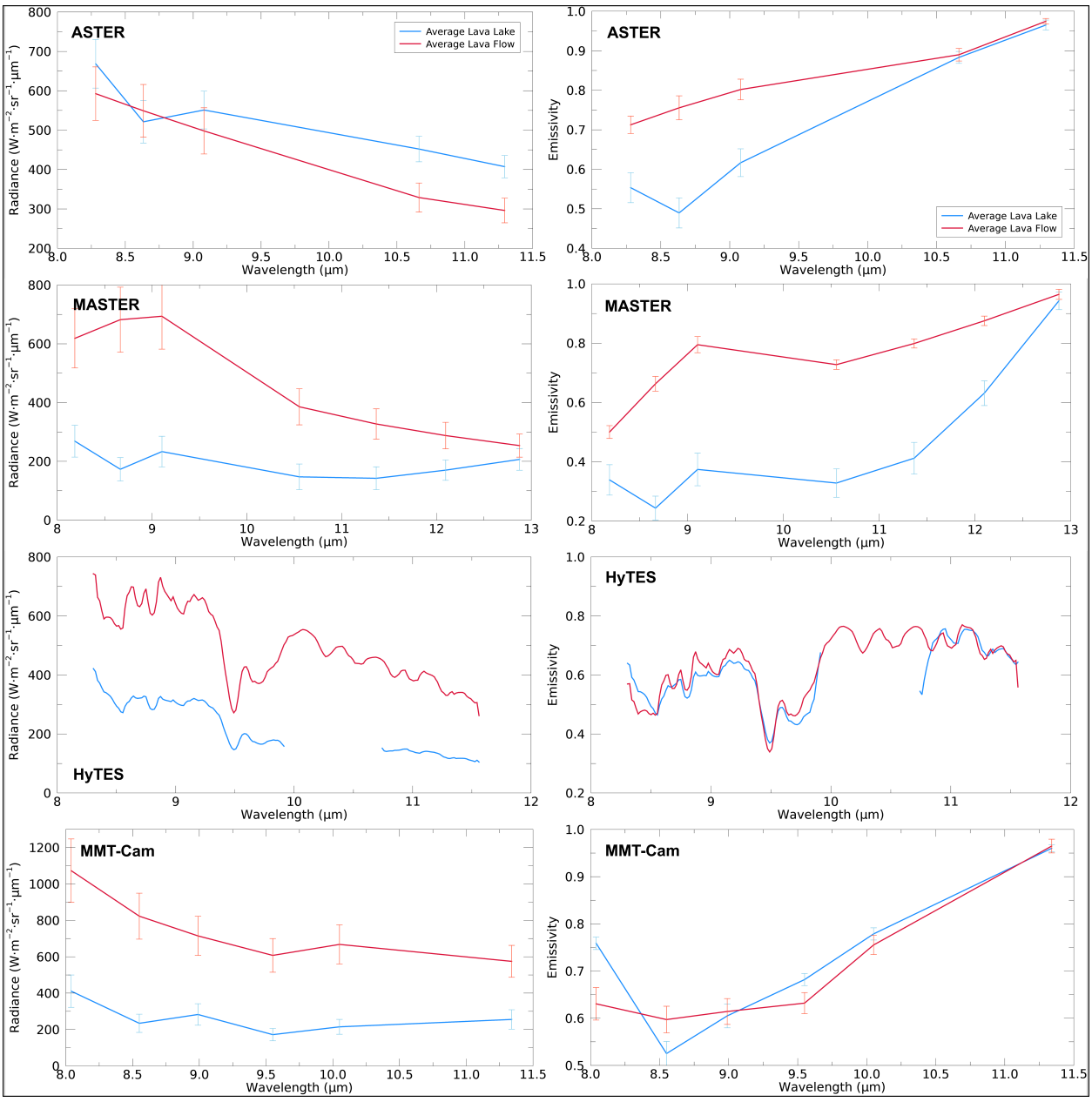

Figure 3.5: (left column) Average molten pixel fraction surface radiance and (right column) emissivity spectra acquired of the Halema'uma'u Crater lava lake (blue) and Pu'u 'Ō'ō lava flows (red) derived from the thermal mixed pixel molten fraction of the ASTER TIR, MASTER TIR, HyTES, and MMT-Cam data. The error bars represent the standard deviation variation in the ROI data. Note there were no HyTES data between 9.92 and 10.75 μm on 02/06/2018 so these data were not included in the lava lake plots.

target. Additionally, greater spatial details of lava surface features were discerned in the HyTES data compared to the MASTER data, likely the result of a higher number of spectral bands (Figure 3.3). In general, the spatial resolution of the instrument strongly correlates to the scale of spatial detail qualitatively observed of the lava surfaces.

In all datasets, the surface radiance increases after the TMP separation analysis as would be expected. The ASTER surface radiance increases the most in the lava lake (2100%) and lava flow (2700%) data, compared to only a 70% and 330% increase in the MMT-Cam data, respectively (Figures 3.6 and Table 3.3). The MASTER and HyTES surface radiances increase by 500% and 200% in the lava lake data and 2800% and 3200% in the lava flow data, respectively. The highest increases were observed at shorter wavelengths (Figure 3.6), which is consistent with Wein's Law where the peak radiance shifts to shorter wavelengths with increasing temperature (Harris, 2013). The TMP separation analysis appears to provide a consistent and reasonable method for extracting the higher temperature molten fractions and allows more accurate values of surface radiance, kinetic temperature, and emissivity to be extracted from the lower spatial resolution datasets.

In general, the pixel-integrated temperatures derived from data prior to the TMP separation analysis show an inverse relationship with spatial resolution, with the larger pixels potentially containing the smallest fraction of molten lava. The ASTER data had the lowest kinetic temperatures and the MMT-Cam had the highest. Compared with the 35-meter spatial resolution HyTES data, however, the 50-meter spatial resolution MASTER data had a higher derived pixel integrated temperature but at a higher variability. All the kinetic temperatures derived from the mixed-pixel data were significantly below that expected for a molten basaltic lava surface ($\sim$1450 K). In contrast, the average derived molten fraction temperature in every dataset was above 1100 K, significantly closer to what is expected for molten basaltic lava. Unmixing the HyTES data produced the highest average molten fraction temperature (1266 K) but with a high variability (404 K), implying there is still significant uncertainty at 35-meter resolution. The MMT-Cam derived molten fraction temperatures span the liquidus temperatures of basaltic lava at the lowest variability, which provides the highest constraint on the derived data. The integration of the TMP calculation into the derivation of temperature improves the accuracy of the measured kinetic temperature associated with the molten lava fraction in all the datasets.

Emissivity spectra derived from these data before the TMP separation analysis had similar spectral morphologies to laboratory-derived results of molten basalts (Abtahi et al., 2002; Lee et al., 2009, 2013). However, the spectral contrast was less than expected from laboratory results,

Table 3.3: The combined spatial and spectral average emissivity and kinetic temperature values pre- and post-thermal mixed pixel (TMP) separation analysis within each ROI for each dataset, including the percentage improvement.

		ASTER TIR	MASTER TIR	HyTES	MMT-Cam
Radiance $(W \cdot m^{-2} \cdot sr^{-1} \cdot \mu m^{-1})$	**Pre-TMP**	19.7 (5.9)	25.8 (9.0)	34.8 (13.8)	162.9 (76.3)
	Post-TMP	493.2 (191.6)	300.6 (111.5)	402.6 (146.7)	454.3 (158.1)
	Change	2400%	1070%	1060%	180%
Emissivity	**Pre-TMP**	0.898 (0.077)	0.723 (0.130)	0.805 (0.114)	0.739 (0.087)
	Post-TMP	0.752 (0.099)	0.584 (0.141)	0.604 (0.260)	0.711 (0.078)
	Change	19%	23%	33%	4%
Temperature (Kelvin)	**Pre-TMP**	354 (24)	425 (64)	408 (33)	736 (163)
	Post-TMP	1242 (337)	1128 (408)	1266 (404)	1226 (330)
	Change	250%	170%	210%	70%

[1]The values in parenthesizes represent the standard deviation variation in the data.

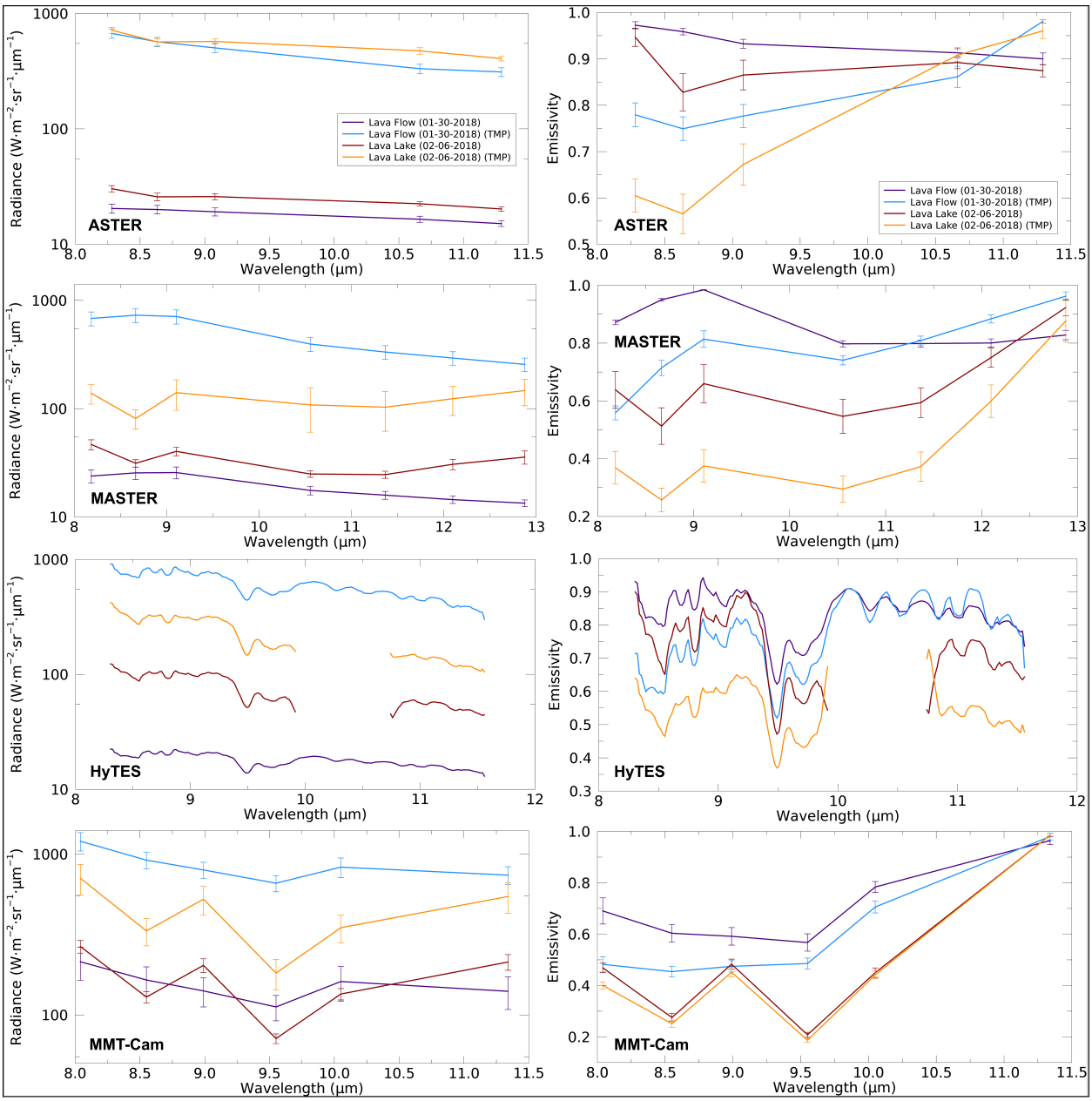

Figure 3.6: Comparison of (left column) surface radiance and (right column) emissivity pre- and post- TMP separation of the molten fraction derived from all the datasets acquired of the Halema'uma'u Crater lava lake on February 6, 2018, and Pu'u 'Ō'ō lava flows on January 30, 2018. The error bars represent the standard deviation variation in the ROI data. Note there were no HyTES data between 9.92 and 10.75 μm on 02/06/2018 so these data were not included in the lava lake plots.

by up to 40% for ASTER (Figure 3.6). The MMT-Cam emissivity values were less than 15% shallower than laboratory data, with the MASTER and HyTES emissivity values being within 20–30% (Figure 3.6). Following the TMP separation analysis, the spectral depths and contrasts increased to values consistent with those derived from laboratory experiments (Figure 3.6) (Abtahi et al., 2002; Lee et al., 2009, 2013). The spectral morphology remained similar with a decrease in emissivity at shorter wavelengths and an increase at longer wavelengths. These results were also more exaggerated in the lava flow data (Figure 3.6), implying that there is high thermal mixing within a pixel representing the lava flow than the lava lake. For example, the improvement in the ASTER data highlights an absorption feature centered at ∼8.5 μm with an increase in emissivity at longer wavelengths compared to absorption features centered at ∼8.0 μm and ∼10.5 μm in the improved MMT-Cam data. The improvements were attributed to variations in spatial and spectral resolution between the two instruments, as well as the difference in band locations that resolve slightly different Si-O bonding and bending. Similar trends were also detected in the HyTES and MMT-Cam data.

3.6 Discussion

Developing a methodology to extract only the molten fraction within every pixel of these datasets and constrain the uncertainty improves the subsequently-derived TIR measurements required for monitoring, scientific analysis, and later modeling studies. The results from the TMP separation analysis show that greatly improved radiance, kinetic temperature, and emissivity values can be extracted at different spatial and spectral resolutions. This methodology can be implemented to a variety of data quickly and uncertainties quantified. The TMP separation analysis is not new but has had limited application in volcanic hazard prediction models and assessments. Prior studies have shown that typical lava surfaces have multiple thermal fractions (up to 8) at moderate spatial resolutions (Realmuto, 1990; Flynn et al., 2001; Wright and Flynn, 2003). However, the processing required to analyze these fractions can be daunting at the scale of an entire flow field or slow in the case of an ongoing eruption. Furthermore, there is a somewhat limited applicability for this level of multiple fraction analysis in current lava flow propagation models where only the maximum molten fraction has the greatest influence on model results (Harris and Rowland, 2001; Favalli et al., 2005). Therefore, improving the analysis of remote sensing data to provide rapid kinetic temperature and

emissivity values of the highest temperature fractions within TIR image pixels will greatly improve and further constrain lava flow propagation models.

3.6.1 Emissivity

The spatial resolution of the TIR datasets have only a limited effect on the morphology of the emissivity spectra but does strongly influence the spectral depth. This result shows that the efficiency of radiative heat flux from a molten surface was overestimated in TIR data at higher spatial resolutions. The emissivity spectra of the molten fraction show improved accuracy in the spectral contrast to those values expected for molten basaltic lava surfaces within the uncertainty calculated (Figure 3.6). The average minimum emissivity decreases by 20%, with the largest decrease observed in the HyTES data (33%) and the smallest decrease observed in the MMT-Cam data (4%). Additionally, larger decreases in emissivity were observed at shorter wavelengths in all the datasets (Figure 3.6), which highlights the non-uniform influence of kinetic temperature on emissivity and the non-uniform mixing of thermal properties within a pixel. Our results show that for future TIR studies of molten basaltic surface, a more appropriate value for the minimum emissivity would be 0.66 rather than the common values of 0.95 to 1.0 used in prior studies (e.g., Abtahi et al. 2002; Harris et al. 2005; Wright et al. 2008; Harris et al. 2010; Ramsey et al. 2019) and thermo-rheological models of lava flow propagation (e.g., Harris and Rowland 2001; Favalli et al. 2005). This minimum emissivity value was consistent with a previous study of 0.55 for a cooling basaltic lava from Pu'u 'Ō'ō at 1323 K (Abtahi et al., 2002) and a laboratory study of melts (albeit silicic ones) that measured emissivity of 0.68 at 1573 K (Lee et al., 2013). However, the use of these higher maximum emissivity values used in these past studies of cooled basaltic lava surfaces is appropriate given the results calculated in this study. The TMP separation analysis ability to identify the molten fractions within a pixel provides a useful approach for deriving and evaluating the actual emissivity of molten surfaces using a variety of TIR instruments independent of spatial and spectral resolution.

3.6.2 Kinetic Temperature

The maximum temperatures derived from all the datasets following the TMP separation are closer to the liquidus temperatures of Hawaiian basalt (Putirka, 1997), within the variability of the data (Table 3.3). The analysis improves the derived kinetic temperatures by up to 250%

(ASTER TIR) and 70% in the MMT-Cam data. Although the eruption temperatures of Hawaiian basalts are well-known from past direct measurements and petrologic analysis, the variability in the temperatures from this approach is critical for evaluating the uncertainty in subsequent studies that rely upon these measurements. The quantification of the temperature uncertainty increases the confidence and understanding of models that use these measurements, allowing more informed conclusions to be drawn from forecasting estimates.

3.6.3 Accuracy Assessment

The ability to measure accurate thermal properties of a surface from calibrated TIR data is influenced by numerous instrument factors including the spatial, spectral, and temporal resolution of the data as well as external factors such as the spatiotemporal variability of the surface itself. Molten lava surfaces vary, over seconds to minutes and centimeters to meters scales, either through lava flow propagation (breakouts) or lava lake overturning. To analyze the influence of spatial and temporal resolution, a variety of TIR datasets with different resolutions were needed. Most importantly, the new MMT-Cam data were used to validate the lower resolution datasets and determine whether both the anomalies and processes (e.g., lava lake overturning and flow crustal formation/-morphology) were captured in the data (Walker, 1993). Typically, lower spatial resolution increases thermal aggregation that leads to an increase in variability and a decrease in the ability to quantify the small-scale details.

Our analysis shows that the airborne and spaceborne data provide reliable and accurate results of the larger-scale anomalies and processes. Typically, anomalies 1.5 to 2 times the size of the spatial resolution of the datasets are required for more accurate estimates of kinetic temperature and emissivity to be derived, whereas even larger volcanic processes are required to be discerned individually. For example, the $\sim$200 meter diameter lava lake and $>$100 meter long lava flows provide good targets for anomaly detection; however, the overturning ($<$50 meters) and crustal formation ($<$1 meter) observed within these active lava regions are not identified in ASTER data and rarely in the airborne TIR data.

The temporal resolution also significantly influences the reliability of the TIR data, especially if the repeat time is greater than hours (which is the case for the ASTER and airborne instruments). For example, the time scale of a lava lake overturning cycle is approximately 10's of minutes in duration and crustal formation is between seconds and minutes in duration, which are poorly

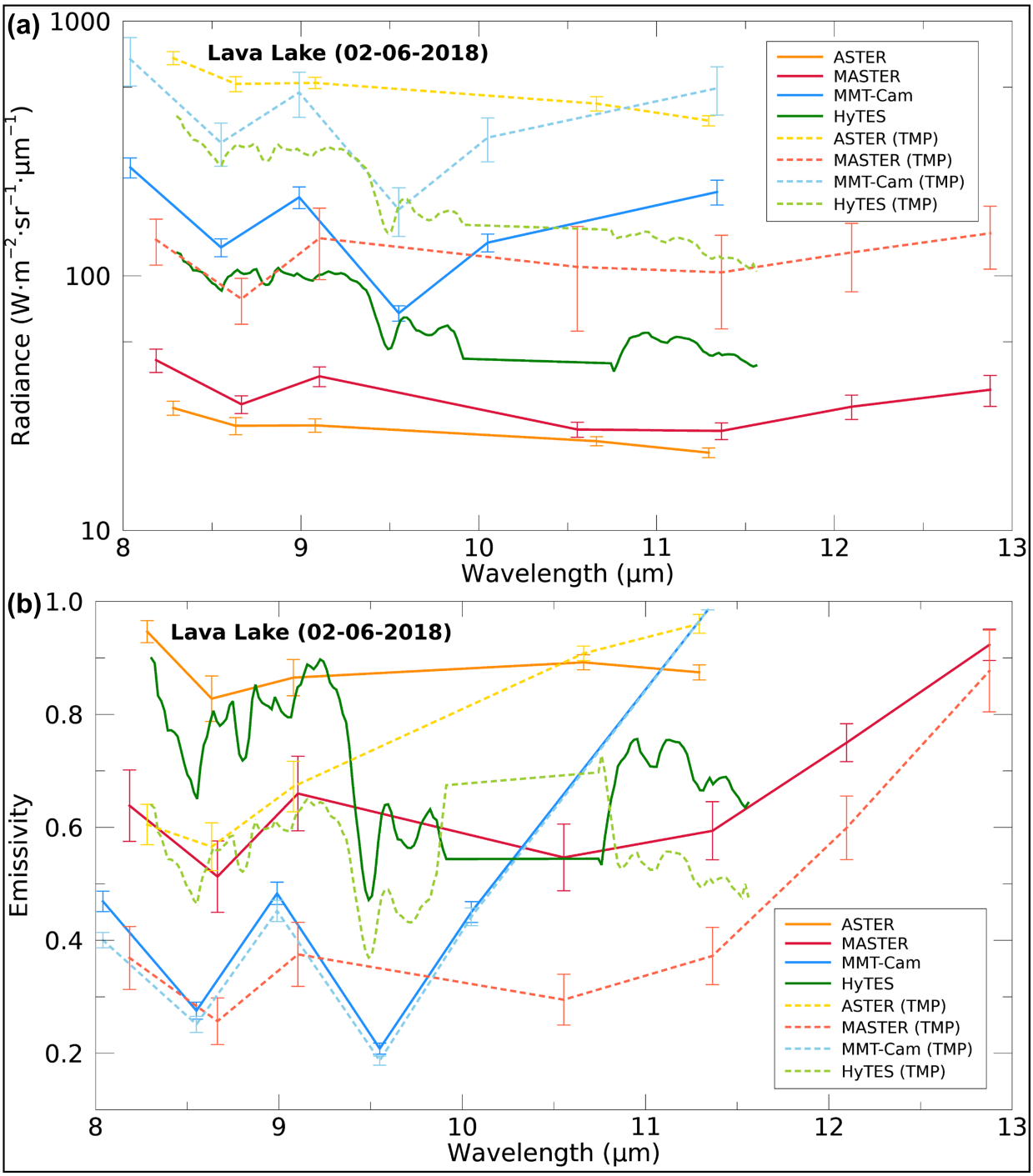

Figure 3.7: The difference between the pre- (solid lines) and post- (dashed lines) TMP separation of the molten fraction for the (a) surface radiance and (b) emissivity at the Halema'uma'u Crater lava lake acquired on February 6, 2018. The error bars represent the standard deviation variation in the ROI data. Note there are no HyTES data between 9.92 and 10.75 μm on 02/06/2018 so these data are not included in the lava lake plots.

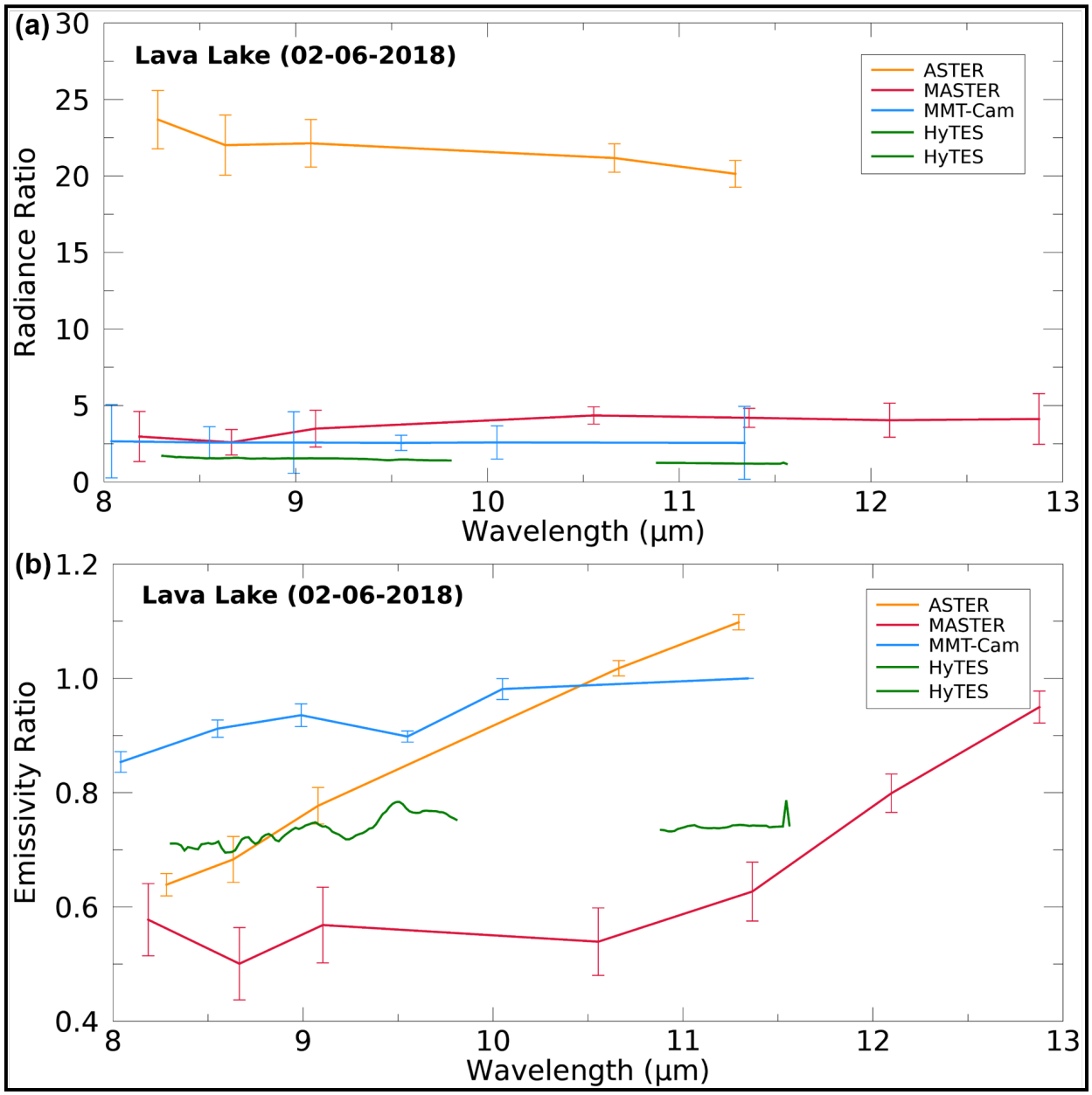

Figure 3.8: The ratio between the pre- and post-TMP separation of the molten fraction for the (a) surface radiance and (b) emissivity for the Halema'uma'u Crater lava lake acquired on February 6, 2018. Values closer to 1.0 require less TMP separation processing. The error bars represent the standard deviation variation in the ROI data. Note there are no HyTES data between 9.92 and 10.75 μm on 02/06/2018 so these data are not included in the lava lake plots.

captured by spaceborne and airborne instruments. As a result, these data underestimate the percentage of molten lava on the surface and lack accuracy in radiance, kinetic temperature, and emissivity measurements. Compared to the MMT-Cam TMP separation analysis, the same analysis of the airborne and spaceborne data underestimates the surface radiance by as much as 430% and 800%, respectively (Figures 3.4, 3.7, 3.8, 3.9, and 3.10). This translates to a lava emissivity error of 5% and 20% with a corresponding kinetic temperature error of 80% and 120%, respectively (Figures 3.4, 3.7, 3.8, 3.9, and 3.10). Separately evaluating the lava lake and lava flow data reveals the airborne and spaceborne data of the lava lake are 30% more accurate compared to the lava flow data, mainly due to the larger spatial scale and more uniform surface state of the lake (Figures 3.4, 3.7, 3.8, 3.9, and 3.10).

Larger pixel sizes also have a higher probability of integrating more than one surface thermal signature, which leads to errors in the data analysis and ultimately subsequent results. The dual-band mixed pixel approach is one possible solution and results showed that it does improve the deviation of thermal properties of molten lava surfaces (Figures 3.7, 3.8, 3.9, and 3.10). Through integration of this technique on medium spatial resolution datasets, the molten surface radiance values are all within 25% of the MMT-Cam values, an improvement of up to 300% (Figures 3.7, 3.8, 3.9, and 3.10). The molten emissivity and kinetic temperature values derived from the airborne and spaceborne data are all within 25% and 10% of the MMT-Cam values (Figures 3.7, 3.8, 3.9, and 3.10), respectively, and more consistent with laboratory and field measurements (Putirka, 1997; Abtahi et al., 2002; Lee et al., 2009, 2013).

3.6.4 Implication and Reasons for Uncertainty

The results extracted from the lava flow data before and after the TMP separation analysis were less uniform across all wavelengths compared to the lava lake data (Figures 3.7, 3.8, 3.9, and 3.10). The ratio of pre- versus post-TMP analysis was higher at shorter wavelengths in the surface radiance data and lower at shorter wavelengths in the emissivity data as expected from the relationship derived in the Planck equation. This ratio is closer to one at longer wavelengths for all the thermal properties, implying the thermal mixing is less of a factor at these wavelengths, again, as predicted based on the mixing of multi-temperature emissions within a pixel. The non-uniform ratio in the lava flow data (most notable at larger pixel sizes) implies a more complex mixing and distribution of thermal fractions and a greater uncertainty in these properties at shorter wavelengths. Hence,

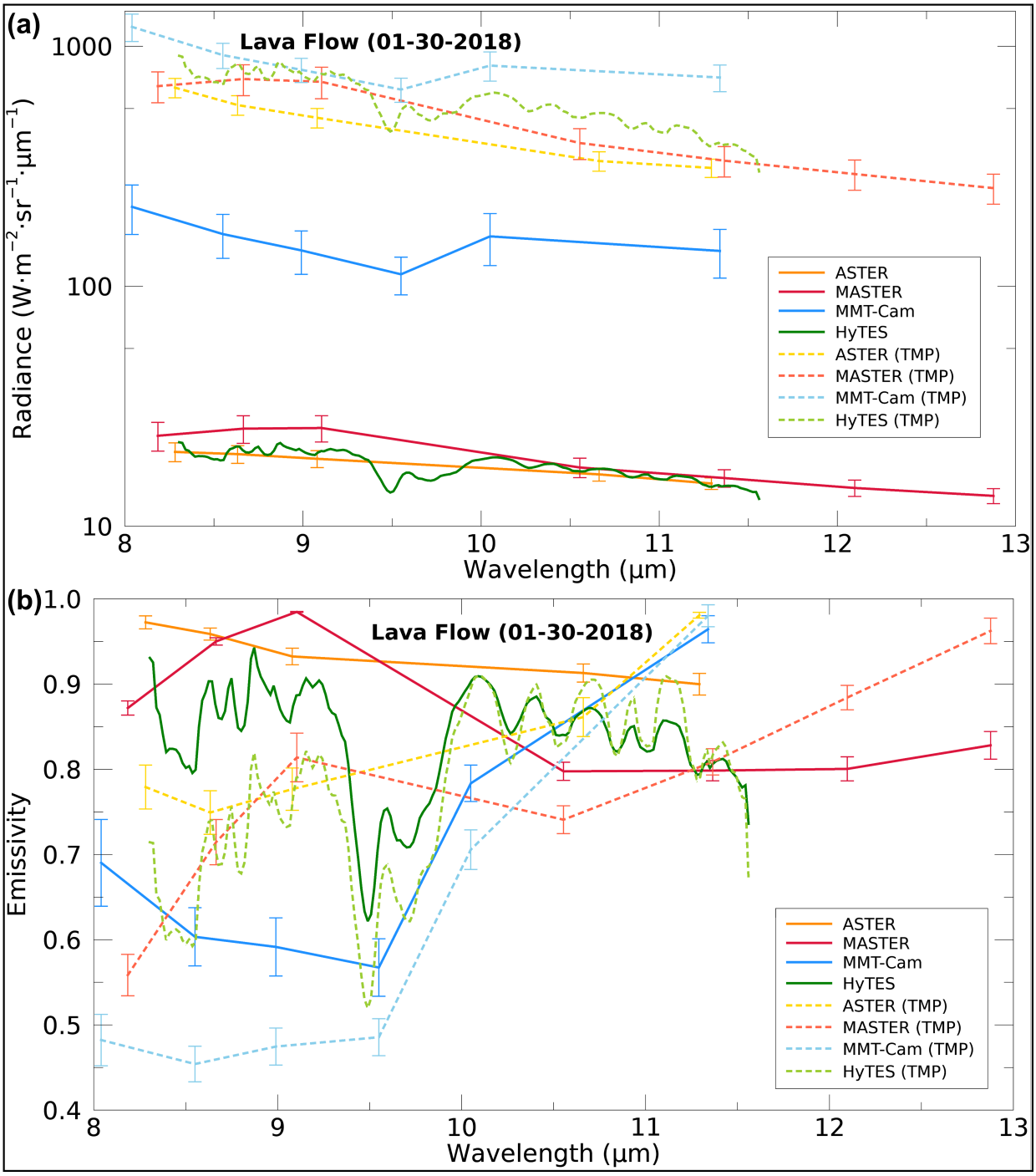

Figure 3.9: The difference between the pre- (solid line) and post- (dashed line) TMP separation of the molten fraction for the (a) surface radiance and (b) emissivity for the Pu'u 'Ō'ō lava flows acquired on January 30, 2018. The error bars represent the standard deviation variation in the ROI data.

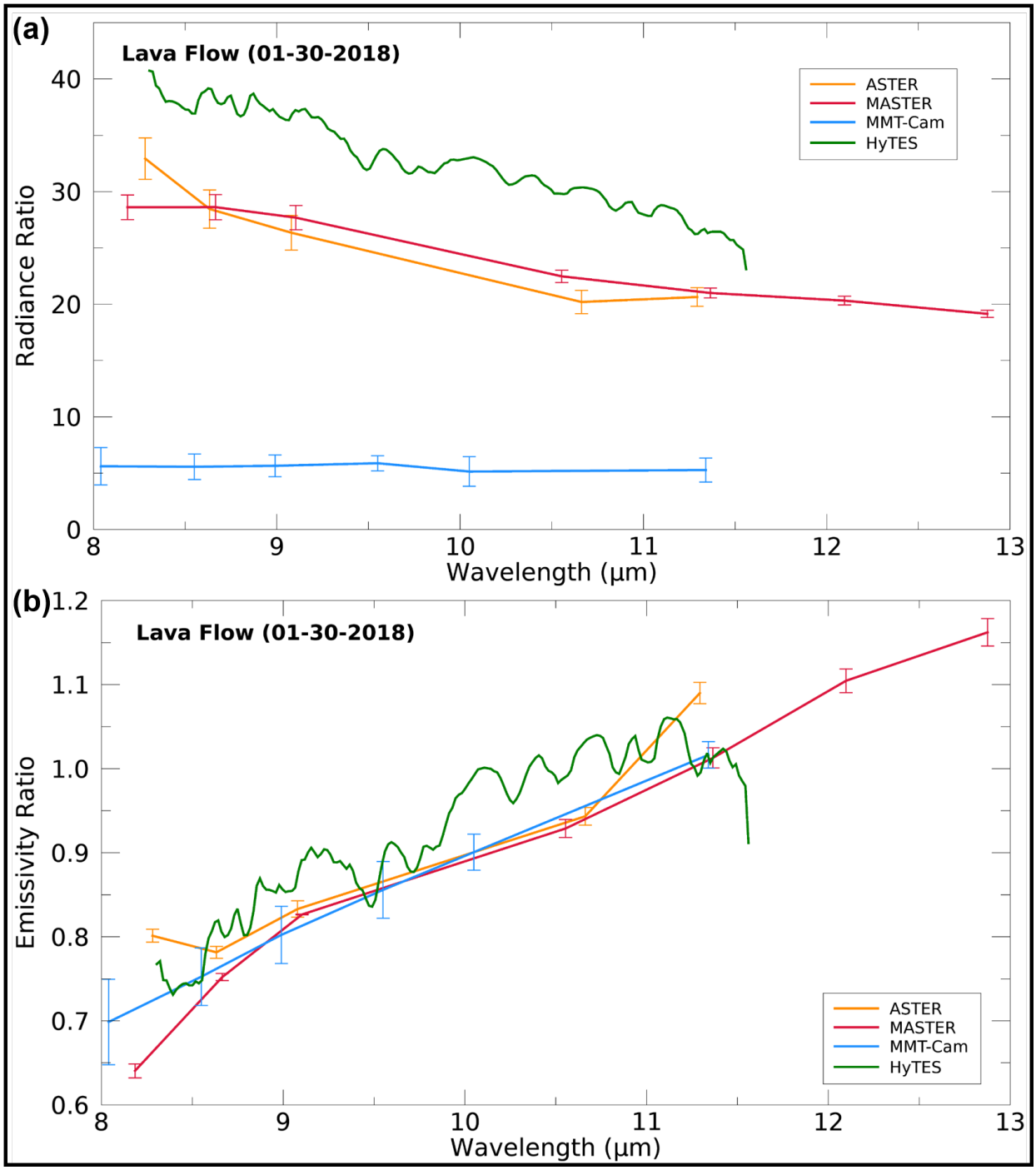

Figure 3.10: The ratio between the pre- and post-TMP separation of the molten fraction for the (a) surface radiance and (b) emissivity for the Pu'u 'Ō'ō lava flows acquired on January 30, 2018. Values closer to 1.0 require less TMP separation processing. The error bars represent the standard deviation variation in the ROI data.

the greatest errors are observed at shorter wavelengths in the mixed pixels and are more extreme in lower spatial resolution datasets (Figures 3.7, 3.8, 3.9, and 3.10). Although the greatest uncertainty and errors are observed in the mixed pixels acquired at lower spatial resolutions; these uncertainties fall within the expected values following the TMP separation for all the datasets.

The variability within each dataset was used to quantify the uncertainty of the derived thermal properties of molten basaltic lava surfaces. Although the dual-band mixed pixel separation approach does produce data similar to laboratory results, it ultimately increases the variability in the derived properties that results in a decrease in precision and therefore, an increase in uncertainty. This uncertainty is related to the spatial resolution of the dataset with lower spatial and spectral resolution data having higher uncertainty. This is a function of smaller proportions of the molten lava fraction being present within a given larger pixel, which can be less than 5% in an ASTER pixel. Figures 3.8 and 3.10 show the ratio in radiance and emissivity between pre- and post-TMP separation analysis, with values close to one requiring the least separation processing. In the majority of instances, the MMT-Cam data requires the least processing and the ASTER data requires the most. However, the HyTES lava lake surface radiance data requires the least separation processing, a function of the hyperspectral resolution, which offsets the lower spatial resolution compared to the MMT-Cam data (Figure 3.8a). Additionally, the HyTES variability in the unmixed surface radiance data was significantly lower than that from MASTER at a very similar spatial resolution. Therefore, where spatial resolution is similar, data uncertainty decreases by using higher spectral resolution data (reducing variability by $\sim$40%), which is highly relevant for future spaceborne instrument design. However, the HyTES lava flow surface radiance data requires the most separation processing (Figure 3.10), which is a function of the HyTES bands having an order of magnitude smaller FWHM than the over instruments ($\sim$0.05 μm compared to $\sim$0.5 μm). As a result, the signal-to-noise ratio is smaller for the HyTES instrument compared to the other instruments and the influence of the smaller FWHM on the derived measurements is exaggerated over smaller thermal anomalies (e.g., lava flows). Nevertheless, TMP separation techniques provide a methodology for more accurately deriving the maximum thermal component within a pixel independent of the measurement specifications of the instrument (e.g., FWHM and spatial resolution).

3.7 Conclusions

The accuracy and uncertainty in the thermal properties derived from remotely acquired TIR data of active lava surfaces were investigated using a variety of instruments acquiring data of two active basaltic lava surfaces (lava lake and lava flow). The effect of spatial and spectral resolution on the measured surface radiance and derived emissivity and kinetic temperature were quantified by comparing them to values expected for Hawaiian basaltic lavas at liquidus temperatures based on prior laboratory and field results (Abtahi et al., 2002; Lee et al., 2013). Because a majority of currently available TIR instruments do not have the radiometric range or spatial resolution to derive the thermal properties of a molten lava surface accurately, the application of a dual-band TMP analysis approach is one solution to improve results. This thermal unmixing can deconvolve the signature of the molten fraction within a pixel. By determining the accuracy and uncertainty in these thermal properties across four different TIR datasets, acquired at the same time and with different spatial and spectral resolutions, the temperature, emissivity, and radiance results were compared and constrained. For example, prior to extracting the molten fraction within each pixel, it was impossible to compare thermal properties (Figure 3.4) as there is a strongly dependency on the instrument position with respect to the surface and the different measurement specifications (Table 3.2). However, post-unmixing, the molten fraction (Figure 3.5) was more directly comparable between these datasets (Table 3.3).

Mixed pixel surface radiance values derived from the ASTER data were ∼2400% underestimated, with the MASTER and HyTES data underestimated by ∼1000%. Similar underestimates were observed in the extracted emissivity and kinetic temperature by approximately 20% and 250% in the ASTER data, and 25% and ∼200% in the MASTER and HyTES data, respectively. However, this impact of spatial resolution is mitigated to a degree by improved spectral resolution. Following the TMP separation analysis, all surface radiance values were within 15% of the expected values, whereas the emissivity and kinetic temperature were within 8% and 12% of the expected values, respectively (Abtahi et al., 2002; Lee et al., 2009, 2013). These results quantify the inherent TIR data uncertainty in the measured and derived thermal properties, demonstrating a significant improvement from previous estimates, and further constrains the errors associated with these values. The more accurate constraint of lava kinetic temperature, emissivity, and the emitted radiance from active surfaces derived from TIR measurements will ultimately improve the accuracy and reduce the unknown uncertainties in future flow models that rely upon these properties (e.g., Guanter

et al. 2019). Furthermore, these datasets can be directly compared with other measurements (i.e., terrain elevation, *in situ* thermocouple temperatures, and deformation change) to improve analysis of the synoptic eruption processes and quantify the uncertainties in the results and conclusions.

4.0 Spatiotemporal Variability of Active Lava Surface Thermal Properties using Ground-Based Multispectral Thermal Infrared Data

4.1 Introduction

Active lava surfaces, represent the surface expressions of the underlying volcanic system and provide critical information about the ongoing eruption dynamics and propagation (Melnik and Sparks, 2002; Kauahikaua et al., 2003; Stovall et al., 2009). Recent lava surface studies have investigated eruption dynamics at Piton de la Fournaise (Reunion Island), Yasur (Vanuatu), Tolbachik (Russia), and Kīlauea (Hawai'i) to constrain the behavior of lava surfaces during cooling (Brothelande et al., 2016; Patrick et al., 2017; Soldati et al., 2018; Ramsey et al., 2019). Improving measurement methods for deriving accurate lava properties and analyzing extrusive eruption behavior will improve our understanding of lava dynamics and activity that are vital for reducing the risks these eruptions can pose on local populations. For example, during the 2018 LERZ eruption at Kīlauea volcano lava flows threatened lives and infrastructure in the Puna District on the southeast coast of the Island of Hawai'i (Global Volcanism Program, 2018). The event lasted four months with 23 fissures erupting more than 0.76 km^3 of lava in and around Leilani Estates subdivision and destroying more than 700 individual residences (Neal et al., 2019).

Basaltic lava behavior is predominantly controlled by radiative cooling together with the effusion rate and flow distance from eruption vent (Pinkerton and Wilson, 1994). The advection and cooling rates of lava surfaces (on flows and lakes) and the strength of internal convection will influence flow morphology (Kerr and Lyman, 2007). Initially, a molten lava surface will emit heat radiatively, but over time and distance the upper lava surface cools to form a glassy crust that continuously thickens. The initial high cooling to advection ratio causes conductive heat flux to increase across the crust and base of the flow, reducing radiative heat flux (Cashman et al., 2013). If the lava flow surface crust forms while effusion continues, the flow can inflate and eventually fail, resulting in breakout events that cause radiative heat flux to once again dominate. If the effusion rate is high enough (or the topography steep enough), more rapid cooling occurs and 'a'ā lavas can form in basaltic compositions (Soule and Cashman, 2005; Cashman et al., 2013). Typically, the final flow length is limited by eruption rate/volume, cooling efficiency, tube formation, and slope (Cashman et al., 2013). Where cooling is limiting, the linear length of erupted lava feature, or propagation

length, is proportional to effusion rate and proximity to the vent (Harris et al., 2007). Predictive models to determine effusion rate based on cooling (as well as model strain rate and apparent viscosity), and hence the flow advance potential, are important for hazard management (Soule and Cashman, 2005). Lava flow propagation and lava lake supply models use derived properties that include effusion rate, viscosity, and cooling rate, in addition to topography data, calculated from a variety of *in situ* or remote measurements (Harris, 2013). Heat budget (e.g., heat flux) and radiometric (e.g., fraction of melt) calculations derived from indirect TIR measurements are used in lava flow propagation and supply rate models. Uncertainty in these derived calculated properties detract from the overall reliability of these models, as they strongly influence the cooling rate and crustal formation. Because a high proportion of these properties are derived from data acquired by TIR instruments, improvements in these measurements will further increase the accuracy and reliability of these models (Ramsey and Harris, 2013).

TIR analysis of volcanic eruptions using ground-based technologies was first conducted in 1901 using thermocouples and was followed a few years later by radiometers and optical pyrometers (MacDonald, 1972). The majority of these initial measurements were acquired at lava lakes, flows, and domes (e.g., Perret 1913; Zies 1937; Bullard 1947) with later measurements investigating edifice flanks, gas emissions, and explosive eruptions (e.g., Shimozuru 1971; Birnie 1973; Huntingdon and Sato 1973). Initially, the measurements acquired were mostly spot temperatures of the surface but later, with the development of imaging systems, arrays of data were acquired. Imaging systems provide better spatial coverage of a surface allowing detailed spatial analysis of the volcanic target (Harris, 2013). However, it was not until the 2000's that radiometry studies were extensively used to monitor and report volcanic activity, predominantly motivated by the increase in portable and affordability of TIR instruments. The continued technological developments in TIR imaging instruments have further improved the spatial and temporal resolutions of the data, enabling the expansion of eruption dynamic analyses and thermal model development studies (Harris, 2013). More recently, new inexpensive ground-based multispectral instruments provide the highest spatiotemporal *in situ* spectral data of cooling lava surfaces, which allows the cooling efficiency of an active surfaces to be determined precisely. Previously, these data have been either been estimated/assumed or derived post-acquisition in a laboratory (Ramsey and Harris, 2013; Thompson et al., 2019).

Kīlauea volcano in Hawai'i is one of the most active effusive volcanoes on Earth and has exhibited nearly continuous lava activity over the last 500 years (Holcomb, 1987). The almost constant

activity provides a good target of opportunity to develop and improve TIR data collection and analysis techniques. Previous studies of lava dynamics at Kīlauea have included investigations of lava emplacement mechanisms (Dietterich et al., 2012), discharge rates (Poland, 2014), and lava pathway forecasting (Koeppen et al., 2013). These can all be aided by higher temporal and spatial resolution multispectral TIR data to improve the accuracy of the derived thermal properties. Ultimately, this improves analyses of small period (seconds) and dimensional (centimeters) scale variability, where lava surfaces rapidly transition from molten to crustal surfaces. Technological advancements in instrumentation have enabled more investigations of lava surfaces over these scales, which are required to improve understanding of micro-scale cooling and crustal formation variability and ultimately relates this to lava propagation potential (Byrnes et al., 2004).

The goal of this study was to improve the accuracy and reliability of the derivation of certain thermal properties (e.g., temperature and emissivity) of active lava and calculations that use these properties (e.g., fraction of melt and heat flux) to refine models of lava eruption dynamics, propagation, and cooling. Results are presented from high-spatiotemporal analysis using ground-based multispectral TIR data of the active lava lake and lava flows at Kīlauea volcano in January – February 2018. The analyses show the importance of concurrent *in situ* emissivity data in deriving not only temperature but heat flux, which are both used to infer lava supply pathways and model lava emplacement. Emissivity provides a quantitative metric of the cooling efficiency of a lava surface and is critical for accurate temperature derivation from TIR data, which are crucial in understanding how lavas cool and the rate of cooling impacts hazard assessments.

4.2 Kīlauea Volcano

Kīlauea volcano is located on the southeast side of the Island of Hawai'i (USA) on the eastern flank of Mauna Loa (Figure 4.1). Kīlauea is the southernmost subaerial basaltic shield volcano in the ∼6000 kilometer long Hawaiian-Emperor seamount/island chain (Global Volcanism Program, 2018). Magma is generated at the volcano by the oceanic intraplate Hawaiian mantle plume and typically produces effusive lava eruptions but some small periods of explosive volcanism have occurred (Holcomb, 1987). In general, the effusive eruptions are long and sustained producing both pāhoehoe (tube- and surface- fed) and 'a'ā lava flows, as well as, long-lived lava lakes (Holcomb, 1987).

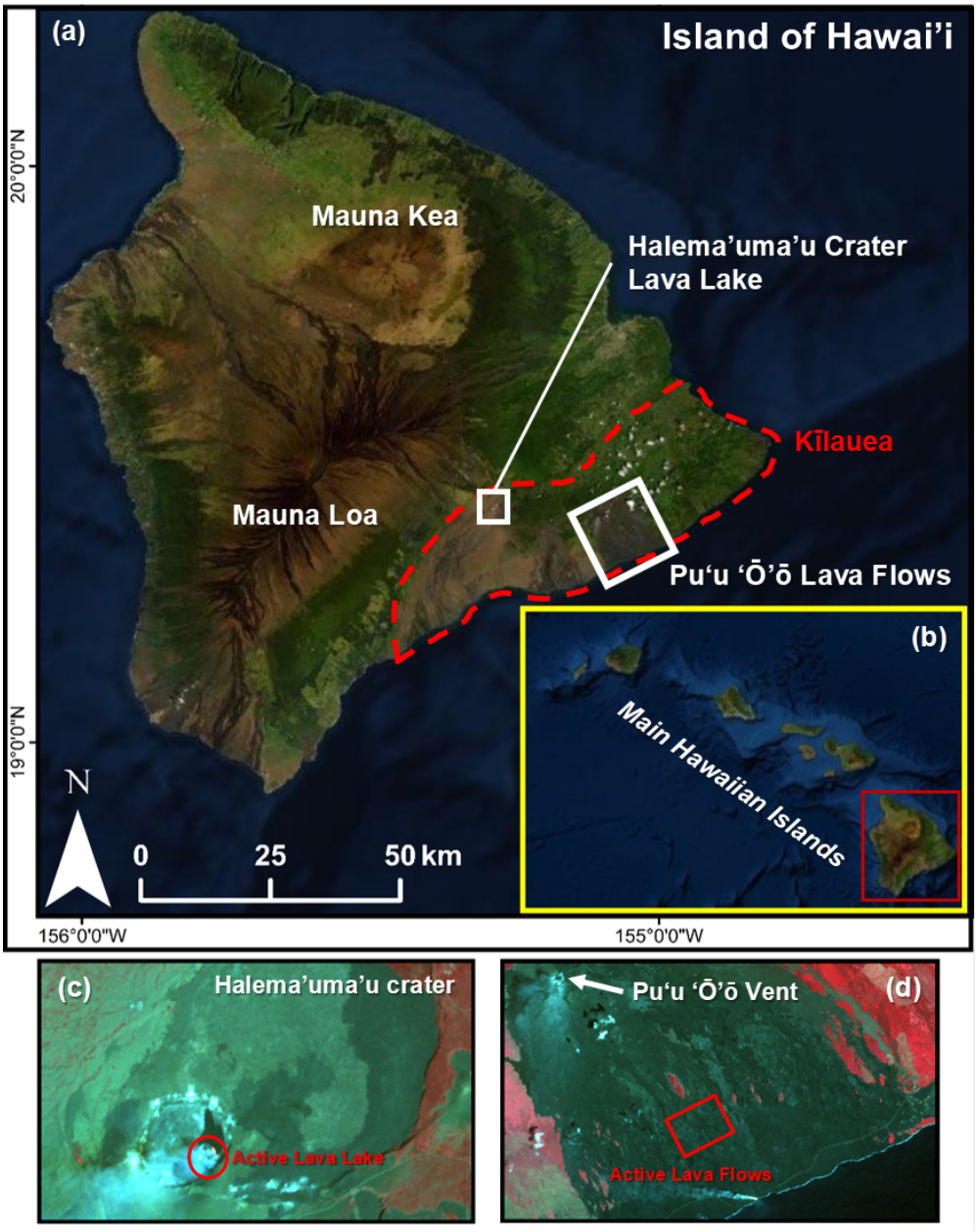

Figure 4.1: (a) Location map of Kīlauea volcano on the Island of Hawai'i with the (b) insert map showing the island's location within the main Hawaiian Island Chain (Source: ESRI and DigitalGlobe). Data from the ASTER visible false-color image (RBG: 0.81 μm, 0.65 μm, and 0.56 μm) of the (c) active lava lake within the Halema'uma'u crater and (d) active lava flows within the Pu'u 'Ō'ō lava flow field. These sites were investigated in January and February 2018 for this study. The ASTER data were acquired at 20:06 UTC on March 7, 2018 (Yamaguchi et al., 1998).

This study was conducted at Kīlauea volcano between January 30 – February 8, 2018. During this campaign there were two active eruption styles present: an overturning lava lake in the Halema'uma'u Crater and a pāhoehoe lava flow field on flank of the Pu'u 'Ō'ō vent. The lava lake was active from 2008 until 2018 and varied in size with a maximum diameter of 250 meters (Figure 4.1) (Patrick et al., 2013, 2018). During this period, fluctuations in lava lake activity were observed with continuous gas emissions and irregular small explosions, that ended with the draining of the lava lake and collapse of the summit in May 2018 (Patrick et al., 2013; Global Volcanism Program, 2018; Neal et al., 2019). In early 2018, the level of lava in the lake was comparably high but not overflowing, at between 100 and 130 meters below the Halema'uma'u Crater rim. Continuous upwelling of lava and gases were observed in the northern portions of the lake resulting in strong overturning (Patrick et al., 2013, 2018).

There has been more than 30 years of effusive activity observed at the Pu'u 'Ō'ō vent that produced numerous lava flow episodes over a large lava flow field (>40 km^2) and ceased activity in May 2018 when the crater collapsed (Orr et al., 2013; Neal et al., 2019). Mostly pāhoehoe lava flows were emplaced from the vent onto the Pulama Pali and coastal plain on the southern flank of Kīlauea. 'A'ā lavas were mostly constrained to the steep slope regions (Holcomb, 1987; Orr et al., 2013). During this study, the lava flows investigated were part of the 61g episode that erupted from the east flank of the Pu'u 'Ō'ō vent and were observed as a series of tube-fed pāhoehoe lava flows emplaced onto the surface (sheet-like and ropey in texture) of the coastal plain at the base of the Pulama Pali (Figure 4.1) (Orr et al., 2013).

4.3 Methodology

4.3.1 Datasets

A field campaign was conducted between January 30 and February 8, 2018 at Kīlauea volcano in Hawai'i, USA (Table 4.1). Ground-based multispectral TIR data were acquired of the lava lake and lava flows using the MMT-Cam imaging system. The MMT-Cam system acquires TIR data at six discrete spectral bands between 8.0 and 11.5 μm using a 640 x 512 pixel focal plane array with a field of view of 45° x 37° (Thompson et al., 2019). Data were continuously acquired (during both day and night observations) with one multispectral image set acquired every 0.5 seconds,

providing the resolution required to observe the temporal and spatial variability of cooling basaltic lava surfaces. The data were collected from the rim of the Halema'uma'u Crater to the southwest of the active lava lake at a horizontal distance of ∼200 meters from the center of the lake and from ∼120 meters vertically above the surface. This corresponds to a pixel size of between 0.22 and 0.75 meters. The lava flow data were acquired within a 0.5 km^2 area on the coastal plain of the Pu'u 'Ō'ō lava flow field approximately 100 meters to the south of the base of the Pulama Pali. The lava flow data were collected at 15 meters from the lava surface, corresponding to a pixel size of between 0.05 and 0.22 meters. Data were collected on six separate occasions, three each at the lava lake and lava flows, although only five acquisition periods were used in this study as the third lava flow period represents a more channelized flow. This study focuses on sheet-like and ropey pāhoehoe lava surface rather than channelized lava, which is the focus of Chapter 5.

Multispectral surface radiance was derived from the raw instrument data using a calibration method to correct for instrument geometric and optical attenuation effects (Appendices A - C). This was achieved using variable, full-aperture blackbodies from 283 to 1023 K to quantify the instrument response from known target temperatures and internal instrument temperatures (Thompson et al., 2019). A horizontal atmospheric model using ground atmospheric measurements collected during data acquisition (e.g., temperature and humidity) and physical collection geometry parameters (e.g., line-of-sight distance) was used to compensate for atmospheric transmission and emission in the data (Rothman et al., 2013; Thompson et al., 2019). The duration of the acquisition periods were no longer than 90 minutes and the atmospheric conditions varied by no more than 3 K and 5 % humidity, which had minimal influence on the atmospheric compensation models (<2%).

4.3.2 Surface Kinetic Temperature and Emissivity

Surface radiance data were converted to surface kinetic temperature and six-point emissivity (using the six spectral bands acquired by the MMT-Cam) using a modified version of the TES algorithm that was first developed for the ASTER spaceborne instrument (Appendix D) (Gillespie et al., 1998). The TES algorithm separates emissivity and temperature from the atmospherically-corrected radiance data using the Planck function and accounts for spectral contrast across the different wavelengths. The algorithm compensates for atmospheric downwelling radiance through an iterative approach to remove reflected sky irradiance from the data and provides a data quality verification to limit data transformation errors (Gillespie et al., 1998). The TES algorithm was

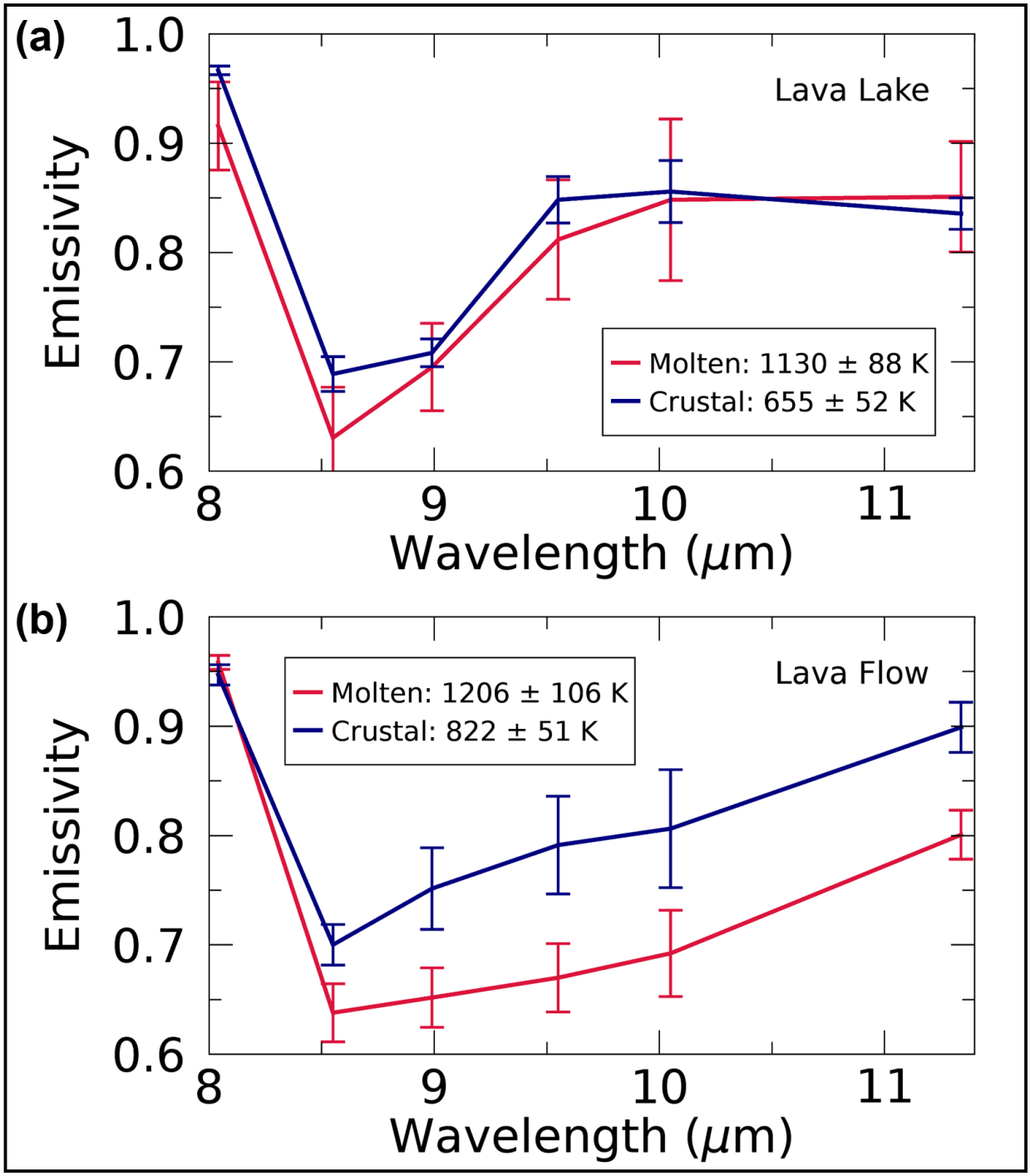

Figure 4.2: MMT-Cam data derived emissivity spectra of molten and crustal lava surfaces acquired at (a) the lava lake in Halema'uma'u Crater on February 2, 2018 and (b) the Pu'u 'Ō'ō lava flow field on January 30, 2018. Typically, the spectral depth of the main absorption feature (~8.55-8.99 μm) decreases and broadens as the molten lava cools and forms a glassy crust.

modified to be compatible with the spatial and spectral resolutions of the MMT-Cam data (Thompson et al., 2019). The cumulative errors in the derivation of kinetic temperature and emissivity, including the calibration processing, are less than 4% (Thompson et al., 2019).

Emissivity is an important parameter as it quantifies the efficiency of a surface to emit radiant energy, important in numerous thermal heat budget calculations such as heat flux (Harris, 2013). Typically, *in situ* emissivity is not measured concurrently; instead, it is assumed or calculated from laboratory data of samples, which is not directly comparable to the actual field surfaces. This investigation utilized the concurrent emissivity measurements at high spatial and temporal resolutions to improve understanding of lava cooling and heat budget calculations that rely on this property of the surface (Figure 4.2). An average of the six-point emissivity data is used in the heat budget calculations in order to make the results comparable to past studies (e.g., Lodato et al. 2007; Patrick et al. 2017; Soldati et al. 2018).

Frequency distribution percentages were generated for the duration of the acquisition periods to represent the spatiotemporal variability in kinetic temperature and emissivity of the active lava surfaces. Frequency distributions were generated for kinetic temperature between 700 and 1500 K at 10 K bin sizes. Emissivity frequency distributions were calculated between 0.3 and 1.0 at 0.005 bin sizes. The individual frequency distributions were then stacked temporally to produce a density plot of the distribution over time for each of the five acquisition periods: January 30, February 2, February 3, February 6, and February 8 in 2018. Separately, the spatial distribution of kinetic temperature and emissivity data at the lava lake and lava flows were investigated in greater detail, at three segments each, to quantify the spatial extent of any variability and relationships between the two properties.

4.3.3 Fraction of Melt and Heat Flux

The surface kinetic temperature and emissivity were incorporated into fraction of melt (or melt fraction) and heat flux calculations for the lava lake and lava flows (Appendices E- F). The fraction of melt parameter represents the proportion of molten lava within each pixel (or data point) of the dataset and follows a similar method used for deriving sub-pixel temperature anomalies within remote sensing datasets (Dozier, 1981; Matson and Dozier, 1981; Harris, 2013). The fractions were calculated by dividing the difference between the temperature of the lava surface (T_s) derived from the MMT-Cam data and the ambient lava temperature (T_a) by the difference between the liquidus

temperature (T_{liq}) of a Hawaiian basalt and the ambient lava temperature (Equation 4.1).

$$Fraction\ of\ Melt = (T_s - T_a)/(T_{liq} - T_a) \tag{4.1}$$

Heat fluxes were calculated for the lava lake and lava flows to quantify the heat flux observed from these two eruptions and understand the spatiotemporal variability with respect to surface kinetic temperature and emissivity. The methods used to calculate the fluxes follow prior approaches described for derivation with satellite and ground-based TIR datasets (Harris, 2013). Heat fluxes were calculated using the MMT-Cam derived surface kinetic temperature (T_s), emissivity (ε), and pixel area (A) values with additional atmospheric and rheological properties obtained from ground measurements and lookup tables (Table 4.1 and Appendices E - F) (Holman, 1992). The total heat flux (Φ_{tot}) values incorporate radiant ($[\varepsilon \cdot \sigma(T_s^4 - T_a^4)]$), convective ($[h_c(T_s - T_a)]$), and conductive ($[-k(\Delta T/\sqrt{(\alpha \cdot \pi \cdot t)})]$) heat fluxes in the relationship below (Equation 4.2).

$$\Phi_{tot} = \left\{ \left[\varepsilon \cdot \sigma(T_s^4 - T_a^4)\right] + \left[h_c(T_s - T_a)\right] + \left[-k\left(\Delta T/\sqrt{(\alpha \cdot \pi \cdot t)}\right)\right] \right\} \cdot A \tag{4.2}$$

where σ is the Stefan-Boltzmann constant, h_c is the heat transfer coefficient, k is thermal conductivity, and α is thermal diffusivity. Windy conditions were experienced during all the acquisition periods and so the heat transfer coefficient was calculated for a forced convection scenario (Equation 4.3).

$$h_c = (k_{air} \cdot Nu)\,/H \tag{4.3}$$

where k_{air} is the thermal conductivity of the air overlying the lava surface and H is the thickness of the air boundary layer, both were derived from lookup tables (Table 4.1) (Holman, 1992). Nu is the Nusselt number and is related to the Reynolds number (Re) for a forced convection scenario, in most instances (Equation 4.4).

$$Nu = 0.332 \cdot Pr^{0.3} \cdot Re^{0.5} \tag{4.4}$$

where Pr is the Prandtl number. Equations 4.5 and 4.6 illustrate the derivation of the Reynolds and Prandtl numbers, respectively.

$$Re = (W \cdot L)\,/v_{air} \tag{4.5}$$

$$Pr = v_{air}/\alpha_{air} \tag{4.6}$$

where W is wind speed and L is the length scale of the wind above the lava surface. v_{air} is kinematic viscosity and α_{air} is thermal diffusivity of the air in the boundary layer overlying the lava surface, both derived from lookup tables (Holman, 1992). The constants used in the heat flux calculations for the five acquisition periods are summarized in Table 4.1.

Table 4.1: Observational and atmospheric conditions during the five acquisition times, including thermal properties.

Data	01/30/2018	02/02/2018	02/03/2018	02/06/2018	02/08/2018
Location	Lava Flows	Lava Lake	Lava Lake	Lava Lake	Lava Flows
Location (GPS)	19.34971°N, 155.04752°W	19.40304°N, 155.28122°W	19.40304°N, 155.28122°W	19.40304°N, 155.28122°W	19.34961°N, 155.04800°W
Acquisition Time (UTC)	20:51	06:11	01:33	21:02	08:13
Observation Height (m.a.s.l.)	122±3	1115±3	1115±3	1115±3	135±3
Pixel Size (m)	0.05 - 0.22	0.22 - 0.75	0.22 - 0.75	0.22 - 0.75	0.05 - 0.1
Rock Thermal Diffusivity [α] (m^2s^{-1})	9.0 x 10^{-7}	9.0 x 10^{-7}	9.0 x 10^{-7}	9.0 x 10^{-7}	9.0 x 10^{-7}
Rock Thermal Conductivity [k] ($Wm^{-1} \cdot K$)	1.50	1.50	1.50	1.50	1.50
Length Scale [L] (Flow Width, m)	20±2	225±5	225±5	225±5	20±2
Atmospheric Temperature (K)	316±3	290±3	301±3	302±3	299±13
Humidity (% RH)	23±5	78±5	58±5	47±5	49±5
Wind Speed [W] (ms^{-1})	5.15±0.5	3.45±0.5	5.38±0.5	6.93±0.5	2.46±0.5
Air Boundary Layer [H] (m)	1.5±0.2	3.0±0.5	3.0±0.5	3.0±0.5	1.5±0.2
Air Thermal Diffusivity [α_{air}] (m^2s^{-1})	2.216 x 10^{-5}	2.216 x 10^{-5}	2.216 x 10^{-5}	2.216 x 10^{-5}	2.216 x 10^{-5}
Air Thermal Conductivity [k_{air}] ($Wm^{-1} \cdot K$)	2.624 x 10^{-2}	2.624 x 10^{-2}	2.624 x 10^{-2}	2.624 x 10^{-2}	2.624 x 10^{-2}
Air Kinematic Viscosity [v_{air}] (m^2s^{-1})	1.569 x 10^{-5}	1.569 x 10^{-5}	1.569 x 10^{-5}	1.569 x 10^{-5}	1.569 x 10^{-5}

[1]Note: the symbols in squared parenthesis (e.g., [W]) relate to a constant or variable in the calculations outlined in the methodology section.

The fraction of melt and heat flux data were spatiotemporally represented in the same style as described for the surface kinetic temperature and emissivity data. Frequency distributions were generated for fraction of melt between 0.0 and 0.8 at 0.01 bin sizes. The heat flux frequency distributions varied due to the wide range of values between acquisition periods. However, the bin sizes remained less than 1.7% of the total range of each dataset. Again, three temporal portions were selected for further detailed spatial analysis during one lava lake and lava flow acquisition period.

4.4 Results

Temporal density frequency distributions were compiled for lava surface kinetic temperature, emissivity, fraction of melt, and heat flux during five separate acquisition periods to evaluate the

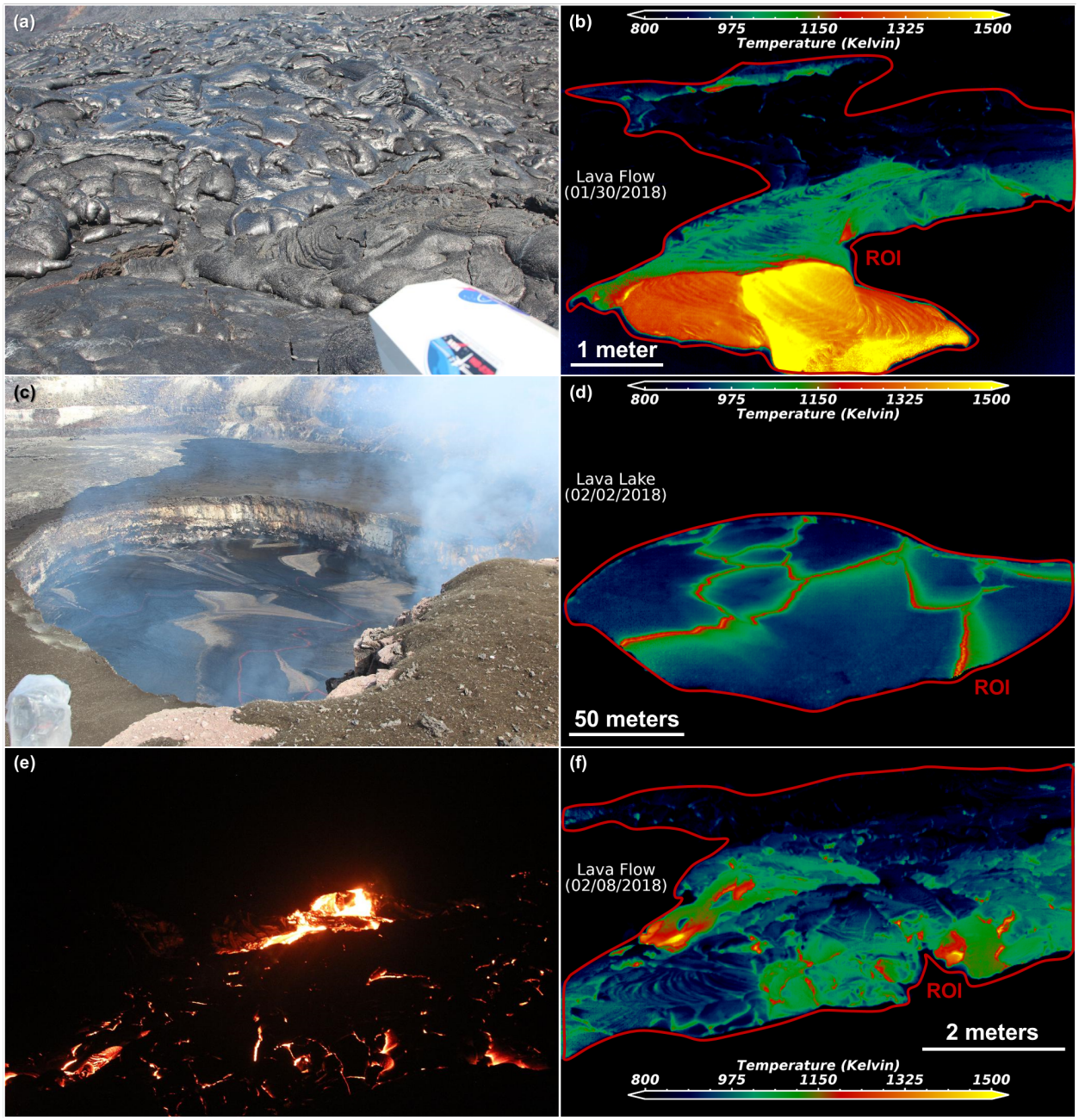

Figure 4.3: (a,c,e) Visible and (b,d,f) TIR image data of the lava lake and lava flows including examples of the ROIs used in the spatiotemporal analysis (red polygons) (photographs taken by J.O. Thompson). (a-b) Image data from the Pu'u 'Ō'ō lava flow field on January 30, 2018; (c-d) image data from the Halema'uma'u Crater lava lake on February 2, 2018 (similar ROIs were used on February 3 and 6, 2018); and (e-f) image data from the Pu'u 'Ō'ō lava flow field on February 8, 2018.

Table 4.2: The main statistical variability within and between acquisition periods.

		Lava Lake			Lava Flow	
		02/02/2018	**02/03/2018**	**02/06/2018**	**01/30/2018**	**02/08/2018**
Temperature (Kelvin)	**Mean**	939	928	973	882	947
	σ	69	97	81	121	109
	Max	970	955	988	970	964
	σ	62	86	77	139	95
	Min	849	910	929	802	912
	σ	76	101	77	108	96
Emissivity	**Mean**	0.757	0.797	0.728	0.680	0.769
	σ	0.058	0.107	0.073	0.074	0.067
	Max	0.788	0.830	0.761	0.724	0.803
	σ	0.055	0.091	0.057	0.058	0.087
	Min	0.724	0.763	0.671	0.597	0.693
	σ	0.068	0.095	0.131	0.114	0.140
Fraction of Melt	**Mean**	0.28	0.26	0.30	0.20	0.26
	σ	0.06	0.09	0.08	0.10	0.10
	Max	0.30	0.29	0.31	0.27	0.28
	σ	0.06	0.08	0.08	0.19	0.12
	Min	0.21	0.23	0.25	0.10	0.21
	σ	0.06	0.09	0.08	0.07	0.07
Total Heat Flux (MW)	**Mean**	1.914	2.203	3.849	0.031	0.044
	σ	0.708	1.152	1.671	0.020	0.027
	Max	2.118	2.446	4.163	0.039	0.047
	σ	0.732	1.202	1.695	0.022	0.028
	Min	1.288	2.045	3.192	0.019	0.032
	σ	0.068	1.084	1.629	0.018	0.021

[2]Note, "σ" indicates the 2-simga standard deviation of the statistic value, across the entire ROIs during the entire acquisition times.

spatial and temporal variability in thermal properties of active lava surfaces during propagation and cooling. The density frequency distributions show the percentage distribution in thermal prop-

erties at one second intervals for the duration of the acquisitions. The distributions are constrained by the defined ROIs for each acquisition period (Figure 4.3) with darker colors representing higher percentage frequencies. Together with these visualizations, the mean (temporal) and standard deviation (spatial) values were compared to investigate variability within and between data acquisitions. Additionally, three time-segments were extracted within one acquisition period at both the lava lake and lava flows to analyze the spatial variability in more detail. The main statistical variations during the acquisition periods are available in Table 4.2.

4.4.1 Lava Lake

On February 2, 2018, multispectral MMT-Cam data were collected at the lava lake during a 12-minute period (Figure 4.3c-d), documenting a minor decrease in overall temperature, fraction of melt, and heat flux with a larger decrease observed in the final 1.5 minutes (Figures 4.4, 4.5, and 4.15). In comparison emissivity increased during this acquisition period (Figures 4.2a, 4.4, 4.5, and 4.15d). The highest mean kinetic temperature (∼970 K), fraction of melt (0.30), and heat flux (2.118 MW) were observed during the first few minutes of the observation with small (<0.014 amplitude) high-frequency variability (>0.1 seconds^{-1}) and low deviation (Figure 4.15). During the observation the values of these properties decreased (∼10-50%) with the deviation increasing in the temperature and fraction of melt data but decreasing in the heat flux data. The mean emissivity increased slightly during the acquisition period (at around 0.757) with a minor increase in deviation (Figures 4.4, 4.5, and 4.15 and Table 4.2).

On February 3, 2018, multispectral TIR data were collected during a 12-minute period at the lava lake, documenting a minor increase in overall kinetic temperature, fraction of melt, and heat flux through the initial minute followed by a gradual decrease before an increase in the final two minutes (Figure 4.6). In comparison, the inverse response was observed in the emissivity data. The highest mean kinetic temperature (955 K), fraction of melt (0.29), and heat flux (2.446 MW) were measured in the final 3 minutes of the acquisition period with a small increase in deviation (<20%) in the temperature and fraction of melt data compared to a small decrease in the heat flux data (∼10%). In the initial 2 minutes, the smallest deviations for these thermal properties were observed. These thermal properties also have a bi-model distribution, especially initial, with a lower convergent peak and a more intense divergent peak. The emissivity measurements revealed small high-frequency mean variability (>0.1 seconds^{-1}) during the acquisition, with the 3-5 minute

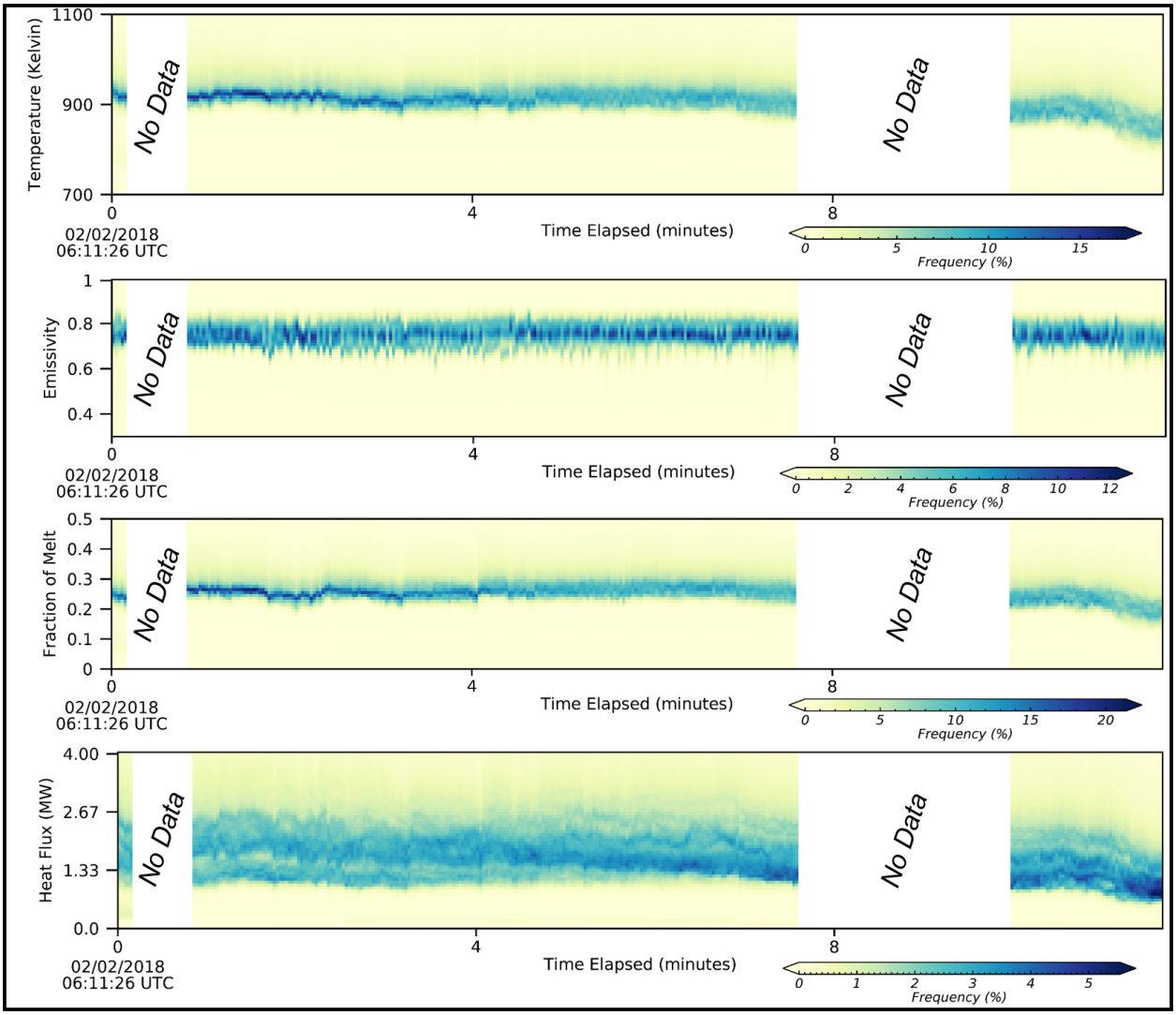

Figure 4.4: Temporal density frequency distributions of the lava lake in the Halema'uma'u Crater of Kīlauea volcano (Hawai'i) using the MMT-Cam, acquired on February 2, 2018 at 06:11:26 UTC. The plots illustrate the spatial variability in thermal properties with time elapsed. Note, the white regions represent periods when no data were acquired due to instrument repositioning and when other targets were studied (e.g., gas emissions).

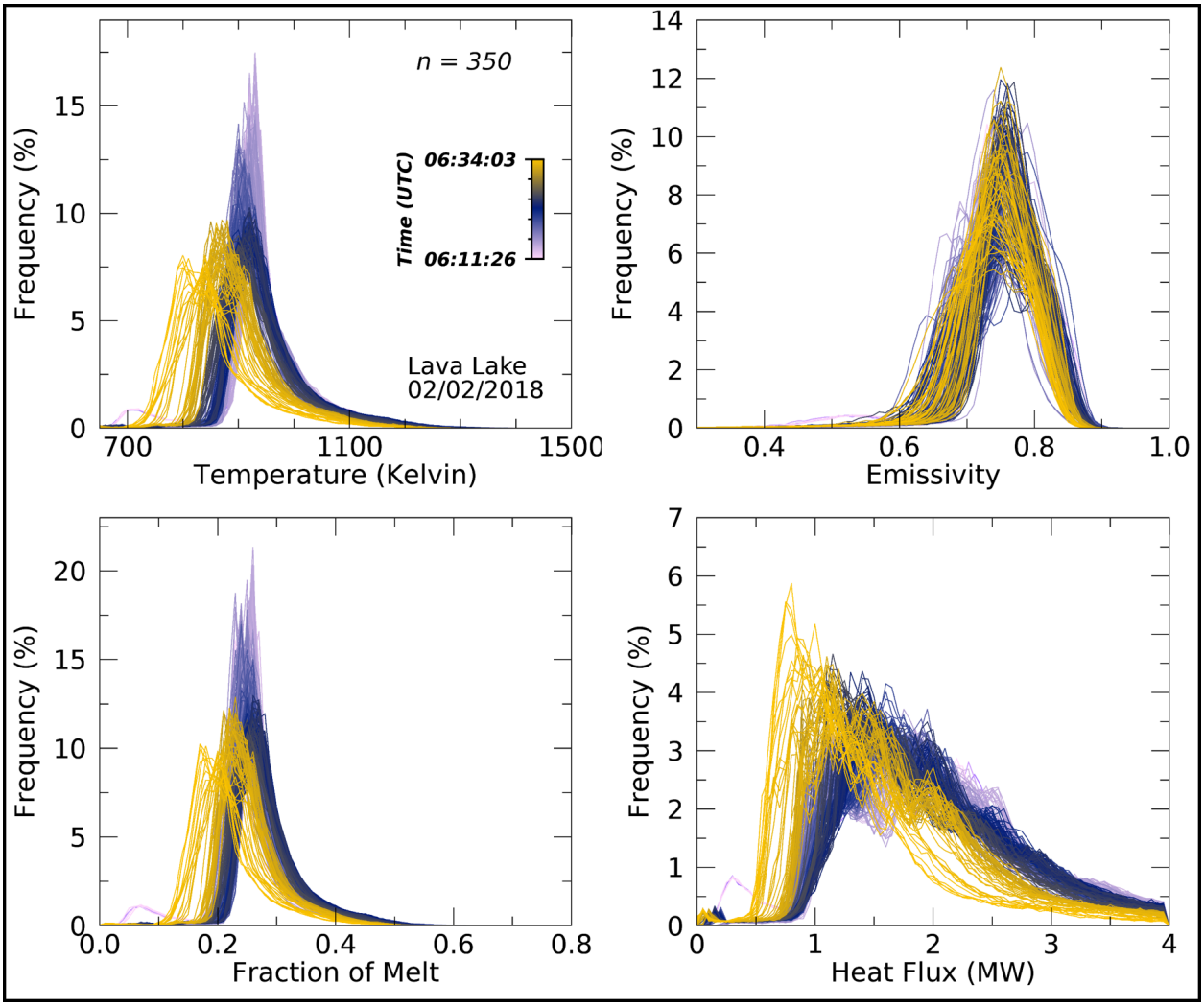

Figure 4.5: Temporal frequency distributions of the lava lake in the Halema'uma'u Crater of Kīlauea volcano (Hawai'i) using the MMT-Cam, acquired on February 2, 2018 at 06:11:26 UTC. Each plot represents the distribution of thermal properties across the active lava lake with the time symbolized through the color gradation. These are cross-sectional visualizations of Figure 4.4.

period having the lowest variation and the final 3 minute period having the highest variation. The final 3 minute period was also associated with the highest temperature measurements. The overall increase in kinetic surface temperature and heat flux during this period coincided with a decrease in variability and suggests a short-term increase in activity (Figure 4.6 and Table 4.2).

On February 6, 2018, multispectral TIR data were collected during a 16-minute period at the lava lake, where the overall kinetic temperature, emissivity, fraction of melt, and heat flux measurements remained mostly constant with high-frequency temporal variability throughout (Figure 4.7). In the initial 2 minute period, the highest mean kinetic temperature (988 K), fraction of melt (0.31), and heat flux (4.163 MW) values were observed with a minor decrease of ∼5-25% during the subsequent 14 minutes. Inversely, mean emissivity increased by ∼15% during the period from 0.671. The overall minor decrease in mean values (inverse for emissivity) coincided with a decrease in variability by up to 35% during the 16-minute period (Figure 4.7 and Table 4.2). The heat flux measurements also revealed bi- and tri- modal distributions during the acquisition with peaks around 1.9, 3.0, and 5.3 MW. The highest peak (∼5.3 MW) waned during the acquisition period with the distribution concentrating into a bi-modal classification (Figure 4.7).

Comparing the results from the three acquisition periods at the lava lake, the highest mean kinetic temperatures were observed during the February 6 acquisition (930 to 988 K) and lowest were observed in the February 2 data (849 to 969 K). The highest deviation was observed in the February 3 data (75 to 110 K) and lowest in the February 6 data (57 to 85 K), with the February 2 data having the most consistent variability (74 to 90 K). The lowest mean emissivity values were observed in the February 3 data (0.663 to 0.730) and the highest mean values were observed in the February 2 data (0.724 to 0.788). The February 6 data had the largest emissivity variability (0.051 to 0.155) and the February 2 data had the lowest (0.041 to 0.085) with the smallest range. The highest mean melt fractions were observed in the February 6 data (0.25 to 0.31) and the lowest in the February 3 data (0.24 to 0.29). The February 2 data had the highest constraint with a standard deviation range from 0.05 to 0.07, compared to lower constraints in the February 3 and 6 data with standard deviation ranges from 0.07 to 0.10 and from 0.07 to 0.09, respectively. Finally, the February 6 data had the highest mean heat flux values (3.192 to 4.163 MW) compared to data acquired on February 2 with the lowest mean values (1.289 to 2.118 MW). The highest variability was also observed in the data from February 6 (1.426 to 1.790 MW) and the lowest in the February 2 data (0.619 to 0.806 MW). Additionally, the majority of the heat flux data had a bi- or tri- modal distribution representing two or three main thermal components contributing to

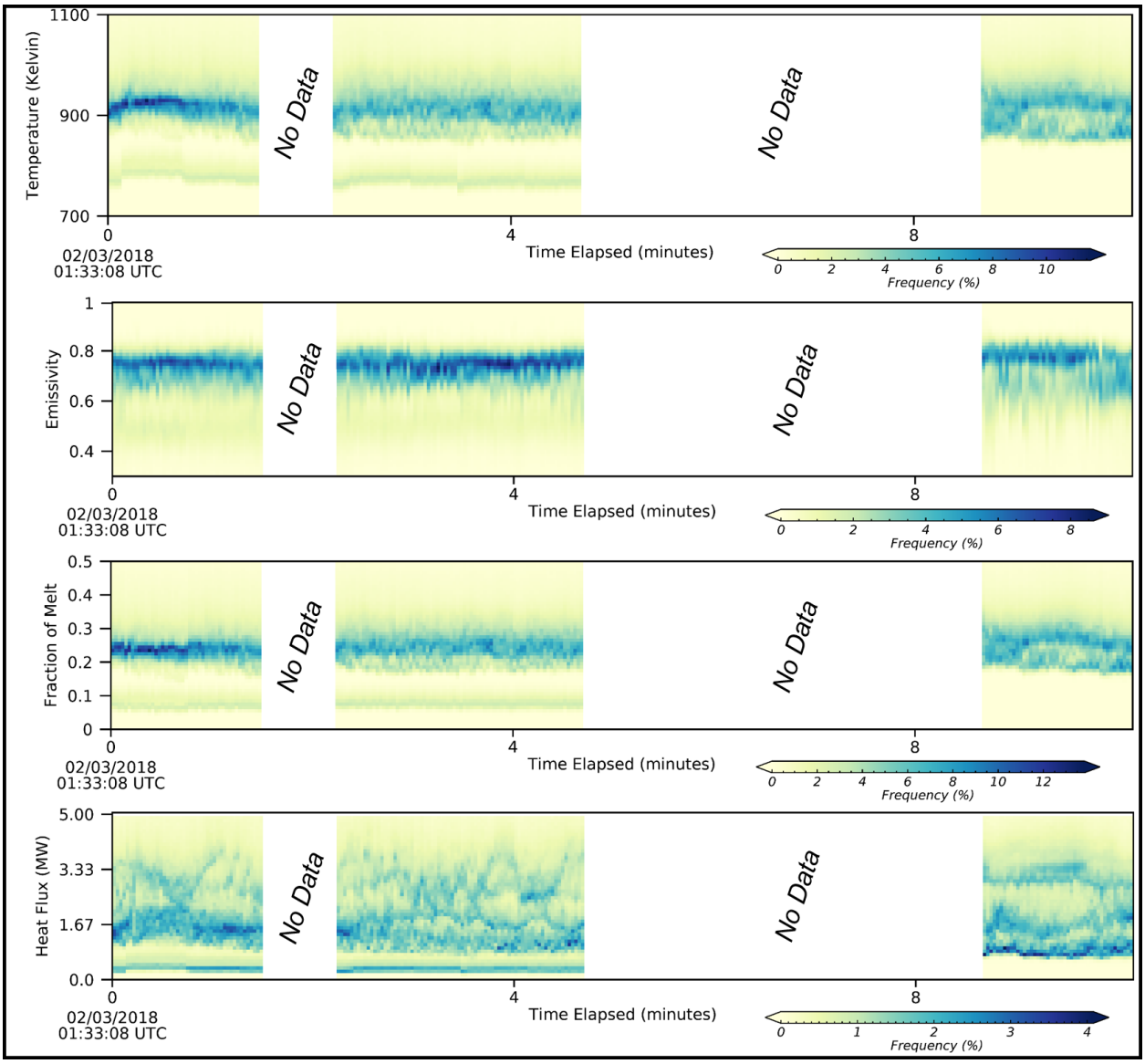

Figure 4.6: Temporal density frequency distributions of the lava lake in the Halema'uma'u Crater of Kīlauea volcano (Hawai'i) using MMT-Cam data, acquired on February 3, 2018 at 01:33:08 UTC. The plots illustrate the spatial variability in thermal properties with time elapsed. Note the white regions represent periods when no data were acquired due to instrument repositioning and when other targets were studied (e.g., gas emissions).

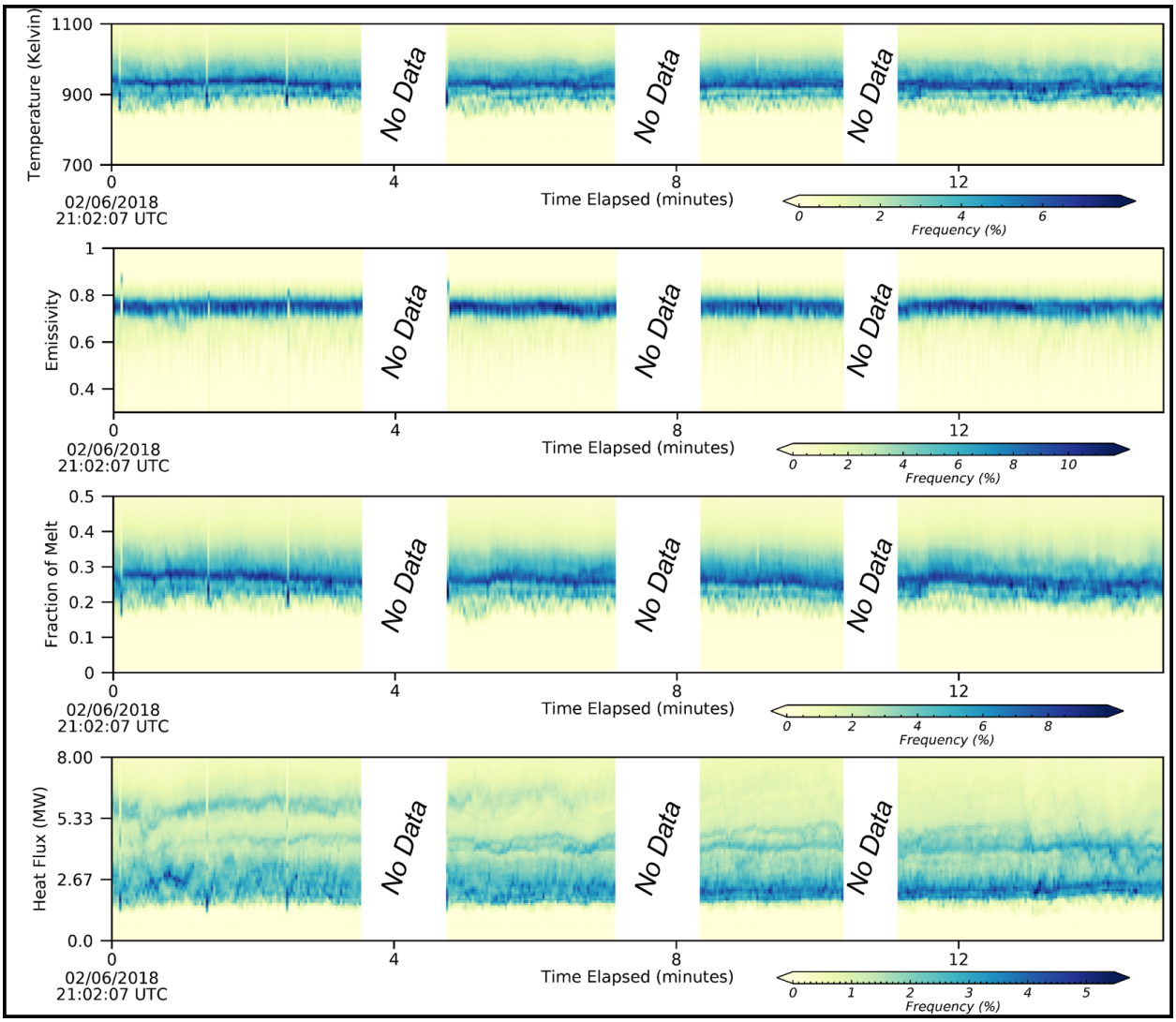

Figure 4.7: Temporal density frequency distributions of the lava lake in the Halema'uma'u Crater of Kīlauea volcano (Hawai'i) using MMT-Cam data, acquired on February 6, 2018 at 21:02:07 UTC. The plots illustrate the spatial variability in thermal properties with time elapsed. Note the white regions represent periods when no data were acquired. No data were acquired at various periods during deployment due to instrument repositioning and when other targets were studied (e.g., gas emissions).

the overall thermal flux of the lava lake. The higher mean values of kinetic temperature, fraction of melt, and heat flux on February 6 implied higher levels of activity were observed during this acquisition period compared to the other days, with February 2 having the lowest activity (Figures 4.4 and 4.7). Generally, higher mean data values were accompanied by higher variability in the data, suggesting there was significant spatial variability that fluctuated dramatically over very short periods (Figures 4.4-4.7 and Table 4.2).

4.4.2 Lava Flows

On January 30, 2018, multispectral TIR data were acquired from a pāhoehoe lava flow during an 84-minute period (Figure 4.3a-b). During this period, surface kinetic temperature, fraction of melt, and heat flux increased, with emissivity slightly decreasing except in the final few minutes were emissivity increased (Figure 4.2b and 4.7). Throughout the 84 minutes, the mean kinetic temperature, fraction of melt, and heat flux increased by ∼25-150% with the greatest increase occurring over the final 10 minutes. Additionally, the deviation also increased over this time by ∼30-50%. The mean emissivity measurements decreased by ∼20% from 0.724 to 0.597 with variability also decreasing by ∼50%. All the data show at least a bimodal distribution of measurements with up to potentially six modal classifications of lava flow thermal properties (Figures 4.8-4.9 and Table 4.2).

On February 8, 2018, multispectral TIR data were collected from a pāhoehoe lava flow during a 30-minute period (Figure 4.3e-f), where the overall kinetic temperature, emissivity, fraction of melt, and heat flux measurements remained mostly constant but increased significantly in variability as time elapsed, with the exception of emissivity that decreased (Figure 4.10 and Table 4.2). The highest mean kinetic temperature (964 K) and lowest mean emissivity (0.693) were observed around 24 minutes after acquisition initiation. However, some of the lowest mean melt fraction and heat flux values were observed at this time. Instead, the highest mean melt fraction (0.28) and heat flux (0.047 MW) values were measured around the 6-minute time. At this time, the mean kinetic temperature and emissivity values were around the overall mean values for this acquisition period. The overall initial decrease in mean kinetic temperature, fraction of melt, and heat flux (but increase in emissivity) coincided with an almost consistent variability during the initial 16-minute period (Figure 4.10). The same trend was observed in the final 7 minutes but at an approximately 50% lower constant variability (Figure 4.10 and Table 4.2). The thermal properties had a more singular

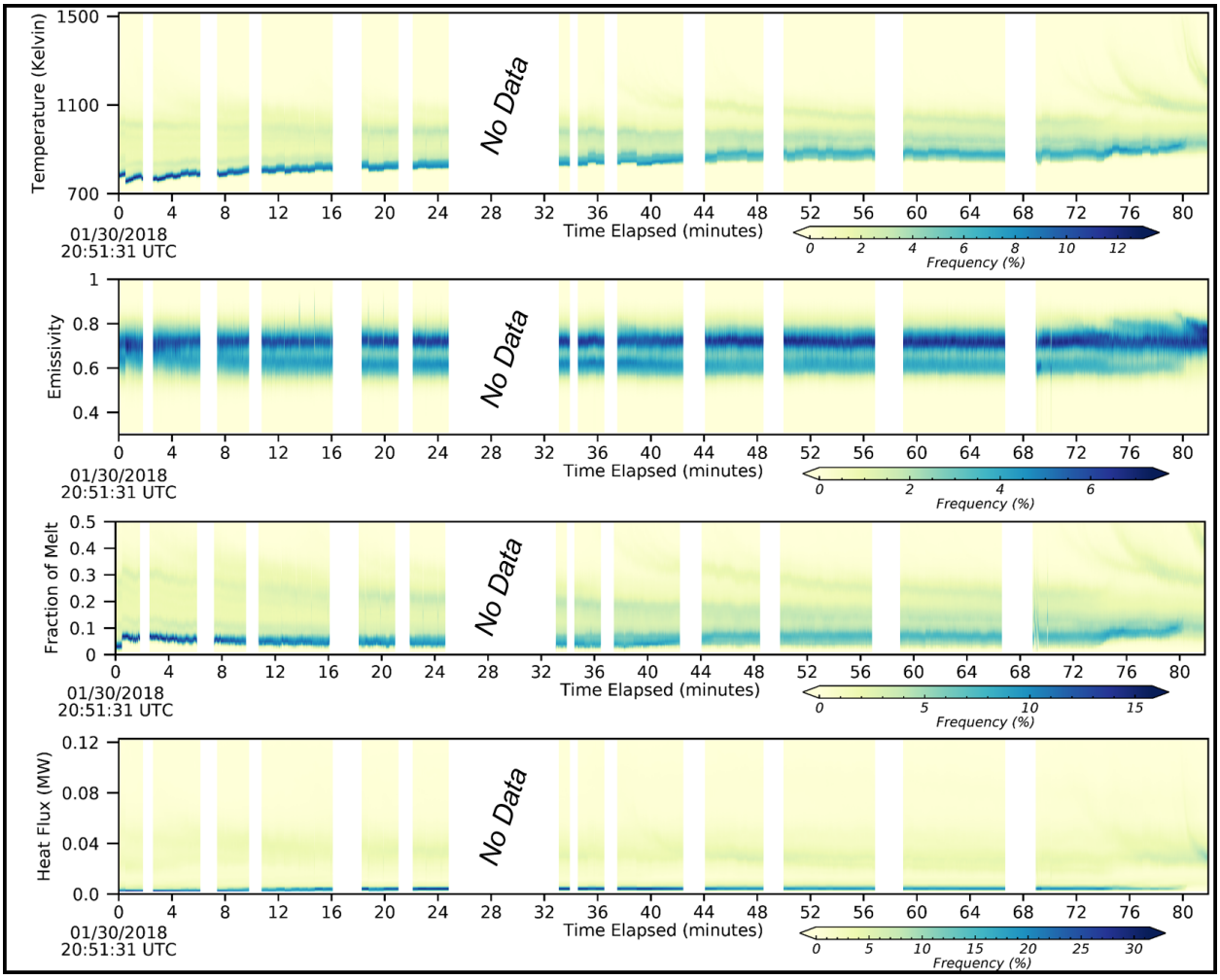

Figure 4.8: Temporal density frequency distributions of a pāhoehoe lava flow on the coastal plain of the Pu'u 'Ō'ō lava flow field of Kīlauea volcano (Hawai'i) using MMT-Cam data, acquired on January 30, 2018 at 20:51:31 UTC. The plots illustrate the spatial variability in thermal properties with time elapsed. Note the white regions represent periods when no data were acquired due to instrument repositioning and when other targets were studied (e.g., gas emissions).

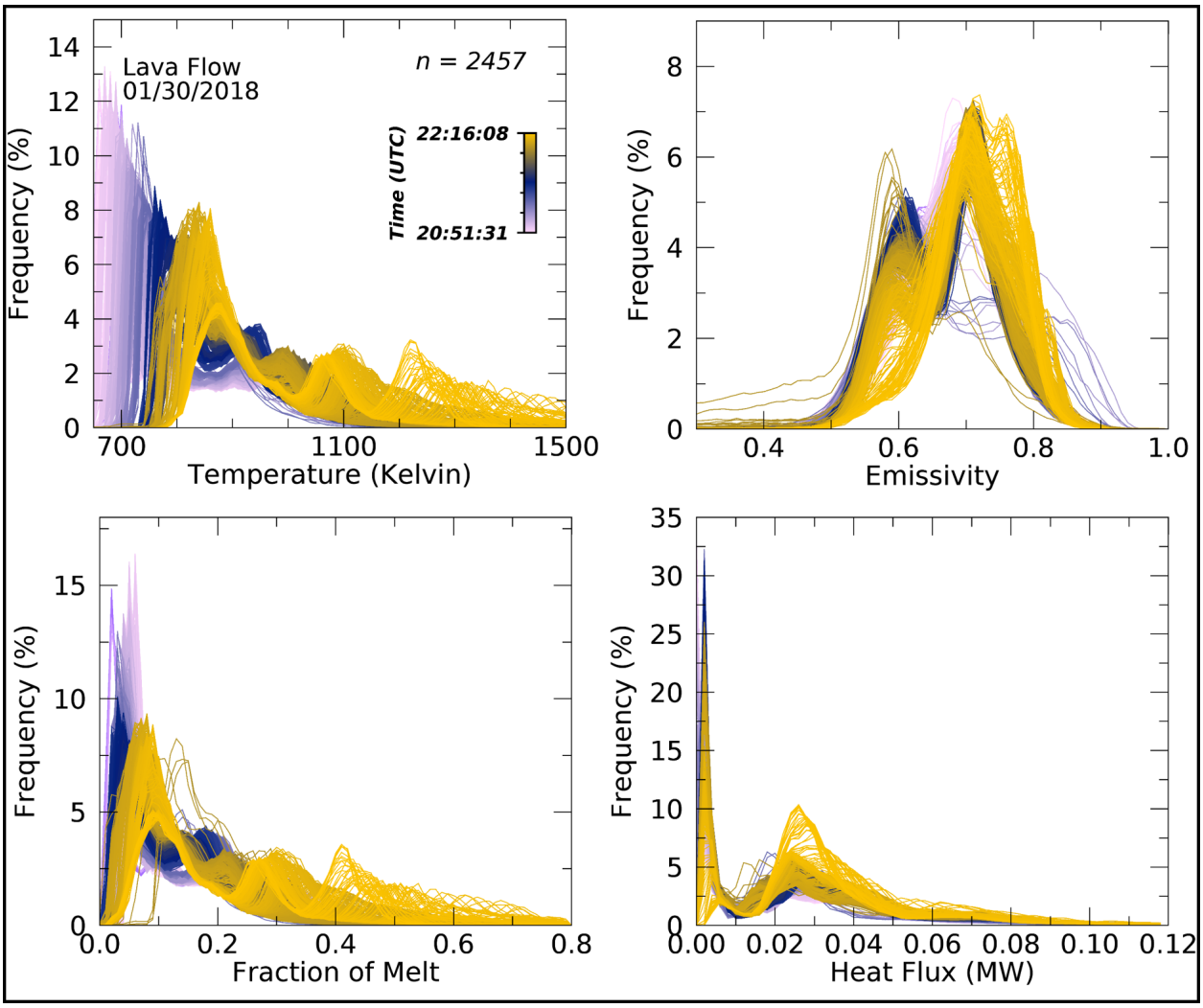

Figure 4.9: Temporal frequency distributions acquired of a pāhoehoe lava flow on the coastal plain of the Pu'u 'Ō'ō lava flow field of Kīlauea volcano (Hawai'i) using the MMT-Cam on January 30, 2018 at 20:51:31 UTC. Each plot represents the distribution of thermal properties across the active lava lake with the time symbolized through the color gradation. These are cross-sectional visualizations of Figure 4.8.

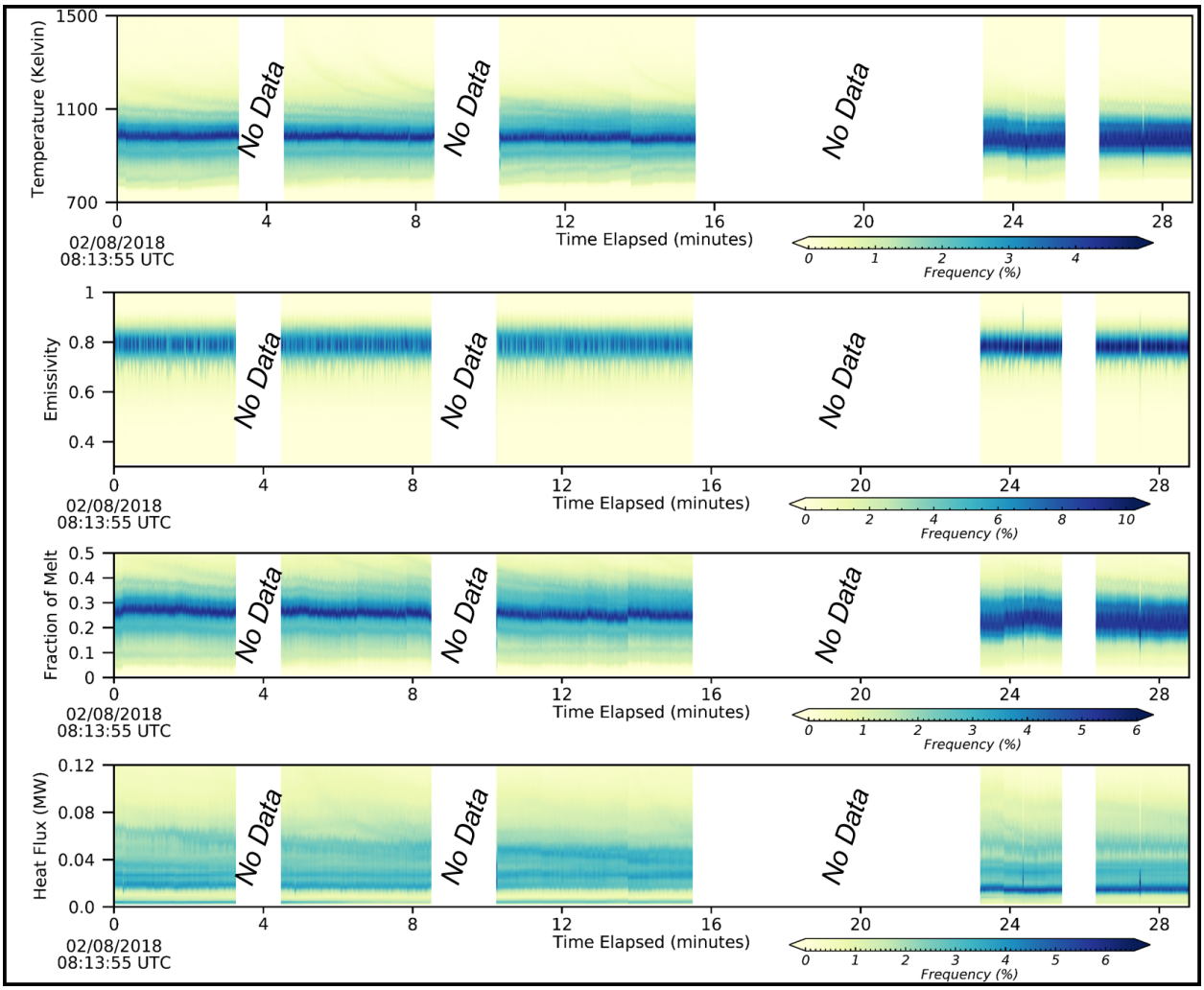

Figure 4.10: Temporal density frequency distributions of a pāhoehoe lava flow on the coastal plain of the Pu'u 'Ō'ō lava flow field of Kīlauea volcano (Hawai'i) using MMT-Cam data, acquired on February 8, 2018 at 08:13:55 UTC. The plots illustrate the spatial variability in thermal properties with time elapsed. Note the white regions represent periods when no data were acquired due to instrument repositioning and when other targets were studied (e.g., gas emissions).

modal distribution during this lava flow, with the exception of the heat flux measurements that highlighted a 3-5 modal distribution classifications (Figure 4.10).

Comparison of results from the two pāhoehoe lava flow acquisition periods on the coastal plain, revealed similar surface kinetic temperatures with the February 8 data having lower variability (∼15%). The lowest mean emissivity values were observed in the January 30 data at 0.660 (σ=0.085) compared to 0.748 on February 8 (σ=0.096). The February 8 data had higher mean melt fractions (0.25) and lower variability (σ=0.10). Additionally, the February 8 data had the highest mean heat flux values (0.039 MW) compared to January 30 (0.029 MW). Generally, higher thermal property values were accompanied by higher variability values. Overall, the measurements acquired of the lava flows on these two occasions were very similar but the heat flux was greater on February 8. In addition, increases in kinetic temperature, fraction of melt, and heat flux were observed during the acquisition period on January 30, compared to mostly constant measurements during the acquisition period on February 8 (Figures 4.8-4.10 and Table 4.2). Therefore, the activity was likely greater on February 8, although there were instances (less than 2 minutes) of greater activity on January 30 that can likely be associated with a large breakout event (e.g., ∼75 minute) (Figures 4.8-4.10).

Evaluating the difference between the thermal properties measured for the lava lake and lava flows revealed higher mean surface kinetic temperature (946 vs. 914 K), fraction of melt (0.28 vs. 0.23), and heat flux (2.655 vs. 0.038 MW) values at the lava lake, as expected. However, the deviation was higher in the lava flow kinetic temperature and fraction of melt measurements. The mean emissivity values were comparable at both eruption settings with slightly higher variability observed at the lava lake (σ= 0.079 vs. 0.071) (Table 4.2). All the thermal properties at the lava lake mostly represented a bimodal distribution compared to multiple modal distributions observed in the lava flow data (Figures 4.5 and 4.8), implying a more complex mixture of surfaces were present during lava propagation (e.g., molten, visco-elastic, and glassy surfaces).

4.4.3 Spatial Extent

Three-time segments were chosen for further detailed spatial analysis of the thermal properties of the lava lake on February 2 and lava flows on January 30. These dates were selected because they had the largest variability within the properties and provided representative observations of the eruption settings during the campaign.

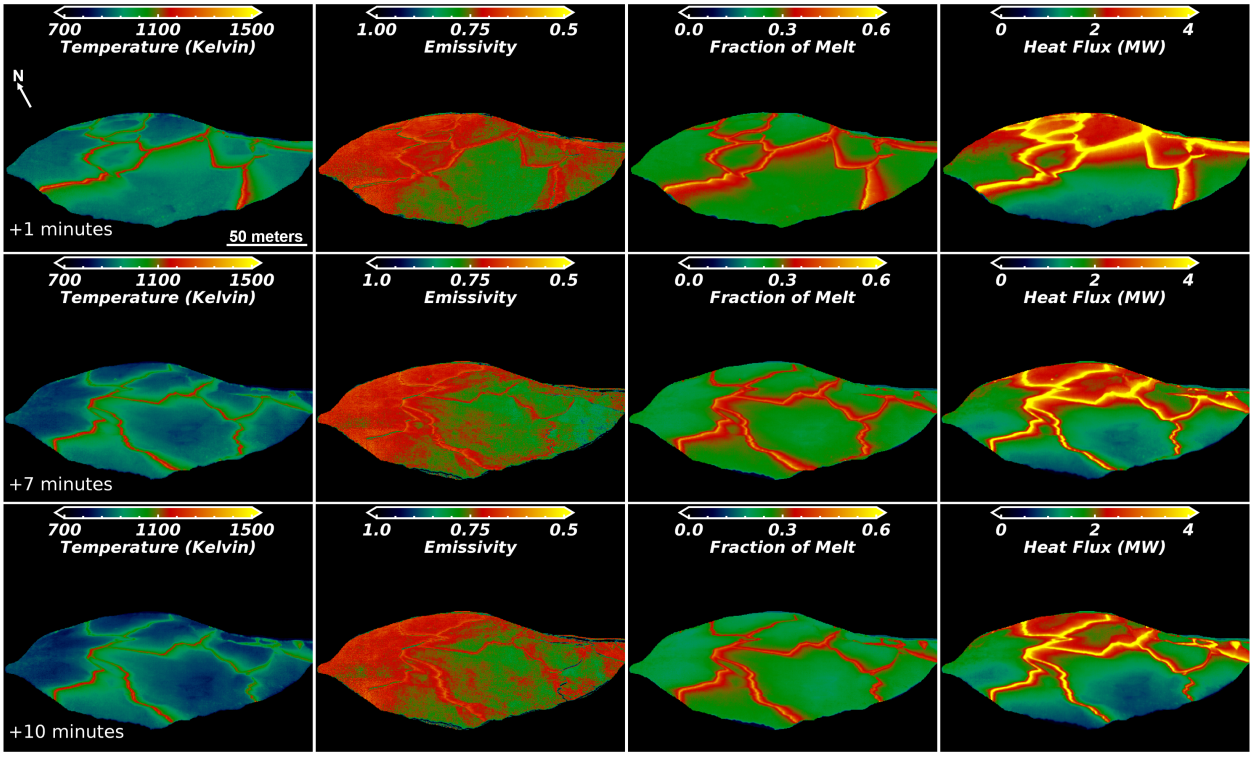

Figure 4.11: Columns from left to right, surface kinetic temperature, emissivity, fraction of melt, and heat flux derived from ground-based multispectral MMT-Cam data of the Halema'uma'u Crater lava lake acquired on February 2, 2018 starting at 06:11:26 UTC. The rows represent spatial variability observed by the MMT-Cam across the lake at (top to bottom) 1, 7, and 11 minutes from the start of data acquisition. The data were acquired from the rim of the Halema'uma'u Crater to the southwest of the lava lake at a horizontal distance of ∼200 meters to the center and ∼120 meters vertically above the surface, corresponding to a pixel size of between 0.22 and 0.75 meters. Note, the emissivity color bar is inverted for easier comparison with the other properties.

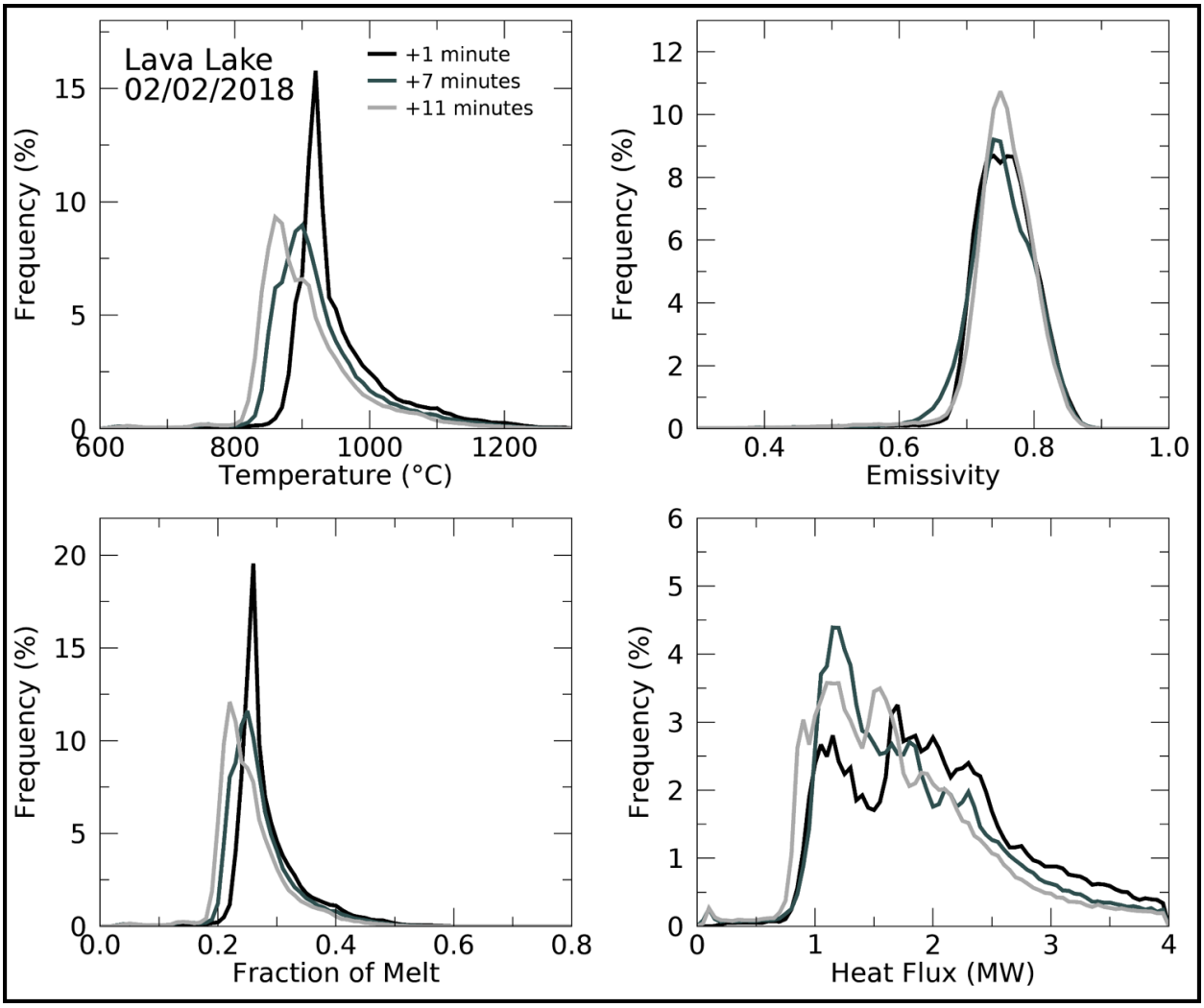

Figure 4.12: Spatial frequency distributions of the lava lake in the Halema'uma'u Crater of Kīlauea volcano (Hawai'i) using MMT-Cam data, acquired on February 2, 2018 at 06:11:26 UTC. Each plot represents the distribution of thermal properties across the active lava lake at the time segments shown in Figure 4.11.

On February 2, time segments at 1, 7, and 11 minute(s) were chosen for spatial analysis at the lava lake (Figures 4.11 and 4.12). At the 1-minute segment the highest concentration of temperatures greater than 1050 K were observed, a result of higher portions of molten cracks to crustal plates across the lava lake surface. This was in contrast to the 11-minute segment that had the highest proportion of cooler (less than 900 K) crustal plates on the lava surface. All the segments had strong modal distributions skewed to higher temperatures. There was a small secondary peak at higher temperatures in the 11-minute segment. The highest proportion of low emissivity values (less than 0.75) were observed in the 1-minute segment and was opposite in the 11-minute segment but the modal distribution was similar at all times. Also, the majority of the lowest emissivity values correlate with the highest temperature portions of the lava lake surface. Higher proportions of melt fractions were observed in the 1-minute and 7-minute segments with the lowest at 11-minutes, a result of the higher percentage of molten cracks on the surface of the lake during these periods. The fraction of melt measurements had a modal distribution with a strong skew to higher fractions. Secondary peaks were observed at higher fractions in the 11-minute segment and at lower fractions in the 7-minute segment. The highest heat fluxes were observed in the 1-minute segment compared to the lowest in the 11-minute segment. This trend correlates with temperature and fraction of melt but inversely with emissivity. All the segments had a broad multi-modal distribution skewed to higher heat fluxes. The 1-minute segment had a strong bimodal distribution at $\sim$1 and 1.75 MW. In these data, fractions of melt were the dominant factor in the heat flux calculation at the lava lake. The highest fluxes were located along and near the molten cracks with the lowest located in the interior of the crustal plates. Additionally, the higher overall heat fluxes were observed in the northern and eastern margins of the lava lake, which correlate with high upwelling activity. The lower overall fluxes were observed in the southern regions of the lava lake, forming a thermal and flux gradient from north to south (Figures 4.11 and 4.12). These data were used, with pixel tracking, to calculate a mean time-average velocity of the entire surface during the acquisition of $\sim$0.07 $m \cdots^{-1}$ to the south.

On January 30, time segments at 24, 71, and 81 minutes past the start of data collection at the lava flows were chosen for detailed spatial analysis (Figures 4.13 and 4.14). At the 81-minute segment the highest concentration of temperatures (greater than 1050 K) and melt fractions were observed, which was a result of the higher portions and larger volume breakouts of molten lava. This was in contrast to the 24-minute segment that had the highest proportion of cooler (less than 900 K) crustal lobes across the lava field and least breakout events (Figures 4.13 and 4.14).

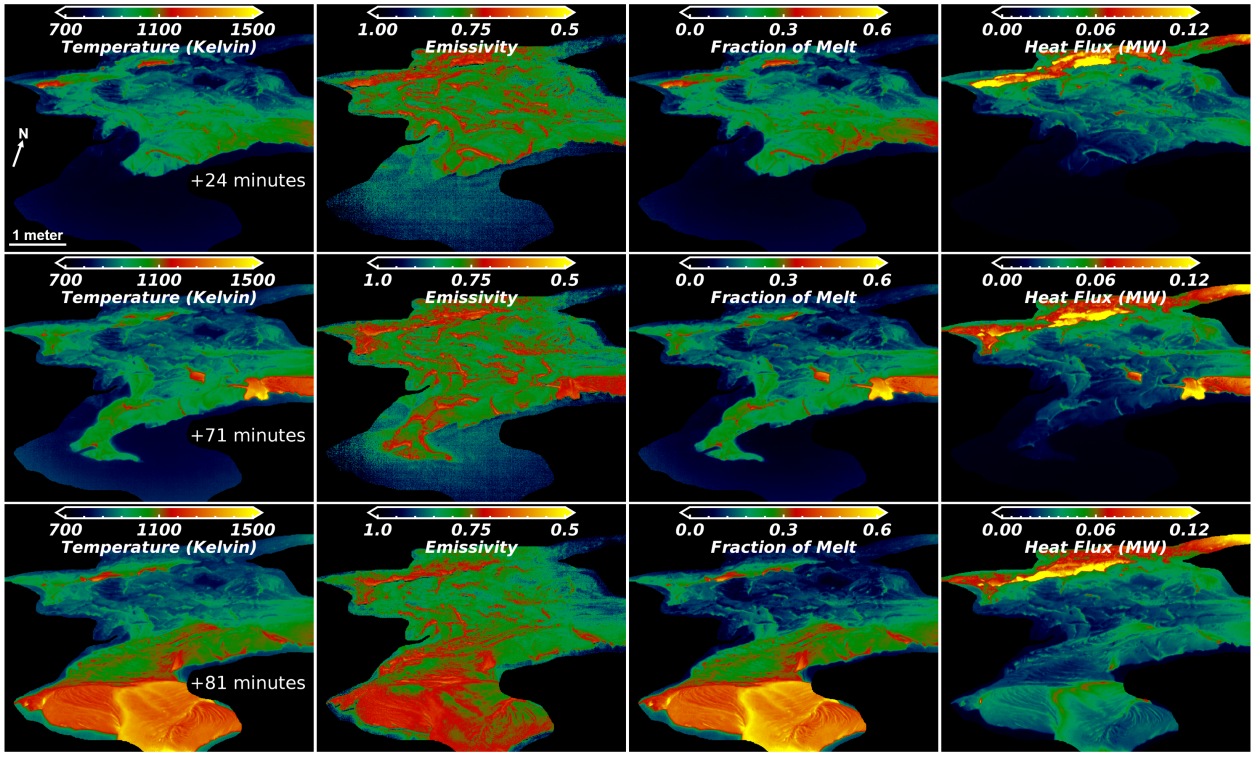

Figure 4.13: Columns from left to right, surface kinetic temperature, emissivity, fraction of melt, and heat flux derived from ground-based multispectral MMT-Cam data of a pāhoehoe lava flow on the coastal plain of the Pu'u 'Ō'ō lava flow field acquired on January 30, 2018 starting at 08:13:55 UTC. The rows represent spatial variability observed using the MMT-Cam data across the flow field at (top to bottom) 24, 71, and 81 minutes from the start of data acquisition. The data were acquired from a horizontal distance of ∼5 meters from the final flow front and ∼2 meters vertically above the surface, corresponding to a pixel size of between 0.05 and 0.22 meters. Note, the emissivity color bar is inverted for easier comparison with the other properties.

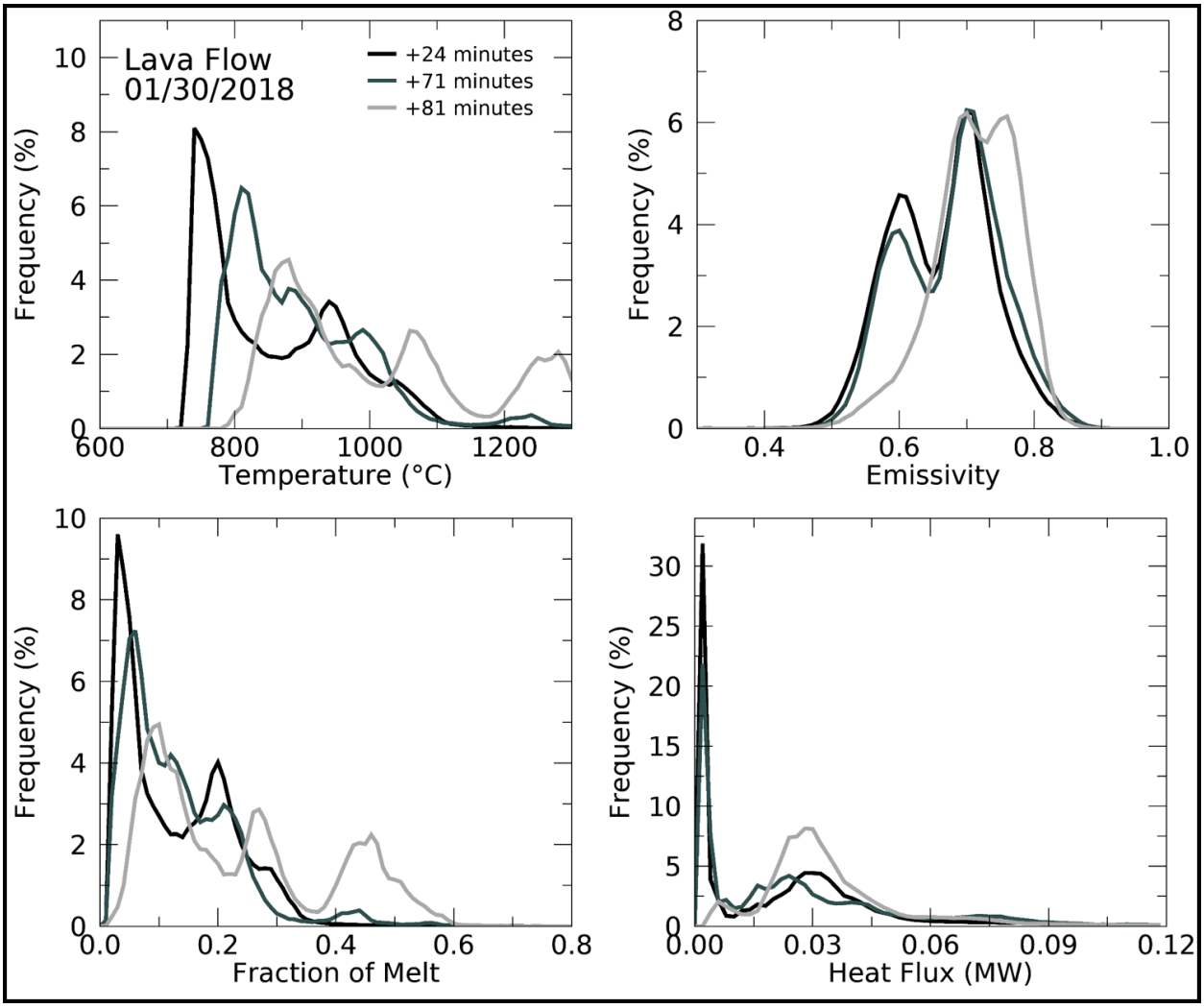

Figure 4.14: Spatial frequency distributions of a pāhoehoe lava flow on the coastal plain of the Pu'u 'Ō'ō lava flow field of Kīlauea volcano (Hawai'i) using MMT-Cam data, acquired on January 30, 2018 at 20:51:31 UTC. Each plot represents the distribution of thermal properties across the active lava flows at the time segments shown in Figure 4.13.

The distributions transition to lower temperatures and melt fractions during the time period and increase from bi- to tri- modal. As expected, the highest proportion of low emissivity values (<0.75) were observed in the 81-minute segment and the lowest in the 24-minute segment. Strong bi- and tri- modal distributions were observed at all three time-segments with skew to molten values. Additionally, the majority of the lowest emissivity values correlate with the highest temperature regions observed across the lava flow field. The heat fluxes were mostly constant between all the time segments, with the 81-minute segment having the highest fluxes. This weakly correlated with the higher kinetic temperature and melt fraction regions within the active lava flow fronts. In the MMT-Cam lava flow data, lower emissivity regions were poorly correlated to higher heat flux regions, with median emissivity values correlating to the highest heat flux values. Additionally, high heat fluxes were observed along a channel at the back of the lava flow field in all the time segments. This highlighted the flow pathway of lava through a small tube to the active front of the lava flow field. This pathway was not inherently obvious in the kinetic temperature, emissivity, and fraction of melt data separately; however, where these data were combined to calculate heat flux the pathways were clearly observed (Figure 4.13).

4.5 Discussion

The data acquired from the lava lake and lava flows at Kīlauea volcano in January - February 2018 using a ground-based multispectral TIR camera system at high spatial and temporal resolutions provide a foundation for improving the derivation of thermal properties of active lava surfaces. TIR analysis is one method used for improving our understanding of eruption dynamics, having been used previously with a singular assumed emissivity to derive numerous eruption properties including temperature, heat flux, and mass flux (Wright and Flynn, 2003; Harris et al., 2005; Sahetapy-Engel and Harris, 2009; Harris, 2013; Patrick et al., 2013, 2017, 2018). However, the use of concurrent *in situ* emissivity measurements provide more detail for extracting and interpreting the heat budget and thermal dynamics of an active lava surfaces during propagation and cooling. Surface kinetic temperature, emissivity, fraction of melt, and heat flux have been calculated for basaltic lava surfaces, totaling more than 150 minutes of observations. The spatial and temporal variability and response of these surface properties have also been characterized here. This analysis provides a detailed structure of the thermal variations and dynamics during both periods of greater

Table 4.3: The mean values calculated using the variable emissivity measurements ($\approx \varepsilon$) acquired in this study compared to an assumed constant emissivity value ($--\varepsilon$) (e.g., 0.95).

Mean Values		**Lava Lake**			**Lava Flow**	
		02/02/2018	**02/03/2018**	**02/06/2018**	**01/30/2018**	**02/08/2018**
Temperature (Kelvin)	$\approx \varepsilon$	939	928	973	882	947
	σ	69	97	81	121	109
	$--\varepsilon$	929	926	973	882	955
	σ	68	97	80	119	106
	$\Delta\varepsilon$ (%)	1.05	0.21	0.00	0.00	-0.89
	σ (%)	1.29	0.32	0.91	1.98	2.65
Emissivity	$\approx \varepsilon$	0.757	0.797	0.728	0.680	0.769
	σ	0.058	0.107	0.073	0.074	0.067
	$--\varepsilon$	0.950	0.950	0.950	0.950	0.950
	σ	0.000	0.000	0.000	0.000	0.000
	$\Delta\varepsilon$ (%)	-20.32	-26.63	-23.37	-28.42	-19.05
	σ (%)	-	-	-	-	-
Fraction of Melt	$\approx \varepsilon$	0.28	0.26	0.30	0.20	0.26
	σ	0.06	0.09	0.08	0.10	0.10
	$--\varepsilon$	0.30	0.28	0.32	0.21	0.28
	σ	0.05	0.09	0.08	0.11	0.12
	$\Delta\varepsilon$ (%)	-7.05	-7.89	-6.03	-8.59	-8.16
	σ (%)	14.00	-2.17	-3.61	-8.18	-15.00
Total Heat Flux (MW)	$\approx \varepsilon$	1.914	2.203	3.849	0.031	0.044
	σ	0.708	1.152	1.671	0.020	0.027
	$--\varepsilon$	2.121	2.567	4.247	0.039	0.057
	σ	0.767	1.402	1.837	0.027	0.034
	$\Delta\varepsilon$ (%)	-9.74	-14.17	-9.38	-21.21	-22.22
	σ (%)	-7.73	-17.83	-9.02	-25.00	-19.57

[3]Note, "$\Delta\varepsilon$" is the percentage difference between the constant and variable emissivity results and "σ" is the standard deviation of the results.

and lesser activity. For example, the mean emissivity of all molten basaltic surfaces was 0.726 at a surface kinetic temperature of 934 K, which comprise approximately ~10% of the areas studied. This variability is important for future analyses using ground, airborne, or spaceborne TIR data

to derive properties such as thermal or mass flux rates.

4.5.1 Temporal Variability

Numerous previous studies have investigated the temporal fluctuations and trends in thermal properties of active lava lakes and flows, especially at Kīlauea (Harris et al., 1998; Byrnes et al., 2004; Koeppen et al., 2013; Orr et al., 2013; Patrick et al., 2013, 2017). However, there has been limited analysis that incorporates concurrent *in situ* emissivity data, which resulted in melt fractions and heat fluxes being overestimated where *in situ* emissivity data are not used (Table 4.3). Therefore, the integration of *in situ* variable emissivity data into thermal investigations of lava surface resulted in more accurate derivation of flux and cooling rates of the surface.

During each acquisition period analyzed here, both low- (<0.01 seconds^{-1}) and high- (>0.2 seconds^{-1}) frequency fluctuations were detected (Figures 4.15 and 4.16). The high frequency fluctuations were characterized as small (<20 meters), short-duration (<5 seconds) spattering events (Patrick et al., 2018) at the lava lake or small breakout events (<15 meters) on the lava flow field (Figures 4.15 and 4.16). The low-frequency fluctuations were characteristic of general medium-term (>100 seconds) increases or decreases in activity and inferred variations in lava supply to the surface (Figures 4.15 and 4.16). These medium-term variations can be the consequence of effusion rate changes that are critical to propagation models that quantify hazard assessment and eruption potential.

At the lava lake, higher activity periods were detected by higher proportions of molten cracks and numerous smaller crustal plates. This is indicative of faster overturning due to increases in the upwelling of heat and material to the surface (Patrick et al., 2018). This corresponds to a response observed in the thermal properties derived from the MMT-Cam data with kinetic temperature, fraction of melt, and heat flux increasing, while emissivity decreased. Similar lava lake TIR analysis had been conducted previously (e.g., Davies et al. 2008; Patrick et al. 2018) but the lack of high-resolution *in situ* multispectral emissivity data causes potential errors in thermal calculations and flux estimates. The overall low-frequency (<0.01 seconds^{-1}) fluctuations observed in the lava flow data are characteristic of the variability in the volume and number of breakout events (Figures 4.15 and 4.16), which is controlled by the supply of lava to the active flow front usually through subsurface tube structures from the Pu'u 'Ō'ō vent (Holcomb, 1987).

The same responses in thermal properties derived in the multispectral TIR data observed in

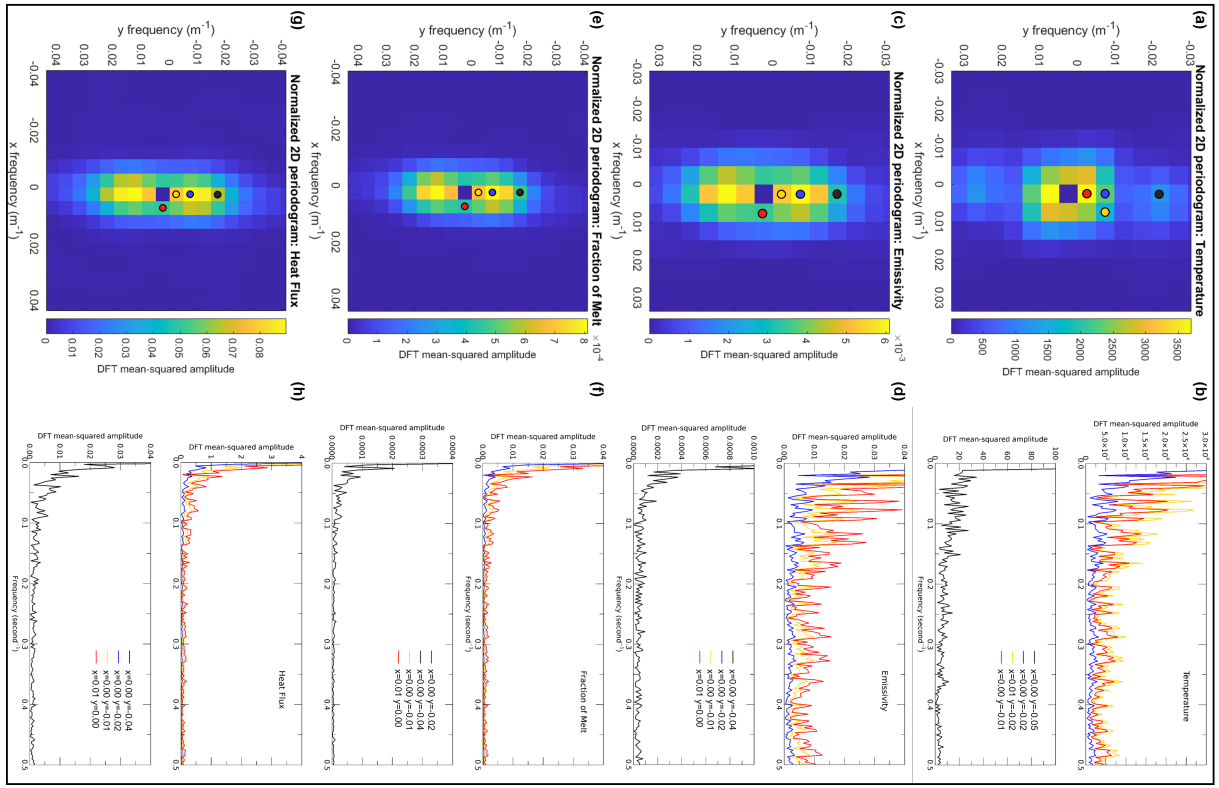

Figure 4.15: Spatiotemporal discrete Fourier transform frequency distributions of the lava lake in the Halema'uma'u Crater of Kīlauea volcano (Hawai'i) using MMT-Cam data, acquired on February 2, 2018 at 06:11:26 UTC. The plots in the left column represent the two dimensional power intensity (amplitude) of the derived thermal properties. Amplitude values closer to and further from the origin (0,0) are associated with lower frequency (longer wavelength) and higher frequency (shorter wavelength) spatial variability, respectively. The plots in the right column represent the one dimensional power intensity (amplitude) of the derived thermal properties temporally at specific spatial frequencies (line colors correspond to spot colors on associated spatial power intensity plots in left column).

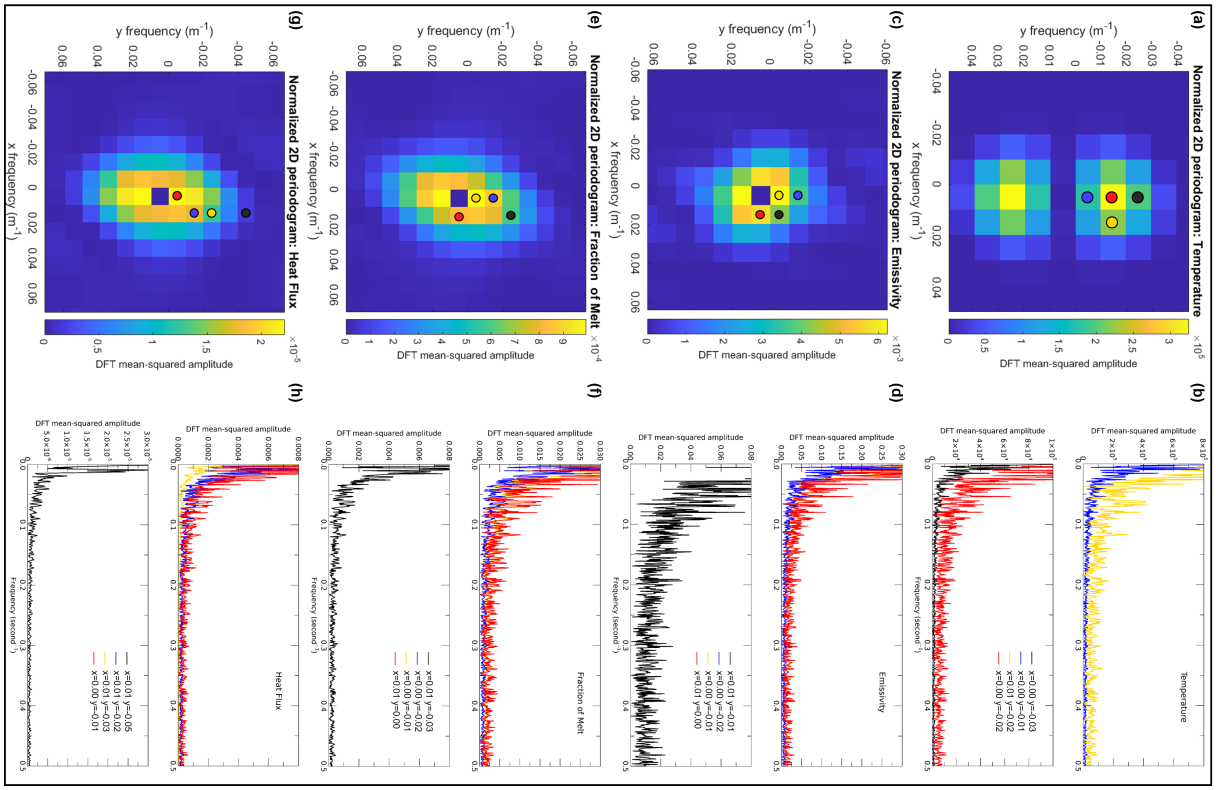

Figure 4.16: Spatiotemporal discrete Fourier transform frequency distributions of a pāhoehoe lava flow on the coastal plain of the Pu'u 'Ō'ō lava flow field of Kīlauea volcano (Hawai'i) using MMT-Cam data, acquired on February 2, 2018 at 06:11:26 UTC. The plots in the left column represent the two dimensional power intensity (amplitude) of the derived thermal properties. Amplitude values closer to and further from the origin (0,0) are associated with lower frequency (longer wavelength) and higher frequency (shorter wavelength) spatial variability, respectively. The plots in the right column represent the one dimensional power intensity (amplitude) of the derived thermal properties temporally at specific spatial frequencies (line colors correspond to spot colors on associated spatial power intensity plots in left column).

the lava lake data during higher activity periods were also detected at the lava flows. However, the response in the heat flux data were not as strong during higher activity periods (where kinetic temperatures were higher), which is partly a consequence of less efficient radiant heat flux from the molten surfaces as quantified in the emissivity data. This emissivity trend had previously been observed in laboratory experiments that investigated radiant heat flux of volcanic melts samples but limited application has been implemented on natural lava flows by using *in situ* measurements (Abtahi et al., 2002; Lee et al., 2013). Additionally, the influence of this trend on heat flux estimations has had limited investigation and is poorly understood, which resulted in overestimates of fluxes previously (Table 4.3).

The temporal variability in heat fluxes during the separate acquisitions highlight the intensity of activity observed at a moment in time. However, limited interpretations about the potential long-term activity can be formed as it is almost impossible to extrapolate the fluctuations in thermal properties between these acquisitions (days). A potential solution would be to combine results from this study with other TIR datasets of the lava lake (including ground- and satellite-based datasets), allowing insights into the long-term heat budget of a volcanic system and improving forecast capabilities with the use of a well constrained background thermal understanding. In the future, TIR dataset acquired using ground-based instruments with similar acquisition (spatial and spectral resolutions) and processing techniques (spatiotemporal analyses) can also be combined to evaluate the long-term thermal processes of these types of volcanic systems.

4.5.2 Spatial Variability

The ability to acquire multispectral TIR data at high spatial resolution from active lava surfaces and incorporate *in situ* emissivity data into thermal analysis of erupting lava improves the retrieval and reliability of results. Instead of assuming emissivity values or deriving values from cooled samples post-campaign in the laboratory, the high spatial resolution analysis provided detailed spatial variability across the active lava lake and lava flow lobes, presenting a better understanding of the thermal mechanisms of overturning, spattering, breakouts, and cooling. Heat flux provided an estimate for inferring subsurface fluxes of heat and material, including upwelling regions within a lava lake and pathways of subsurface lava to the active flow front. These can be difficult to discern solely from temperature data analysis that does not intrinsically account for emissivity and pixel size. The ability to identify subsurface fluxes is useful for inferring potentially active regions within

a flow field that can help provide more accurate and quantitative forecasting predictions. Overall, the multispectral TIR derived thermal properties of the lava lake showed a highly dynamic system within a small spatial region (<0.5 km^2) and provided quantitative evidence for potential upwelling regions and breakout activity locations. The strong bimodal distribution of the thermal properties of the lava lake suggest the discrete thermal properties of both the molten and crustal portions of the lake and aid in the characterization of the lake. For example, the spatial frequency analysis highlights a low frequency (high wavelength: 100 meters) variability in a north-south trend at a high amplitude (e.g., 600 K) (Figure 4.15).

This study emphasizes the importance of directly measuring emissivity at multiple discrete wavelengths to more accurately derive surface kinetic temperature and heat flux estimates of a lava surface (Table 4.3). For example, if this study assumed a constant emissivity of 0.95, analysis reveals that surface temperatures of the lava lake would have been underestimated by 0.5% and melt fractions overestimated by ∼7% (Table 4.3). As a consequence, the heat flux would have been overestimated by ∼11% (Table 4.3), which can result in inaccurate lava flow propagation model predictions (see Chapter 5). These variations are not acceptable as they are greater than the average errors and uncertainty in the emissivity (< 3%), fraction of melt (< 5%), and heat flux (< 6%) data, with the exception of surfaces temperature (< 3%) (Thompson et al., 2019; Thompson and Ramsey, 2020) (see Chapters 2 and 3).

During this campaign, upwelling and spattering at the lava lake were concentrated in the northern and eastern regions (Figure 4.15), which was highlighted in the kinetic temperature, emissivity, fraction of melt, and heat flux data. In contract, lower thermal responses were observed in the southern regions (higher emissivity values), suggesting migration vectors and subsequent downwelling in this region (Patrick et al., 2018). On February 2, 2018, the time-average surface velocity was ∼0.07 $m \cdot s^{-1}$ to the south, which is similar to velocities observed at other lava lakes (Figure 4.11) (Harris et al., 2005). Additionally, as expected, higher velocities correlate to higher periods of heat flux, implying greater supply of hotter material to the surface of the lake during these times.

In the lava flow data, elevated kinetic temperature, fraction of melt, and heat flux values and depressed emissivity values were observed at breakout locations along the margins of the lava flow field. The spatial frequency analysis confirms the majority of the breakouts occured in the southern and northwestern portions of the lava flow field (Figure 4.16). The multi-modal spatial distributions imply there were multiple thermal components across the lava flows during propagation, likely including molten lava, viscoelastic crust, and glassy crust. The spatial distribution analysis revealed

there was an almost continuous transition of thermal components (e.g., temperature and surface physical state) contributing to the properties measured and not a discrete number of characteristic components or surfaces.

Over time, the responses in measurements to observed activity migrated as the focus of the activity transition from one part of the flow field to another. This was significantly more obvious in the heat flux data that highlight the potential supply pathway of juvenile lava to the flow field front and active lobes stalling. The heat flux data highlights thermal anomalies not obvious on the surface because it accounts for all major heat transfer processes (conduction, convection, radiation), each of which are weighted dependent on the surface kinetic temperature and pixel area. On January 30, 2018, lava was supplied to the front (south) through a narrow tube-like feature in the northeast of the observation area. Initially, activity was concentrated in the north of the flow field but transitioned to the front during the observation, implying the migration of juvenile lava into this portion of the flow front during the 82 minutes.

Additionally, at 81 minutes into the lava flow acquisition, the heat flux at the active front was low compared to the supply tube, which was a result of lower emissivity measurements where molten lava is on the surface. This is a factor as radiant heat flux dominates prior to a crust forming and, to a lesser extent, the decrease in pixel size. Therefore, we can assume that the overall heat flux is less efficient where radiant heat flux dominates compared to where convective and conductive heat flux dominates due to lower emissivity being measured. It can be implied that a lava surface cools at a greater rate after a viscoelastic crust forms as an increase in emissivity is observed with cooling and crustal formation. This is emphasized by comparing the results of this study with the results if a constant emissivity value of 0.95 was assumed instead. Assuming an emissivity of 0.95 would have overestimated the heat flux by up to 25% in the lava flow data (Table 4.3).

This study shows a strong spatial correlation between heat flux and kinetic temperature, fraction of melt, and inversely emissivity. However, heat flux and emissivity exhibit a more complex correlation as lower emissivity molten lava surfaces result in lower heat fluxes being estimated, specifically radiant heat flux. This implies previous calculations that used a higher uniform emissivity overestimated the radiant heat flux (by at least 15%), especially for molten portions of the lava surface and prior to a crust forming. This leads to inaccurate calculations of cooling rates and final lava flow propagation length.

4.6 Conclusions

High-resolution ground-based multispectral TIR data were presented for the active lava lake and lava flows at Kīlauea volcano in January - February 2018 showing the thermal variability and eruption dynamics of these eruptions at this time. The high spatial and temporal resolution data, with additional spectral information, of these cooling lava surfaces provided detailed observations of thermal fluctuations as the lava surfaces cooled, overturned, and propagated. The spectral resolution allows *in situ* emissivity measurements to be acquired in great detail, improving subsequent calculations for temperature and heat flux, specifically radiant heat flux. Even though limited data were acquired over a large time series, the fundamental variability in eruption dynamics were observed and compared.

This study identified both low- and high- frequency temporal variability in thermal properties from the summit lava lake at Kīlauea volcano with up to 25% and 5% frequency fluctuation from the mean, respectively. The high-frequency temporal variability is less pronounced in the lava flow data (<1%); however, the low-frequency temporal variability was up to 25% during these observations. These thermal fluctuations provided insights into the eruption dynamics and changes in activity intensity that have been strongly correlated to visual verification observations. On January 30, 2018, spatial analysis of an active lava flow front illustrated the high variability of thermal properties related to eruption activity and the heat flux calculations quantified potential lava supply pathways to the active front and breakout zones. On February 2, 2018, the spatial analysis of the lava lake showed the migration of surface plates and thermal properties from the northern to southern regions of the lake. Additionally, strong bimodal distributions of thermal properties were observed at the lava lake, representing the crustal plates (∼80%) and the molten cracks (∼20%) on the surface with the proportions of each remaining mostly constant during the observation periods.

Overall, the high-resolution TIR data enhances the spatiotemporal analysis achieved using a ground-based instrument with greater detail of low- and high- frequency variabilities discerned. The addition of concurrent *in situ* spectral measurements improves the reliability and accuracy of derived properties that rely on these detailed measurements (e.g., heat flux). The emissivity data have shown that the emissivity values of erupting molten lavas are lower than previously calculated (by at least 20%), which results in lower heat fluxes (at least 15%) due to less efficient radiative cooling of molten lava. Therefore, previous thermal budget calculation using very high

spatial resolution data (<30 meters) overestimated the radiant heat flux from molten lava prior to cooling and crustal formation (Table 4.3). All of these data can be combined to improve eruption dynamics and activity predictions to reduce hazard risk on local populations during an effusive eruption. In the future, this can be further improved by permanently installing similar ground-based multispectral TIR instruments at active volcanoes to evaluate the long-term trends of the volcanic system, to better constrain background activity at a volcano and improve hazard assessments with accurate heat flux measurements.

5.0 Influence of Variable Emissivity on Lava Flow Propagation Modeling

5.1 Introduction

Volcanic lava flow modeling is a powerful tool for quantitatively forecasting lava propagation and subsequently improving the accuracy and reliability of hazard assessments associated with lava flow inundation. This importance is reinforced by recent eruptions at Kīlauea (Hawai'i), Piton de la Fournaise (La Réunion), Etna (Italy), and Pacaya (Guatemala) that produced lava flows and posed serious risks to local populations and infrastructure. For example, in the summer of 2018, activity at Kīlauea volcano emplaced numerous stable channelized lava flows up to 15 kilometers long in the Puna district (southeast corner of the Island of Hawai'i), destroying over 700 homes and properties (Neal et al., 2019; USGS, 2018). The utilization of a robust lava flow propagation model during an eruption where populations are at risk would provide useful guidance to hazard response coordinators so more informed risk reduction measures are enacted. Unfortunately, the majority of these models require prior knowledge of lava rheology and/or thermal properties that can be time consuming to acquire and result in long lead times (a few days) to collate and process data. Additionally, it is critical to acquire an accurate DEM, identify the precise location of the vent, and accurately calculate the mass flux at the vent. While recent work at Mt. Etna has improved the modeling processing speed to near real time, more improvements are required, including the global integration of the framework being developed fro Mt. Etna (Cappello et al., 2019; Ganci et al., 2019).

Numerous factors control the runout distance and dispersion of a lava flow, including topographic slope, effusion rate, crystal and vesicle content, and thermal insulation (e.g., tube formation) (Harris et al., 1998; Cashman et al., 1999; Gregg and Fink, 2000). The majority of basaltic lava flow propagation models assume that temperature is dependent on yield strength and/or viscosity, both of which are inversely proportional to temperature (Park and Iversen, 1984; Dragoni and Tallarico, 1994; Harris and Rowland, 2001). Many models have been developed to simulate flow velocity, flow distribution, and spreading rate to evaluate overall flow evolution and heat flux (Harris et al., 1998; Harris and Rowland, 2001; Bilotta et al., 2012). These thermo-rheological models suggest that the thermal and morphological evolution of basaltic flows are constrained by the relationship between the cool glassy crust and hot viscous core (Miyamoto and Sasaki, 1997,

1998; Miyamoto and Papp, 2004; Miyamoto and Crown, 2006). However, the majority of these models assume a constant emissivity, which oversimplifies the calculated thermal flux (as shown in Chapter 4).

Many prior studies have developed lava flow propagation models (e.g., Harris and Rowland 2001; Avolio et al. 2006; Bilotta et al. 2012) that rely on thermal measurements as input parameters, such as temperature and emissivity, to calculate propagation and predict runout distributions/distances. These thermal components can be estimated or assumed from previous field or laboratory studies, but more recent studies have integrated measurements acquired from satellite instruments (Ramsey and Harris, 2013; Ramsey et al., 2019). For example, the Advanced Very High Resolution Radiometer (AVHRR) TIR data were used as input parameters in the integrated FLOWGO and DOWNFLOW models to estimate the lava flow runout from the 1991-1993 Mt. Etna eruption (Harris and Rowland, 2001; Favalli et al., 2005; Wright et al., 2008). Additionally, AVHRR and Moderate Resolution Imaging Spectroradiometer (MODIS) TIR data were incorporated into the MAGFLOW model to predict the emplacement of lava flows during the 2004, 2006, and 2011 Mt. Etna eruptions (Negro et al., 2008; Herault et al., 2009; Vicari et al., 2009, 2011). The integration of these remotely acquired and repeatable measurements have improved lava flow model predictions; however, additional enhancements in TIR measurements and derived calculations (e.g., heat flux) can be achieved, especially if integrating in near real time (Ramsey and Harris, 2013).

The majority of current lava propagation models assume a constant value for radiant heat flux efficiency (emissivity) that leads to inaccuracies in forecasting crustal formation and runout distance (Ramsey and Harris, 2013; Ramsey et al., 2019). Therefore, it is proposed that the greatest improvements in these models can be achieved through real time integration of *in situ* multispectral TIR data during an active flow propagation. This would improve the errors and uncertainties arising from lower resolution data and calculations of heat flux through better estimations of the efficiency radiant heat is emitted from a molten surface during cooling (Ramsey and Harris, 2013; Ramsey et al., 2019). Quantifying the fundamental variation in emissivity with cooling and crustal formation of lava surfaces will improve model-derived effusion and cooling rates (as will the capability to forecast future changes).

Emissivity is a unitless property that quantifies the efficiency at which radiant energy is emitted by a material and is typically measured in the infrared region of electromagnetic light spectrum. The property is related to the atomic bond vibrational motion exhibited by the material and is therefore dependent on wavelength, composition, temperature, rheology, and surface expression.

As no perfect emitters (blackbody surfaces) exist in nature, the variation at each wavelength is used to help characterize the properties of the material, such as rock composition. Previously, emissivity measurements have identified and quantified surface roughness, state changes (fraction of melt), and particle size distributions (e.g., Simurda et al. 2019; Williams et al. 2019; Thompson and Ramsey 2020). Also, studies investigating changes in emissivity of cooling molten lava have suggested that emissivity increases during cooling and subsequent crustal formation (Abtahi et al., 2002; Lee et al., 2013; Thompson and Ramsey, 2020). Therefore, it is likely that emissivity has been overestimated (<25%) in past modeling efforts, especially for higher temperature and molten surfaces (>900 K). In turn, overestimated heat flux calculations result in similar overestimation for cooling rates and consequently lead to the underestimation of final propagation runout distances (<7%) (Harris et al., 1998; Harris and Rowland, 2001; Harris, 2013; Ramsey et al., 2019). These variations lead to lower accuracy in lava propagation results and reduce the confidence of hazard assessments derived from these models.

This study investigated how variations in emissivity with temperature influences the propagation distances of channelized lava flows. Ground-based multispectral TIR data were acquired from a small lava flow formed at a tumulus (at Kīlauea volcano, Hawai'i) to derive and constrain the variability of emissivity, fraction of melt, heat flux, and the channel geometries during lava cooling and all phases of flow propagation. The temperature dependent emissivity relationship was developed into a module and incorporated into the PyFLOWGO model to evaluate the effect on final runout distance. To further validate this approach for larger flows, the PyFLOWGO model with the variable emissivity module was then used to simulated the fissure 8 lava flow emplacement produced during the 2018 LERZ eruption at Kīlauea volcano, Hawai'i. The effectiveness of the modified model with the additional module was assessed and high-resolution multispectral TIR data acquired on May 30, 2018 were used to verify the results.

5.2 Background

5.2.1 Kīlauea Volcano

Kīlauea is a basaltic shield volcano on the southeastern side of the Island of Hawai'i (HI, USA) that has been erupting almost continuously over the past 500 years (Holcomb, 1987). Magma

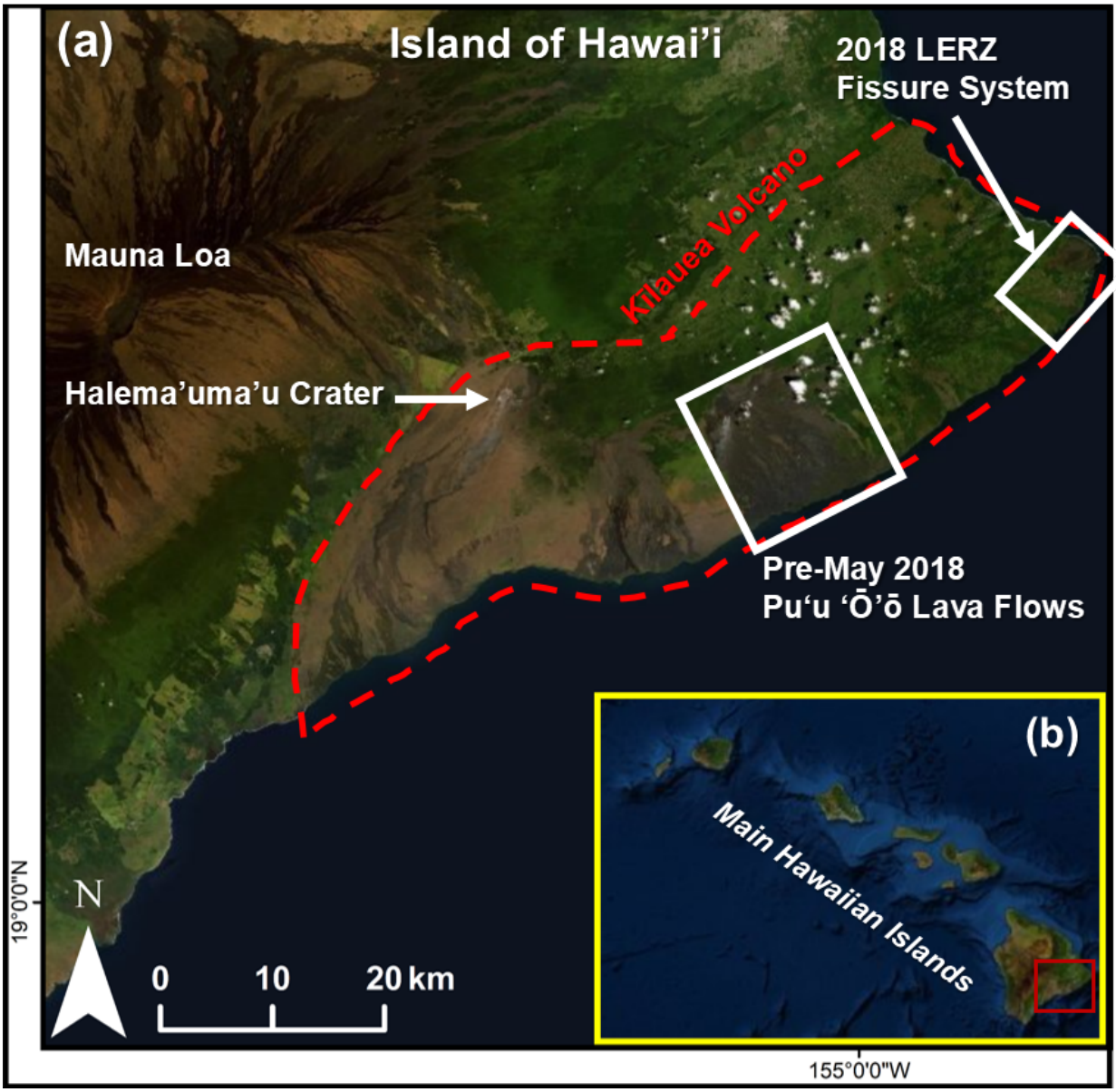

Figure 5.1: (a) Location map of Kīlauea volcano on the Island of Hawai'i with the (b) insert map showing the island's location within the main Hawaiian Island Chain (Source: ESRI and DigitalGlobe). The two eruptions investigated in this study are: the tumulus-fed lava flow in the pre-May 2018 Pu'u 'Ō'ō lava flow field and the fissure 8 lava flow emplacement in the 2018 LERZ fissure system.

from the mantle is supplied to a shallow (<3 kilometers) reservoir system below the main summit caldera where it can migrate and erupt over a >80 kilometer long rift system. Typically, the magma is erupted and emplaced effusively but occasional phreatomagmatic explosive events have been observed at the summit over the recent eruptive history (Holcomb, 1987). Effusive lava activity produces both 'a'ā and pāhoehoe (tube- and surface- fed) lava flows that are sustained and long-lived (Holcomb, 1987; Orr et al., 2013). Prior to May 2018, two main eruption styles were observed at Kīlauea volcano: (i) an overturning lava lake in the Halema'uma'u Crater (Patrick et al., 2013, 2018) and (ii) an extensive lava flow field from vents in the East Rift Zone including from the Pu'u 'Ō'ō vent (Figure 5.1) (Wolfe et al., 1987; Heliker and Mattox, 2003; Orr et al., 2013). The lava lake was active from 2008 to 2018 and produced volcanic gas emissions and small ash plumes from a ∼250 meter diameter crater (Patrick et al., 2013, 2018). More than 35 years of activity produced an extensive lava flow field (>40 km^2) on the southeastern coastal plain from vents around the Pu'u 'Ō'ō summit (Figure 5.1). More then 60 separate episodes were observed during this time with approximately 4.4 km^3 of lava emplaced, mostly as a series of tube-fed sheet-like and ropey pāhoehoe flows (Wolfe et al., 1987; Heliker and Mattox, 2003; Orr et al., 2013; Neal et al., 2019).

5.2.2 2018 Lower East Rift Zone Eruption

In March 2018, the magma system beneath Kīlauea volcano started to pressurize at a relatively high rate (Neal et al., 2019). As a consequence, inflation was observed at the Kīlauea summit, Pu'u 'Ō'ō vent, and along the 20 kilometer conduit connecting the two with increases in lava levels observed at each of the lakes. Previously these pressurization event have resulted in new vents opening around the Pu'u 'Ō'ō vent. However, on April 30, 2018, the pressurization propagated down rift to the east. On May 3, 2018, the intrusion erupted lava on the surface as a series of fissures near the Leilani Estates subdivision on the southeast of the island (Patrick et al., 2019). Over the next few weeks lava erupted from 24 fissures with activity focusing at fissure 8 vent on May 27, 2018. The eruption activity was centralized at fissure 8 for the next two months and within six days lava had propagated 12.47 kilometers to enter the Pacific Ocean at Kapoho Bay on June 3 (Figure 5.2a) (Neal et al., 2019). Initially, effusion rates of the eruption were estimated between 100 and 500 $m^3 s^{-1}$, with average rates increasing over the next few months and maximum pulse rates of up to 2000 $m^3 s^{-1}$ being reported in July (Neal et al., 2019; Patrick et al., 2019). Lava fountains up to 80 meters high were observed at the vent and erupted lava coalesced in a ∼30 meter wide

spillway before flowing into a ∼430 meter wide perched pāhoehoe channel (Figure 5.2b-c) (Patrick et al., 2019). Distally, the lava channel widths were between ∼40 and ∼300 meters. On August 4, the lava effusion activity ceased after ∼1 km^3 of bulk lava was emplaced in the LERZ region (Neal et al., 2019). The eruption destroyed critical infrastructure and more than 700 buildings (Patrick et al., 2019).

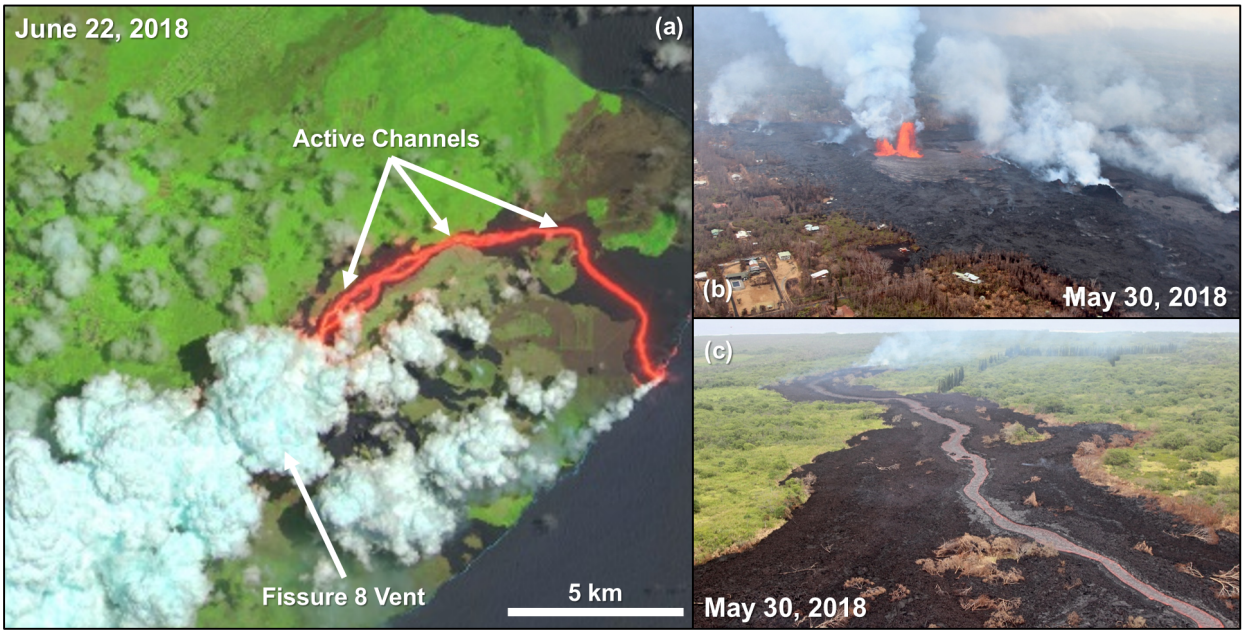

Figure 5.2: (a) Level-1C Sentinel-2B image of the active LERZ fissure 8 lava flow emplacement acquired on June 22, 2018 with channels 4 (0.665 μm), 3 (0.560 μm), 2 (0.490 μm) in red, green, blue, respectively (modified from Copernicus Sentinel data, 2018). The spatial resolution is 10 meters per pixel. The increase color (red-yellow) indicates the highest surface temperatures. (b - c) Aerial photographs of the fissure 8 lava flow emplacement on May 30, 2018, captured at an altitude of ∼250 meters (photographs taken by J.O. Thompson). (b) The lava fountain at vent (approximately 80 meters high). (c) The distal open lava channels showing approximately 30-50% crustal fraction within the channel.

5.2.3 PyFLOWGO

FLOWGO is a one-dimensional numerical model that forecasts lava flow propagation within a channel using cooling limiting flow propagation assumptions (Harris and Rowland, 2001). PyFLOWGO

is an enhancement that allows improved initialization, iteration, and application of the original FLOWGO model (Chevrel et al., 2018). FLOWGO uses a series of heat flux (heat loss) parameters with Jeffrey's principals for Newtonian and adaptive Bingham flows to determine the velocity of a lava volume flowing along a channel (Figure 5.3) (Moore, 1987; Harris and Rowland, 2001). Specifically, the modeled lava flow is assumed to be an incompressible Bingham fluid that is constrained to a channel and so the high dispersion typically observed at the flow front is not well defined. There are four major assumptions that define the FLOWGO model and its application: (1) the initial lava flow propagation velocity is defined by the initial effusion rate at the vent for a certain channel depth and width; (2) the lava flows must be confined to a channel with no continuous roofing or tubing development; (3) the vertical thermal structure of the lava flow is divided into three layer: a cooler basal crust, a homogeneous high-temperature molten core, and a chilled surface crust; and (4) the model simulates the propagation of a channel-confined control volume unhindered by the flow front. Additionally, the thermal and rheological evolution of the lava flow are tracked during propagation. The model combines the measured downflow changes in distribution extent and the best fit between results to produce a physically and thermally robust model (Harris and Rowland, 2001; Chevrel et al., 2018). Downflow variations in velocity are calculated by estimating the crystallization, cooling, viscosity, and yield strength of the lava, with the crystallization being the most influential factor on flow length. The model is cooling-limited that is determined through the lava heat flux (loss) calculations until the surface cools and propagation velocity reduces significantly that the flow does not have the ability to flow further downslope (Figure 5.3). Input parameters include initial eruption conditions, channel extent, thermal fluxes, and properties of the lava, with a slope profile have the greatest influence on final runout distance (Figure 5.3) (Harris and Rowland, 2001; Harris, 2008). Typically, the slope profile is derived from a pre-eruption DEM and probabilistic models can be used to determine most likely flow pathways downslope before FLOWGO is utilized to determine propagation distance (Wantim et al., 2013; Harris and Rowland, 2015; Ramsey et al., 2019)

There are three main phases in the FLOWGO model: (1) determining the velocity of the lava based on the modified Jeffrey's equations; (2) calculating the heat flux from the lava during each distance step; and (3) determining the change in thermo-rheological conditions of the control volume at each step (Harris and Rowland, 2001, 2015; Chevrel et al., 2018). The velocity of the lava is calculated by evaluating the yield strength of the core of the flow and the shear stress at the base of the flow. If the shear stress required for the lava to propagate at the base is greater than the

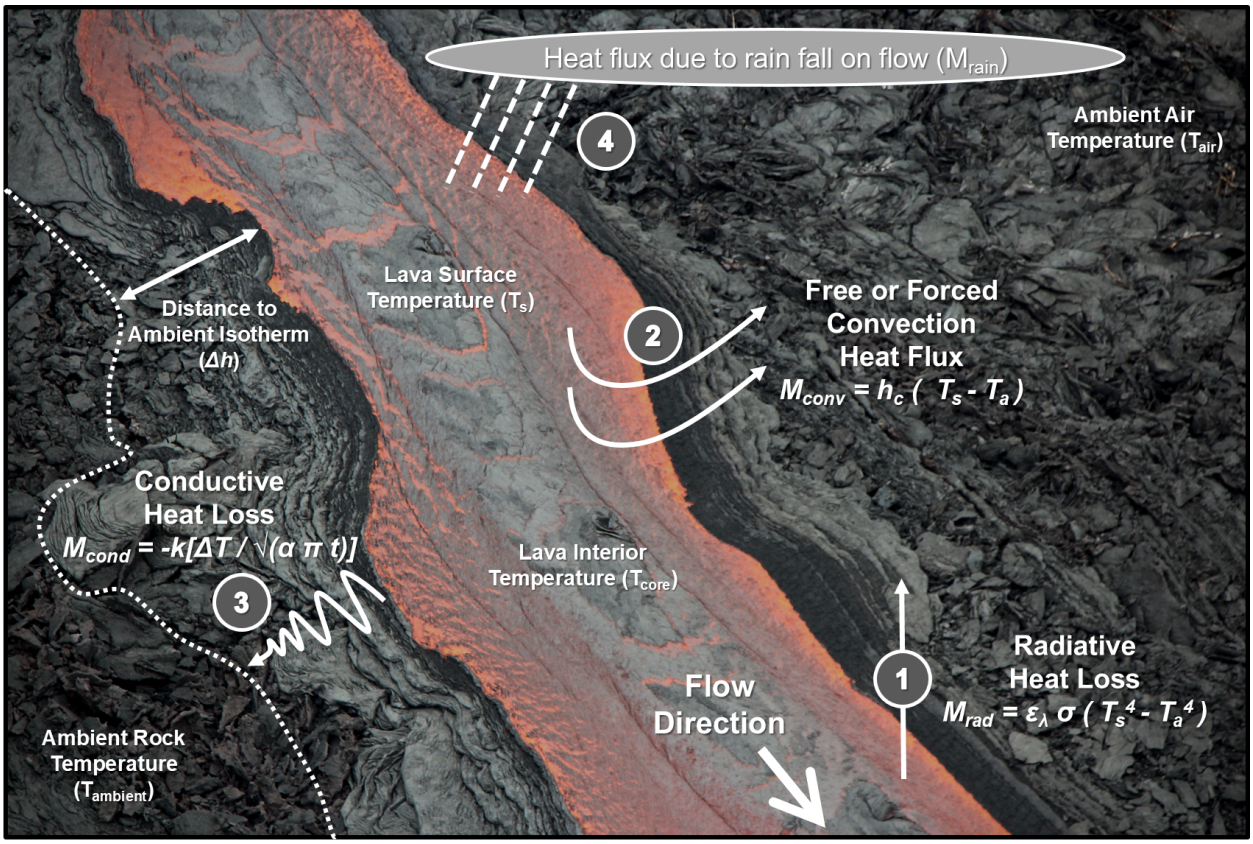

Figure 5.3: A schematic showing the typical heat fluxes from the surface of an active lava flow and parameters used in the flux calculations. All four main heat fluxes identified are used in the FLOWGO model to simulate the propagation of a channel confined lava flow. Modified from Harris (2013). Background photograph taken by J.O. Thompson.

shear rate in the flow core then the lava will stall (Harris and Rowland, 2001; Chevrel et al., 2018). The velocity calculations also account for the lava thickness, accelation due to gravity down the pre-eruption slope, dense rock equivalent density, core and surface temperature, viscosity (crystal and melt), and crystal content (Harris and Rowland, 2001; Chevrel et al., 2018).

The heat flux from the lava was originally calculated using a two-component model of the surface representing the hot molten and cooler crustal endmembers to determine an effective surface temperature (T_{eff}) (Equation 5.1) (Harris and Rowland, 2001).

$$T_{eff} = \left[f_{crust} \cdot T_c^4 + (1 - f_{crust})T_h^4\right]^{0.25} \tag{5.1}$$

where f_{crust} is the fraction of surface crust, T_c is the crustal temperature and T_h is the hot molten temperature. The effective temperature is then used in the heat flux calculations (Equation 5.3) to determine cooling rates (Harris and Rowland, 2001; Chevrel et al., 2018). However, the original calculations did not account for the change in emissivity between molten and crustal lava surfaces. A two-component emissivity model was developed to account for this change by determining the effective emissivity (ε_{eff}) dependent on the fraction of crust and molten surfaces (Equation 5.2) (Ramsey et al., 2019).

$$\varepsilon_{eff} = \varepsilon_c \cdot f_{crust} + \varepsilon_h \cdot (1 - f_{crust}) \tag{5.2}$$

where ε_c is the emissivity of the crust (0.95) and ε_h is the emissivity of the hot molten surface (0.6) (Harris, 2013; Lee et al., 2013; Ramsey and Harris, 2016; Ramsey et al., 2019). The effective emissivity was then used with the effective temperature in the heat flux calculations to improve the accuracy of the results (Equation 5.3) (Ramsey et al., 2019). This study further improves this assumption by determining the emissivity of the crust and molten surfaces dependent on the effective temperatures and accounts for changes during propagation. It is vital to accurately represent the emissivity of the lava surface as it is used in the calculation of radiative heat flux in a power quartic relationship with temperature (Equation 4.2), meaning a small change in emissivity causes an exponential change in radiative heat flux. Therefore, cooling rates can be incorrectly calculated and runout distances poorly constrained. After the heat fluxes have been calculated, the FLOWGO model determines crystal growth through a linear relationship with cooling rate (Harris and Rowland, 2001, 2015; Chevrel et al., 2018). The change in fractional crust coverage is also calculated in this phase and is dependent on an exponential relationship with flow velocity (Harris and Rowland, 2001; Chevrel et al., 2018).

The final phase of the FLOWGO model comprises of progressing the thermo-rheological properties (e.g., temperatures and viscosity) of the control volume. During the evolution, mass is conserved and a constant depth is assumed, with the velocity and channel width varying downflow (Harris and Rowland, 2001, 2015; Chevrel et al., 2018). The thermo-rheological properties of the control volume are updated for each step distance downflow until the model predicts a flow velocity that is too low to continue propagation. At this point, the model ceases and results of the final run distance properties and parameters are published.

The FLOWGO model has been successfully applied in other studies that have investigated flow propagation to inform hazard assessments of previous eruptions to infer potential future eruptions (e.g., Wright et al. 2008; Riker et al. 2009; Harris et al. 2011; Wantim et al. 2013; Ramsey et al. 2019). Additional studies have utilized FLOWGO for comparative investigations with other lava propagation models and to provide input parameters for newly developed probabilistic analyses (e.g., Cordonnier et al. 2016; Mossoux et al. 2016). The flexibility and adaptability of FLOWGO enables this variety of studies and is aided by the selectability of numerous modules within the model to calculate various parameters so that the natural flow can be best simulated (Harris et al., 2007; Chevrel et al., 2018). For example, different rheological modules can be exploited to calculate relative viscosity and different crystallization models can be used to calculate the rate of crystallization with varying input factors controlling the rate (Harris and Rowland, 2001, 2015; Chevrel et al., 2018). In this study, the most simplistic modules with the fewest assumptions are used to simulate the limited prior knowledge known about rheology, geochemistry, and composition of an erupting basaltic lava during an ongoing eruption when hazard assessments of lava propagation are vitally important.

TIR measurements and derived properties, including surface temperature, emissivity, composition, and vesicularity, are input parameters in the PyFLOWGO model (Harris and Rowland, 2001; Chevrel et al., 2018). However, the techniques used to measure and assume these properties are limited and at this time inaccurate, culminating in numerous uncertainties and errors propagating through to model results. For example, prior studies have shown that molten lava surfaces have lower emissivity values than previously assumed, which can result in decreases in downflow heat fluxes and increase in final runout distance caused by the less efficient radiative cooling (Abtahi et al., 2002; Lee et al., 2013; Ramsey and Harris, 2013; Ramsey et al., 2019; Thompson and Ramsey, 2020). Therefore, this study develops a framework for rapidly integrating high-resolution ground-based multispectral TIR data into the PyFLOWGO model and incorporate varying thermal

parameters to increase the accuracy of the results.

5.3 Methodology

5.3.1 High Resolution Ground-Based Data

High-resolution multispectral TIR data were collected using the newly developed MMT-Cam that acquires six-point surface radiance data between 7.5 and 12 μm at high spatial (<1 meter) and temporal (<1 second) resolutions (Thompson et al., 2019). The data were calibrated for instrument attenuation and optical transmittance through long-period variable-temperature blackbody testing (Thompson et al., 2019). The instrument calibrated at-sensor radiance data were then corrected for atmospheric emission and transmission using the SpectralCalc horizontal path atmospheric simulator with the HITRAN database (Rothman et al., 2013; GATS, 2019; Thompson et al., 2019). Atmospheric temperature, humidity, and path length measurements collected in the field were incorporated into the model to produce an accurate representation of the atmospheric gas species present during acquisition periods. Surface radiance data were finally converted to surface kinetic temperature and emissivity using a modified Temperature-Emissivity Separation (TES) algorithm first developed for the ASTER spaceborne instrument (Gillespie et al., 1998). The modification accounted for the high spatial resolution and variable spectral responses of the MMT-Cam instrument compared to the specifications of the satellite instruments for which the TES algorithm was original developed (Thompson et al., 2019). Band-to-band registration errors caused by instrument jitter during deployment were removed using a fast Fourier transform based algorithm that shifts all the bands with respect to a reference band. Heat budget estimates were calculated from the effective surface kinetic temperature (T_{eff}), ambient surface temperature (T_a), and spectral emissivity (ε_λ) data including total heat flux (Φ_{tot}) and fraction of melt. Heat flux (Φ_{tot}) was calculated using a similar method as described in Harris and Rowland (2001) and Harris (2013) with the following equation (Equation 5.3):

$$\Phi_{tot} = \left\{ \left[\varepsilon_\lambda \cdot \sigma (T_{eff}^4 - T_a^4) \right] + \left[h_c (T_{eff} - T_a) \right] + \left[-k \left(\Delta T / \sqrt{(\alpha \cdot \pi \cdot t)} \right) \right] \right\} \cdot A \qquad (5.3)$$

where σ is the Stefan-Boltzmann constant, h_c is the heat transfer coefficient, k is thermal conductivity, α is thermal diffusivity, and A is pixel area. Windy conditions were experienced during

all the acquisition periods, so the heat transfer coefficient was calculated for a forced convection scenario.

The fraction of melt within each pixel was estimated using a methodology originally developed for deriving sub-pixel temperature anomalies within satellite datasets (Dozier, 1981; Matson and Dozier, 1981; Harris, 2013) and is defined in the following equation (Equation 5.4):

$$Fraction\ of\ Melt = (T_{eff} - T_a)/(T_{liq} - T_a) \tag{5.4}$$

where T_{liq} is the liquidus temperature of a Hawaiian basalt (Abtahi et al., 2002).

On February 3, 2018, ground-based multispectral TIR data were acquired of a lava breakout from a tumulus on the coastal plain of Kīlauea volcano (Figures 5.1, 5.4a, and 5.6). The lava emplaced during this small event was tube-fed from the Pu'u 'Ō'ō vent. The tumulus produced a small breakout lava flow (approximately six meters long) that was used for deriving the emissivity dependency on temperature and refining the PyFLOWGO model with this new relationship (Figures 5.4 and 5.6). In lava flow propagation predictions, it is important to quantify the thermally-derived properties of lava flows at all stages of cooling and propagation from the initial effusion to crustal formation and re-mobilization (breakout events). Therefore, at each stage, the thermal properties were determined and analyzed to evaluate the effect on varying partial crustal formation and runout distance. The evolution of lava surface properties during propagation were then used to develop a variability emissivity module, dependent on surface temperature, for the PyFLOWGO heat flux budget calculations to improve the constraint on cooling rates and flow velocity in the model.

The dependency of temperature on emissivity was quantified over the active region of the tumulus during the entire breakout event. The variability in emissivity with temperature was analyzed and subsequently modeled for the six individual bands acquired by the MMT-Cam system and then combined to provide an average dependency over the entire TIR wavelength region. The emissivity relationships are incorporated into the radiant heat budget calculations of PyFLOWGO to change emissivity with surface temperature of the lava during propagation. Transects along the center of the tumulus-fed flow were defined during the complete evolution of the breakout. Surface kinetic temperature, emissivity, fraction of melt, and heat flux were analyzed for later direct comparison with the PyFLOWGO results. Additional measurements were acquired of the final flow runout distance and flow widths at various stages to constrain and verify the model. A sample was also collected to provide an estimate of vesicularity fraction used in the model. A thin section revealed a bulk rock vesicularity of between 35% and 50%.

Figure 5.4: Field photographs of the (a) tumulus-fed lava flow on February 3, 2018 and (b-d) fissure 8 lava flow emplacement on May 30, 2018 (photographs taken by J.O. Thompson). (b) is an image of the lava fountain (approximately 80 meters high) and intial lava spillway; (c) is an image of the perched pāhoehoe channel; and (d) is an image of the distal lava channels and active flow front.

On May 30, 2018, the MMT-Cam was also deployed on a helicopter over the LERZ to acquire multispectral TIR data of the channelized lava flows originating from fissure 8 (Figures 5.2, 5.4, and 5.5). During the deployment, data were acquired of the lava fountain (approximately 80 meters high), lava spillway, perched pāhoehoe channel, distal lava channels, and active flow front (Figures 5.2 and 5.4). On May 30, the active perched pāhoehoe channel was ∼280 meters wide and the distal lava channels were between ∼40 and 140 meters wide. Surface kinetic temperature, emissivity, fraction of melt, and heat flux were calculated at each location to compare with and constrain the PyFLOWGO results.

5.3.2 Moderate Spatial Resolution Satellite Data

The slope profile of the fissure 8 lava flow emplacement channel was produced using a 10 meter digital elevation model (DEM) derived from the United States Geological Survey's 7.5 minute DEM Quads (National Oceanic and Atmospheric Administration, 2007). The profile path was constructed using an overlay TIR map of Kīlauea's LERZ fissures system produced on June 4, 2018. This was the day after the channelized lava flow from fissure 8 entered the Pacific Ocean at Kapoho Bay after propagating 12.47 kilometers from the vent (U.S. Geological Survey, 2018). This path was used in the PyFLOWGO modeling as there are limited external forces (predominantly topography and meteorological conditions) influencing the propagation of the lava flows prior to the lava interacting with the Pacific Ocean. It was likely that the topography changed during the early phase of the eruption, however, the relative changes in slope profile were likely minimal, having limited influence of the results.

5.3.3 PyFLOWGO Modeling

To accurately predict flow propagation, a modified radiative heat flux module was developed for the PyFLOWGO model that accounts for variable emissivity related to surface temperature downflow. This causes the efficiency of radiant heat flux to modulate during lava propagation, therefore providing a better estimate of the cooling rate. This will subsequently affect the final runout distance. The variability in emissivity is dependent on the surface temperature and computed in the PyFLOWGO radiant heat flux calculations. Emissivity has an exponential influence on the radiant heat flux calculation as a result of the quartic correlation between temperature and radiant heat flux (first portion of Equation 5.3). The linear emissivity-temperature relationship

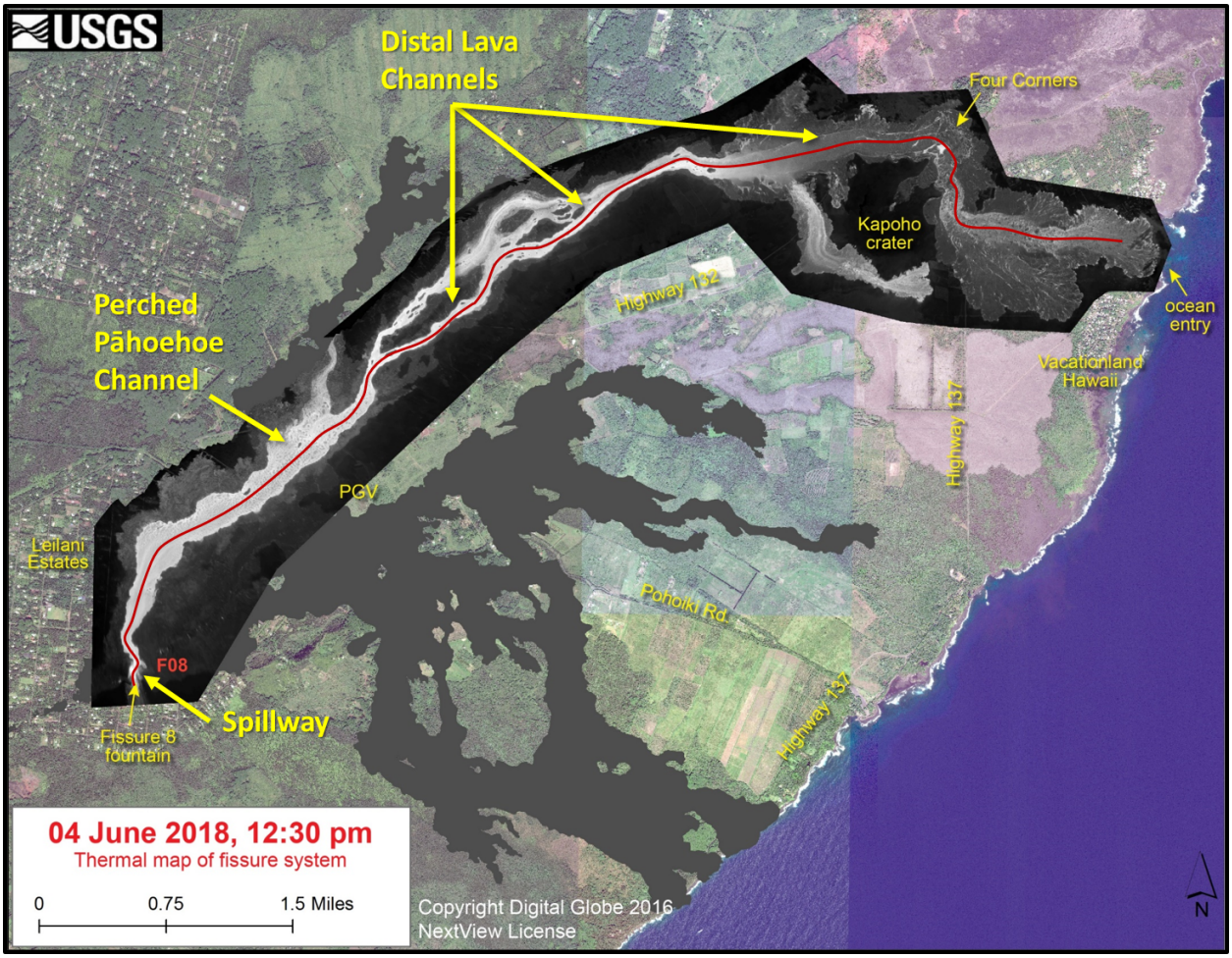

Figure 5.5: A TIR map of the LERZ fissure system on June 4, 2018 overlain on Digital Globe imagery (modified from U.S. Geological Survey 2018). The red line indicates the central channel used in the PyFLOWGO models simulations. The active channel width validation measurements were also acquired using this TIR map.

was derived from the average 6-point TIR emissivity values measured by the MMT-Cam during a small tumulus-fed lava flow emplacement, with a coefficient of determination of ∼0.94 (Figures 5.12 and 5.13, and Table 5.1). The linear regression was then used to develop a new radiant heat flux module that can directly replace the existing module in the original PyFLOWGO model. The modified PyFLOWGO model with the new temperature-dependent variable emissivity module was first tested on the small tumulus-fed flow (erupted on February 3, 2018) to constrain the new input parameters and analyze the sensitivity. The model was simulated at 0.1-meter intervals over the 6.3-meter tumulus-fed lava flow. The results were compared to the un-modified PyFLOWGO results to assess the benefit of using this approach. A constant emissivity value of 0.95 was used in the un-modified PyFLOWGO models as this has been the typical value used in previous thermal monitoring and modeling studies (e.g., Wright and Flynn 2003; Wright et al. 2008; Spampinato et al. 2011; Harris 2013; Patrick et al. 2017). Additionally, the results were verified using data acquired with the MMT-Cam during the eruption. The terrain and channel conditions were determined from ground observations with the initial channel width and depth measured at 0.15 and 0.1 meters, respectively. The initial bulk effusion rate was calculated at 0.11 $m^3 s^{-1}$ with other initial conditions attained from typical or average values derived in other studies of Hawaiian basaltic lavas (Table 5.2). The initial topography was approximated using ground measurements of changes in elevation and horizontal distance.

After the modified PyFLOWGO model was tested, it was used to simulate the 12.47 kilometer long lava flow that originated from fissure 8 at 10-meter downflow intervals. The terrain conditions were calculated from the 10-meter DEM and the channel conditions were measured from a TIR survey conducted by the USGS on June 4, one day after the lava flow entered the Pacific Ocean (Figure 5.5). The survey revealed the proximal spillway channel was ∼30 meters wide, the active perched pāhoehoe channel was ∼360 meters wide, and the distal lava channels were between ∼40 and 280 meters wide. The initial bulk effusion rate was obtained from previous studies and similar thermo-rheological values that were used in the tumulus-fed lava flow modeling were carried over into the fissure 8 scenario (Tables 5.2 and 5.3).

5.4 Results

5.4.1 Downflow Variations in Thermal Properties

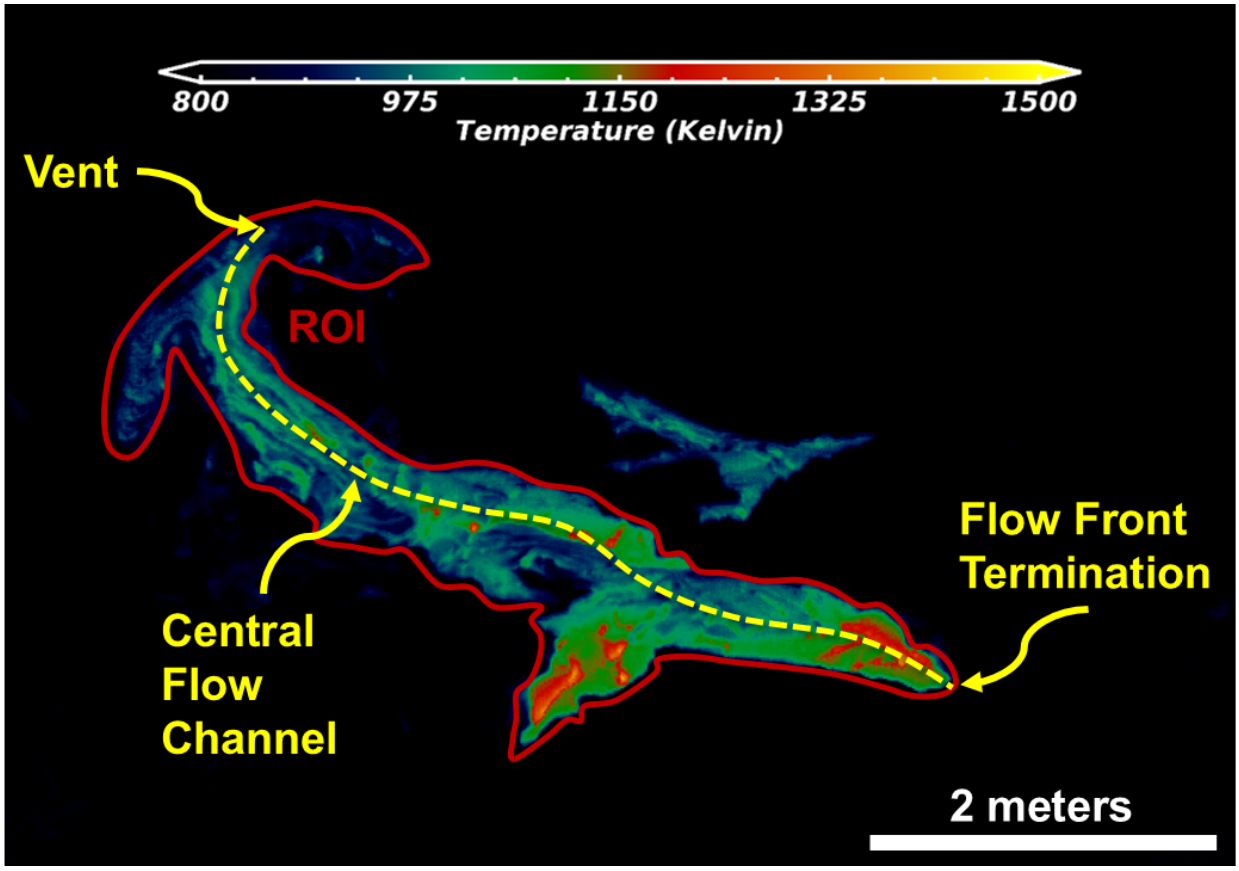

Figure 5.6: Temperature image of the final runout of the tumulus-fed lava flow derived from MMT-Cam data acquired on February 3, 2018. The yellow dashed line represents the main channel used in the PyFLOWGO simulations. The red polygon represents the ROIs used in the analyses.

5.4.1.1 Tumulus-Fed Lava Flow

The downflow evolution of two thermal properties (surface kinetic temperature and emissivity) measured using the MMT-Cam and two main products derived from these measurements (fraction of melt and heat flux) were analyzed for the 6.3 meter tumulus-fed lava flow. The temporal transects for surface kinetic temperature highlighted high initial temperatures (up to 1450 K) 1-2 meters and 3-4 meters from the vent, where the largest active breakouts were observed during this time period (Figure 5.7). As the emplacement progressed, the highest temperatures were observed further from

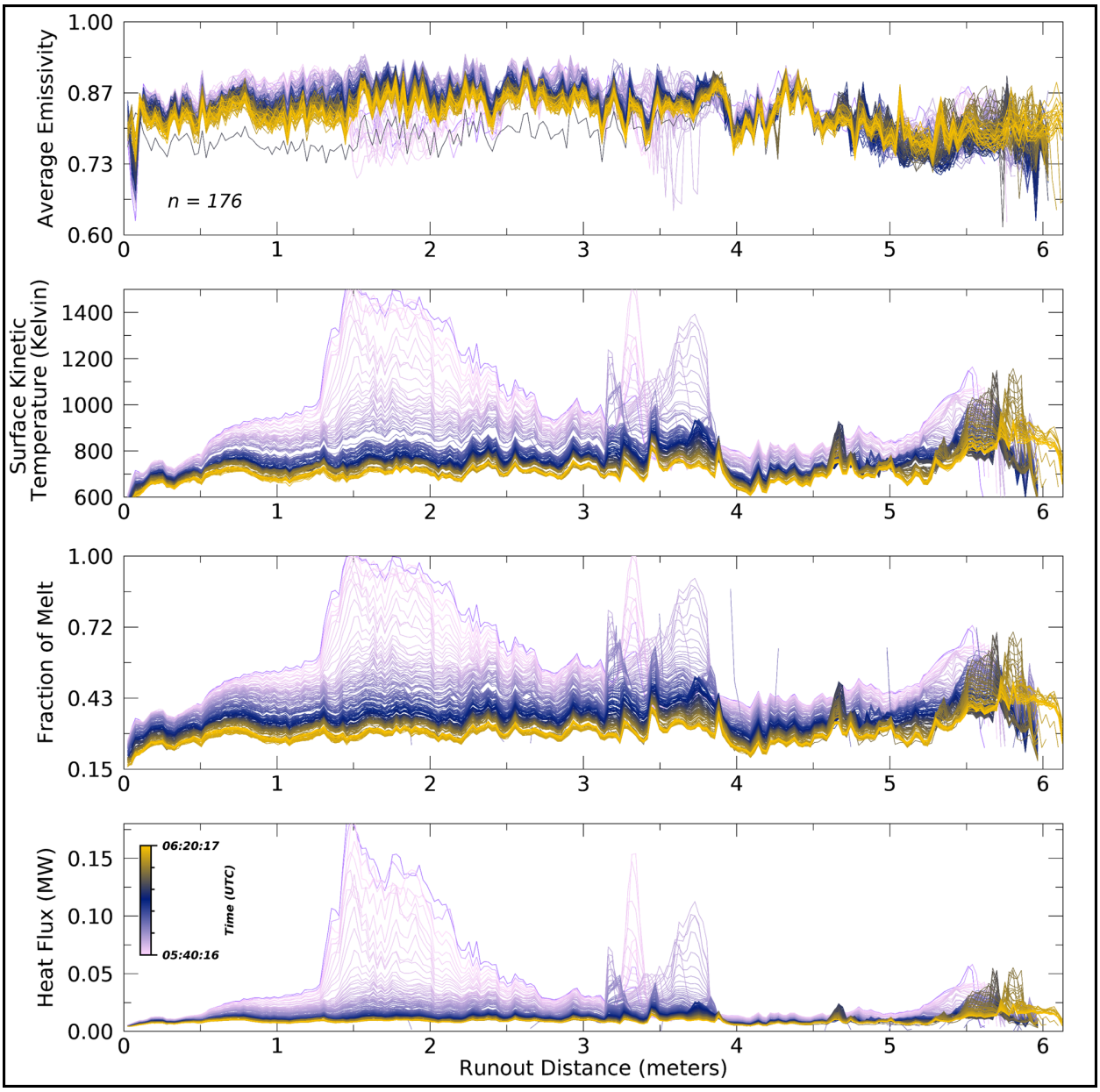

Figure 5.7: Temporal transects of the 6-point average emissivity, surface kinetic temperature, fraction of melt, and total heat flux along the central channel of the 6.3-meter tumulus-fed lava flow. The original vent is at a distance of 0 meters (see Figure 5.6). The data were acquired using the MMT-Cam at an approximate distance of 10 meters from the target. The transect line colors transition from purple to yellow during the ∼40-minute breakout event.

the vent, with major peaks at 3-4 meters, ∼4.7 meters, and 5.2-6.3 meters from the vent. Observed lower emissivity values (as low as 0.65) correspond with the locations of higher temperatures, especially at 3.5-3.8 meters and 5.5-6.3 meters from the vent (Figure 5.7). The transects show a near-linear inverse relationship between surface kinetic temperature and emissivity.

The fraction of melt temporal transect data revealed a similar trend to the surface kinetic temperature data (Figure 5.7). A melt fraction up to 0.99 was observed between 1-2 meters and 3-4 meters from the vent, with minima of 0.15 in the less active regions of the flow. Higher fractions of melt were observed further from the vent as time progressed and the flow continued to propagate. A similar variability trend was detected for heat fluxes (Figure 5.7). Additionally, fewer major breakout events were highlighted in the heat flux data due to the higher contrast from the background flux. For example, there was a small breakout at ∼4.7 meters from the vent after 06:00:00 UTC that was discerned in the heat flux data (Figure 5.7).

Overall, a general decrease in thermal output was observed during the lava flow emplacement with higher values (lower emissivity) transitioning further from the vent as time elapsed (Figure 5.7). These results revealed the progression of a small lava flow during emplacement including periods where the flow stalled and reactivated. During the emplacement, transitions of a molten lava to a viscoelastic crust to a glassy crust were observed and the responses in thermal properties were differentiated. These measurements and estimations were later used for comparison with thermo-rheological modeling of this lava flow.

5.4.1.2 2018 Fissure 8 Lava Flow

On May 30, 2018, the MMT-Cam was deployed on a helicopter to acquire multispectral TIR data of the fissure 8 lava flow emplacement at various points along the entire runout length. The MMT-Cam calibrated and corrected radiance data were converted to surface kinetic temperature and emissivity data, and then used to derive the fraction of melt and total heat flux. Three main sites were investigated for thermal analysis: the lava fountain at the vent, the perched pāhoehoe lava channel, and the distal lava channels. The thermal properties measured and calculated using the MMT-Cam were used to constrain the thermal input parameters of the PyFLOWGO model and validate the results.

At the vent, a ∼80 meter high lava fountain was observed feeding the lava flow that travelled to the east. The highest temperatures, fraction of melt, and total heat fluxes were observed at the base of the lava fountain, with the inverse response observed in the emissivity data (Figure

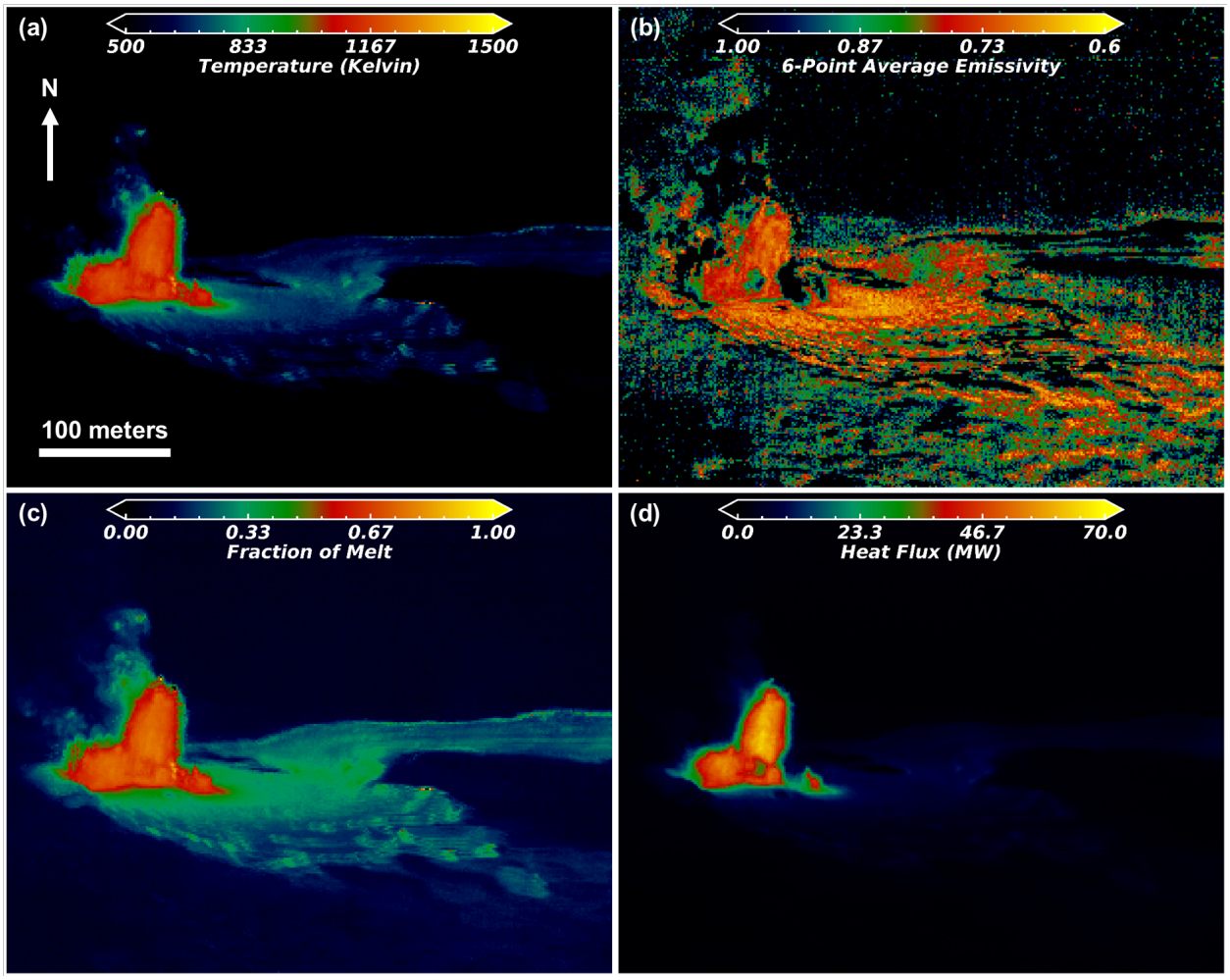

Figure 5.8: Thermal properties of the vent region of the fissure 8 lava flow emplacement during the LERZ eruption of Kīlauea volcano in 2018. The properties were derived from MMT-Cam data acquired on May 30, 2018, deployed on a helicopter looking North. The highest temperatures, fractions of melt, and heat flux were observed in the fountain, specifically at the base, with an inverse response in the emissivity data. The data were acquired from a distance of 1500 meters from the lava fountain, resulting in a pixel size of 1.56 meters.

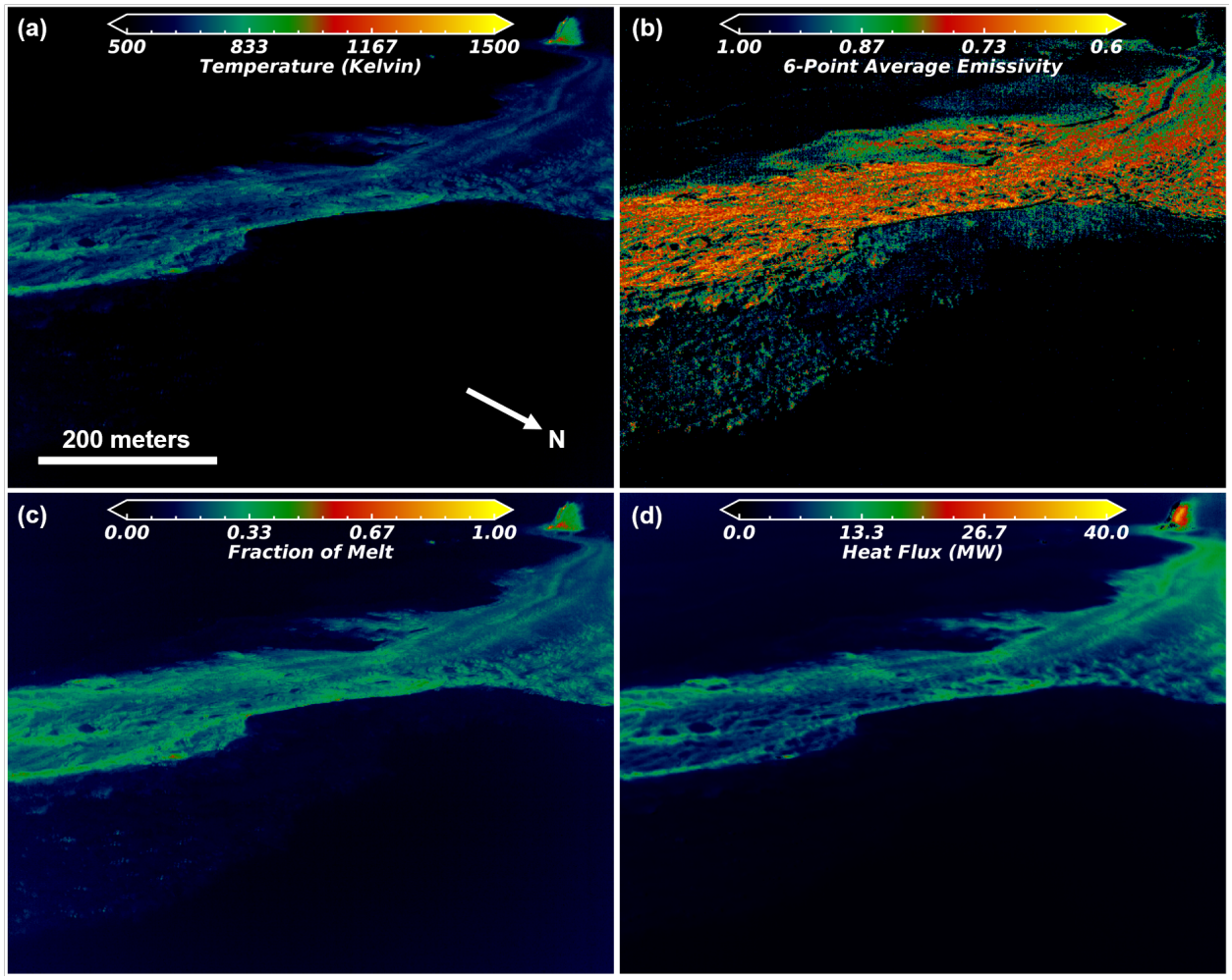

Figure 5.9: Thermal properties of the perched pāhoehoe channel region of the fissure 8 lava flow emplacement during the LERZ eruption of Kīlauea volcano in 2018. The properties were derived from MMT-Cam data acquired on May 30, 2018, that was deployed on a helicopter looking south-west. Generally, the highest temperatures, fractions of melt, and heat flux were observed in the margins between the pāhoehoe plates with an inverse response in the emissivity data. The data were acquired from a distance of 1250 meters from the center of the lava channel, resulting in a pixel size of 1.24 meters.

5.8). The fraction of melt data discerned the pathway of molten lava from the lava fountain to the perched pāhoehoe channel to the east along a ∼30 meter wide spillway. Generally, the average emissivity was lower around the vent, as well as, some channel pathways in the spillway. Also, the emissivity was lower above the lava fountain, due to the strong absorption of volcanic gases emitted from the vent. In addition, the TIR data highlighted other smaller breakouts/eruptions of molten or cooling lava at more distal distances from the vent to the south, away from the main channel (Figure 5.8).

MMT-Cam TIR data of the perched pāhoehoe channel revealed a complex surface of molten lava and rafted crustal pāhoehoe plates (Figure 5.9). The kinetic temperature and fraction of melt data implied the surface was dominated by cooler rafts of pāhoehoe plates (>80%) with minimal molten lava. The average emissivity was still relatively low with the majority of the channel surface having a value of ∼0.75 but narrow channels with lower emissivity (as low as 0.6) were discerned. The heat flux values were also lower in this region of the flow compared to the vent. However, narrow regions of elevated fluxes were detected that were not obvious in the other thermal properties, suggesting the presence of subsurface pathways of the lava to the flow front. Overall, the thermal properties of this region indicate that the surface was dominated by crustal plates with minimal thermal heat flux, resulting in a fairly well insulated lava flow.

TIR data of the distal lava channels characterized the variations in thermal properties along and across the channels as the flow propagated further downslope (Figure 5.10). A variety of lava channel morphologies were differentiated, including poorly insulated channels, well insulated rafted channels, and small lava tubes (Figure 5.10a). The surface kinetic temperature and fraction of melt data were able to accurately distinguish the presence of cooler crustal lava rafts flowing on the surface of the channel and more molten exposed regions. Surface temperatures up to 1475 K were measured on the molten surface compared to average temperature of ∼1000K that were measured on the crustal rafts. A similar difference was observed in the fraction of melt data with average values of ∼0.9 and ∼0.55 calculated for the molten and crustal regions, respectively. Laterally, the cooler crustal lava rafts were constrained to the center of the lava channels and the molten regions to the margins. The lateral variability was more apparent in wider channels compared to narrow ones where the mixture of surfaces were less visible. The emissivity data had the inverse response to temperature and fraction of melt variations, with lower emissivity values measured in the molten regions. Small lower emissivity regions (<2 meters) were detected on the levees with values as low as ∼0.8, suggesting the presence of a complex surface of cooling lava and minor breakout events.

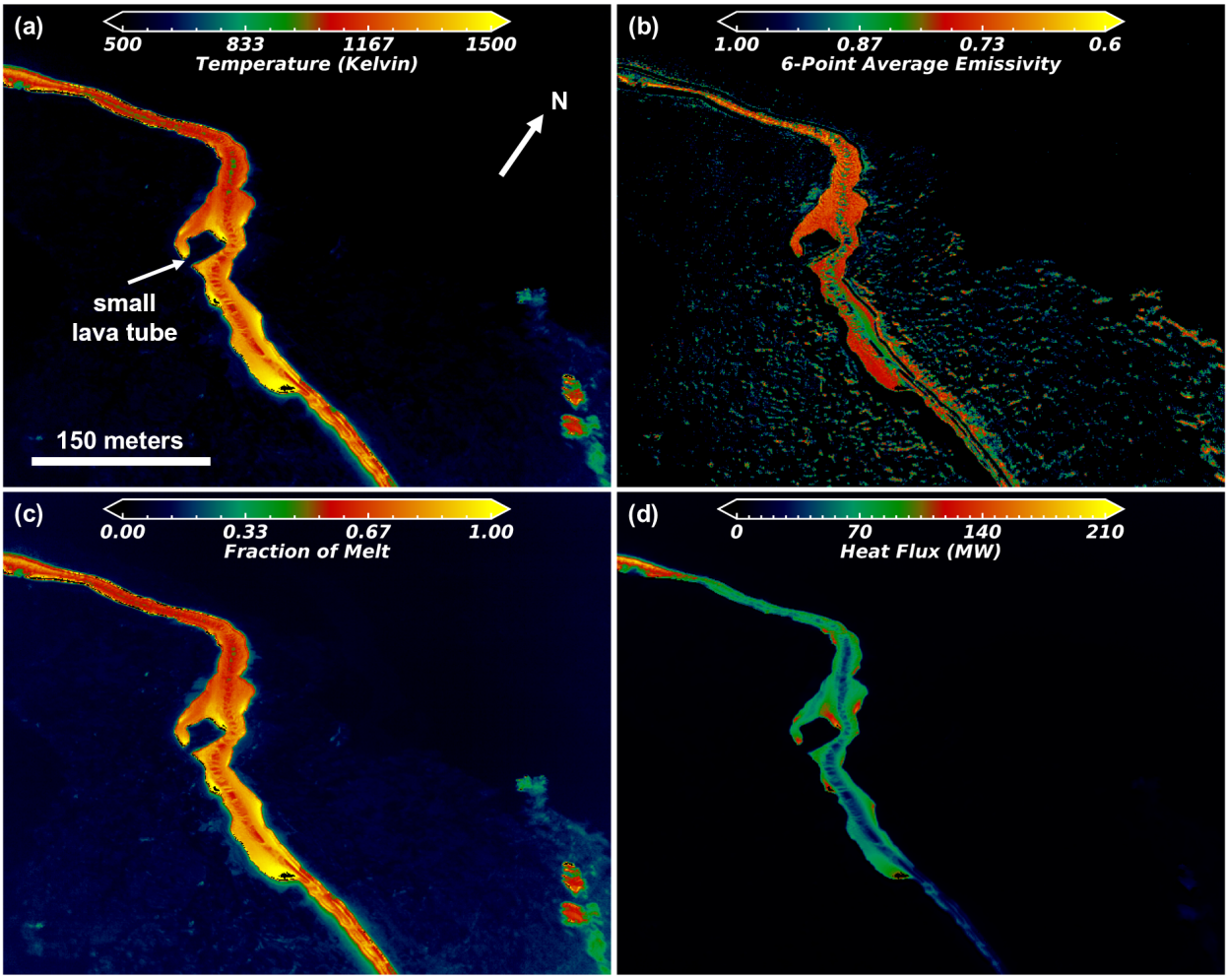

Figure 5.10: Thermal properties of the distal channel region of the fissure 8 lava flow emplacement during the LERZ eruption of Kīlauea volcano in 2018. The properties were derived from MMT-Cam data acquired on May 30, 2018, that was deployed on a helicopter looking northwest. Generally, the highest temperatures, fractions of melt, and heat flux were observed at the margins of the channel with an inverse response in the emissivity data. The data were acquired from a distance of 700 meters from the center of the lava channel, resulting in a pixel size of 1.01 meters.

The major heat fluxes were constrained to the main flow channel with depressed values on the surfaces of the crustal rafts and elevated values at the margins. Additionally, elevated heat fluxes were calculated at the initiation of the small lava tube (Figure 5.10d).

5.4.2 Variable Emissivity Module

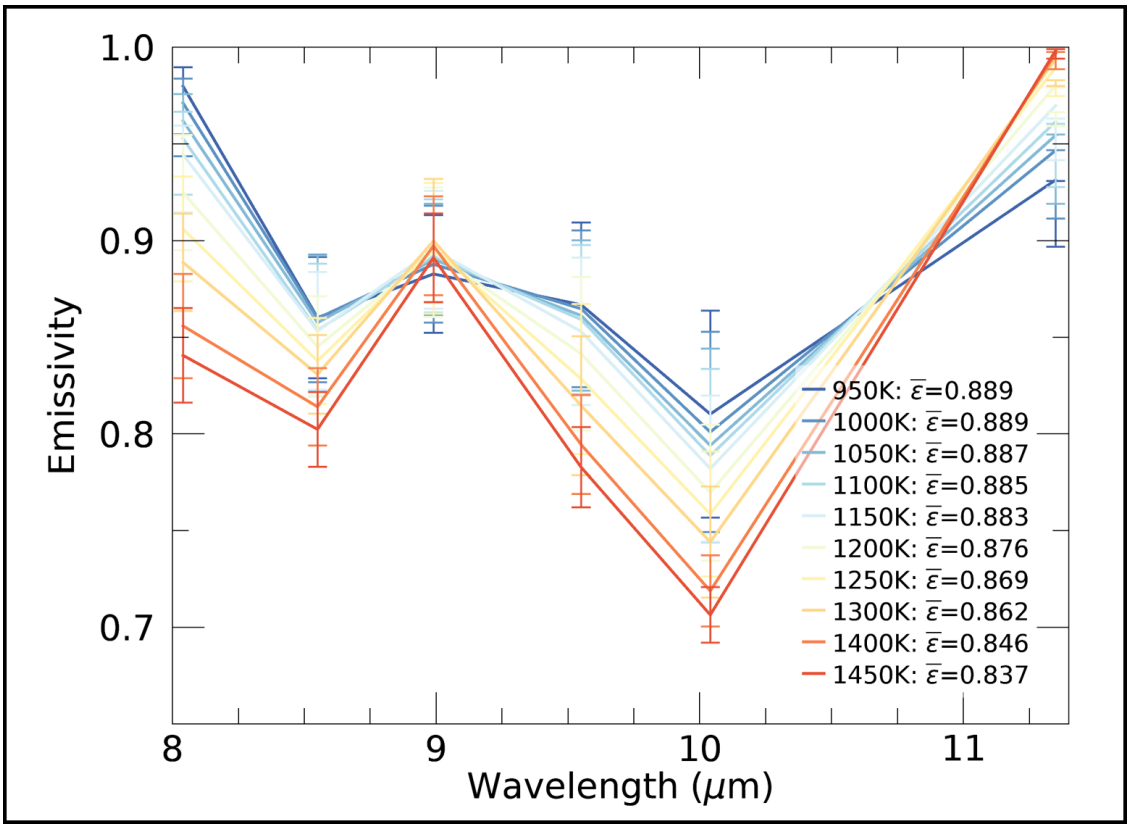

Figure 5.11: Spectral emissivity changes of lava surfaces during cooling and physical state change (liquid to solid) from 1450 to 950 K. The data were acquired using the MMT-Cam of the tumulus-fed lava flow on February 3, 2018. The error bars represent the 2-sigma standard deviation of the emissivity values at each wavelength and surface kinetic temperature. In general, during cooling the emissivity values increase and a broader absorption feature develops. Note, $\bar{\varepsilon}$ represents the average 6-point emissivity at each surface kinetic temperature.

The correlation between surface kinetic temperature and emissivity within the active regions of the tumulus-fed lava flow during its entire emplacement was evaluated to determine the dependency of temperature and lava physical state on emissivity (Figures 5.11 and 5.12). This relationship was

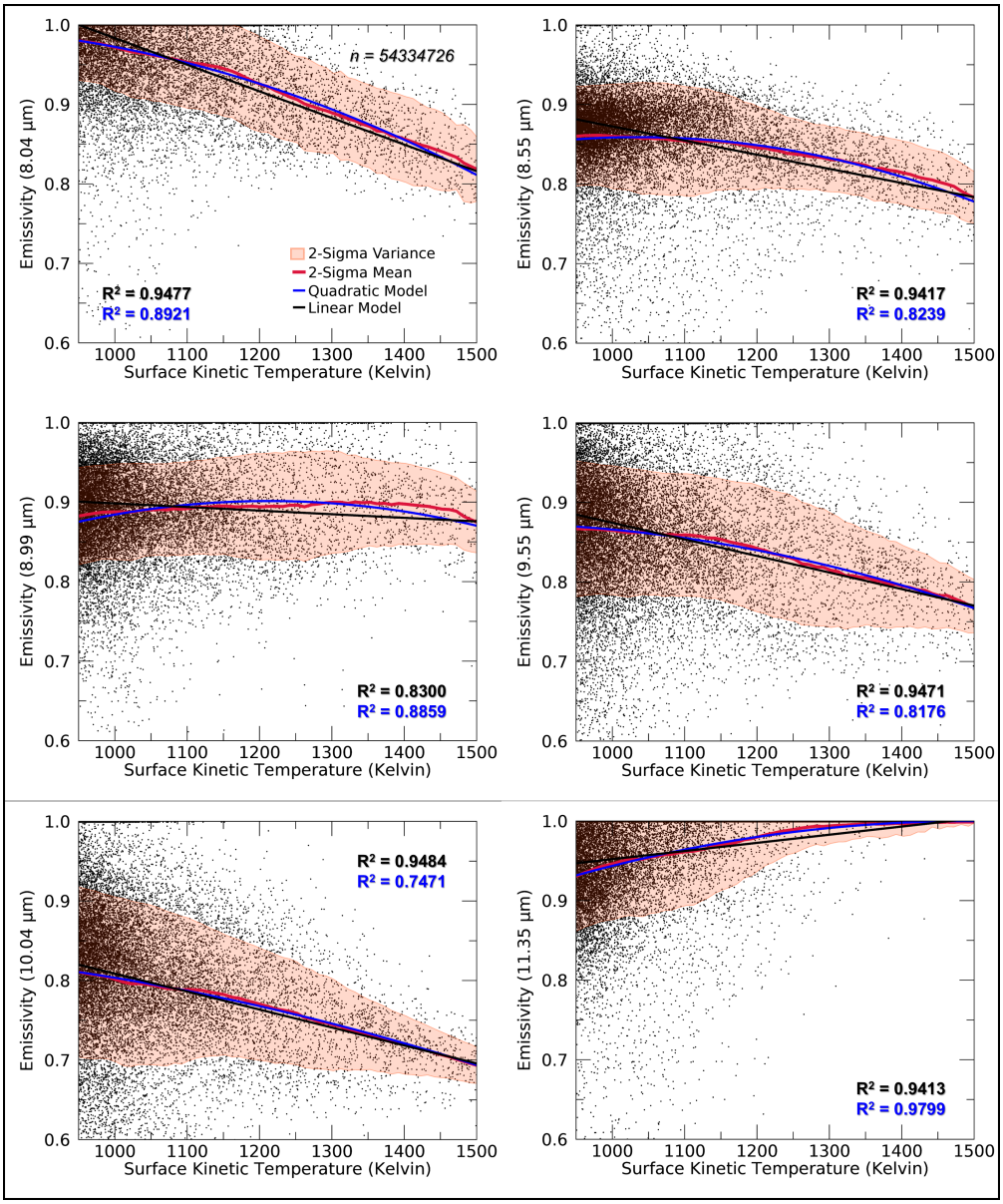

Figure 5.12: Emissivity dependent surface kinetic temperature plots for each wavelength band acquired by the MMT-Cam of the 6.3-meter tumulus-fed lava flow. Data from the entire active region of the lava flow during propagation were plotted to determine the relationship between these thermal properties. The red faded regions highlight the 2-sigma variance spread of the emissivity with temperature and the red line representing the mean. The black and blue lines represent the computed linear and quadratic regressions, respectively. Data were acquired from the ROI shown in Figure 5.6. Note, only a random 50% of the data are plotted due to computational demand but all the data are used in the calculations.

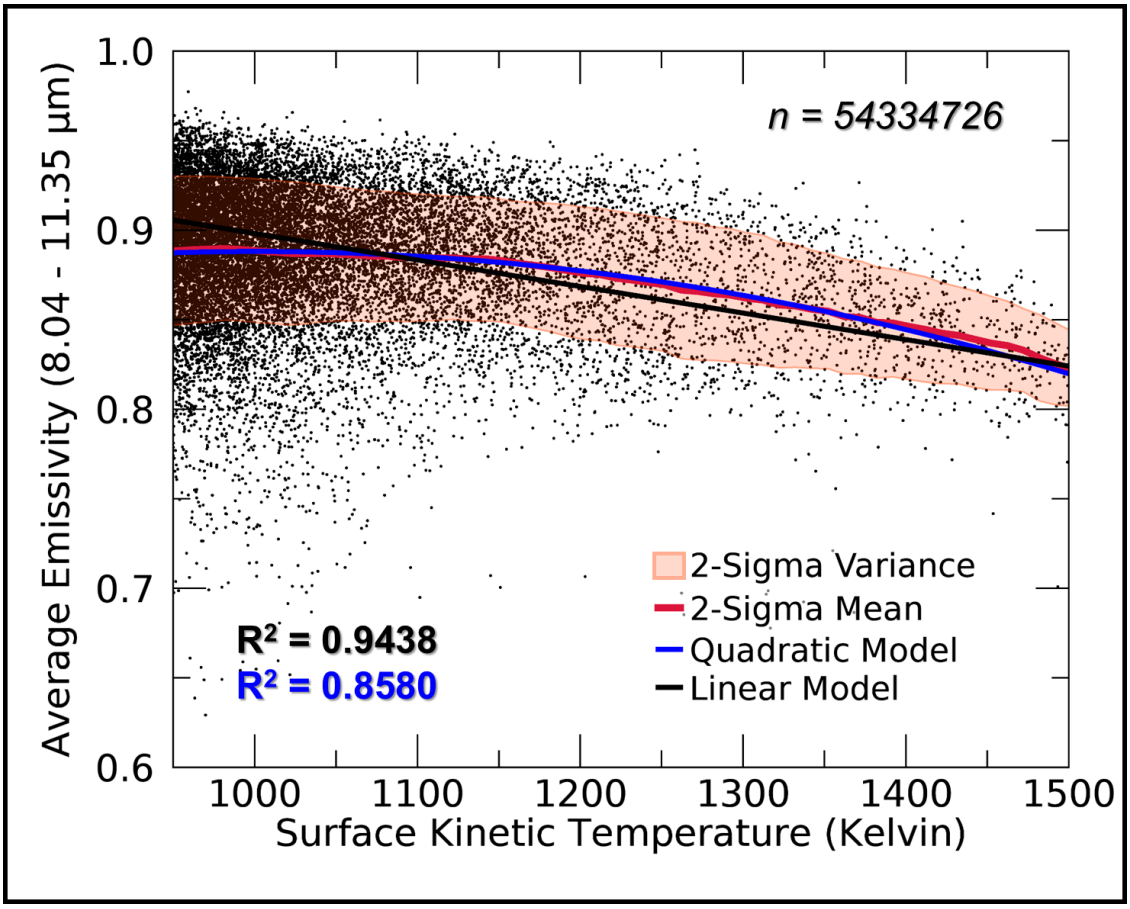

Figure 5.13: 6-point average emissivity dependent surface kinetic temperature plot across the TIR wavelength region (8-12 μm) acquired by the MMT-Cam of the 6.3-meter tumulus-fed lava flow. Data from the entire active regions of the lava flow during propagation were incorporated to determine the relationship between these thermal properties. The red faded region highlights the 2-sigma variance spread of the emissivity with temperature and the red line representing the mean. The black and blue lines represent the computed linear and quadratic regressions, respectively. Data were acquired from the ROI shown in Figure 5.6. Note, only a random 50% of the data are plotted due to computational demand but all the data are used in the calculations.

Table 5.1: Table of the regression constants and the coefficients of determination for the linear and quadratic modeled dependency of surface kinetic temperature on emissivity.

Wavelength	**Linear**			
(μm)	**P0**	**P1**	$\mathbf{R^2}$	
8.04 - 11.35	1.04630140	-0.00014814	0.9438	
8.04	1.31818130	-0.00033481	0.9477	
8.55	1.05007420	-0.00017767	0.9417	
8.99	0.94343585	-0.00004518	0.8300	
9.55	1.08229770	-0.00020805	0.9471	
10.04	1.03426870	-0.00022565	0.9484	
11.35	0.84949398	0.00010254	0.9413	
Wavelength	**Quadratic**			
(μm)	**P0**	**P1**	**P2**	$\mathbf{R^2}$
8.04 - 11.35	0.61289281	0.00054969	-0.00000027	0.8577
8.04	0.84341657	0.00042969	-0.00000030	0.8921
8.55	0.45587271	0.00077846	-0.00000038	0.8239
8.99	0.34731215	0.00091345	-0.00000038	0.8859
9.55	0.72528195	0.00036599	-0.00000023	0.8176
10.04	0.81568968	0.00012582	-0.00000014	0.7471
11.35	0.48516530	0.00068905	-0.00000023	0.9799

established across the liquidus temperatures for a typical basaltic lava (∼1250-1450 K) and the standard temperatures of lava surfaces during emplacement (∼900-1450K) at each of the six discrete spectral bands acquired by the MMT-Cam. The 8.04, 8.55, 9.55, and 10.04 μm bands revealed a strong inverse correlation between surface kinetic temperature and emissivity. However, there was a mostly constant relationship (minor inverse) in the 8.99 μm band and a positive relationship in the 11.35 μm band. These trends were then combined with equal weighting (the FWHM of the MMT-

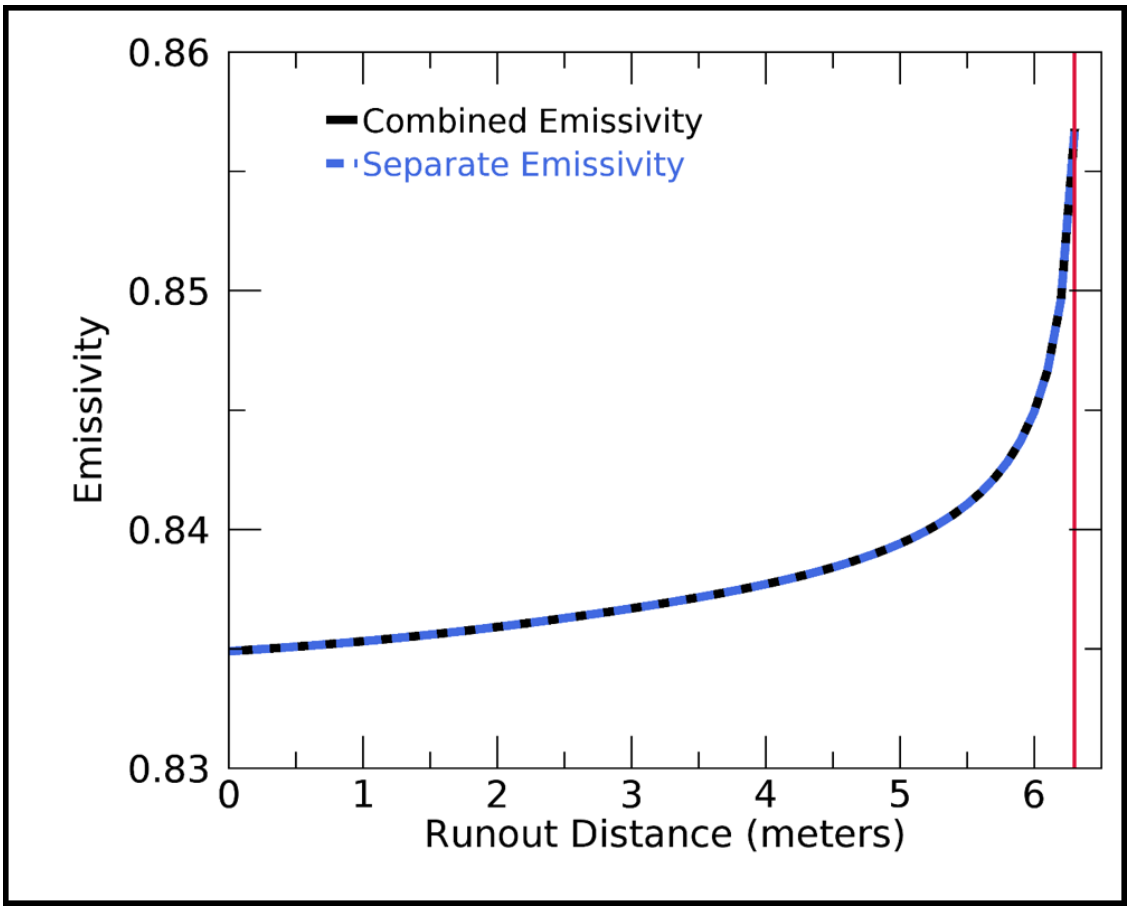

Figure 5.14: Comparison between the combined (black solid line) and separated (blue dashed line) multispectral emissivity data derived in the PyFLOWGO model for the 6.3-meter tumulus-fed lava flow. There is no variation between the computational methods but the combined multispectral emissivity data is computed faster. The red vertical line represents the final runout distance observed on the ground.

Cam bands are equal) to characterize the average emissivity dependency across the TIR wavelength region. The combined relationship revealed a minor inverse relation (Figure 5.13). Additionally, the spectral emissivity data revealed that during cooling of basaltic lava surfaces the initial two strong absorption features transitioned to a shallower broader absorption feature (Figure 5.11).

Regression analysis indicated that both linear and quadratic models accurately represent the relationship between surface kinetic temperature and emissivity of molten lavas during cooling for each band and the combined data (Figures 5.12 and 5.13, and Table 5.1). As a result, the linear regression was chosen for the new module to be integrated into the PyFLOWGO model due to its simplicity and minor improvement in overall representation accuracy compared to the quadratic regression. Also, only the combined average 6-point emissivity regression was integrated for simplicity with the existing architecture of the PyFLOWGO model and nominal difference would be achieved if the separate emissivity band regressions were used (Figure 5.14).

5.4.3 Lava Flow Propagation Modeling

5.4.3.1 Tumulus-Fed Lava Flow

PyFLOWGO simulated the 6.3-meter tumulus-fed lava flow using the initial conditions and parameters described in Table 5.2. An inverse exponential declining slope was determined based on ground measurements of the tumulus, with a change in elevation of 5.9 meters and a horizontal distance of 10.0 meters. Active channel widths were measured using the data acquired from the MMT-Cam during the activity. These were accurate due to the very small pixel resolution (<0.01 meters) but the angle of observation (not nadir) caused minimal underestimation of the measurements (Ball and Pinkerton, 2006). The underestimates were most noticeable in the lower parts of the flow (runout distances of 3-6 meters) where the flow was on a lower incline and flowing more perpendicular to the measurement line-of-sight. The initial channel width at the vent was measured at 0.15 meters and the depth at 0.1 meters. These channel measurements, along with initial velocity measurements, were used to calculate an initial effusion rate of 0.11 $m^3 s^{-1}$. The other input parameters were either obtained during the eruption (e.g., crustal fraction), through later analysis (e.g., vesicularity), or by making assumptions based on previous analysis of basaltic flows in Hawai'i (e.g., viscosity) (Harris and Rowland, 2001; Minitti et al., 2007). An initial crustal fraction of 0.1 was constrained using field observations of the lava effusion at the vent and from melt fraction calculations using the MMT-Cam data. The vesicle fraction of 0.3 was constrained from

thin section analysis of a sample collected directly from the active tumulus. A viscosity estimation of 220 Pa·s was acquired from previous studies on the fluid viscosity dependency on temperature at Kīlauea (Shaw, 1972; Harris and Rowland, 2015). All the initial parameters and corresponding references used to simulate the tumulus-fed lava flow are in Table 5.2.

Table 5.2: All the PyFLOWGO input models, modules, and parameters that were used to simulate the 6.3-meter tumulus-fed lava flow on the coastal plain of Kīlauea volcano on February 3, 2018.

Models	**Selection**	**Reference**
Crystallization Rate	basic	Harris and Rowland (2001); Chevrel et al. (2018)
Melt Viscosity	basic	Giordano et al. (2008)
Relative Viscosity	er	Einstein-Roscoe model from Chevrel et al. (2018)
Relative Viscosity Bubbles	no	
Yield Strength	ryerson	Ryerson et al. (1988)
Crust Temperature	constant	Harris and Rowland (2001); Chevrel et al. (2018)
Effective Cover Crust	basic	Harris and Rowland (2001); Chevrel et al. (2018)
Vesicle Fraction	constant	Harris and Rowland (2001); Chevrel et al. (2018)
Heat Budget Modules	**Selection**	**Reference**
Radiation	lin_emi	This study
Conduction	yes	Harris and Rowland (2001)
Convection	yes	Harris and Rowland (2001)
Rain	no	Harris and Rowland (2001)
Viscous Heating	no	Harris and Rowland (2001)
Initial Input Parameters	**Value**	**Reference**
Step Size (m)	0.1	This study
Effusion Rate (m^3s^{-1})	0.11	This study from MMT-Cam data (Thompson et al., 2019)
Width (m)	0.15	This study from MMT-Cam data (Thompson et al., 2019)
Depth (m)	0.1	This study
Gravity (ms^{-2})	9.81	
Eruption Temperature (K)	1473	This study from MMT-Cam data (Thompson et al., 2019)
Lava Viscosity (Pa·s)	220.0	Shaw (1972); Harris and Rowland (2015)
Crystal Fraction	0.1	This study from MMT-Cam data (Thompson et al., 2019)
DRE Density (kg m^3)	2744	Shaw (1972); Harris and Rowland (2015)
Vesicle Fraction	0.3	This study
Liquidus Temperature (K)	1235	This study from MMT-Cam data (Thompson et al., 2019)
Basal Temperature (K)	623	This study from MMT-Cam data (Thompson et al., 2019)
Distance from Core to Base (%)	10.0	Harris and Rowland (2001); Chevrel et al. (2018)
Wind Speed (ms^{-1})	2.68	This study
Air C_H	0.0036	Harris and Rowland (2001); Chevrel et al. (2018)
Air Temperature (K)	310.3	The study
Air Density (kg m^{-3})	0.4412	Harris and Rowland (2001); Chevrel et al. (2018)
Air S. Heat Capacity (J kg^{-1} K^{-1})	1099	Harris and Rowland (2001); Chevrel et al. (2018)
Buffer between T_{core} and T_{hot} (K)	20.0	Harris and Rowland (2001); Chevrel et al. (2018)
Crust Cover Fraction	0.1	This study from MMT-Cam data (Thompson et al., 2019)
Velocity Dependency of Crust (m s^{-1})	-0.16	Harris and Rowland (2001); Chevrel et al. (2018)
Crust Temperature (K)	623	This study from MMT-Cam data (Thompson et al., 2019)
Emplacement Crystal Growth	0.08	Harris and Rowland (2001); Chevrel et al. (2018)
Solid Temperature (K)	1237	Putirka (1997)
Latent heat of Crystallization (K kg^{-1})	350000	Harris and Rowland (2001); Chevrel et al. (2018)

The results of the PyFLOWGO model of the tumulus-fed lava flow using the original radiation heat budget module and the new variable emissivity radiation heat budget module derived from the

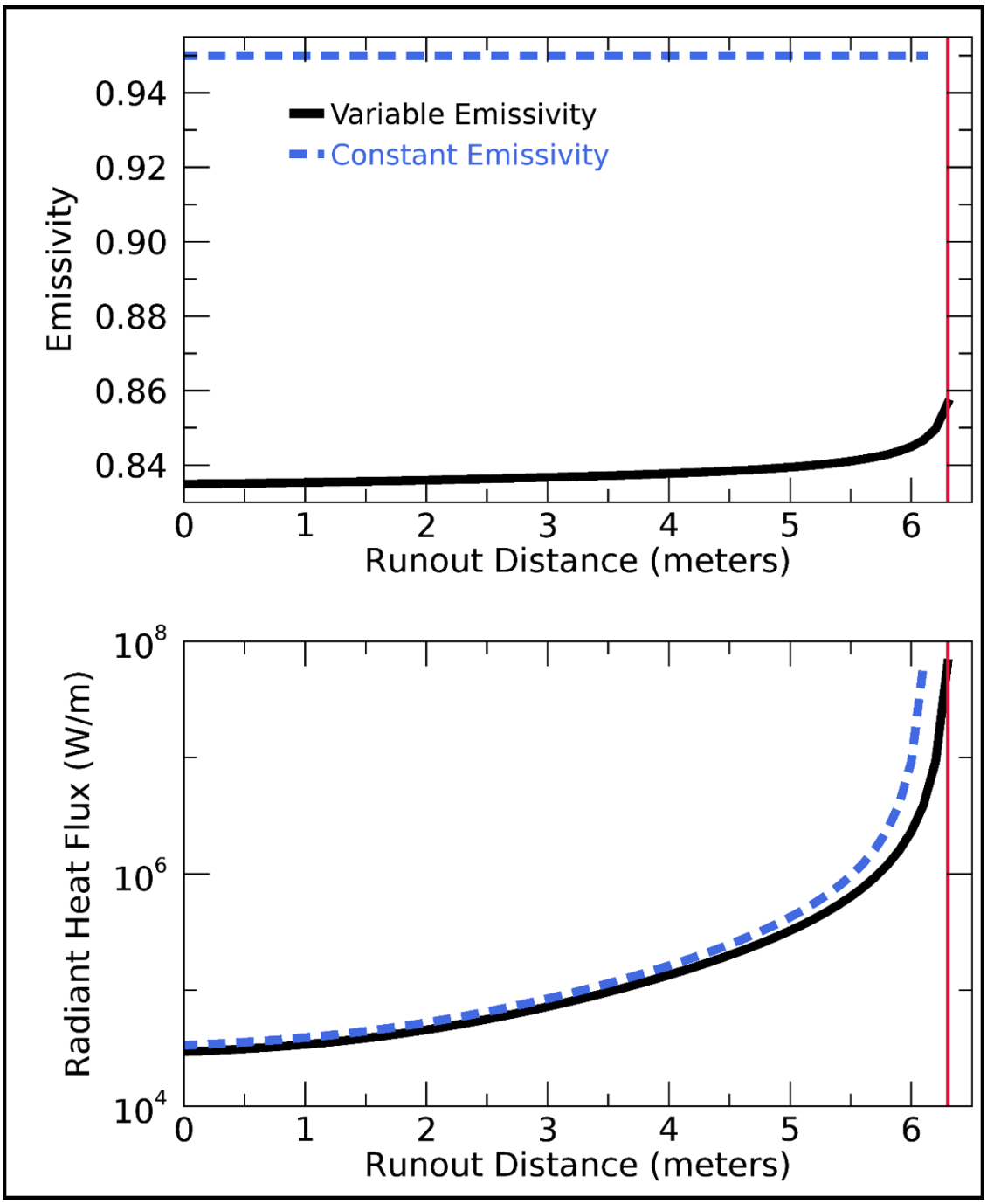

Figure 5.15: Comparison between the variation in (top) emissivity and (bottom) radiant heat flux during the tumulus-fed lava flow propagation computed using the variable emissivity module (black solid line) and constant emissivity module (blue dashed line). The input parameters are given in Table 5.2 and the red vertical line represents the final runout distance observed on the ground.

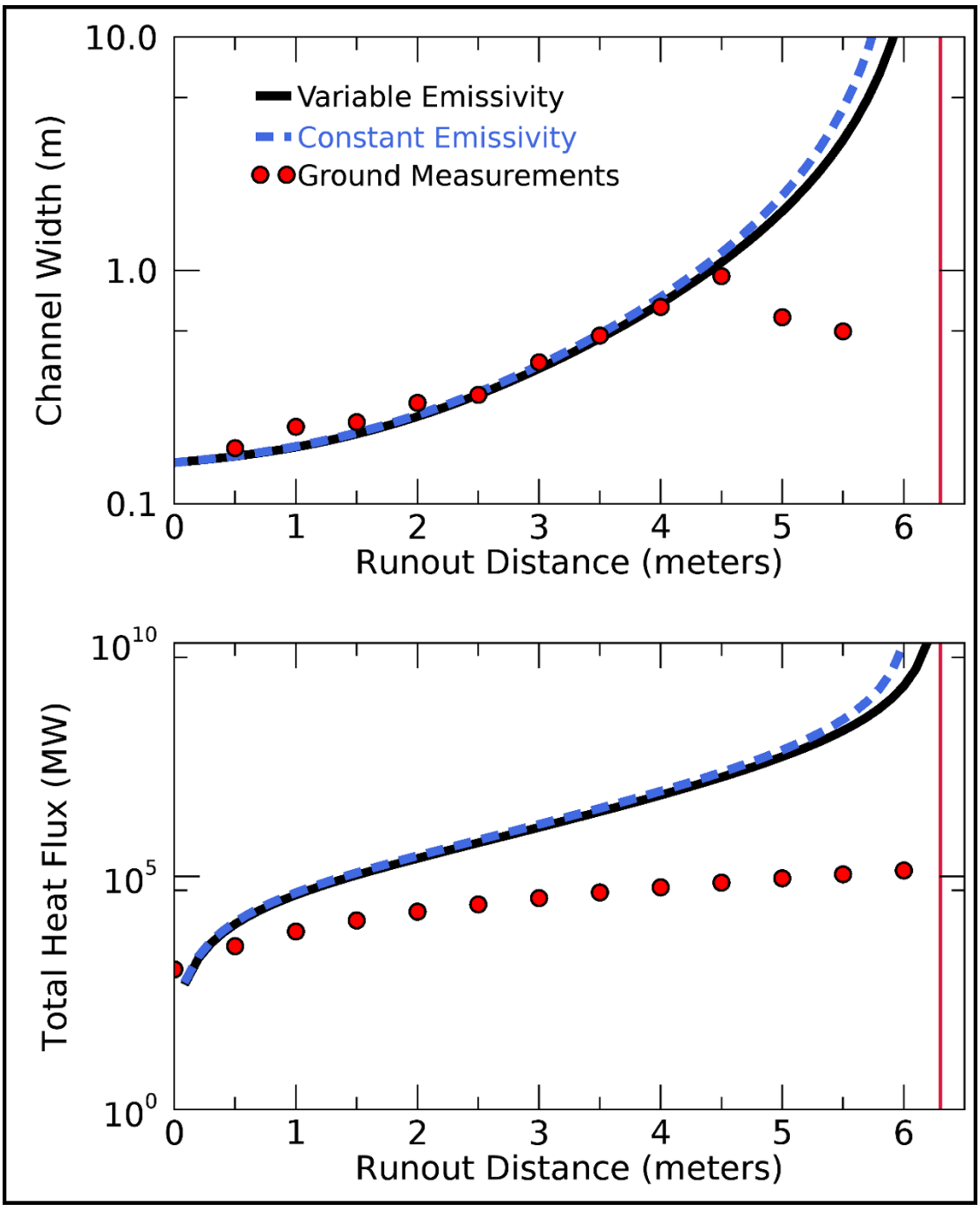

Figure 5.16: Comparison between the PyFLOWGO results (lines) and *in situ* ground measurements (red dots) derived from MMT-Cam data of the tumulus-fed lava flow (top) channel widths and (bottom) total heat fluxes. The *in situ* measurements validate the integration of the variable emissivity module with PyFLOWGO as these results had greater agreement than the un-modified PyFLOWGO results (especially in the channel width data and closer to the vent). The red vertical line represents the final runout distance observed on the ground.

MMT-Cam data were compared. The assessment revealed that the resulting final runout distance increased by ∼5% using the new variable emissivity module over the previously assumed constant emissivity of 0.95, which also had greater agreement with the field observations (Figures 5.15-5.18). The increase was mostly the result of the lower radiant heat flux compared to the original constant version (Figure 5.15). For example, at 6.0 meters, where the original constant emissivity module simulated the lava flow stalling, the variable emissivity module estimated ∼75% less radiant heat flux. The reduction in radiant heat flux reduced the cooling rate contributing to the simulation running further downflow (Figure 5.15).

The new variable emissivity module for PyFLOWGO was validated by comparing the model channel widths and total heat flux results with those derived from the MMT-Cam data (Figure 5.16). The modeled channel widths show a good correlation with MMT-Cam results until the flow reached a runout distance of ∼4.5-5 meters. Beyond the 4.5 meters runout distance, the tumulus-fed lava flow separates into multiple smaller lava flow channels causing the width of the main channel to decrease. This phenomenon was not simulated by the model and instead the results predicted the channel width to increase exponentially. The greatest agreement with the *in situ* measurements were with the variable emissivity adapted model. Additionally, the total heat flux calculated in the PyFLOWGO model were generally higher than those derived from the MMT-Cam data (Figure 5.16). The values increased in divergence with increased runout distance with over an order of magnitude difference observed further downflow. However, the variable emissivity adapted results agreed best with the *in situ* measurements compared to the constant emissivity module result.

The variable emissivity module reduced the cooling rate of the simulated tumulus-fed lava flow caused by a reduction in radiant heat flux and resulted in higher derived temperatures compared to the original model (Figure 5.17). The greatest impact was observed further downflow within the last 20% of the flow length. At a runout distance of 6.0 meters, where the original PyFLOWGO model simulation ceased, the derived temperatures were 4.9-5.4% higher using the variable emissivity module resulting in the flow continuing (Figure 5.17). Additionally, the simulated final surface and core temperatures were lower using the variable emissivity module by 2 K but at a greater runout distance (Figure 5.17).

In these PyFLOWGO model simulations, there were minimal differences between using the new variable emissivity module and the original constant emissivity module within the initial ∼50% runout distance of the flow (Figure 5.18). The greatest difference was observed in the final runout distance (∼5%) with the results using variable emissivity module propagating further downflow and

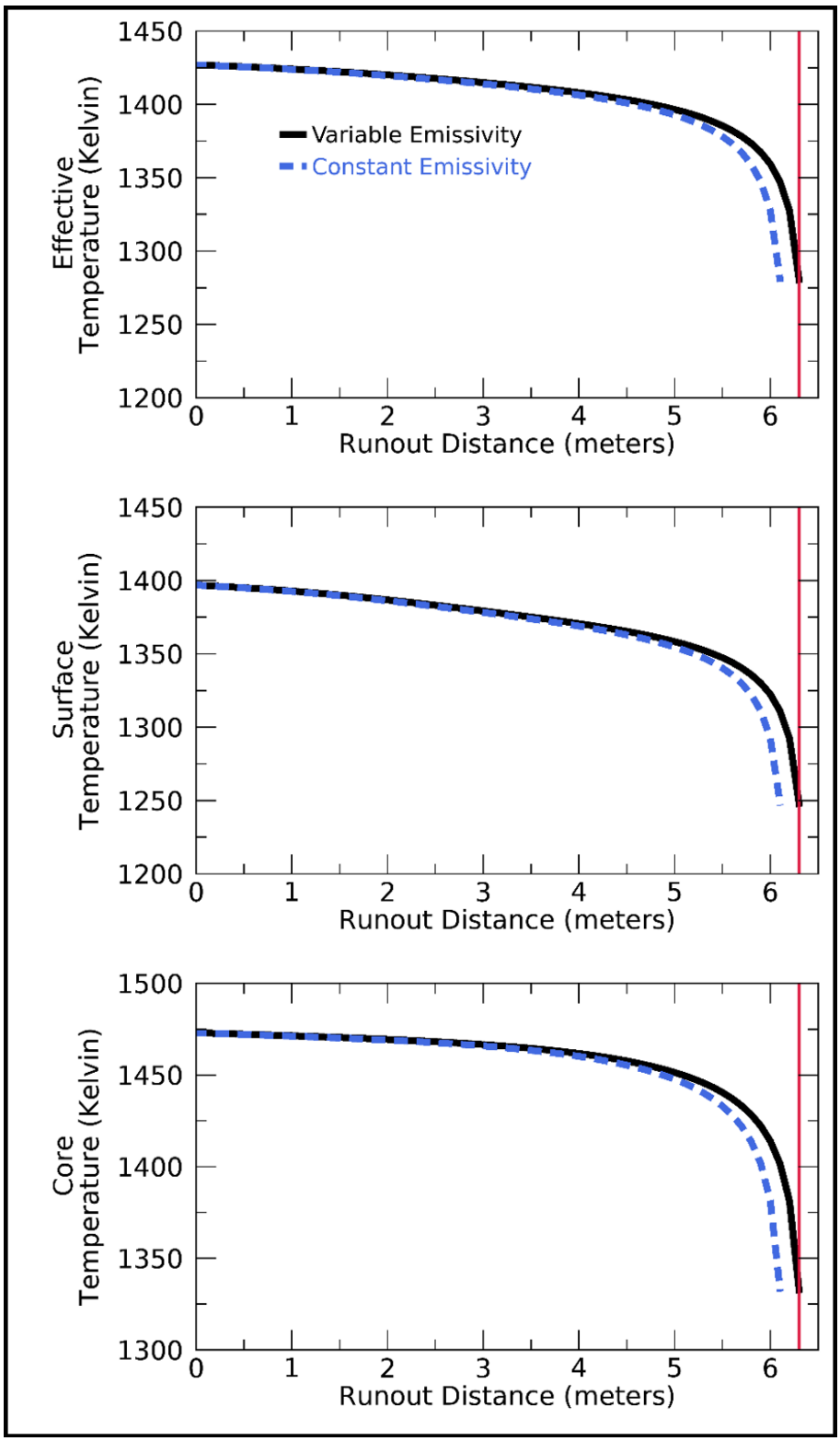

Figure 5.17: The (top) effective, (middle) surface, and (bottom) core temperature variations downflow of the tumulus-fed lava flow comparing the PyFLOWGO simulation using the variable emissivity (black solid line) and constant emissivity (blue dashed line) modules. The cooling rate is slower and the final temperatures were lower in the PyFLOWGO results using the variable emissivity module. The red vertical line represents the final runout distance observed on the ground.

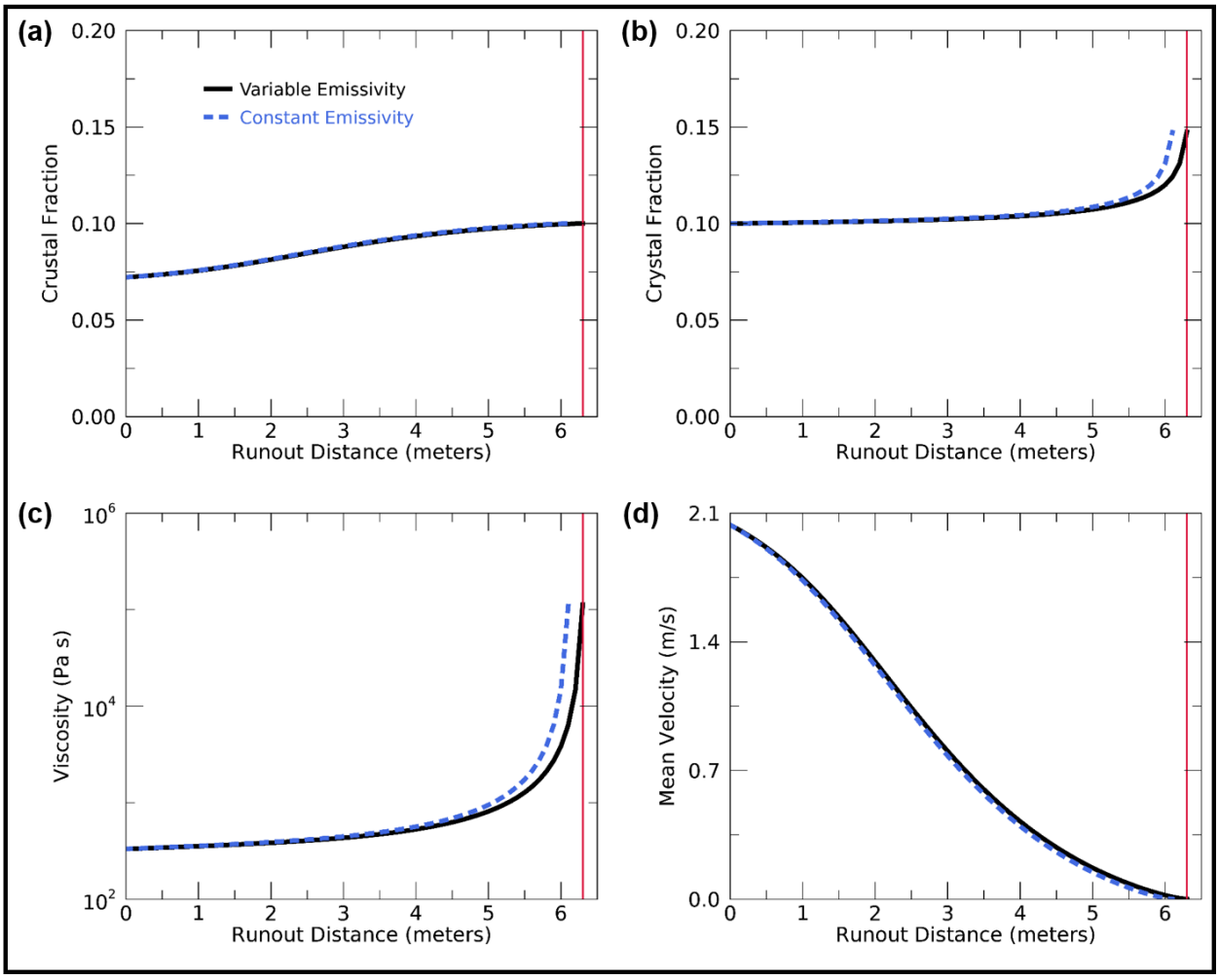

Figure 5.18: Thermo-rheological variations downflow of the tumulus-fed lava flow comparing the FLOWGO model simulation results using the variable emissivity (black solid line) and constant emissivity (blue dashed line) modules. The results using the original emissivity module consistently underpredicted the actual runout distance. The red vertical line represents the final runout distance observed on the ground.

higher matching with the *in situ* ground measurements. Generally, the results using this module had comparatively slower rates of change. For example, the rate of change in mean velocity is ∼3.2% slower in simulations using the variable emissivity module (Figure 5.18d). However, the different emissivity modules had no or minimal effect on the rate of change in crustal fraction, with only the final fraction varying due to the longer evolution simulated using the variable emissivity module (Figure 5.18a). Additionally, the final thermo-rheological properties vary between the two modules with the variable emissivity module producing results that vary and evolve further before the lava flow simulation ceases, including higher viscosity and crystal fractions (Figures 5.18b and c).

5.4.3.2 2018 Fissure 8 Lava Flow Emplacement

Next, the modified PyFLOWGO model was used to simulate the 12.47 kilometer open channel lava flow from fissure 8 prior to it entering the Pacific Ocean on June 3, 2018. After this date, the lava flow mostly emplaced lava into the Pacific Ocean, building a delta, and developed more complex tube systems. Additionally, the effusion rate increased to <2000 m^3s^{-1} after the initial few days of emplacement (post ocean emplacement), which is unable to be accounted for using the PyFLOWGO model. Therefore, the lava flow was not simulated beyond June 3 because the PyFLOWGO model is designed for open channel lava flow that emplace on land in the atmosphere. The lava flow was supplied from a lava fountain at the fissure and had three main divisions: a proximal spillway, an intermediate perched pāhoehoe channel, and distal channels (Patrick et al., 2019). Channel width measurements were acquired at periodic distances downflow using mosaics of TIR images published by the USGS created using a broadband TIR camera deployed on a helicopter (U.S. Geological Survey, 2018). On June 4, the average widths of the spillway, perched pāhoehoe channel and distal channel were 30 meters, 340 meters, and 150 meters, respectively. These values were used to validate the results of the simulation, but were likely overestimates as the lava flow entered the Pacific Ocean the day prior to the acquisition of these measurements. The initial effusion rate was constrained using previous studies that calculated the effusion rate from fissure 8 during the three months of activity between 100 and 2000 m^3s^{-1}, with the effusion rates peaking in July and the initial effusion rate constrained to 50-500 m^3s^{-1} (Neal et al., 2019; Patrick et al., 2019). As the PyFLOWGO model was only simulated until the flow entered the Pacific Ocean (June 3) an initial effusion rate of 500 m^3s^{-1} was selected. The other initial model parameters remained the same or similar to the values used in the tumulus-fed lava flow simulations (Table

5.2). The initial viscosity was reduced to 14-44 Pa·s to account for the increase fluid mobility of this lava flow compared to the more viscous tumulus-fed lava flow, based on prior studies investigating Hawaiian lava flows (Shaw, 1972; Harris and Rowland, 2015). The initial parameters that differ from the parameters used in the tumulus-fed lava flow simulations are listed in Table 5.3.

Table 5.3: The PyFLOWGO input parameters that differ from those in Table 5.2 that were used to simulate the 12.47 kilometer LERZ fissure 8 lava flow emplacement of Kīlauea volcano between May 27 and June 3, 2018.

Initial Input Parameters	**Value**	**Reference**
Step Size (m)	10.0	This study
Effusion Rate (m^3s^{-1})	500	This study from MMT-Cam data (Thompson et al., 2019)
Width (m)	10.0	This study from MMT-Cam data (Thompson et al., 2019)
Depth (m)	5.0	This study
Lava Viscosity (Pa·s)	30.0	Shaw (1972); Harris and Rowland (2015)
Vesicle Fraction	0.1	This study
Distance from Core to Base (%)	10.0	Harris and Rowland (2001); Chevrel et al. (2018)
Buffer between T_{core} and T_{hot} (K)	30.0	Harris and Rowland (2001); Chevrel et al. (2018)
Crust Cover Fraction	0.5	This study from MMT-Cam data (Thompson et al., 2019)
Emplacement Crystal Growth	0.3	Harris and Rowland (2001); Chevrel et al. (2018)

The differences between the PyFLOWGO results using the constant and variable emissivity modules were computed, with the other modules and constants remaining the same. Overall, integration of the variable emissivity module resulted in the final runout distance increasing by ∼7%, from 10.68 kilometers to 12.47 kilometers (Figures 5.19-5.21). Similar to the tumulus simulation, the increase was predominantly caused by the reduction in cooling rates as a result of lower calculated radiant heat flux using lower emissivity values (Figure 5.19). The lower emissivity constrained the lower efficiency of radiant heat flux from the molten or partly molten surface of the lava flow during propagation. The variable emissivity module resulted in the final radiant heat flux being ∼32% lower compared to the constant emissivity module results. This was further observed in the surface temperature results where the variable emissivity module simulated comparatively higher temperatures throughout the runout distance (Figure 5.19). The divergence between the results using the two emissivity modules increased with runout distance.

The PyFLOWGO results of the fissure 8 lava flow emplacement were validated by comparing the modeled downflow channel widths with ground measurements acquired using a TIR image mosaic map produced by the USGS (U.S. Geological Survey, 2018) (Figure 5.20). Generally, there is strong agreement between the model results and the ground measurements. The greatest divergence is observed in the proximal region (0.1-4.0 kilometers from the vent) where the wide

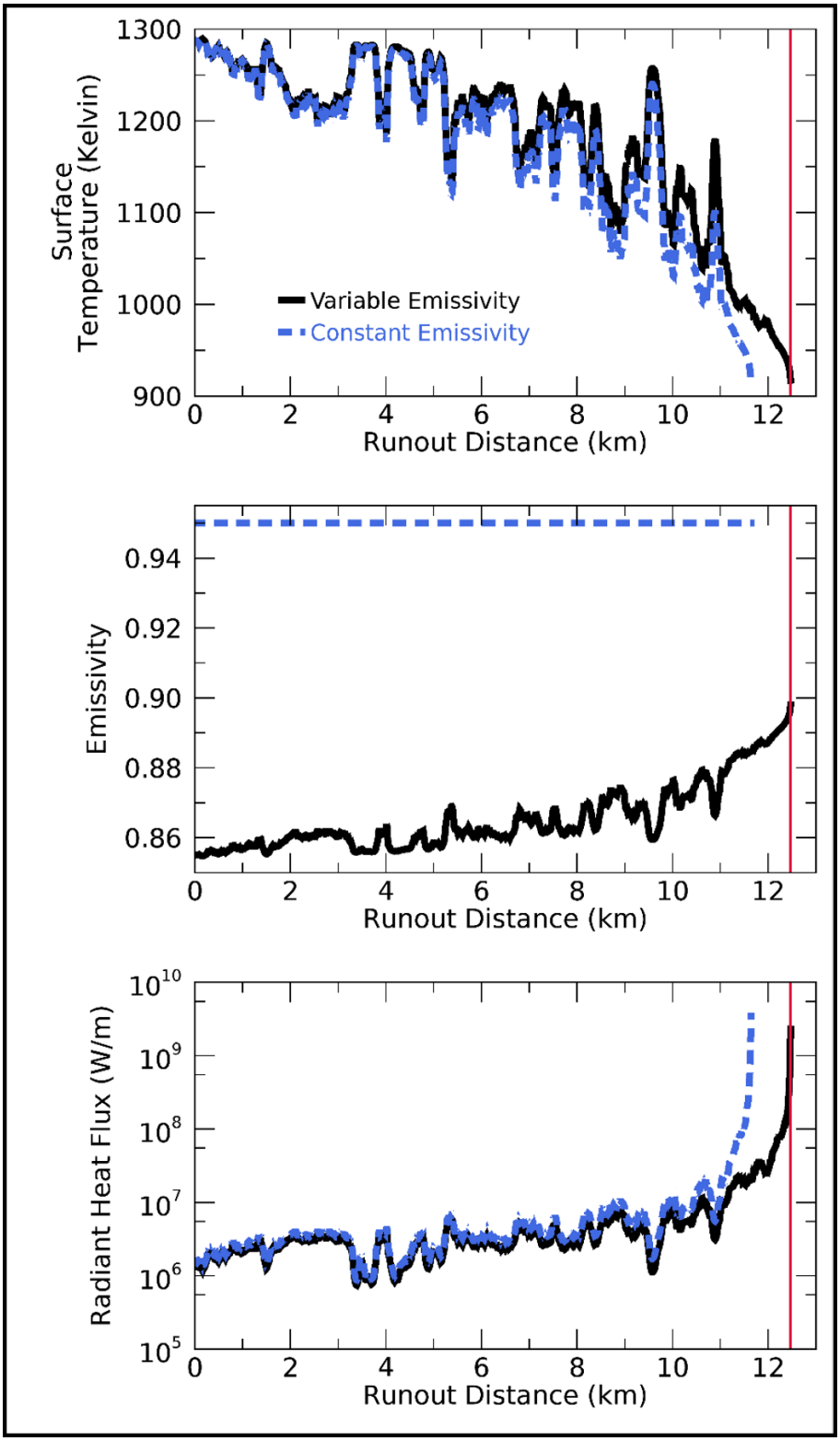

Figure 5.19: Comparison between the variation in (top) surface temperature, (middle) emissivity, and (bottom) radiant heat flux during the 2018 fissure 8 lava flow emplacement from May 27 to June 3 when the flow reached the Pacific Ocean. The thermal properties of the lava flow were simulated using the variable emissivity module (black solid line) and constant emissivity module (blue dashed line) in the PyFLOWGO model. A greater divergence in results are observed with runout distance. The input parameters are given in Tables 5.2 and 5.3, and the red vertical line represents the final runout distance observed on the ground.

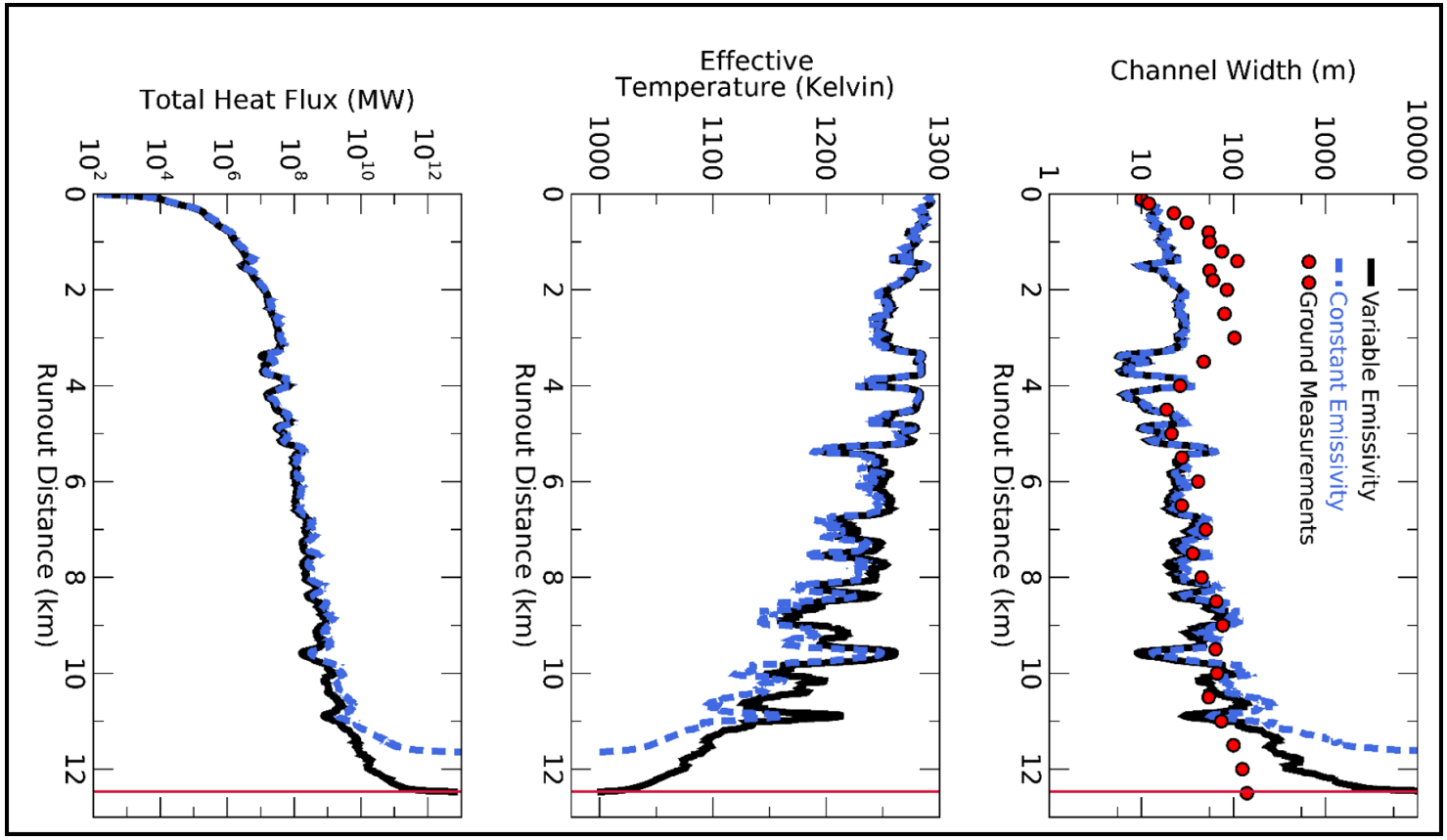

Figure 5.20: Comparison between the variability of model results (lines) and ground measurements (red dots) derived from TIR maps of the downflow (top) channel widths of the 2018 fissure 8 lava flow emplacement between May 27 and June 3. The *in situ* measurements validate the integration of the variable emissivity module with PyFLOWGO, however, there is poor agreement close to the vent in the perched pāhoehoe channel region. Variations in the simulated (middle) effective temperature and (bottom) total heat flux using the variable (black solid line) and constant (blue dashed line) emissivity module in the PyFLOWGO model. The red vertical line represents the final runout distance observed on the ground.

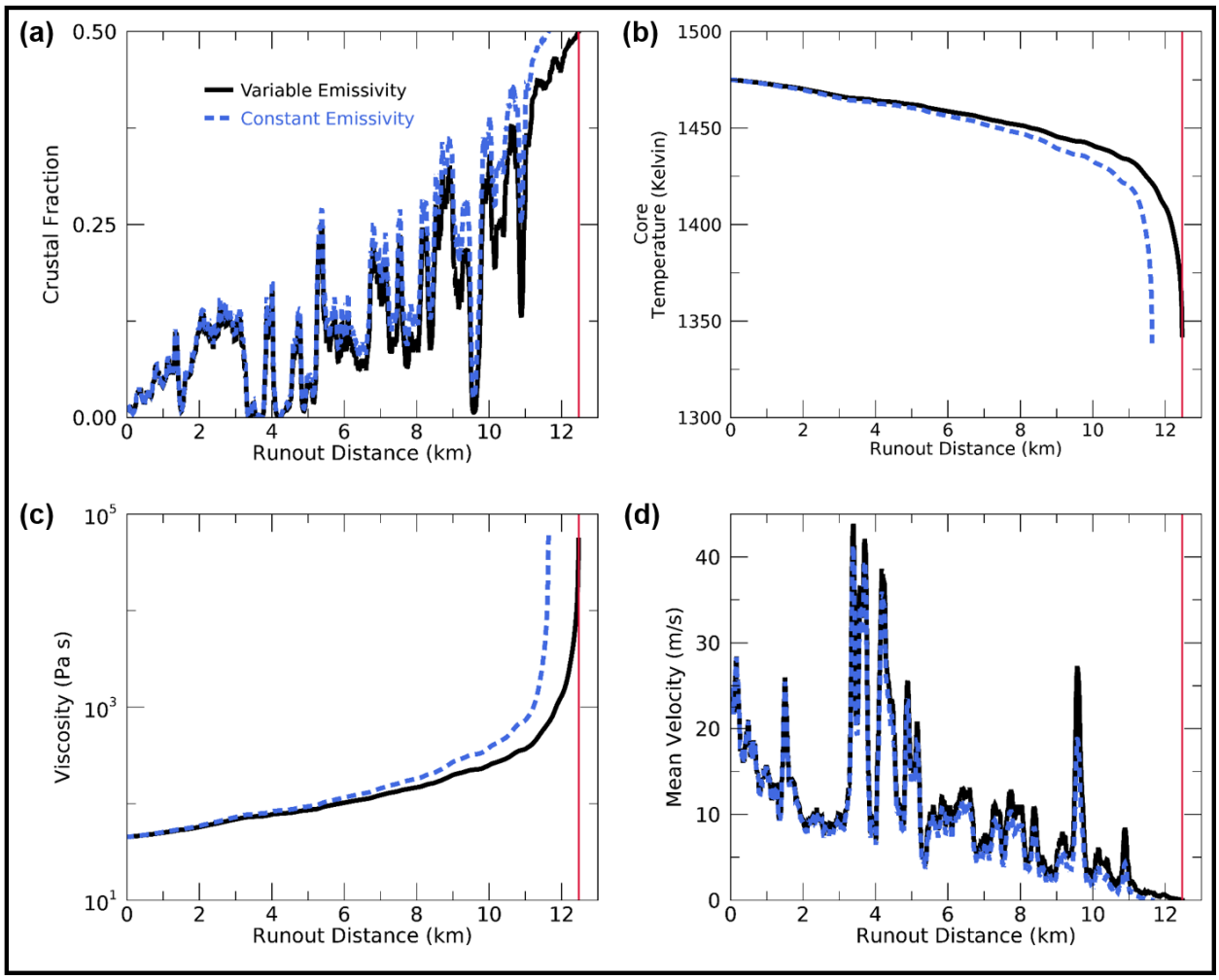

Figure 5.21: Thermo-rheological variations downflow of the 2018 fissure 8 lava flow emplacement (May 27 to June 3) comparing the FLOWGO model results using the variable emissivity (black solid line) and constant emissivity (blue dashed line) modules. The results using the constant emissivity module consistently underpredicted the actual runout distance as a consequence of higher cooling rates. The red vertical line represents the final runout distance observed on the ground.

perched pāhoehoe channel formed. The results simulated using the variable emissivity module had a stronger agreement at greater runout distances (>9 kilometers) compared to the constant emissivity module results. The simulated effective temperatures showed similar variability as the surface temperature result, with higher temperatures calculated for runout distances using the variable emissivity module (Figure 5.20). The modeled effective temperature was ∼9% higher using the variable emissivity module at the final runout distance of the flow simulated, compared to using the constant emissivity module (at 11.64 kilometers). The modeled final total heat flux using the variable emissivity module was also 32% lower and the same percentage difference as calculated in the radiant heat flux comparison (Figure 5.20). Overall, the variable emissivity module produced results consistent with slower cooling rates.

The broader thermo-rheological results calculated using the variable emissivity module were similar as those using the original emissivity module but the results are more consistent with slower cooling rates associated with less efficient radiant heat flux (Figure 5.21). This caused lower crustal fractions and viscosities and higher core temperatures and mean velocities to be simulated with runout distance. Overall, the average rate change of these thermo-rheological properties was ∼7% lower using the variable emissivity module and the final runout distance was more consistent with the ground measurements for all the results (12.47 kilometers).

5.5 Discussion

Variability in the emissivity of lava during propagation and subsequent cooling from a molten to solid crustal surface has been quantified using a ground-based TIR instrument. High spatiotemporal multispectral TIR data were acquired of a small tumulus-fed lava flow to constrain the dependency of temperature on emissivity during lava cooling and physical state change. A strong near-linear inverse relationship was observed between the average 6-band TIR emissivity and surface temperature. The unique multispectral TIR data acquired by the MMT-Cam revealed mostly inverse trends at all the bands in the TIR region but the bands at ∼9.0 μm and ∼11.35 μm had a constant and positive correlation, respectively. This highlighted the strong variability in emissivity with wavelength as a result of the atomic structure of the lava changing during cooling and phase change from a liquid to solid. However, the general inverse correlation observed across the TIR region emphasized the importance of modeling the effect of changing emissivity on thermal

heat budget calculations of lava flows to accurately determine cooling and propagation. This led to the development of a variable emissivity relationship dependent on surface temperature across the eruption and cooling temperatures of basaltic lavas (700 – 1500 K). The advanced module directly replaced the current constant emissivity basic module used to calculate radiation heat budget in the PyFLOWGO model.

Analysis of the MMT-Cam data identified average emissivity values of 0.85-0.88 across the liquidus temperatures (∼1200-1300K) and as low as 0.75 at typical eruption temperatures of basaltic lava (up to 1475 K) (Putirka, 1997; Harris, 2013). These are all significantly lower than the typically assumed emissivity of 0.95 used in thermal calculations of lavas at all temperatures. Previous studies have shown that this can result in a 20-30% reduction in radiant heat flux and total heat flux (Thompson and Ramsey, 2017, 2018; Ramsey et al., 2019). However, the consequence of this reduction in heat flux on lava flow propagation and thermo-rheological calculations have not been the focus of previous investigations (e.g., Ramsey et al. 2019).

The incorporation of the variable emissivity module into the PyFLOWGO model was validated by simulating the 6.3-meter tumulus-fed lava flow observed on February 3, 2018, on the coastal plain to the south of the Pu'u $\bar{O}$'$\bar{o}$' vent. Ground measurements constrained the majority of the physical (e.g., channel widths) and thermo-rheological (e.g., eruption temperature, vesicularity, and crustal fraction) properties of the lava flow to limit any differences in the response of the PyFLOWGO model simulations to only be contributed by the emissivity module. Utilization of the variable emissivity module consistently produced results similar to the actual runout distance of the tumulus-fed lava flow observed in the field, calculating a 6.3-meter distance compared to only 6.0-meter distance simulated using the basic constant emissivity module (an increase of ∼5%). Ultimately, this controlled test validated the integration of the variable emissivity module and demonstrated the importance of incorporating a more advanced module that more accurately depicts the changing surface properties. The difference in final runout distance simulated between the two emissivity modules appeared minimal, however, because the small scale of this flow (time elapsed and final runout length) provided limited opportunity for all the thermo-rheological properties to evolve completely. Therefore, applying the PyFLOWGO model with the advanced module to a larger channelized lava flow (more typical for hazard management applications) evaluated the scalability of the module. It was expected that the relative difference between the final runout distances simulated by the two emissivity modules would remain consistent at all scales (∼5%), but would be more significant at longer lengths based on actual distance.

Both versions of the PyFLOWGO model were then used to simulate the 2018 LERZ fissure 8 lava flow emplacement from May 27 to June 3, prior to the flow entering the Pacific Ocean after flowing 12.47 kilometers from the vent. The lava flow continued to propagate into the Pacific Ocean for several weeks but this was unable to be modeled using PyFLOWGO as the effusion rate increased after the initial emplacement and the ocean environment caused additional complications. However, if the effusion rate was constant during the entire emplacement and the flow front had remained subaerial the advance PyFLOWGO results suggested that the lava flow would have stalled at a runout distance of ∼12.47 km. Comparison of the basic and advanced emissivity module PyFLOWGO results demonstrated that the use of a constant emissivity value underestimated the final flow runout distance by ∼7%. Additionally, to assess the reliability of the modified PyFLOWGO model for near real-time hazard assessment situations, input values were limited to standard values for the lava flow type (basaltic) so the collection any additional geochemical datasets are not required, apart from a previously acquired DEM and a small TIR data acquisition at the eruption site. The model results were also consistent with surface thermal properties derived from the MMT-Cam data acquired during a helicopter campaign over the lava flow on May 30, 2018.

In both PyFLOWGO lava flow models, the greatest difference between the two module simulations (basic and advanced emissivity modules) were observed further downflow, around the liquidus temperatures of the basaltic lava, where there is a complex mixture of lava surfaces (molten, viscoelastic crusts, and glassy crusts). It is across these temperatures and surface physical states that emissivity varied the most, having the greatest affect on radiant heat flux. In the fissure 8 lava flow emplacement simulations, the variable emissivity module reduced the final radiant heat flux and total heat flux by ∼30%, which caused a reduction in the cooling rate and subsequent increase in runout distance. Within the model, this reduced the rate of crustal formation, decreased the viscosity, and increased the flow velocity, resulting in a simulation with a greater runout distance. The heat flux reductions were significantly greater in the tumulus-fed lava flow simulations (∼75%) and can be contributed to the small overall scale of the lava flow and limited evolution potential due to its small size. Therefore, this study of both the tumulus-fed and fissure 8 lava flow emplacement models demonstrates that the difference between the final runout distances is increasingly more significant with longer flows. For example, the difference in final runout distance for the fissure 8 emplacement is ∼830 meters.

The effect of the uncertainty in the temperature dependent emissivity linear regression on

the final runout distance modeled by PyFLOWGO was determined using a Monte Carlo-like methodology. This constrained the variability in the final runout distance caused by the linear regression uncertainty by randomly repeating the lava flow propagation simulations of the tumulus-fed lava flow and fissure 8 lava flow emplacement 10000 times (Figure 5.22). The uncertainty in the linear regression parameters were quantified by randomly generating these values 10000 times over the range of the 2-sigma standard deviation of the regression model parameters ($P0 = 0.007873; P1 = 0.00000612$) in a normal Gaussian distribution (Figures 5.22b and d). These values were then used in the advanced module within PyFLOWGO to iterate the lava flow simulations 10000 times. The uncertainty in the final runout distances of the tumulus-fed lava flow was $\sim$0.5% with a total variability of $\sim$3% (Figure 5.22a). In comparison, the uncertainty in the final runout distance of the fissure 8 lava flow emplacement was $\sim$2% with a total variability of $<$1% (Figure 5.22c). Therefore, the uncertainty in the temperature dependent emissivity linear regression is insignificant and significantly less than the improvement in accuracy of the final runout distance ($< 7\%$) caused by implementing the advanced variable emissivity module within the PyFLOWGO model.

The PyFLOWGO model runs (for both tumulus-fed and fissure 8 lava flow emplacement) were verified using ground measurements of channel widths, with total heat flux measurements additionally used for the tumulus-fed lava flow simulation verification. For the early and mid-sections of the flow, there was strong agreement between both simulations and ground measurements, with the variable emissivity module result having stronger agreement. However, the width measurements in each lava flow simulation (both the tumulus-fed and fissure 8 flow emplacement) were greatly overestimated over the final $\sim$10% of the runout distance, compared to the ground measurements. This is due to the divergence of the lava flow into multiple channels in these regions and that only the main channel widths were measured. Additionally, the FLOWGO model was not developed to simulate this small scale divergence but rather to imitate the pathway and distribution of the main lava flow channel. Therefore, if all the divergent channel widths were cumulated, the ground measurements would agree better with the simulated widths in the distal region of the flow. The cumulative widths of the tumulus-fed and fissure 8 emplacement lava flow fronts were $\sim$2 and $\sim$2500 meters, respectively. This is an improvement of $\sim$300% and $>$1000% in the final tumulus-fed and fissure 8 emplacement lava flow widths, respectively, compared to the single main channel final widths. The 2018 LERZ fissure 8 lava flow emplacement simulations also underestimated the near vent channel widths where the well-insulated perched pāhoehoe channel was observed. The

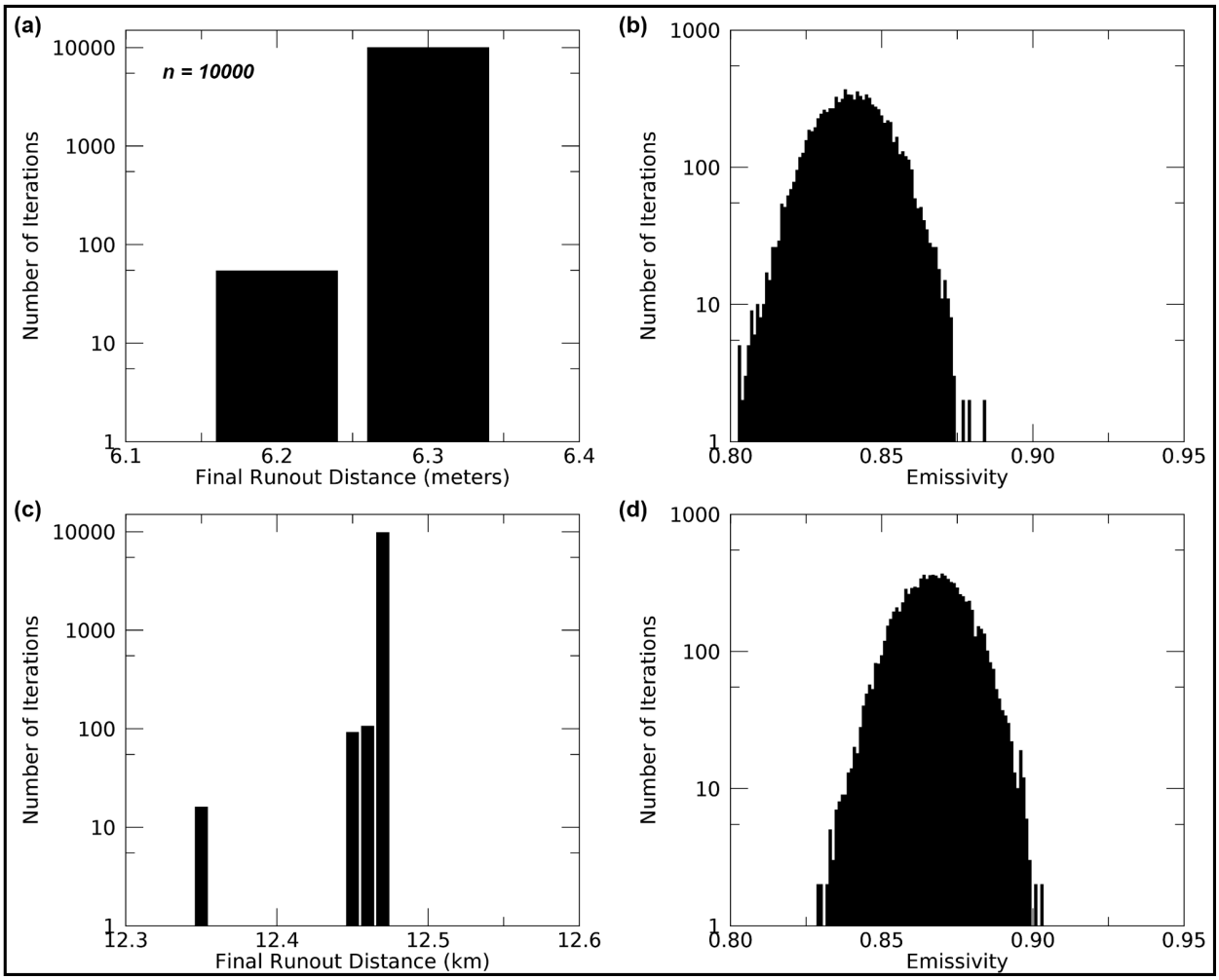

Figure 5.22: The uncertainty and variability in the final runout distance of the (a) tumulus-fed lava flow and (c) LERZ fissure 8 lava flow emplacement caused by the temperature dependent emissivity regression model uncertainty (b and d). The plots illustrate the results using a Monte Carlo-like methodology with 10000 iterations of the PyFLOWGO model using the advanced variable emissivity module. The emissivity distributions (b and d) represent the average emissivity computed by the advanced variable emissivity module during the entire duration of the PyFLOWGO models.

FLOWGO model was not designed to simulate well-insulated channels, like those observed proximal to the fissure 8 vent, and calculated a narrower and poorly insulated channel instead. Nevertheless, FLOWGO was able to accurately predict the final flow runout distance, implying a channelized lava flow is not required to be poorly insulated along its entire runout distance to be accurately simulated by the model.

The distinct difference in total heat flux values calculated from ground measurements and the models of the tumulus-fed lava flow are due to both scale and across flow thermal variability. Within a crossflow transect, typically there will be a temperature gradient from the center to the margin resulting in non-uniform heat flux across the flow. The step-wise calculation in PyFLOWGO oversimplifies this variability by assigning a singular temperature value for the entire width based on two-component thermal mixing that will overestimate the heat flux. To specify, the PyFLOWGO model divides the lava flow into discrete downflow increments (e.g., 0.1 meter increments for the tumulus-fed flow) and matches the defined channel width to estimate total heat flux. However, the MMT-Cam has a higher spatial resolution (<0.01 meters) both across and down flow, capturing the complexity of the thermal variability (multiple thermal components on lava flow surface). The MMT-Cam calculates the heat flux for each pixel and then sum each pixel value over a comparable area to the model to give total heat flux. Therefore, PyFLOWGO likely overestimated the total heat flux. Furthermore, as the channel width increases, the heat flux calculated by the model will become increasingly overestimated, resulting in larger discrepancies with the ground measurements. Additionally, previous investigations have proposed that the discrepancy between remote sensing derived (satellite sensor) and predicted (PyFLOWGO model) heat flux values can also be caused by the heat flux of the overlying air boundary layer contributing to the remote sensing derived measurements (Ramsey et al., 2019). It has been suggested that the hot air boundary layer could cause overestimates in heat flux from lava surfaces by a factor of at-least two derived from remote sensing datasets (Harris, 2013; Ramsey et al., 2019). However, as the MMT-Cam data were acquired from an acute viewing geometry the contribution of the hot air boundary layer is minimal (Figures 5.6, 5.8, 5.9, and 5.10).

Overall, emissivity is an important property that must be considered the thermal evolution of molten lava during propagation and cooling. The efficiency by which a surface emits radiation is strongly controlled by the physical state of the surface and consequently the surface temperature, although other properties influence this, including composition and surface morphology also influence this. Therefore, it is important to quantify and account for the change in emissivity as lava

surfaces cool in flow propagation models due to the strong effect on flux rates (∼30% decrease) and thus propagation potential (>5% increase). If emissivity is not determined correctly, the final runout distance is underestimated and hazard assessments will be inaccurate, potentially endangering local populations. PyFLOWGO has a high potential to accurately simulate a channelized lava flow with limited prior knowledge of the geochemistry and rheology of the active lava. However, by improving the constraint on emissivity within the model during the evolution of a lava flow, the importance of time-intensive analysis to determine accurate compositional and rheological properties of the lava are less critical. This enables the faster implantation of PyFLOWGO to simulate active and high-risk lava flows at a broader suite of volcanoes around the Earth, especially at volcanoes where less prior knowledge is available. Nevertheless, this new temperature-dependent emissivity module for calculating radiant heat flux is applicable for lava with similar eruption and liquidus temperatures as the Hawaiian basaltic lavas modeled in this investigation. For example, more silicic lavas have lower eruption and liquidus temperatures and therefore would have a different temperature-dependent emissivity variability. As a result, similar investigations need to be conducted to evaluate the variability in emissivity with temperature at a variety of lava compositions that are typically observed on Earth. These investigations could potentially be accomplished in a laboratory or in the field and would not be required for all new lava flows but for the general lava composition classifications. This will enable a similar lava flow propagation modeling methodology, developed in this study to be applied to the majority of active lava flows in near real-time.

5.6 Conclusions

Lava flow propagation modeling provides a vital tool for assessing hazards associated with lava flows. There are numerous models that aim to accurately predict the distribution and runout distances of lava flows and most use a constant assumed emissivity value for the lava surface to calculate the heat fluxes from the surface during propagation. However, emissivity varies with temperature and other surface properties (mostly related to the Si-O atomic bond structure) and thus has been over simplified in these calculations.

High-resolution multispectral TIR data were acquired from a small tumulus-fed lava flow on the coastal plain of Kīlauea volcano in February 2018. The MMT-Cam acquired data during the complete evolution of the flow from initial breakout to final runout length. These data were

used to constrain the correlation between emissivity and temperature across the TIR region at all eruption temperatures and lava surface states (e.g., molten, viscoelastic, glassy crust). There were small variations in the relationship between emissivity and temperature across the TIR region but generally a strong inverse correlation was found. The relationship was then used to create a variable emissivity module that was integrated into the PyFLOWGO model to improve the ability of the thermo-rheological model to accurate account for emissivity variability during lava flow propagation and cooling. The modified PyFLOWGO model using the advanced variable emissivity module was tested by simulating the 6.3 meter tumulus-fed lava flow and results were compared to original PyFLOWGO simulations. The MMT-Cam derived data and visible observations were used to constrain the input parameters and validate the results. Overall, the modified PyFLOWGO model more accurately predicted the final runout distance of the tumulus-fed lava flow and strongly correlated with the validation measurements. The variable emissivity module increased the runout distance by >5% and reduced the heat flux in the final 20% of the flow by up to 75%.

The modified PyFLOWGO model was then used to simulate the LERZ fissure 8 lava flow emplacement at Kīlauea volcano from May 27 to June 3, 2018. Limited prior knowledge was used to determine the input parameters of this lava flow, to assess the applicability of the modified PyFLOWGO in a disaster scenario. MMT-Cam data were used to validate the results, along with a TIR mosaic map survey produced by the USGS during the eruption and a DEM. The modified PyFLOWGO model accurately simulated the fissure 8 lava flow emplacement prior to the flow front entering the Pacific Ocean on June 3. Compared to the original PyFLOWGO simulations, the variable emissivity module calculated a greater final runout distance by ∼7% and a reduction in heat flux of ∼30% during the final 20% of flow propagation. Therefore, the variable emissivity does affect the results of lava flow propagation models and should be accounted for during cooling.

Overall, lava flow modeling is limited by the accuracy of input parameters and prior knowledge of thermo-rheological properties of a lava, as well as the ability to accurately simulate the physical and chemical processes occurring as the lava propagates. The development and integration of a new variable emissivity module within the PyFLOWGO model that accounts for changing surface temperature downflow aims to increase the accuracy of the heat flux processes and subsequently improve runout distance predictions. This can reduce the processing time of simulating active lava flows and the reliability of results, to better inform hazard assessments and reduce lava flow vulnerability of local populations.

6.0 Conclusions and Future Directions

The ability to accurately derive the thermal radiant emissions of active lava surfaces is important for understanding the cooling rate and propagation potential of a lava flow. The fundamental changes in the efficiency of energy emitted by a surface during cooling and changes in surface state from molten to crustal must be quantified to accurately represent the thermal regime of a natural lava flow in a model. To achieve this, analysis of multiple TIR datasets were conducted to define the variability in emissivity with temperature over a variety of different spatial, spectral, and temporal resolutions, and to define the corresponding errors. The variability in emissivity during lava propagation and cooling was quantified and the impact on heat flux determined to evaluate the influence on lava flow propagation modeling.

The MMT-Cam is a six-band multispectral TIR imaging instrument that can measure emitted spectral radiant energy from a surface between 8 and 12 μm. The camera system is capable of measuring the surface kinetic temperature and emissivity of numerous geological surfaces from molten lava over 1200 K to crystalline rocks at ambient temperatures. The wavelength regions captured by the system enable the differentiation of silica rocks and transition of atomic structure with temperature. A robust pixel-based calibration procedure was developed and implemented to correct for filter transmissions and instrument geometric effects, including detector temperature drift during deployment, to remove image and spectral artifacts. As the MMT-Cam has two gain settings, the calibration was tested on low temperature hand samples and dynamic high temperature molten lava surfaces at the Syracuse University Lava Project. Testing validated that the MMT-Cam accurately retrieves thermal properties of a wide range of geological surfaces over a range of temperatures and compositions. Additionally, the wavelength regions captured by the MMT-Cam are comparable to current satellite-based instruments and can inform the performance metrics for potential future satellite sensors with similar technological architectures. The spatial, spectral, and temporal resolutions of the MMT-Cam make it ideal for analyzing active lava flows to improve understanding of changing emissivity during propagation and cooling.

The MMT-Cam data were compared with aerial and satellite TIR data acquired from active lava lakes and lava flows at Kīlauea volcano in Hawai'i during NASA airborne campaigns in January-February 2017 and 2018. The accuracy and uncertainty of lava surface thermal properties derived from these datasets were determined and compared to evaluate the effect of spatial and spectral

resolution on surface radiance, kinetic temperature, and emissivity. A dual-band mixed pixel separation analysis was conducted to improve the determination of the thermal properties of the molten lava surfaces within a pixel. The ability to acquire accurate thermal properties of an active lava surface at a variety of resolutions can increase the potential for using these measurements for future analysis. For example, by deconvolving the thermal properties of the molten fraction with a mixed pixel, the results can be directly compared between different datasets as there is less dependency on the individual specifications of the datasets. The results revealed that the surface radiance derived from the pixel integrated datasets underestimated the values by up to 2400% and 1000% in the satellite and airborne data, respectively. Similarly, the kinetic temperature and emissivity values were underestimated by up to 250% and 25%, respectively. Comparison between hyperspectral and multispectral airborne data, at similar spatial resolutions, revealed that the impact of spatial resolution on thermal properties was lower in higher spectral resolution data. The thermal mixed pixel separation analysis increased the accuracy of all the derived thermal properties of the molten lava surfaces to within 15% of the expected values. Additionally, the analysis quantified the uncertainty and errors associated with these measurements that can be appropriately propagated into future lava surface analysis. For example, some of these measurements and errors can be integrated into near-real time lava flow propagation models to improve the simulation results and uncertainties. Overall, this analysis evaluated the accuracy of various TIR remote sensing datasets to derive the thermal properties of active lava on the surface and evaluate the importance of combining datasets to gain a more detailed thermal analysis of an entire volcanic system at various resolutions.

The MMT-Cam imaging system was deployed at Kīlauea volcano (Hawai'i) in January-February 2018 to also investigate the thermal budget variability of active lava surfaces at both the lava lake and lava flows. The high spatial and temporal resolution data acquired from cooling lava surfaces provides detailed observations of the fluctuations in lava surfaces during cooling, overturning, breaking out, and propagating. These data provided multispectral information about the lava surfaces in detail that have not been accurately acquired previously. The emissivity measurements improved the temperature and heat flux calculations by directly measuring the efficiency of radiant heat flux with changing temperature and physical state of the lava surfaces. As a consequence, it is likely that previous thermal analysis investigations of active lava surfaces overestimated the total heat flux by at least 20%, if a constant emissivity value was assumed. This study also revealed low- and high- frequency temporal variability in the thermal properties measured or derived at the lava lake with up to 20% and 5% fluctuation from the mean, respectively. The variability was consistent with

visual observations of short and medium term increases in eruption activity, including higher proportion of molten cracks and spattering at the lava lake. The high spatial resolution data revealed the migrations of the crustal surfaces across the lava, highlighting upwelling and downwelling zones. The fraction of melt calculations accurately identified the proportion of crustal plates to molten margins and suggested the proportions remained mostly constant during the entire campaign. In the lava flow observations, the higher spatial resolution multispectral data highlighted subsurface propagation pathways and active breakout fronts, characterized by higher temperatures and heat fluxes. Overall, the ability to acquire multispectral measurements of active lava surfaces *in situ* at high spatiotemporal resolutions improved the accuracy of thermal properties and represented the fluctuation in heat flux in greater detail.

Accurate lava flow propagation modeling provides a vital tool for improving the reliability of hazard assessments of lava flows. The majority of models account for the thermal variability downflow, including heat fluxes. However, typically a constant assumed emissivity value is used to calculate the radiant heat flux which can lead to overestimates and faster cooling rates being simulated. Therefore, a variable emissivity modules dependent on temperature was developed using the MMT-Cam data and incorporated into the PyFLOWGO model to evaluate the effect of accounting for this variability on final runout distance. The module was developed and refined using a small (6.3-meter) channelized breakout lava flow on the coastal plain of Kīlauea volcano. The simulation results revealed that the new variable emissivity module increased the runout distance by ∼5% (0.3 meters) compared to the original PyFLOWGO results. This new module was then used to simulate a 12.47 kilometer lava flow in the Lower East Rift Zone from the fissure 8 lava flow emplacement between May 27 and June 3, 2018. The new module increased the runout distance by 830 meters (∼7%), as a result of lower heat fluxes and slower cooling rates. The model simulation results were validated using ground-truthing data from the MMT-Cam, USGS, and visual observations, demonstrating that the use of the new module within the PyFLOWGO model was able to more accurately simulated the properties in both test cases. The improved estimate in final runout distance (an increase of at least 5%) will have significant impact on the risks a lava flow poses to infrastructure and provides vital extra time for local population and agencies to prepare for lava inundation. Therefore, in the future it is vital to account for emissivity varying in lava flow propagation models that rely strongly on thermal modeling for determining runout distances.

These studies highlighted the importance of accurate high-resolution multispectral TIR data for quantifying the entire thermal regime of an active lava surface to improve the fundamental un-

derstanding of lava dynamics at all scales. A method has been established to acquire multispectral TIR data from the ground either during a campaign or permanently and should be implemented wherever possible at active effusive volcanoes. It is becoming easier and more important to combine multiple TIR datasets to improve understanding of eruption dynamics and precursor activity to reduce hazard risk on local populations during an effusive eruption. These studies provided a methodology for utilizing and directly comparing multiple datasets acquired from the ground, air, and space to improve the overall thermal understanding of the entire volcanic system at a variety of scales. In the future, this can be further improved by installing permanent multispectral TIR instrument surveillance systems at active volcanoes to reconstruct the long-term trends and fluctuations of the volcanic system, to better constrain the background activity of a volcano. Finally, lava flow propagation models can be improved through utilizing more robust thermal models of the radiant heat flux from the lava surface that varies during propagation. The variability in emissivity is likely not consistent for all volcanic systems on Earth. Therefore, laboratory investigations and further ground-based multispectral TIR field studies investigated the variability in emissivity at eruption temperatures are required to more accurately utilize this critical attribute for every lava flow. Overall, this will improve the reliability and accuracy of lava flow propagation models during an eruption and reduce the vulnerability lava flows pose on local populations and infrastructure.

The thermal properties of active lava surfaces vary during propagation and cooling. Therefore, by improving acquisition and analytical techniques of TIR data over multiple resolutions, a better quantification of the variability in thermal properties can be estimated. Lava surfaces are complex mixtures of temperatures and surface physical states that can be difficult to deconvolve, but by improving TIR data acquisition techniques and processing these issues can be reduced. The emissivity of a surface is an important property to consider in thermal calculations and is influenced by numerous factors, but across typical lava eruption temperatures, temperature and physical state are the dominant controls. This causes emissivity to fluctuate by $\sim$30% as lava surfaces cool and form glassy crusts. Previously, this change in emissivity has had limited consideration in lava surface thermal analyses. However, this work has shown that by accounting for this variability, heat flux estimates are reduced by at least 20%, causing an increase in the runout distance simulated by lava propagation models by at least 5%. Overall, by increasing understanding of the thermal radiant emissions from active lava surfaces, more informed hazard assessments are developed and the risk lava flows pose to local populations are reduced.

Appendix A MMT-Cam Calibration Temporal Model

Below is the IDL code used to calculate the model for accounting for internal temperature of the MMT-Cam

```
PRO MMTCAM_CALIBRATION_TEMPORAL_MODEL

;James Thompson
;University of Pittsburgh
;2020

;This code calculates the model for accounting for internal temperature of the A65.

;                 ;;;;;;;;;;;;;;;;;;;;;;;;;;;;;;;;;;;;;;;;;;;;;;;;;;;;;;;;;;;;;;;;;;;

;close all variables
close, /all

;set up colour plotting
device, decomposed=0
loadct, 4

restore, 'Z:\jthompson\FLIR\CALIBRATION\MMT-Cam_temp\TC_template.sav'
TC_A65 = read_ascii('Z:\jthompson\FLIR\CALIBRATION\MMT-Cam_temp\LowGain\TC\
    TemperatureLog[17_30_57][9_27_2018].log', TEMPLATE=TC_template)
TC_A65_1 = TC_A65.field1
TC_A65_2 = TC_A65.field2
TC_BB = read_ascii('Z:\jthompson\FLIR\CALIBRATION\MMT-Cam_temp\LowGain\TC\
    TemperatureLog[17_31_07][9_27_2018].log', TEMPLATE=TC_template)
TC_BB_1 = TC_BB.field1
```

```
TC_BB_2 = TC_BB.field2

temp_time = findgen(121)/60
temp_time_s = findgen(121)

TC_A65_HH = float(strmid(TC_A65_1, 0, 2))
TC_A65_MM = float(strmid(TC_A65_1, 3, 2))
TC_A65_SS = float(strmid(TC_A65_1, 6, 2))
TC_A65_DHH = ((TC_A65_MM/60 ) + (TC_A65_SS/3600))
TC_A65_TIME = (TC_A65_HH + TC_A65_DHH) - (TC_A65_HH(0) + TC_A65_DHH(0))

TC_BB_HH = float(strmid(TC_BB_1, 0, 2))
TC_BB_MM = float(strmid(TC_BB_1, 3, 2))
TC_BB_SS = float(strmid(TC_BB_1, 6, 2))
TC_BB_DHH = ((TC_BB_MM/60) + (TC_BB_SS/3600))
TC_BB_TIME = (TC_BB_HH + TC_BB_DHH) - (TC_BB_HH(0) + TC_BB_DHH(0))

TC_BB_2_s = TS_smooth(TC_BB_2,301)
TC_A65_2_s = TS_smooth(TC_a65_2,61)

TC_BB_time_loc = value_locate(TC_BB_time,temp_time)
TC_BB_2_i = TC_BB_2_s(TC_BB_TIME_loc)
z_TC_BB_2_i = ( TC_BB_2_i - mean(TC_BB_2_i) ) / stddev(TC_BB_2_i)

TC_A65_time_loc = value_locate(TC_A65_time,temp_time)
TC_A65_2_i = TC_A65_2_s(TC_A65_TIME_loc)

time_to_a65_poly4_lowgain = poly_fit(temp_time_s,TC_A65_2_i, 4, yfit=time_a65_yfit)
time_to_a65_poly4_lowgain = reform(time_to_a65_poly4_lowgain)

err = fltarr(121) +0.00001
startpara = [0.D,0.D,0.D]
```

```
a65_to_time_inexp_lowgain = MPFITFUN('myinexp', TC_A65_2_i, temp_time_s, err,startpara,yfit
    =a65_time_yfit)

 file  = strarr(121)
TC_bb_norm = fltarr(121)
temp_data_t = fltarr(640,512,7,121)
temp_data_t_off = fltarr(640,512,7,121)
 all_y_errors  = fltarr(640,512,7,4)

 yfit0  = fltarr(640,512,121)
 yfit1  = fltarr(640,512,121)
 yfit2  = fltarr(640,512,121)
 yfit3  = fltarr(640,512,121)
 yfit4  = fltarr(640,512,121)
 yfit5  = fltarr(640,512,121)
 yfit6  = fltarr(640,512,121)
a65_temp_corr_lin = fltarr(640,512,7,2)

d_TC_A65_2_i = fltarr(40)
d_temp_data_t_off = fltarr(640,512,7,40)
 d_all_y_errors  = fltarr(640,512,7,4)
 d_yfit0  = fltarr(640,512,40)
 d_yfit1  = fltarr(640,512,40)
 d_yfit2  = fltarr(640,512,40)
 d_yfit3  = fltarr(640,512,40)
 d_yfit4  = fltarr(640,512,40)
 d_yfit5  = fltarr(640,512,40)
 d_yfit6  = fltarr(640,512,40)
d_a65_temp_corr_lin = fltarr(640,512,7,2)
 all_pos  = fltarr(40)

;import  tiff
```

```
for t=0, 120 do begin
;tt=t*10
if (t GE 0) and (t LT 10) then begin
tt = t
file(t) = 'Z:\jthompson\FLIR\CALIBRATION\MMT-Cam_temp\LowGain\Data\BB-low
    -00000'+strtrim(string(tt),1)+'.tif'

endif else begin
if (t GE 10) and (t LT 100) then begin
tt = t
file(t) = 'Z:\jthompson\FLIR\CALIBRATION\MMT-Cam_temp\LowGain\Data\BB-low
    -0000'+strtrim(string(tt),1)+'.tif'

endif else begin
if (t GE 100) then begin
tt = t
file(t) = 'Z:\jthompson\FLIR\CALIBRATION\MMT-Cam_temp\LowGain\Data\BB-low
    -000'+strtrim(string(tt),1)+'.tif'

endif

endelse
endelse

qt = query_tiff(file(t), s)
t_n_frames = s.NUM_IMAGES
data_t = uintarr(640,512,t_n_frames)

for i = 0,t_n_frames-1 DO BEGIN
data_t(*,*,i) = read_tiff(file(t), image_index=i)
data_t(*,*,i) = reverse(data_t(*,*,i),2) ;reform the data array so data is in correct
    orientation
```

```
endfor

; define dimensions of picked data
data_dimensions = size(data_t, /L64, /dimensions)
sensorx = data_dimensions(0)
sensory = data_dimensions(1)

;create empty arrays
ref_rad = fltarr(t_n_frames)

;location on data frame to investigate
ref_x = 319
ref_y = 255

;create temporal curves of variables in data
for i=0, t_n_frames-1 do begin
ref_rad(i) = stddev(data_t(*,*,i))
endfor

;ref_rad = ref_rad / (-1)

;sum number of total frames for use with graphs later
s_n_frame = findgen(t_n_frames)

;create kernal (signal template) to convol against the min temp plot to smooth the curve,
;increasing definition of major peaks in curve. Improves peakfinder accuracy and reliability .
kernal = [0,0,1,1,1,1,1,0,0]
convolution = convol(ref_rad, kernal, /normalize)
peak_info = peakfinder(convolution, /opt)

;create peak arrays
n_peaks = n_elements(peak_info(0,*))
```

```
;frames = n_elements(where(peak_info(5,*) GT 5, count)) ;not required
peak_frame = fltarr(n_peaks)
peak_value = fltarr(n_peaks)

;condense peak data so only major peaks remain
peak_y_pos = median(ref_rad) + ((max(ref_rad)-median(ref_rad))/4) ;find peak location in y dim
for i=0, n_peaks-1 do begin
if peak_info(4,i) GT 0.15 then begin ; above 5% significance, applicable for the data because
    it works
peak_frame(i) = peak_info(0,i)
endif

if peak_info(2,i) GT peak_y_pos then begin ;this number is only important for the graphs
peak_value(i) = peak_info(2,i)
endif
endfor
;ignore bad peaks
peak_frame = peak_frame[where(peak_frame NE 0)]
peak_value = peak_value[where(peak_value NE 0)]

;number of filter wheel cycles in data
n_cycles = n_elements(peak_frame)
picked_data_t = fltarr(640,512,(7*(n_cycles-1)))

for i=0, n_cycles-2 do begin
if peak_frame(i+1)-peak_frame(i+0) GE 40 then begin
s_cycle = i
endif
endfor

for i=0,639 do begin
for j=0, 511 do begin
```

```
;pick frames
pick_frame_0 = round(((peak_frame(s_cycle+1)-peak_frame(s_cycle))/7) * 0)
temp_data_t(i,j,0,t) = data_t(i,j,(peak_frame(s_cycle)+pick_frame_0-3))

pick_frame_1 = round(((peak_frame(s_cycle+1)-peak_frame(s_cycle))/7) * 1)
temp_data_t(i,j,1,t) = data_t(i,j,(peak_frame(s_cycle)+pick_frame_1-4))

pick_frame_2 = round(((peak_frame(s_cycle+1)-peak_frame(s_cycle))/7) * 2)
temp_data_t(i,j,2,t) = data_t(i,j,(peak_frame(s_cycle)+pick_frame_2-3))

pick_frame_3 = round(((peak_frame(s_cycle+1)-peak_frame(s_cycle))/7) * 3)
temp_data_t(i,j,3,t) = data_t(i,j,(peak_frame(s_cycle)+pick_frame_3-3))

pick_frame_4 = round(((peak_frame(s_cycle+1)-peak_frame(s_cycle))/7) * 4)
temp_data_t(i,j,4,t) = data_t(i,j,(peak_frame(s_cycle)+pick_frame_4-0))

pick_frame_5 = round(((peak_frame(s_cycle+1)-peak_frame(s_cycle))/7) * 5)
temp_data_t(i,j,5,t) = data_t(i,j,(peak_frame(s_cycle)+pick_frame_5-0))

pick_frame_6 = round(((peak_frame(s_cycle+1)-peak_frame(s_cycle))/7) * 6)
temp_data_t(i,j,6,t) = data_t(i,j,(peak_frame(s_cycle)+pick_frame_6+1))

endfor
endfor

endfor

d_z_TC_BB_2_i = z_TC_BB_2_i(*) - z_TC_BB_2_i(0)

for i=0, 639 do begin
for j=0,511 do begin
```

```
;creat calibrations poly5
temp_data_t_off(i,j,0,*) = temp_data_t(i,j,0,*) - temp_data_t(i,j,0,0)
temp_data_t0 = reform(temp_data_t_off(i,j,0,*))
lin0 = linfit(TC_A65_2_i, temp_data_t0, yfit=yfit, covar=y_errors)
yfit0(i,j,*) = yfit
a65_temp_corr_lin(i,j,0,*) = lin0
All_y_errors(i,j,0,*)=y_errors

temp_data_t_off(i,j,1,*) = temp_data_t(i,j,1,*) - temp_data_t(i,j,1,0)
temp_data_t1 = reform(temp_data_t_off(i,j,1,*))
lin1 = linfit(TC_A65_2_i, temp_data_t1, yfit=yfit, covar=y_errors)
yfit1(i,j,*) = yfit
a65_temp_corr_lin(i,j,1,*) = lin1
All_y_errors(i,j,1,*)=y_errors

temp_data_t_off(i,j,2,*) = temp_data_t(i,j,2,*) - temp_data_t(i,j,2,0)
temp_data_t2 = reform(temp_data_t_off(i,j,2,*))
lin2 = linfit(TC_A65_2_i, temp_data_t2, yfit=yfit, covar=y_errors)
yfit2(i,j,*) = yfit
a65_temp_corr_lin(i,j,2,*) = lin2
All_y_errors(i,j,2,*)=y_errors

temp_data_t_off(i,j,3,*) = temp_data_t(i,j,3,*) - temp_data_t(i,j,3,0)
temp_data_t3 = reform(temp_data_t_off(i,j,3,*))
lin3 = linfit(TC_A65_2_i, temp_data_t3, yfit=yfit, covar=y_errors)
yfit3(i,j,*) = yfit
a65_temp_corr_lin(i,j,3,*) = lin3
All_y_errors(i,j,3,*)=y_errors

temp_data_t_off(i,j,4,*) = temp_data_t(i,j,4,*) - temp_data_t(i,j,4,0)
temp_data_t4 = reform(temp_data_t_off(i,j,4,*))
```

```
lin4 = linfit (TC_A65_2_i, temp_data_t4, yfit=yfit, covar=y_errors)
yfit4(i,j,*) = yfit
a65_temp_corr_lin(i,j,4,*) = lin4
All_y_errors(i,j,4,*)=y_errors

temp_data_t_off(i,j,5,*) = temp_data_t(i,j,5,*) - temp_data_t(i,j,5,0)
temp_data_t5 = reform(temp_data_t_off(i,j,5,*))
lin5 = linfit (TC_A65_2_i, temp_data_t5, yfit=yfit, covar=y_errors)
yfit5(i,j,*) = yfit
a65_temp_corr_lin(i,j,5,*) = lin5
All_y_errors(i,j,5,*)=y_errors

temp_data_t_off(i,j,6,*) = temp_data_t(i,j,6,*) - temp_data_t(i,j,6,0)
temp_data_t6 = reform(temp_data_t_off(i,j,6,*))
lin6 = linfit (TC_A65_2_i, temp_data_t6, yfit=yfit, covar=y_errors)
yfit6(i,j,*) = yfit
a65_temp_corr_lin(i,j,6,*) = lin6
All_y_errors(i,j,6,*)=y_errors

for d=0,39 do begin
d_temp = 23 + (d*0.5)

d_TC_A65_2_i(d) = nearest_element(d_temp, TC_A65_2_i, pos)

d_temp_data_t_off(i,j,0,d) = temp_data_t_off(i,j,0,pos)
d_temp_data_t_off(i,j,1,d) = temp_data_t_off(i,j,1,pos)
d_temp_data_t_off(i,j,2,d) = temp_data_t_off(i,j,2,pos)
d_temp_data_t_off(i,j,3,d) = temp_data_t_off(i,j,3,pos)
d_temp_data_t_off(i,j,4,d) = temp_data_t_off(i,j,4,pos)
d_temp_data_t_off(i,j,5,d) = temp_data_t_off(i,j,5,pos)
d_temp_data_t_off(i,j,6,d) = temp_data_t_off(i,j,6,pos)
```

```
all_pos(d) = pos
endfor

d_temp_data_t0 = reform(d_temp_data_t_off(i,j,0,*))
d_lin0 = linfit(d_TC_A65_2_i, d_temp_data_t0, yfit=yfit, covar=y_errors)
d_yfit0(i,j,*) = yfit
d_a65_temp_corr_lin(i,j,0,*) = d_lin0
d_all_y_errors(i,j,0,*)=y_errors

d_temp_data_t1 = reform(d_temp_data_t_off(i,j,1,*))
d_lin1 = linfit(d_TC_A65_2_i, d_temp_data_t1, yfit=yfit, covar=y_errors)
d_yfit1(i,j,*) = yfit
d_a65_temp_corr_lin(i,j,1,*) = d_lin1
d_all_y_errors(i,j,1,*)=y_errors

d_temp_data_t2 = reform(d_temp_data_t_off(i,j,2,*))
d_lin2 = linfit(d_TC_A65_2_i, d_temp_data_t2, yfit=yfit, covar=y_errors)
d_yfit2(i,j,*) = yfit
d_a65_temp_corr_lin(i,j,2,*) = d_lin2
d_all_y_errors(i,j,2,*)=y_errors

d_temp_data_t3 = reform(d_temp_data_t_off(i,j,3,*))
d_lin3 = linfit(d_TC_A65_2_i, d_temp_data_t3, yfit=yfit, covar=y_errors)
d_yfit3(i,j,*) = yfit
d_a65_temp_corr_lin(i,j,3,*) = d_lin3
d_all_y_errors(i,j,3,*)=y_errors

d_temp_data_t4 = reform(d_temp_data_t_off(i,j,4,*))
d_lin4 = linfit(d_TC_A65_2_i, d_temp_data_t4, yfit=yfit, covar=y_errors)
d_yfit4(i,j,*) = yfit
d_a65_temp_corr_lin(i,j,4,*) = d_lin4
d_all_y_errors(i,j,4,*)=y_errors
```

```
d_temp_data_t5 = reform(d_temp_data_t_off(i,j,5,*) )
d_lin5 = linfit (d_TC_A65_2_i, d_temp_data_t5, yfit=yfit, covar=y_errors)
d_yfit5(i,j,*) = yfit
d_a65_temp_corr_lin(i,j,5,*) = d_lin5
d_all_y_errors (i,j,5,*)=y_errors

d_temp_data_t6 = reform(d_temp_data_t_off(i,j,6,*) )
d_lin6 = linfit (d_TC_A65_2_i, d_temp_data_t6, yfit=yfit, covar=y_errors)
d_yfit6(i,j,*) = yfit
d_a65_temp_corr_lin(i,j,6,*) = d_lin6
d_all_y_errors (i,j,6,*)=y_errors



endfor
endfor
;    ;;;;;;;;;;;;;;;;;;

stop
END
```

Appendix B MMT-Cam Calibration Counts to Radiance Model

Below is the IDL code used calculate the model for converting A65 raw counts data to radiance data. The geometric effects of the instrument are accounted for.

```
PRO MMTCAM_CALIBRATION_COUNTS_TO_RADIANCE_MODEL

;James Thompson
;University of Pittsburgh
;2020

;This code calculates the model for converting A65 raw counts data to radiance data.
;The geometric effects of the instrument are accounted for.

;       ;;;;;;;;;;;;;;;;;;;;;;;;;;;;;;;;

;close all variables
close, /all

;set up colour plotting
device, decomposed=0
loadct, 4

;restore expected radiance values and raw FLIR A65 count values
restore, 'Z:\jthompson\IDL\Calibration\A65\FinalScripts\v2\LowGain\CTR\Constants\
    all_bb_a65_21_cnt_lowgain.sav'
a65_bb = all_bb_a65_21_cnt_lowgain
restore, 'Z:\jthompson\IDL\Calibration\A65\FinalScripts\v2\LowGain\CTR\Constants\
    BB_actual_rad_a65_all_14.sav'
```

```
BB_rad = transpose(BB_actual_rad_a65_all_14)

;build empty arrays for calibration constants and statistics
r2_ctr_poly2_all_a65_21_lowgain = fltarr(640,512,7)
perror_ctr_poly2_all_a65_21_lowgain = fltarr(640,512,7,3)
cons_ctr_poly2_all_a65_21_lowgain = fltarr(640,512,7,3)
allyfitmp_ctr_poly2_lowgain = fltarr(640,512,7,13)

;for loop for calculating the calibration constants and statistics for each pixel and band
    across all temperatures

;i is nth filter
for i=0, 6 do begin
;j is nth column element
for j=0, 639 do begin
;k is nth row element
for k=0, 511 do begin

a_m_rad = a65_bb(j,k,i,*)
a_m_rad = reform(a_m_rad)

;calculate quadratic model between expected radiance values and raw FLIR A65 count values
BB_rad_i = reform(BB_rad(i,*))
mympfit = robust_poly_fit(a_m_rad, BB_rad_i,2,yfit,sig)
cons_ctr_poly2_all_a65_21_lowgain(j,k,i,*) = mympfit

;calculate quadratic model statistics
sst1 = total( (BB_rad_i-mean(BB_rad_i))^2 )
ssr1 = total( (BB_rad_i-yfit)^2 )
r2_ctr_poly2_all_a65_21_lowgain(j,k,i)= 1-(ssr1/sst1)

perror_ctr_poly2_all_a65_21_lowgain(j,k,i,*) = sig
```

```
allyfitmp_ctr_poly2_lowgain(j,k,i,*) = yfit

endfor
endfor
endfor

;save all variables
save, cons_ctr_poly2_all_a65_21_lowgain, filename='Z:\jthompson\IDL\Calibration\A65\
    FinalScripts\v2\LowGain\CTR\Calibration\cons_ctr_poly2_all_a65_21_lowgain.sav'
save, cons_ctr_poly2_all_a65_21_lowgain, filename='Z:\jthompson\IDL\Calibration\A65\
    FinalScripts\v2\LowGain\CTR\Constants\cons_ctr_poly2_all_a65_21_lowgain.sav'
save, perror_ctr_poly2_all_a65_21_lowgain, filename='Z:\jthompson\IDL\Calibration\A65\
    FinalScripts\v2\LowGain\CTR\Calibration\perror_ctr_poly2_all_a65_21_lowgain.sav'
save, r2_ctr_poly2_all_a65_21_lowgain, filename='Z:\jthompson\IDL\Calibration\A65\
    FinalScripts\v2\LowGain\CTR\Calibration\r2_ctr_poly2_all_a65_21_lowgain.sav'
save, allyfitmp_ctr_poly2_lowgain, filename='Z:\jthompson\IDL\Calibration\A65\FinalScripts\
    v2\LowGain\CTR\Calibration\allyfitmp_ctr_poly2_lowgain.sav'

stop
END
```

Appendix C MMT-Cam Calibration

Below is the IDL code to convert MMT-Cam raw counts data to radiance data using the constant defined in the calibration models in Appendices A and B.

```
PRO MMTCAM_CALIBRATION

;James Thompson
;University of Pittsburgh
;2020

;This code converts FLIR A65 raw counts data to radiance data using the constant defined in
     the calibration models.

;                 ;;;;;;;;;;;;;;;;;;;;;;;;;;;;;;;;;;;;;;;;;;;;;;;;;;;;;;;;;;;;;;;;;;;

;close all variables
close, /all

;set up colour plotting
device, decomposed=0
loadct, 4

;
                              ;;;;;;;;;;;;;;;;;;;;;;;;;;;;;;;;;;;;;;;;;;;;;;;;;;;;;;;;;;;;;;;;;;;;;;;;;;;;;;;;;;;;;;;;;;;;;;;;;;;;;;

;input files and variables
;
                              ;;;;;;;;;;;;;;;;;;;;;;;;;;;;;;;;;;;;;;;;;;;;;;;;;;;;;;;;;;;;;;;;;;;;;;;;;;;;;;;;;;;;;;;;;;;;;;;;;;;;;;
```

```
;               ;;;;;;;;;;;;;;;;;;;;;;;;;;;;;;;;;;;;;;;;;;;;;;;;;;;;;;;;;;
; select  working directory containing  all  the  files
input_dir  =  dialog_pickfile (/directory ,  path='Z:\jthompson\Hawaii␣2018', Title='Select␣
    directory␣containing␣all␣the␣files␣to␣be␣processed')

; select  text  file  containing  all  data filenames
filenames_in  =  dialog_pickfile (path=input_dir, FILTER='*.txt',Title='Select␣Filenames␣File')

; select  and input text  file  containing  all   initial  FLIR A65 internal temperatures (celsius)
initial_a65_temp_in  =  dialog_pickfile (path=input_dir, FILTER='*.txt',Title='Select␣initial␣
    FLIR␣A65␣internal␣temperature␣text␣file␣(celsius)')
initial_a65_temp_all  = read_ascii( initial_a65_temp_in )
initial_a65_temp_all  =  initial_a65_temp_all . field1

;input radiance quadratic  calibration  model constants
restore ,  'Z:\jthompson\IDL\Calibration\A65\FinalScripts\v2\LowGain\CTR\Constants\
    cons_ctr_poly2_all_a65_21_lowgain.sav'
cali_con  = cons_ctr_poly2_all_a65_21_lowgain

;input temperature calibration model constants
restore ,  'Z:\jthompson\IDL\Calibration\A65\FinalScripts\v2\LowGain\CTR\Constants\
    a65_temp_corr_lin_r_lowgain.sav'
a65_temp_corr_lin_lowgain = a65_temp_corr_lin_r_lowgain
restore ,  'Z:\jthompson\IDL\Calibration\A65\FinalScripts\v2\LowGain\CTR\Constants\
    a65_to_time_inexp_r_lowgain.sav'
a65_to_time_inexp_lowgain = a65_to_time_inexp_r_lowgain
restore ,  'Z:\jthompson\IDL\Calibration\A65\FinalScripts\v2\LowGain\CTR\Constants\
    time_to_a65_poly5_r_lowgain.sav'
time_to_a65_poly5_lowgain = time_to_a65_poly5_r_lowgain
restore ,  'Z:\jthompson\IDL\Calibration\A65\FinalScripts\v2\LowGain\CTR\Constants\
    a65_to_time_lookup_table_r_lowgain.sav'
```

```
;read and input filenames
OPENR, lun, filenames_in, /GET_LUN
;read one line at a time, saving the result into array
filenames = ''
line = ''
WHILE NOT EOF(lun) DO BEGIN & $
READF, lun, line & $
filenames = [filenames, line] & $
ENDWHILE
;close the file and free the file unit
FREE_LUN, lun
;input filenames into array and define acquisition times
filenames = filenames(1:*)
 n_files    = n_elements(filenames)
  total_cycles_per_file   = fltarr( n_files )
 total_cycles  = 0
 splits  = 0
last_FileDDD = 0
rottime = 2.0 / 86400.0

;start of mega loop to calibrate all files ...
for nf=0, n_files-1 do begin

;select filename for each loop
filenameloc = filenames(nf)
filename = filenameloc
datafilename = filename

;define input tiff files
input = input_dir + filename + '.tif\'
```

```
;define secondary directory
secondary_dir = input_dir + filename + '\'
 file_mkdir , secondary_dir

;define output directory
output_dir = secondary_dir+'Outputs\'
 file_mkdir , output_dir

; select  initial  A65 internal temperature for each loop
initial_a65_temp  =  initial_a65_temp_all (nf)

;import selected  tiff  files  into environment
qt = query_tiff (input, s)
t_n_frames = s.NUM_IMAGES
un_data = uintarr(640,512,t_n_frames)

;build arrays with raw counts data
for i = 0,t_n_frames−1 DO BEGIN
un_data(∗,∗,i) = read_tiff (input, image_index=i)
;reform the data array so data is in correct orientation
un_data(∗,∗,i) = reverse(un_data(∗,∗,i),2)
endfor

;
                              ;;;;;;;;;;;;;;;;;;;;;;;;;;;;;;;;;;;;;;;;;;;;;;;;;;;;;;;;;;;;;;;;;;;;;;;;;;;;;;;;;;;;;;;;;;;;;;;;;;;;;;;;;;;;;;;;;;;

;constants and variables
;
                              ;;;;;;;;;;;;;;;;;;;;;;;;;;;;;;;;;;;;;;;;;;;;;;;;;;;;;;;;;;;;;;;;;;;;;;;;;;;;;;;;;;;;;;;;;;;;;;;;;;;;;;;;;;;;;;;;;;;



;wavelength band centers
```

```
wave = [10.25, 8.04, 8.55, 8.99, 9.55, 10.04, 11.35] * 1e-6

;define radiance constants c1 and c2
c1 = 2 * !CONST.pi * !CONST.h * (!CONST.c^2) * 1e-6
c2 = !CONST.h * ( !CONST.c / !CONST.k )

; define dimensions of input data
data_dimensions = size(un_data, /L64, /dimensions)
sensorx = data_dimensions(0)
sensory = data_dimensions(1)

;
                                    ;;;;;;;;;;;;;;;;;;;;;;;;;;;;;;;;;;;;;;;;;;;;;;;;;;;;;;;;;;;;;;;;;;;;;;;;;;;;;;;;;;;;;;;;;;;;;;;;;;;;

;pick band frames with data stream
;
                                    ;;;;;;;;;;;;;;;;;;;;;;;;;;;;;;;;;;;;;;;;;;;;;;;;;;;;;;;;;;;;;;;;;;;;;;;;;;;;;;;;;;;;;;;;;;;;;;;;;;;;



;create empty arrays
ref_rad = fltarr(t_n_frames)

;location on data frame to investigate
ref_x = 319
ref_y = 255

;create temporal datasets of variables in data
for i=0, t_n_frames-1 do begin
ref_rad(i) = stddev(un_data(*,*,i))
endfor

;sum number of total frames for use with graphs later
```

```
s_n_frame = findgen(t_n_frames)

;create kernal (signal template) to convol against the min temp plot to smooth the curve,
;increasing definition of major peaks in curve. Improves peakfinder accuracy and reliability .
kernal =  [0,1,1,1,1,1,1,1,1,1,0]   ;  [0,0,1,1,1,1,1,1,0,0]
convolution = convol(ref_rad, kernal, /normalize)
peak_info = peakfinder(convolution, /opt)

;create peak arrays
n_peaks = n_elements(peak_info(0,*))
;frames = n_elements(where(peak_info(5,*) GT 5, count)) ;not required
peak_frame = fltarr(n_peaks)
peak_value = fltarr(n_peaks)

;condense peak data so only major peaks remain
peak_y_pos = median(ref_rad) + ((max(ref_rad)-median(ref_rad))/4) ;find peak location in y dim
for i=0, n_peaks-1 do begin
if peak_info(4,i) GE 0.2 then begin ; above 5% significance, applicable for the data because it
      works: 0.2 for LL and 0.2 for LF
peak_frame(i) = peak_info(0,i)
endif

if peak_info(2,i) GT peak_y_pos then begin ;this number is only important for the graphs
peak_value(i) = peak_info(2,i)
endif
endfor
;ignore bad peaks
peak_frame = peak_frame[where(peak_frame NE 0)]
peak_value = peak_value[where(peak_value NE 0)]

;determine if there are incomplete cycles
peak_frame_1 = [peak_frame(1:*),peak_frame(n_elements(peak_frame)-1)+80]
```

```
peak_frame_short = (WHERE(peak_frame_1−peak_frame LT 60, count))
peak_frame_long = (WHERE(peak_frame_1−peak_frame GT 81, count))
peak_frame_wrong = [peak_frame_short,peak_frame_long]
n_peak_frame_wrong = n_elements(peak_frame_wrong)

;peaks per cycle
PPS = 7.0
PPScorrection = 0.0

;number of filter wheel cycles in data
n_cycles = floor(n_elements(peak_frame))
n_points = n_elements(peak_frame) * PPS
picked_data = fltarr(sensorx,sensory,(PPS*(n_cycles)))

; build array of only good frames (average of two frames): bands 0− to PPS
for i=0, n_cycles−2 do begin

index = where( (peak_frame_wrong EQ i), count)
if count EQ 0 then begin
;locate broadband
pick_frame_0 = round(((peak_frame(i+1)−peak_frame(i))/PPS) * 0) +1.0
picked_data(*,*,(0+(PPS*i))) = (un_data(*,*,(peak_frame(i)+pick_frame_0)) )

;locate band 1
pick_frame_1 = round(((peak_frame(i+1)−peak_frame(i))/PPS) * 1) −0.0 +PPScorrection
picked_data(*,*,(1+(PPS*i))) = (un_data(*,*,(peak_frame(i)+pick_frame_1)) )

;locate band 2
pick_frame_2 = round(((peak_frame(i+1)−peak_frame(i))/PPS) * 2) −1.0 +PPScorrection
picked_data(*,*,(2+(PPS*i))) = (un_data(*,*,(peak_frame(i)+pick_frame_2)) )

;locate band 3
```

```
pick_frame_3 = round(((peak_frame(i+1)−peak_frame(i))/PPS) ∗ 3) −2.0 +PPScorrection
picked_data(∗,∗,(3+(PPS∗i))) = (un_data(∗,∗,(peak_frame(i)+pick_frame_3)) )

;locate band 4
pick_frame_4 = round(((peak_frame(i+1)−peak_frame(i))/PPS) ∗ 4) −3.0 +PPScorrection
picked_data(∗,∗,(4+(PPS∗i))) = (un_data(∗,∗,(peak_frame(i)+pick_frame_4)) )

;locate band 5
pick_frame_5 = round(((peak_frame(i+1)−peak_frame(i))/PPS) ∗ 5) −4.0 +PPScorrection
picked_data(∗,∗,(5+(PPS∗i))) = (un_data(∗,∗,(peak_frame(i)+pick_frame_5)) )

;locate band 6
pick_frame_6 = round(((peak_frame(i+1)−peak_frame(i))/PPS) ∗ 6) −5.0 +PPScorrection
picked_data(∗,∗,(6+(PPS∗i))) = (un_data(∗,∗,(peak_frame(i)+pick_frame_6)) )
endif

endfor

; ;; remove bad cycles with incomplete cycles
picked_data_new = picked_data[where(picked_data NE 0)]
picked_data_new_in = WHERE(picked_data_new EQ !values.F_NAN, count)
picked_data_new_in0 = WHERE(picked_data_new EQ 0, count)

;remove first and last cycle (QA/QC)
new_n_points = n_points − ((n_peak_frame_wrong+1)∗PPS)
collate_picked_data_new = fltarr(sensorx,sensory,new_n_points)

;put data stream back into arrays
for i=0, new_n_points−1 do begin
for j=0, sensory−1 do begin
for k=0, sensorx−1 do begin
```

```
xpoint = k
ypoint = j*(sensorx)
zpoint = i*(sensorx)*(sensory)
xyzpoint = xpoint+ypoint+zpoint

collate_picked_data_new(k,j,i) = picked_data_new(xyzpoint)

endfor
endfor
endfor

;put array back ionto original name and check (QA/QC)
picked_data=collate_picked_data_new
new_ref_rad = stddev(stddev(collate_picked_data_new,dimension=1),dimension=1)
new_convolution = convol(new_ref_rad, kernal, /normalize)

;remove first and last cycle (QA/QC) and save all picked data (uncalibrated)
last_band = new_n_points-8
all_picked_un_data = picked_data(*,*,7:last_band)
SAVE, FILENAME = output_dir+datafilename+'_all_picked_un_data.sav', all_picked_un_data

;plot picked data stream and save
w1 = window(dimensions=[800,500])
s_plot = plot(ref_rad, font_size=24, 'k-3', ytitle='$\sigma$_Counts', layout=[1,2,1],yminor
    =1, xminor=1, YTICKLEN=0.02, $
XTICKLEN=0.05,margin=[0.25,0.15,0.15,0.15], /current)
cv_plot = plot(convolution, 'k-3', layout=[1,2,2], font_size=24,xtitle='Frame_Number', ytitle
    ='Convolved!C$\sigma$_Counts', /current,yminor=1, $
xminor=1, YTICKLEN=0.02, XTICKLEN=0.05,margin=[0.25,0.15,0.15,0.15])
cv_plot = plot(new_convolution, 'b-3', /overplot)
signpeakconplot = plot(peak_frame, peak_value, 'o2', sym_color='k', sym_filled=1,
    sym_fill_color='k',/OVERPLOT, NAME='Peak_locations')
```

```
w1.save, output_dir+datafilename+'_datalocations.png', resolution=300
w1.close


;
                              ;;;;;;;;;;;;;;;;;;;;;;;;;;;;;;;;;;;;;;;;;;;;;;;;;;;;;;;;;;;;;;;;;;;;;;;;;;;;;;;;;;;;;;;;;;;;;;;;;;;;;;;;;;;;;;;;;;;;;;;


; calibrate data
;
                              ;;;;;;;;;;;;;;;;;;;;;;;;;;;;;;;;;;;;;;;;;;;;;;;;;;;;;;;;;;;;;;;;;;;;;;;;;;;;;;;;;;;;;;;;;;;;;;;;;;;;;;;;;;;;;;;;;;;;;;;



; define dimensions of picked data
picked_dimensions = size(all_picked_un_data, /L64, /dimensions)
p_n_frames = picked_dimensions(2)
p_n_cycles = floor(p_n_frames/PPS)

; define dimensions of calibration constants
con_dimensions = size(cali_con, /L64, /dimensions)
 cali_picked_rad_data = fltarr(picked_dimensions(0),picked_dimensions(1),picked_dimensions(2))
 cali_picked_rad_data_plus = fltarr(picked_dimensions(0),picked_dimensions(1),picked_dimensions
     (2))
 count_off_all = fltarr(picked_dimensions(0),picked_dimensions(1),picked_dimensions(2))

; calibration loop
; l is nth cycles
for l=0, p_n_cycles-1 do begin

; define internal temperature of A65 for each cycle
 if l EQ 0 then begin
a65_to_time_lookup_table_temp = reform(a65_to_time_lookup_table_r_lowgain(0,*))
a65_to_time_lookup_table_time = reform(a65_to_time_lookup_table_r_lowgain(1,*))

```

```
initial_a65_temp_val  = nearest_element(initial_a65_temp,  a65_to_time_lookup_table_temp,
    temp_index)
a65_to_time = a65_to_time_lookup_table_time(temp_index)

endif
if  l  GT 0 then begin
a65_to_time = a65_to_time + (0.5/60.0) ;minutes
endif
a65_temp = time_to_a65_poly5_lowgain(0) + (time_to_a65_poly5_lowgain(1)*a65_to_time) + (
    time_to_a65_poly5_lowgain(2)*(a65_to_time^2)) + (time_to_a65_poly5_lowgain(3)*(a65_to_time
    ^3)) + (time_to_a65_poly5_lowgain(4)*(a65_to_time^4)) + (time_to_a65_poly5_lowgain(5)*(
    a65_to_time^5))

;  j  is  nth column element
for  j=0, sensorx-1 do begin
;  k  is  nth row element
for  k=0, sensory-1 do begin

;calibrate  broadband
count_off_0  = a65_temp_corr_lin_lowgain(j,k,0,0)  + (A65_temp * a65_temp_corr_lin_lowgain(j,k
    ,0,1))
x0 = all_picked_un_data(j,k,(0+(PPS*l))) - count_off_0
cali_picked_rad_data(j,k,(0+(PPS*l))) =  cali_con(j,k,0,0)  + (cali_con(j,k,0,1)*x0) + (cali_con
    (j,k,0,2)*(x0^2))

;calibrate  band 1
count_off_1  = a65_temp_corr_lin_lowgain(j,k,1,0)  + (A65_temp * a65_temp_corr_lin_lowgain(j,k
    ,1,1))
x1 = all_picked_un_data(j,k,(1+(PPS*l))) - count_off_1
cali_picked_rad_data(j,k,(1+(PPS*l))) = ( cali_con(j,k,1,0)  + (cali_con(j,k,1,1)*x1) + (
    cali_con(j,k,1,2)*(x1^2)) )  *1.2
```

```
; calibrate  band 2
count_off_2  = a65_temp_corr_lin_lowgain(j,k,2,0)  + (A65_temp * a65_temp_corr_lin_lowgain(j,k
    ,2,1))
x2 = all_picked_un_data(j,k,(2+(PPS*l))) - count_off_2
cali_picked_rad_data(j,k,(2+(PPS*l))) =  cali_con(j,k,2,0)  + (cali_con(j,k,2,1)*x2) + (cali_con
    (j,k,2,2)*(x2^2))

; calibrate  band 3
count_off_3  = a65_temp_corr_lin_lowgain(j,k,3,0)  + (A65_temp * a65_temp_corr_lin_lowgain(j,k
    ,3,1))
x3 = all_picked_un_data(j,k,(3+(PPS*l))) - count_off_3
cali_picked_rad_data(j,k,(3+(PPS*l))) =  cali_con(j,k,3,0)  + (cali_con(j,k,3,1)*x3) + (cali_con
    (j,k,3,2)*(x3^2))

; calibrate  band 4
count_off_4  = a65_temp_corr_lin_lowgain(j,k,4,0)  + (A65_temp * a65_temp_corr_lin_lowgain(j,k
    ,4,1))
x4 = all_picked_un_data(j,k,(4+(PPS*l))) - count_off_4
cali_picked_rad_data(j,k,(4+(PPS*l))) =  cali_con(j,k,4,0)  + (cali_con(j,k,4,1)*x4) + (cali_con
    (j,k,4,2)*(x4^2))

; calibrate  band 5
count_off_5  = a65_temp_corr_lin_lowgain(j,k,5,0)  + (A65_temp * a65_temp_corr_lin_lowgain(j,k
    ,5,1))
x5 = all_picked_un_data(j,k,(5+(PPS*l))) - count_off_5
cali_picked_rad_data(j,k,(5+(PPS*l))) =  (cali_con(j,k,5,0)  + (cali_con(j,k,5,1)*x5) + (
    cali_con(j,k,5,2)*(x5^2))) *1.005

; calibrate  band 6
count_off_6  = a65_temp_corr_lin_lowgain(j,k,6,0)  + (A65_temp * a65_temp_corr_lin_lowgain(j,k
    ,6,1))
x6 = all_picked_un_data(j,k,(6+(PPS*l))) - count_off_6
```

```
cali_picked_rad_data(j,k,(6+(PPS*l))) = (cali_con(j,k,6,0) + (cali_con(j,k,6,1)*x6) + (
    cali_con(j,k,6,2)*(x6^2))) * 1.08


;save temperature offset
 count_off_all (j,k,(0+(PPS*l))) = count_off_0
 count_off_all (j,k,(1+(PPS*l))) = count_off_1
 count_off_all (j,k,(2+(PPS*l))) = count_off_2
 count_off_all (j,k,(3+(PPS*l))) = count_off_3
 count_off_all (j,k,(4+(PPS*l))) = count_off_4
 count_off_all (j,k,(5+(PPS*l))) = count_off_5
 count_off_all (j,k,(6+(PPS*l))) = count_off_6


endfor


endfor


initial_a65_temp = a65_temp


endfor


;save calibrated data
 prior_cali_picked_rad_data = cali_picked_rad_data
save, Filename = output_dir+datafilename+'_cali_picked_rad_data.sav', cali_picked_rad_data


;                    ;;;;;;;;;;;;;;;;;;;;;;;;;;;;;;;;;;;;;;;;;;;;;;;;;;;;;;;;;;;;;;;;;;;;;;;;;;;;;;;;
;OUTPUT DATA FOR USE WITH OTHER APPLICATIONS
;                    ;;;;;;;;;;;;;;;;;;;;;;;;;;;;;;;;;;;;;;;;;;;;;;;;;;;;;;;;;;;;;;;;;;;;;;;;;;;;;;;;
;;save calibrated 6-band radiance to bsq file to open in ENVI (including associated header file
    ) for all filters


;create_packet arrays
rad_6_array = fltarr(sensorx,sensory,6,p_n_cycles)
```

```
;create directories
dir_bsq = output_dir+'Cali_Rad\'
file_mkdir, dir_bsq

;Header file template
harris = 'ENVI'
desc = 'description = {}'
samples = 'samples = '+strtrim(string(sensorx),1)
lines = 'lines = '+strtrim(string(sensory),1)
bands = 'bands = 6'
head_off = 'header offset = 0'
f_type = 'file type = ENVI Standard'
d_type = 'data type = 4'
inter = 'interleave = bsq'
s_type = 'sensor type = Unknown'
b_ord = 'byte order = 0'
wave_unit = 'wavelength units = Micrometers'
wave = 'wavelength = {8.040000, 8.550000, 8.990000, 9.550000, 10.040000, 11.350000}'

;create and output packets and header files
for i=0, p_n_cycles-1 do begin
output_filename = dir_bsq+datafilename+'_'+strtrim(string(i+1), 1)+'.bsq'
output_header_filename = dir_bsq+datafilename+'_'+strtrim(string(i+1), 1)+'.hdr'
m = 1+(PPS*i)
n = 6+(PPS*i)
packet = cali_picked_rad_data(*,*,m:n)
rad_6_array(*,*,*, i) = packet
packet(*,*,*)=reverse(packet(*,*,*),2)
openw, unit, output_filename, /get_lun
writeu, unit, packet
free_lun, unit
```

```
openw, unit, output_header_filename, /get_lun
printf, unit, harris
printf, unit, desc
printf, unit, samples
printf, unit, lines
printf, unit, bands
printf, unit, head_off
printf, unit, f_type
printf, unit, d_type
printf, unit, inter
printf, unit, s_type
printf, unit, b_ord
printf, unit, wave_unit
printf, unit, wave
free_lun, unit
close, /all
end

;                      ;;;;;;;;;;;;;;;;;;;;;;;;;;;;;;;;;;;;;;;;;;;;;;;;;;;;;;;;;;;;;;;;;;;;;;;;;;;;
;;save uncalibrated 6-band radiance to bsq file to open in ENVI (including associated header
    file) for all filters

;create_packet arrays
un_rad_6_array = fltarr(sensorx,sensory,6,p_n_cycles)

;create directories
dir_bsq = output_dir+'UnCali_Rad\'
file_mkdir, dir_bsq

;Header file template
harris = 'ENVI'
```

```
desc = 'description = {}'
samples = 'samples = '+strtrim(string(sensorx),1)
lines = 'lines = '+strtrim(string(sensory),1)
bands = 'bands = 6'
head_off = 'header offset = 0'
f_type = ' file type = ENVI Standard'
d_type = 'data type = 4'
inter = 'interleave = bsq'
s_type = 'sensor type = Unknown'
b_ord = 'byte order = 0'
wave_unit = 'wavelength units = Micrometers'
wave = 'wavelength = {8.040000, 8.550000, 8.990000, 9.550000, 10.040000, 11.350000}'

;create and output packets and header files
for i=0, p_n_cycles-1 do begin
output_filename = dir_bsq+datafilename+'_'+strtrim(string(i+1), 1)+'.bsq'
output_header_filename = dir_bsq+datafilename+'_'+strtrim(string(i+1), 1)+'.hdr'
m = 1+(PPS*i)
n = 6+(PPS*i)
packet = all_picked_un_data(*,*,m:n)
un_rad_6_array(*,*,*, i) = packet
packet(*,*,*)=reverse(packet(*,*,*),2)
openw, unit, output_filename, /get_lun
writeu, unit, packet
free_lun, unit

openw, unit, output_header_filename, /get_lun
printf, unit, harris
printf, unit, desc
printf, unit, samples
printf, unit, lines
printf, unit, bands
```

```
printf, unit, head_off
printf, unit, f_type
printf, unit, d_type
printf, unit, inter
printf, unit, s_type
printf, unit, b_ord
printf, unit, wave_unit
printf, unit, wave
free_lun, unit
close, /all
end


;                         ;;;;;;;;;;;;;;;;;;;;;;;;;;;;;;;;;;;;;;;;;;;;;;;;;;;;;;;;;;;;;;;;;;;;;;;;;;;;;;;;
;;save calibrated broadband radiance to bsq file to open in ENVI (including associated header file)


close, /all
;create directories
bbdir_bsq = output_dir+'Broadband_Rad\'
file_mkdir, bbdir_bsq


;Header file template
harris = 'ENVI'
desc = 'description␣=␣{␣}'
samples = 'samples␣=␣'+strtrim(string(sensorx),1)
lines = 'lines␣=␣'+strtrim(string(sensory),1)
bands = 'bands␣=␣1'
head_off = 'header␣offset␣=␣0'
f_type = 'file␣type␣=␣ENVI␣Standard'
d_type = 'data␣type␣=␣4'
inter = 'interleave␣=␣bsq'
s_type = 'sensor␣type␣=␣Unknown'
```

```
b_ord = 'byte_order = 0'
wave_unit = 'wavelength_units = Micrometers'
wave = 'wavelength = {10.25000}'

;create and output packets and header files
for i=0, p_n_cycles-1 do begin
output_filename = bbdir_bsq+datafilename+'_'+strtrim(string(i+1), 1)+'.bsq'
output_header_filename = bbdir_bsq+datafilename+'_'+strtrim(string(i+1), 1)+'.hdr'
m = (PPS*i)
packet = cali_picked_rad_data(*,*,m)
packet(*,*,*)=reverse(packet(*,*,*),2)
openw, unit, output_filename, /get_lun
writeu, unit, packet
free_lun, unit

openw, unit, output_header_filename, /get_lun
printf, unit, harris
printf, unit, desc
printf, unit, samples
printf, unit, lines
printf, unit, bands
printf, unit, head_off
printf, unit, f_type
printf, unit, d_type
printf, unit, inter
printf, unit, s_type
printf, unit, b_ord
printf, unit, wave_unit
printf, unit, wave
free_lun, unit
close, /all
end
```

```
close, /all


;                     ;;;;;;;;;;;;;;;;;;;;;;;;;;;;;;;;;;;;;;;;;;;;;;;;;;;;;;;;;;;;;;;;;;;;;;;;;;;;;;;;
;video outputs
;   ;;;;;;;;;;;
cali_video_data  = cali_picked_rad_data
 file  = output_dir+'caliraddata.mp4'
fps  = 2
oVid = IDLffVideoWrite(file)
vidStream = oVid.AddVideoStream(picked_dimensions(0), picked_dimensions(1), fps)

FOR i=0, picked_dimensions(2)-1 DO BEGIN
images = cali_video_data(*,*, i)
window, 0, XSIZE=sensorx, YSIZE=sensory
tvscl, images
cgcolorbar, /vertical, charsize=1.8, position =[0.1,0.96,0.9,0.98],  textthick=2, title='
    Radiance␣(W.m$\up-2$.sr$\up-1$.'+STRING(181B)+'m$\up-1$)'
frame = TVRD(/TRUE)
time = oVid.Put(vidStream, frame)
ENDFOR
oVid = 0


;   ;;;;;;;;;;;
cali_video_data  = cali_picked_rad_data
 file  = output_dir+'calibbraddata.mp4'
fps  = 2
oVid = IDLffVideoWrite(file)
vidStream = oVid.AddVideoStream(sensorx, sensory, fps)

FOR i=0, p_n_cycles-1 DO BEGIN
images = cali_video_data(*,*,( i*PPS))
```

```
window, 0, XSIZE=sensorx, YSIZE=sensory
tvscl, images
cgcolorbar, /vertical, charsize=1.8, position =[0.1,0.96,0.9,0.98], textthick=2, title='
    Radiance (W.m$\up-2$.sr$\up-1$.'+STRING(181B)+'m$\up-1$)'
frame = TVRD(/TRUE)
time = oVid.Put(vidStream, frame)
ENDFOR
oVid = 0


;  ;;;;;;;;;;;;
picked_video_data = all_picked_un_data
file  = output_dir+'uncaliraddata.mp4'
fps = 2
oVid = IDLffVideoWrite(file)
vidStream = oVid.AddVideoStream(picked_dimensions[0], picked_dimensions[1], fps)

FOR i = 0, picked_dimensions[2]-1 DO BEGIN
images = picked_video_data(*,*,i)
window, 0, XSIZE=sensorx, YSIZE=sensory
tvscl, images
frame = TVRD(/TRUE)
time = oVid.Put(vidStream, frame)
ENDFOR
oVid = 0


;print loop number processed
print, string(nf+1)+' / '+string(n_files)


endfor
;     ;;;;;;;;;;;;;;;;;;;;;;;;;
;end of mega loop
;     ;;;;;;;;;;;;;;;;;;;;;;;;;
```

```
stop
END
```

Appendix D MMT-Cam TES

Below is the IDL code to convert MMT-Cam at-sensor radiance data to surface kinetic temperature and emissivity.

```
PRO MMTCAM_TES

;James Thompson
;University of Pittsburgh
;2020

;This code converts MMT-Cam at-sensor radiance data to surface kinetic temperature and
    emissivity.

;                ;;;;;;;;;;;;;;;;;;;;;;;;;;;;;;;;;;;;;;;;;;;;;;;;;;;;;;;;;;;;;;;;;;;;;;;

;close all variables
close, /all

;set up colour plotting
device, decomposed=0
loadct, 4

;select working directory containing all the files
input_dir = dialog_pickfile (/directory, path='Z:\jthompson\Hawaii_2018\', FILTER='*.sav',
    Title='Select_directory_containing_all_the_files_to_be_processed')

;select text file containing all data filenames
filenames_in = dialog_pickfile (path=input_dir, FILTER='*.txt',Title='Select_Filenames_File')
```

```
; select  atmospheric transmission data
inputatm = dialog_pickfile(FILTER='*.txt',Title='Select transmission file during acquisition',
    PATH=input_dir)
;input atmospheric transmission data
all_data_trans  = read_ascii(inputatm, data_start=23)
all_data_trans  = all_data_trans.field1

; select  and input downwelling radiance data
mess3 = 'Please select the downwelling radiance file. Thank you.'
wm3 = dialog_message(mess3, /CENTER, Title='Downwelling File', /INFORMATION)
input3 =  dialog_pickfile (FILTER='*.sav',Title='Select sav Downwelling File')
restore, input3

; select  and input atmospheric transmission data during downwelling radiance acquisition
mess6 = 'Please select the transmission file during downwelling collection. Thank you.'
wm6 = dialog_message(mess6, /CENTER, Title='transmission file during DWN', /
    INFORMATION)
input6 =  dialog_pickfile (FILTER='*.txt',Title='Select transmission file during DWN')
all_dwn_trans = read_ascii(input6, data_start=23)
all_dwn_trans = all_dwn_trans.field1

;read and input filenames
OPENR, lun, filenames_in, /GET_LUN
;Read one line at a time, saving the result into array
filenames = ''
line = ''
WHILE NOT EOF(lun) DO BEGIN & $
READF, lun, line & $
filenames = [filenames, line] & $
ENDWHILE
;Close the file and free the file unit
FREE_LUN, lun
```

```
filenames  = filenames(1:*)
 n_files    = n_elements(filenames)
  total_cycles_per_file   = fltarr ( n_files )
 total_cycles  = 0
 splits  = 0
last_FileDDD = 0
rottime = 2.0 / 86400.0

; start  of  mega loop to calibrate  all   files  ...
for  nf=0, n_files -1 do begin

; select  filename  for  each loop
filenameloc  = filenames(nf)
filename  = filenameloc
datafilename = filename

; restore  calibrated  radiance data
input1 = input_dir + filename + '\Outputs\'+filename+'_cali_picked_rad_data.sav'
 restore ,  input1

; define  outputs directory
output_dir  = input_dir + filename + '\Outputs\Atm_TES\'
 file_mkdir ,  output_dir

;   ;;;;;;
;max emissivity
emax = 0.999

TIC
;
                                ;;;;;;;;;;;;;;;;;;;;;;;;;;;;;;;;;;;;;;;;;;;;;;;;;;;;;;;;;;;;;;;;;;;;;;;;;;;;;;;;;;;;;;;;;;;;;;;;;;;;;
```

```
;constants and variables
;
                                ;;;;;;;;;;;;;;;;;;;;;;;;;;;;;;;;;;;;;;;;;;;;;;;;;;;;;;;;;;;;;;;;;;;;;;;;;;;;;;;;;;;;;;;;;;;;;;;;;;;;;;;;;;;;;;;;;;;;;;



;Input emin vs MMD coefficients (from MMTCam_MMD_calibration.m)
MMDc = [0.9937, 0.7497, 0.7890]; original

;MMT-Cam Central Bandwidths in microns
wave = [8.04,  8.55,  8.99,  9.55,  10.04,  11.35] * 1e-6;

;Planck  coefficients
c1 = 2 * !CONST.pi * !CONST.h * (!CONST.c^2) * 1e-6 ; W.m-2
c2 = !CONST.h * ( !CONST.c / !CONST.k ) ; um.K

;Number of iterations for  itertively  removing reflected  downwelling radiance
it  = 20


;
                                ;;;;;;;;;;;;;;;;;;;;;;;;;;;;;;;;;;;;;;;;;;;;;;;;;;;;;;;;;;;;;;;;;;;;;;;;;;;;;;;;;;;;;;;;;;;;;;;;;;;;;;;;;;;;;;;;;;;;;;


;define  dimensions of radiance data
rad_dimensions = size(cali_picked_rad_data ,  /L64, /dimensions)
sensorx = rad_dimensions(0)
sensory = rad_dimensions(1)
p_n_frames = rad_dimensions(2)
p_n_cycles  = floor(p_n_frames/7)

;reformate data into  data cube (x,y,bands,cycles),  remove broadband data
all_rad_data6  =  fltarr(sensorx,sensory,6, p_n_cycles)

for p=0, p_n_cycles-1 do begin
```

```
m = 1+(7*p)
n = 6+(7*p)
rad_data = cali_picked_rad_data (*,*, m:n)
all_rad_data6 (*,*,*, p) = rad_data

endfor


;                    ;;;;;;;;;;;;;;;;;;;;;;;;;;;;;;;;;;;;;;;;;;;;;;;;;;;;;;;;;;;;;;;;;;;;;;;;;;;
;      ;;;;;;;;;;;;;;;;;;;;;           Registration            ;;;;;;;;;;;;;;;;;;;;;;;;;;;;;;;;
;                    ;;;;;;;;;;;;;;;;;;;;;;;;;;;;;;;;;;;;;;;;;;;;;;;;;;;;;;;;;;;;;;;;;;;;;;;;;;;
;define arrays and output arrays for band-to-band registration
 cycle_shift  = fltarr (2,6)
 all_shifts  = intarr (2,6, p_n_cycles)
extra_all_rad_data6  = fltarr (sensorx+20,sensory+20,6,p_n_cycles)
 shift_all_rad_data6  = fltarr (sensorx,sensory,6, p_n_cycles)


;
for p=0, p_n_cycles-1 do begin


ref0  = reform(all_rad_data6 (*,*,0, p))
imags0 = reform(all_rad_data6 (*,*,1:5, p))


;define FFT with centroid matching
subreg,  ref0 ,imags0, shifts ,method="X"


 cycle_shift (*,1:5)  = shifts
; all_shifts (*,*, p) =  cycle_shift


for f=0,5 do begin


for xy=0,1 do begin
```

```
if  cycle_shift (xy,f)LE 0 then begin
 cycle_shift (xy,f) = floor( cycle_shift (xy,f))
endif

if  cycle_shift (xy,f)GT 0 then begin
 cycle_shift (xy,f) = ceil( cycle_shift (xy,f))
endif

endfor

; shift  data dur to FFT results
 shift_all_rad_data6 (*,*, f,p) = shift( reform(all_rad_data6 (*,*, f,p)), reform( cycle_shift (0, f)),
       reform( cycle_shift (1, f)) )

endfor

 all_shifts (*,*, p) =  cycle_shift

endfor

;maintain the orginal data
no_reg_all_rad_data6 = all_rad_data6

;make array slightly smaller so no image warping issues
reg_all_rad_data6 = shift_all_rad_data6 (10:629,10:501,*,*)
all_rad_data6 = reg_all_rad_data6

; define dimensions of new radiance data
rad_dimensions = size(all_rad_data6, /L64, /dimensions)
sensorx = rad_dimensions(0)
sensory = rad_dimensions(1)
```

```
p_n_frames = rad_dimensions(2)
 p_n_cycles  = rad_dimensions(3)

print, 'finished ␣band␣to␣band␣co−registration...␣now␣TES␣processing...'

;                  ;;;;;;;;;;;;;;;;;;;;;;;;;;;;;;;;;;;;;;;;;;;;;;;;;;;;;;;;;;;;;;;;;;;;;;;;
;                  ;;;;;;;;;;;;;;;;;;;;;;;;;;;;;;;;;;;;;;;;;;;;;;;;;;;;;;;;;;;;;;;;;;;;;;;;
;                  ;;;;;;;;;;;;;;;;;;;;;;;;;;;;;;;;;;;;;;;;;;;;;;;;;;;;;;;;;;;;;;;;;;;;;;;;

;
                              ;;;;;;;;;;;;;;;;;;;;;;;;;;;;;;;;;;;;;;;;;;;;;;;;;;;;;;;;;;;;;;;;;;;;;;;;;;;;;;;;;;;;;;;;;;;;;;;;;;;;;;

;TES Algorithm
;
                              ;;;;;;;;;;;;;;;;;;;;;;;;;;;;;;;;;;;;;;;;;;;;;;;;;;;;;;;;;;;;;;;;;;;;;;;;;;;;;;;;;;;;;;;;;;;;;;;;;;;;;;


;determine transmissions at MMT−Cam wavelngths

;wave centre
wave_cen = [8.040000,  8.550000,   8.990000,   9.550000, 10.040000, 11.350000]
;wave min
wave_min = [7.790000,  8.300000,  8.740000,   9.300000, 9.790000, 11.100000]
;wave max
wave_max = [8.290000,  8.800000,  9.240000,  9.800000, 10.290000, 11.600000]

;make arrays for TES algorthim outputs
low_rad_trans_index = fltarr (6)
high_rad_trans_index = fltarr (6)
avg_rad_trans = fltarr (6)
surf_atm_radiance = fltarr (sensorx,sensory ,6, p_n_cycles)
 trans_surf_radiance  = fltarr (sensorx,sensory ,6, p_n_cycles)
```

```
it_stop  = fltarr(sensorx,sensory,p_n_cycles)
qa_stop  = fltarr(sensorx,sensory,p_n_cycles)
surf_atm_radiance = fltarr(sensorx,sensory,6,p_n_cycles)
TESemi = fltarr(sensorx,sensory,6,p_n_cycles)
TESemi_s = fltarr(sensorx,sensory,6,p_n_cycles)
NEMemi = fltarr(sensorx,sensory,6,p_n_cycles)
TESLST = fltarr(sensorx,sensory,p_n_cycles)
TESLST_s = fltarr(sensorx,sensory,p_n_cycles)
NEMtemp = fltarr(sensorx,sensory,p_n_cycles)

;define atmospheric transmission for each band
for b=0, 5 do begin

;for radiance data
low_rad_trans_value = nearest_element(wave_min(b), all_data_trans(0,*), minp)
low_rad_trans_index(b) = minp

high_rad_trans_value = nearest_element(wave_max(b), all_data_trans(0,*), maxp)
high_rad_trans_index(b) = maxp

rad_trans_all  = all_data_trans(1 ,minp:maxp)
avg_rad_trans(b) = avg(rad_trans_all)

;for downwelling data
low_dwn_trans_value = nearest_element(wave_min(b), all_dwn_trans(0,*), minp)
low_dwn_trans_index(b) = minp

high_dwn_trans_value = nearest_element(wave_max(b), all_dwn_trans(0,*), maxp)
high_dwn_trans_index(b) = maxp

dwn_trans_all = all_dwn_trans(1 ,minp:maxp)
```

```
avg_dwn_trans(b) = avg(dwn_trans_all)

endfor

for c=0, p_n_cycles-1 do begin
for i=0,sensorx-1 do begin
for j=0,sensory-1 do begin
;for c=0, p_n_cycles-1 do begin

;correct surface radiance for tranmission
trans_surf_radiance(i,j,*,c) = all_rad_data6(i,j,*,c) / avg_rad_trans
surfradin = reform(trans_surf_radiance(i,j,*,c))

;correct irradiance for transmission
trans_avg_all_dwn_rad_6(i,j,*) = avg_all_dwn_rad_6(i,j,*) / avg_dwn_trans
skyradin = reform(trans_avg_all_dwn_rad_6(i,j,*))

;     ;;;;;;;;;;;;;;;;;;;;;
;NEM Module
;     ;;;;;;;;;;;;;;;;;;;;;

R = fltarr(n_elements(wave));
T = fltarr(n_elements(wave));

for b = 0,n_elements(wave)-1 do begin

; Estimate ground-emitted radiance
R(b) = surfradin(b) - ((1-emax)*skyradin(b));

T(b) = (c2/wave(b))*((alog((c1*emax)/(!CONST.pi*R(b)*(wave(b)^5)) + 1))^(-1));

endfor
```

```
; Tnem is the maximum brightness temperature
Tnem = max(T);

; Compute NEM emissivity
e = fltarr(n_elements(wave));
for b = 0,n_elements(wave)-1 do begin

; Compute blackbody radiance using Tnem
Bb = c1/((wave(b)^5)*!CONST.pi*(exp(c2/(wave(b)*Tnem))-1));

; Compute emissivity
e(b) = R(b)/Bb;

endfor

; Iteratively correct for downwelling radiance
Rold = R ;
diffold = [!values.f_nan, !values.f_nan, !values.f_nan];
for k = 0,it-1 do begin

if (k EQ it-2) then QA = 2;

;emax = max(e)
Re = fltarr(n_elements(wave));
Te = fltarr(n_elements(wave));
diff = fltarr(n_elements(wave));

for b = 0,n_elements(wave)-1 do begin
Re(b) = surfradin(b) - ((1-e(b))*skyradin(b));
Te(b) = (c2/wave(b))*((alog((c1*e(b))/(!CONST.pi*Re(b)*(wave(b)^5)) + 1))^(-1))
diff(b) = Re(b) - Rold(b);
```

```
endfor

;compute the delta of corrected radiances - For convergence to occur, it must occur in all
    bands.
lim_dcon = 0.0005 ; originally 0.05 changed to 0.04
dcon = avg(abs(diff)); need to be less than 0.05
if (k GT 1) AND (dcon LT lim_dcon) then QA = 0;
if (k GT 1) AND (dcon LT lim_dcon) then break

;check for divergence
lim_ddiv = 0.0005
ddiv = avg(abs(diff))-avg(abs(diffold));
if (k GT 1) AND (ddiv GT lim_ddiv) then QA = 1
if (k GT 1) AND (ddiv GT lim_ddiv) then break

Tnem = max(Te);

e = fltarr(n_elements(wave));
for b = 0,n_elements(wave)-1 do begin

endfor
Bb = c1/((wave(b)^5)*!CONST.pi*(exp(c2/(wave(b)*Tnem))-1))
e(b) = Re(b)/Bb

endfor

Rold = Re;
diffold = diff;

endfor

ef = e
```

```
Tnemf = Tnem
Reff = Re


;     ;;;;;;;;;;;;;;;;;;;;
; Ratio module
;     ;;;;;;;;;;;;;;;;;;;;

bm = mean(ef);

bbeta = fltarr(n_elements(wave));
for b = 0,n_elements(wave)-1 do begin
bbeta(b) = ef(b)/bm;
endfor

;     ;;;;;;;;;;;;;;;;;;;;
; NEW MMD module modified
;     ;;;;;;;;;;;;;;;;;;;;

MMD = max(bbeta)-min(bbeta);

emin = MMDc(0)-(MMDc(1)*MMD^MMDc(2));

escale = (1 - (emin / bm)) / 2

emisf = fltarr(n_elements(wave));
emisf_s = fltarr(n_elements(wave));
for b = 0,n_elements(wave)-1 do begin
emisf(b) = bbeta(b)*(emin/min(bbeta))
escale_bbeta = (1 - bbeta(b)) * escale
emisf_s(b) = bbeta(b)*((emin/min(bbeta))-escale_bbeta)
endfor
```

```
;      ;;;;;;;;;;;;;;;;;;;;
; Calculate surface temperature
;      ;;;;;;;;;;;;;;;;;;;;

eb = max(emisf, bmax);
LST = (c2/wave(bmax))*((alog((c1*eb)/(!CONST.pi*Reff(bmax)*(wave(bmax)^5)) + 1))^(-1))

;scaled
eb_s = max(emisf_s, bmax_s);
LST_s = (c2/wave(bmax_s))*((alog((c1*eb_s)/(!CONST.pi*Reff(bmax_s)*(wave(bmax_s)^5)) + 1)
     )^(-1))

;           ;;;;;;;;;;;;;;;;;;;;;;;;;;;;;;;;;;;;;;;;
;;End of TES
;           ;;;;;;;;;;;;;;;;;;;;;;;;;;;;;;;;;;;;;;;;


;           ;;;;;;;;;;;;;;;;;;;;;;;;;;;;;;;;;;;;;;;;
;build output arrays
;           ;;;;;;;;;;;;;;;;;;;;;;;;;;;;;;;;;;;;;;;;

;surface radiance - sky irradiance
surf_atm_radiance(i,j,*,c) = R

;TES retrieved emissivity
TESemi(i,j,*,c) = emisf

;NEM emissivity
NEMemi(i,j,*,c) = ef

;TES surface temperature
TESLST(i,j,c) = LST
```

```
;NEM surface temperature
NEMtemp(i,j,c) = Tnemf


;Scaled TES retrieved emissivity
TESemi_s(i,j,*,c) = emisf_s


;Scaled TES surface temperature
TESLST_s(i,j,c) = LST_s
;
;           ;;;;;;;;;;;;;;;;;;;;;;;;;;;;;;;;;;;;;;


endfor
endfor
print, 'processed cycle: '+strtrim(string(c+1),1)+' / '+strtrim(string(p_n_cycles),1)
endfor


print, 'finished processing ... now saving...'


;                      ;;;;;;;;;;;;;;;;;;;;;;;;;;;;;;;;;;;;;;;;;;;;;;;;;;;;;;;;;;;;;;;;;;;;;;;;;;;;;;;;;;;;;;
;           ;;;;;;;;;;;;;;;;;;;;;;;;;;;;;;;;;;;;;;;;;;
;;QA/QC
;           ;;;;;;;;;;;;;;;;;;;;;;;;;;;;;;;;;;;;;;;;;;
; ;;;;  remove erronious data new


for c=0, p_n_cycles-1 do begin


for i=0,sensorx-1 do begin
for j=0,sensory-1 do begin


;greater than


if (TESLST(i,j,c) GT 1500.0) then begin
```

```
TESLST(i,j,c) = !VALUES.F_NAN
TESemi(i,j,*,c) = !VALUES.F_NAN
surf_atm_radiance(i,j,*,c) = !VALUES.F_NAN
endif

if (TESLST_s(i,j,c) GT 1500.0) then begin
TESemi_s(i,j,*,c) = !VALUES.F_NAN
TESLST_s(i,j,c) = !VALUES.F_NAN
endif

if (NEMtemp(i,j,c) GT 1500.0) then begin
NEMtemp(i,j,c) = !VALUES.F_NAN
NEMemi(i,j,*,c) = !VALUES.F_NAN
endif

; Less than

if (TESLST(i,j,c) LT 280.0) then begin
TESLST(i,j,c) = !VALUES.F_NAN
TESemi(i,j,*,c) = !VALUES.F_NAN
surf_atm_radiance(i,j,*,c) = !VALUES.F_NAN
endif

if (TESLST_s(i,j,c) LT 280.0) then begin
TESemi_s(i,j,*,c) = !VALUES.F_NAN
TESLST_s(i,j,c) = !VALUES.F_NAN
endif

if (NEMtemp(i,j,c) LT 280.0) then begin
NEMtemp(i,j,c) = !VALUES.F_NAN
NEMemi(i,j,*,c) = !VALUES.F_NAN
endif
```

```
endfor
endfor
endfor

;                    ;;;;;;;;;;;;;;;;;;;;;;;;;;;;;;;;;;;;;;;;;;;;;;;;;;;;;;;;;;;;;;;;;;;;;;;;;;;;;;;;;
;          ;;;;;;;;;;;;;;;;;;;;;;;;;;;;;;;;;;;;;;
;output data
;          ;;;;;;;;;;;;;;;;;;;;;;;;;;;;;;;;;;;;;;

save, Filename = output_dir+'it_stop.sav', it_stop
save, Filename = output_dir+'qa_stop_qa.sav', qa_stop
save, Filename = output_dir+'TESemi.sav', TESemi
save, Filename = output_dir+'NEMemi.sav', NEMemi
save, Filename = output_dir+'TESLST.sav', TESLST
save, Filename = output_dir+'NEMtemp.sav', NEMtemp
save, Filename = output_dir+'surf_atm_radiance.sav', surf_atm_radiance
save, Filename = output_dir+'TESemi_s.sav', TESemi_s
save, Filename = output_dir+'TESLST_s.sav', TESLST_s

;                    ;;;;;;;;;;;;;;;;;;;;;;;;;;;;;;;;;;;;;;;;;;;;;;;;;;;;;;;;;;;;;;;;;;;;;;;;;;;;;;;;;
;                    ;;;;;;;;;;;;;;;;;;;;;;;;;;;;;;;;;;;;;;;;;;;;;;;;;;;;;;;;;;;;;;;;;;;;;;;;;;;;;;;;;;

;; save rad to bsq file to open in ENVI (including associated header file) for all filters

; create directories
dir_bsq = output_dir+'surf_atm_radiance\'
file_mkdir, dir_bsq

; Header file template
harris = 'ENVI'
desc = 'description␣=␣{␣Atmospherically␣Corrected␣Radiance␣}'
```

```
samples = 'samples = '+strtrim(string(sensorx),1)
lines   = 'lines = '+strtrim(string(sensory),1)
bands = 'bands = 6'
head_off  = 'header offset = 0'
f_type  = ' file type = ENVI Standard'
d_type = 'data type = 4'
inter  = 'interleave = bsq'
s_type  = 'sensor type = Unknown'
b_ord = 'byte order = 0'
wave_unit = 'wavelength units = Micrometers'
wave = 'wavelength = {8.040000,  8.550000,  8.990000,  9.550000, 10.040000, 11.350000}'

; create and output packets and header files
for i=0, p_n_cycles-1 do begin
output_filename = dir_bsq+'TESsar_'+strtrim(string(i+1), 1)+'.bsq'
output_header_filename = dir_bsq+'TESsar_'+strtrim(string(i+1), 1)+'.hdr'
packet = reform(surf_atm_radiance(*,*,*,i))
packet(*,*,*)=reverse(packet(*,*,*),2)
openw, unit, output_filename, /get_lun
writeu, unit, packet
free_lun, unit

openw, unit, output_header_filename, /get_lun
printf, unit, harris
printf, unit, desc
printf, unit, samples
printf, unit, lines
printf, unit, bands
printf, unit, head_off
printf, unit, f_type
printf, unit, d_type
printf, unit, inter
```

```
printf, unit, s_type
printf, unit, b_ord
printf, unit, wave_unit
printf, unit, wave
free_lun, unit
close, /all
endfor
;          ;;;;;;;;;;;;;;;;;;;;;;;;;;;;;;;;;;;;;;;;;;;;;;;;;;

;                ;;;;;;;;;;;;;;;;;;;;;;;;;;;;;;;;;;;;;;;;;;;;;;;;;;;;;;;;;;;;;;;;;;;;;;;;;;;;;;;;
;; save TES to bsq file to open in ENVI (including associated header file) for all filters (if
    aporpriate)

;;TESemi

; create directories
dir_bsq = output_dir+'TESemi\'
file_mkdir, dir_bsq

; Header file template
harris = 'ENVI'
desc = 'description␣=␣{␣TES␣retrieved␣emissivity␣}'
samples = 'samples␣=␣'+strtrim(string(sensorx),1)
lines = 'lines␣=␣'+strtrim(string(sensory),1)
bands = 'bands␣=␣6'
head_off = 'header␣offset␣=␣0'
f_type = 'file␣type␣=␣ENVI␣Standard'
d_type = 'data␣type␣=␣4'
inter = 'interleave␣=␣bsq'
s_type = 'sensor␣type␣=␣Unknown'
b_ord = 'byte␣order␣=␣0'
wave_unit = 'wavelength␣units␣=␣Micrometers'
```

```
wave = 'wavelength␣=␣{8.040000,␣␣8.550000,␣␣8.990000,␣␣9.550000,␣10.040000,␣11.350000}'

; create and output packets and header files
for i=0, p_n_cycles−1 do begin
output_filename = dir_bsq+datafilename+'_'+strtrim(string(i+1), 1)+'.bsq'
output_header_filename = dir_bsq+datafilename+'_'+strtrim(string(i+1), 1)+'.hdr'
packet = reverse(reform(TESemi(∗,∗,∗,i)), 2)
openw, unit, output_filename, /get_lun
writeu, unit, packet
free_lun , unit

openw, unit, output_header_filename, /get_lun
printf, unit, harris
printf, unit, desc
printf, unit, samples
printf, unit, lines
printf, unit, bands
printf, unit, head_off
printf, unit, f_type
printf, unit, d_type
printf, unit, inter
printf, unit, s_type
printf, unit, b_ord
printf, unit, wave_unit
printf, unit, wave
free_lun , unit
close , /all
endfor

;                    ;;;;;;;;;;;;;;;;;;;;;;;;;;;;;;;;;;;;;;;;;;;;;;;;;;;;;;;;;;;;;;;;;;;;;;;;;;;;;;;;;;

;;TES_NEMemi
```

```
; create directories
dir_bsq = output_dir+'NEMemi\'
file_mkdir, dir_bsq

; Header file template
harris = 'ENVI'
desc = 'description = {NEM retrieved emissivity}'
samples = 'samples = '+strtrim(string(sensorx),1)
lines = 'lines = '+strtrim(string(sensory),1)
bands = 'bands = 6'
head_off = 'header offset = 0'
f_type = 'file type = ENVI Standard'
d_type = 'data type = 4'
inter = 'interleave = bsq'
s_type = 'sensor type = Unknown'
b_ord = 'byte order = 0'
wave_unit = 'wavelength units = Micrometers'
wave = 'wavelength = {8.040000, 8.550000, 8.990000, 9.550000, 10.040000, 11.350000}'

; create and output packets and header files
for i=0, p_n_cycles-1 do begin
output_filename = dir_bsq+datafilename+'_'+strtrim(string(i+1), 1)+'.bsq'
output_header_filename = dir_bsq+datafilename+'_'+strtrim(string(i+1), 1)+'.hdr'
packet = reverse(reform(NEMemi(*,*,*,i)), 2)
openw, unit, output_filename, /get_lun
writeu, unit, packet
free_lun, unit

openw, unit, output_header_filename, /get_lun
printf, unit, harris
printf, unit, desc
```

```
printf, unit, samples
printf, unit, lines
printf, unit, bands
printf, unit, head_off
printf, unit, f_type
printf, unit, d_type
printf, unit, inter
printf, unit, s_type
printf, unit, b_ord
printf, unit, wave_unit
printf, unit, wave
free_lun, unit
close, /all
endfor

;                ;;;;;;;;;;;;;;;;;;;;;;;;;;;;;;;;;;;;;;;;;;;;;;;;;;;;;;;;;;;;;;;;;;;;;;;;;;;;;;;;

;;TESLST

; create directories
dir_bsq = output_dir+'TESLST\'
file_mkdir, dir_bsq

; Header file template
harris = 'ENVI'
desc = 'description␣=␣{␣TES␣retrieved␣Land␣Surface␣Temperature␣}'
samples = 'samples␣=␣'+strtrim(string(sensorx),1)
lines = 'lines␣=␣'+strtrim(string(sensory),1)
bands = 'bands␣=␣1'
head_off = 'header␣offset␣=␣0'
f_type = 'file␣type␣=␣ENVI␣Standard'
d_type = 'data␣type␣=␣4'
```

```
inter  = 'interleave␣=␣bsq'
s_type = 'sensor_type␣=␣Unknown'
b_ord = 'byte_order␣=␣0'
wave_unit = 'wavelength_units␣=␣Micrometers'

; create and output packets and header files
for i=0, p_n_cycles−1 do begin
output_filename = dir_bsq+datafilename+'_'+strtrim(string(i+1), 1)+'.bsq'
output_header_filename = dir_bsq+datafilename+'_'+strtrim(string(i+1), 1)+'.hdr'
packet = reverse(reform(TESLST(∗,∗,i)), 2)
openw, unit, output_filename, /get_lun
writeu, unit, packet
 free_lun , unit

openw, unit, output_header_filename, /get_lun
printf, unit, harris
printf, unit, desc
printf, unit, samples
printf, unit, lines
printf, unit, bands
printf, unit, head_off
printf, unit, f_type
printf, unit, d_type
printf, unit, inter
printf, unit, s_type
printf, unit, b_ord
printf, unit, wave_unit
 free_lun , unit
 close , /all
endfor

;                   ;;;;;;;;;;;;;;;;;;;;;;;;;;;;;;;;;;;;;;;;;;;;;;;;;;;;;;;;;;;;;;;;;;;;;;;;;;;;;;;;
```

```
;;NEMtemp

; create directories
dir_bsq = output_dir+'NEMtemp\'
file_mkdir, dir_bsq

; Header file template
harris = 'ENVI'
desc = 'description = {NEM retrieved Temperature}'
samples = 'samples = '+strtrim(string(sensorx),1)
lines = 'lines = '+strtrim(string(sensory),1)
bands = 'bands = 1'
head_off = 'header offset = 0'
f_type = 'file type = ENVI Standard'
d_type = 'data type = 4'
inter = 'interleave = bsq'
s_type = 'sensor type = Unknown'
b_ord = 'byte order = 0'
wave_unit = 'wavelength units = Micrometers'

; create and output packets and header files
for i=0, p_n_cycles-1 do begin
output_filename = dir_bsq+datafilename+'_'+strtrim(string(i+1), 1)+'.bsq'
output_header_filename = dir_bsq+datafilename+'_'+strtrim(string(i+1), 1)+'.hdr'
packet = reverse(reform(NEMtemp(*,*,i)), 2)
openw, unit, output_filename, /get_lun
writeu, unit, packet
free_lun, unit

openw, unit, output_header_filename, /get_lun
printf, unit, harris
```

```
printf, unit, desc
printf, unit, samples
printf, unit, lines
printf, unit, bands
printf, unit, head_off
printf, unit, f_type
printf, unit, d_type
printf, unit, inter
printf, unit, s_type
printf, unit, b_ord
printf, unit, wave_unit
free_lun, unit
close, /all
endfor

;                      ;;;;;;;;;;;;;;;;;;;;;;;;;;;;;;;;;;;;;;;;;;;;;;;;;;;;;;;;;;;;;;;;;;;;;;;;;;;;;;;;;;;;;;;;
;; save Scaled TES to bsq file to open in ENVI (including associated header file) for all filters (if aporpriate)

;;TESemi_s

; create directories
dir_bsq = output_dir+'TESemi_s\'
file_mkdir, dir_bsq

; Header file template
harris = 'ENVI'
desc = 'description␣=␣{␣Scaled␣TES␣retrieved␣emissivity␣}'
samples = 'samples␣=␣'+strtrim(string(sensorx),1)
lines = 'lines␣=␣'+strtrim(string(sensory),1)
bands = 'bands␣=␣6'
head_off = 'header␣offset␣=␣0'
```

```
f_type = ' file type = ENVI Standard'
d_type = 'data type = 4'
inter = 'interleave = bsq'
s_type = 'sensor type = Unknown'
b_ord = 'byte order = 0'
wave_unit = 'wavelength units = Micrometers'
wave = 'wavelength = {8.040000, 8.550000, 8.990000, 9.550000, 10.040000, 11.350000}'

; create and output packets and header files
for i=0, p_n_cycles-1 do begin
output_filename = dir_bsq+datafilename+'_'+strtrim(string(i+1), 1)+'.bsq'
output_header_filename = dir_bsq+datafilename+'_'+strtrim(string(i+1), 1)+'.hdr'
packet = reverse(reform(TESemi_s(*,*,*,i)), 2)
openw, unit, output_filename, /get_lun
writeu, unit, packet
free_lun, unit

openw, unit, output_header_filename, /get_lun
printf, unit, harris
printf, unit, desc
printf, unit, samples
printf, unit, lines
printf, unit, bands
printf, unit, head_off
printf, unit, f_type
printf, unit, d_type
printf, unit, inter
printf, unit, s_type
printf, unit, b_ord
printf, unit, wave_unit
printf, unit, wave
free_lun, unit
```

```
close, /all
endfor


;                    ;;;;;;;;;;;;;;;;;;;;;;;;;;;;;;;;;;;;;;;;;;;;;;;;;;;;;;;;;;;;;;;;;;;;;;;;;;;;;;
;                    ;;;;;;;;;;;;;;;;;;;;;;;;;;;;;;;;;;;;;;;;;;;;;;;;;;;;;;;;;;;;;;;;;;;;;;;;;;;;;;


;;TESLST_s


; create directories
dir_bsq = output_dir+'TESLST_s\'
file_mkdir, dir_bsq


; Header file template
harris = 'ENVI'
desc = 'description␣=␣{␣Scaled␣TES␣retrieved␣Land␣Surface␣Temperature␣}'
samples = 'samples␣=␣'+strtrim(string(sensorx),1)
lines = 'lines␣=␣'+strtrim(string(sensory),1)
bands = 'bands␣=␣1'
head_off = 'header␣offset␣=␣0'
f_type = 'file␣type␣=␣ENVI␣Standard'
d_type = 'data␣type␣=␣4'
inter = 'interleave␣=␣bsq'
s_type = 'sensor␣type␣=␣Unknown'
b_ord = 'byte␣order␣=␣0'
wave_unit = 'wavelength␣units␣=␣Micrometers'


; create and output packets and header files
for i=0, p_n_cycles-1 do begin
output_filename = dir_bsq+datafilename+'_'+strtrim(string(i+1), 1)+'.bsq'
output_header_filename = dir_bsq+datafilename+'_'+strtrim(string(i+1), 1)+'.hdr'
packet = reverse(reform(TESLST_s(*,*,i)), 2)
openw, unit, output_filename, /get_lun
```

```
writeu, unit, packet
free_lun , unit


openw, unit, output_header_filename, /get_lun
printf, unit, harris
printf, unit, desc
printf, unit, samples
printf, unit, lines
printf, unit, bands
printf, unit, head_off
printf, unit, f_type
printf, unit, d_type
printf, unit, inter
printf, unit, s_type
printf, unit, b_ord
printf, unit, wave_unit
free_lun , unit
close , /all
endfor


;                            ;;;;;;;;;;;;;;;;;;;;;;;;;;;;;;;;;;;;;;;;;;;;;;;;;;;;;;;;;;;;;;;;;;;;;;;;;;;;;;;;
;                  ;;;;;;;;;;;;;;;;;;;;;;;;;;;;;;;;;;;;;;;;;;;;;;;;;;;
print, 'done...␣enjoy!'
TOC
print, string(nf+1)+'␣/␣'+string(n_files)
endfor
;end of mega loop
stop
END
```

Appendix E Pixel Size Calculation

Below is the IDL code to calculate the pixel size across the entire FPA of the MMT-Cam.

```
PRO PIXEL_SIZE_CALC

;James Thompson
;University of Pittsburgh
;2020

;This code calculates the pixel size across the entire FPA of the MMT−Cam.

;                 ;;;;;;;;;;;;;;;;;;;;;;;;;;;;;;;;;;;;;;;;;;;;;;;;;;;;;;;;;;;;;;;;;;;

;close all variables
close, /all
;set up colour plotting
device, decomposed=0
loadct, 4

;camera angular field of view
;Bv
cameraVFOV = TextBox(Title='Provide␣VFOV␣of␣camera...', Label='Camera␣VFOV␣(degrees):
    ␣', Cancel=cancelled, XSize=200, Value='37.0')
Bv = float(cameraVFOV)
Bvrad = Bv ∗ ( !const.pi / 180.0 )

;Bh
cameraHFOV = TextBox(Title='Provide␣HFOV␣of␣camera...', Label='Camera␣HFOV␣(degrees):
    ␣', Cancel=cancelled, XSize=200, Value='45.0')
```

```
Bh = float(cameraHFOV)
Bhrad = Bh * ( !const.pi / 180.0 )

;vpixels
cameravpixels = TextBox(Title='Provide number of vertical pixels of camera...', Label='
    Vertical pixels: ', Cancel=cancelled, XSize=200, Value='512.0')
Vpixels = float(cameravpixels)

;hpixels
camerahpixels = TextBox(Title='Provide number of horizontal pixels of camera...', Label='
    Horizontal pixels: ', Cancel=cancelled, XSize=200, Value='640.0')
Hpixels = float(camerahpixels)

;horizontal distance to target
horizontal_distance_to_target = TextBox(Title='Provide horizontal distance to target...',
    Label='Distance (m): ', Cancel=cancelled, XSize=200, Value='270.0')
D = float( horizontal_distance_to_target )

; vertical height above/below target
vertical_height_target = TextBox(Title='Provide vertical height above/below target (negative
    if target below camera)...', Label='Height (m): ', Cancel=cancelled, XSize=200, Value='
    -120.0')
v = float( vertical_height_target )

;output file name
output_filename = TextBox(Title='Provide output file name...', Label='filename: ', Cancel=
    cancelled, XSize=200, Value='LL-033_06_21_24_632_T')



;       ;;;;;;;;;;;;;;;;;;;;;;;;;;;;;;;;;;;;;;;;;;;;
; view angle from camera to target (vertical)
```

```
if v LE 0 then begin
vv = v * (-1)
Orad = atan(D/vv)
endif else begin
if v GT 0 then begin
Orad = atan(D/v)
endif
endelse

rad90 = ( 90.0 / 180.0 ) * !const.pi

;          ;;;;;;;;;;;;;;;;;;;;;;;;;;;;;;;;;;
;IFOV

; vertical  IFOV (radians) a1
VBifov = ( Bvrad / Vpixels )

;horizontal  IFOV (radians) a1
HBifov = ( Bhrad / Hpixels )

;          ;;;;;;;;;;;;;;;;;;;;;;;;;;;;;;;;;;
;pixel  dimensions for  downwards or upwards onto horizontal surface

;build  arrays  to   fill
VLp = fltarr(Hpixels,Vpixels)
HLp = fltarr(Hpixels,Vpixels)



xcenter  = round(Hpixels/2.0)
ycenter  = round(Vpixels/2.0)

for x=0, Hpixels-1 do begin
```

```
for y=0,Vpixels-1 do begin

DVpixels = y - ycenter
DHpixels = x - xcenter

;dowdwards pixels away from center pixel
;for pixels in y (V)
if v LE 0 then begin
;make no negative
vv = v * (-1)
VOO0 = (Orad)
;near field
if DVpixels LT 0 then begin
;make no negative
;number of pixels from center
NDVpixels = DVpixels * (-1)
;pixel increment angle
Va0 = VBifov * NDVpixels
;angle from camera to pixel
VOOn = VOO0 - Va0
;Line-of-sight to middle of pixel
VDlos = vv / cos(VOOn)
;pixel vertical demensions
VLinner = vv * tan(VOOn-(VBifov/2))
VLouter = vv * tan(VOOn+(VBifov/2))
VLp(x,y) = VLouter - VLinner

;do for pixels in x axis (H)
;to left of center (<320)
if DHpixels LT 0 then begin
;make no negative
;number of pixels from center
```

```
NDHpixels = DHpixels * (-1)
;pixel increment angle
Ha0 = HBifov * NDHpixels
;angle from camera to pixel horizontal
HOOn = Ha0
;pixel horizontal demensions
HLinner = VDlos * tan(HOOn-(HBifov/2))
HLouter = VDlos * tan(HOOn+(HBifov/2))
HLp(x,y) = HLouter - HLinner
endif else begin
;to right of center (>320)
if DHpixels GE 0 then begin
;make no negative
;number of pixels from center
NDHpixels = DHpixels
;increment angle to pixel
Ha0 = HBifov * NDHpixels
;angle from camera to pixel horizontal
HOOn = Ha0
;pixel horizontal demensions
HLinner = VDlos * tan(HOOn-(HBifov/2))
HLouter = VDlos * tan(HOOn+(HBifov/2))
HLp(x,y) = HLouter - HLinner
endif
endelse

endif else begin
;far field
if DVpixels GE 0 then begin
;pixel increment angle
Va0 = VBifov * DVpixels
;angle from camera to pixel
```

```
VOOfr = VOO0 + Va0
;Line-of-sight to middle of pixel
VDlos = vv / cos(VOOfr)
;pixel vertical demensions
VLinner = vv * tan(VOOfr-(VBifov/2))
VLouter = vv * tan(VOOfr+(VBifov/2))
VLp(x,y) = VLouter - VLinner

;do for pixels in x axis (H)
;to left of center (<320)
if DHpixels LT 0 then begin
;make no negative
;number of pixels from center
NDHpixels = DHpixels * (-1)
;pixel increment angle
Ha0 = HBifov * NDHpixels
;angle from camera to pixel horizontal
HOOn = Ha0
;pixel horizontal demensions
HLinner = VDlos * tan(HOOn-(HBifov/2))
HLouter = VDlos * tan(HOOn+(HBifov/2))
HLp(x,y) = HLouter - HLinner
endif else begin
;to right of center (>320)
if DHpixels GE 0 then begin
;make no negative
;number of pixels from center
NDHpixels = DHpixels
;pixel increment angle
Ha0 = HBifov * NDHpixels
;angle from camera to pixel horizontal
HOOn = Ha0
```

```
;pixel horizontal demensions
HLinner = VDlos * tan(HOOn-(HBifov/2))
HLouter = VDlos * tan(HOOn+(HBifov/2))
HLp(x,y) = HLouter - HLinner
endif
endelse

endif
endelse

endif else begin
;upwards pixels away from center pixel
;for pixels in y (V)
if v GE 0 then begin
VO0 = rad90 - Orad
;near field
if DVpixels LT 0 then begin
;make no negative
;number of pixels from center
NDVpixels = DVpixels * (-1)
;pixel increment angle
Va0 = VBifov * NDVpixels
;angle from camera to pixel
VOn = VO0 - Va0
;Line-of-sight to middle of pixel
VDlos = D / cos(VOn)
;pixel vertical demensions
VLinner = D * tan(VOn-(VBifov/2))
VLouter = D * tan(VOn+(VBifov/2))
VLp(x,y) = VLouter - VLinner

;do for pixels in x axis (H)
```

```
;to left of center (<320)
if DHpixels LT 0 then begin
;make no negative
;number of pixels from center
NDHpixels = DHpixels * (-1)
;pixel increment angle
Ha0 = HBifov * NDHpixels
;angle from camera to pixel horizontal
HOOn = Ha0
;pixel horizontal demensions
HLinner = VDlos * tan(HOOn-(HBifov/2))
HLouter = VDlos * tan(HOOn+(HBifov/2))
HLp(x,y) = HLouter - HLinner
endif else begin
;to right of center (>320)
if DHpixels GE 0 then begin
;make no negative
;number of pixels from center
NDHpixels = DHpixels
;pixel increment angle
Ha0 = HBifov * NDHpixels
;angle from camera to pixel horizontal
HOOn = Ha0
;pixel horizontal demensions
HLinner = VDlos * tan(HOOn-(HBifov/2))
HLouter = VDlos * tan(HOOn+(HBifov/2))
HLp(x,y) = HLouter - HLinner
endif
endelse



endif else begin
```

```
;far  field
if  DVpixels GE 0 then begin
;pixel  increment angle
Va0 = VBifov * DVpixels
;angle  from camera to pixel
VOfr = VO0 + Va0
;Line-of-sight to middle of pixel
VDlos = D / cos(VOfr)
;pixel  vertical  demensions
VLinner = D * tan(VOfr-(VBifov/2))
VLouter = D * tan(VOfr+(VBifov/2))
VLp(x,y) = VLouter - VLinner

;do for  pixels  in  x axis  (H)
;to  left  of  center  (<320)
if  DHpixels LT 0 then begin
;make no negative
;number of pixels from center
NDHpixels = DHpixels * (-1)
;pixel  increment angle
Ha0 = HBifov * NDHpixels
;angle  from camera to pixel horizontal
HOOn = Ha0
;pixel  horizontal  demensions
HLinner = VDlos * tan(HOOn-(HBifov/2))
HLouter = VDlos * tan(HOOn+(HBifov/2))
HLp(x,y) = HLouter - HLinner
endif else begin
;to  right  of  center  (>320)
if  DHpixels GE 0 then begin
;make no negative
;number of pixels from center
```

```
NDHpixels = DHpixels
;pixel increment angle
Ha0 = HBifov * NDHpixels
;angle from camera to pixel horizontal
HOOn = Ha0
;pixel horizontal demensions
HLinner = VDlos * tan(HOOn-(HBifov/2))
HLouter = VDlos * tan(HOOn+(HBifov/2))
HLp(x,y) = HLouter - HLinner
endif
endelse

endif
endelse
endif
endelse



endfor
endfor

pixelarea = VLp * HLp

;       ;;;;;;;;;;;;;;;;;;;;;;;;;;;;;;;;;;;;;;;;;;;;
output_dir = 'Z:\jthompson\FLIR\pixelsize\'

w1 = window(dimensions=[1000,768])
im2 = image(pixelarea, RGB_TABLE=4, POSITION=[0,0,1,1], FONT_SIZE=24,
    BACKGROUND_TRANSPARENCY=100, /current)
c2 = colorbar(target=im2,orientation=0, POSITION=[0.12,0.945,0.9,0.965], TITLE='Pixel area
    (meters)',FONT_SIZE=20, TEXTPOS = 0, $
TICKDIR = 0,BORDER_ON = 1,FONT_STYLE = 'Italic', thick=2, COLOR='white')
```

```
w1.save, output_dir+output_filename+'_pixelarea_heatmap.png', resolution=300
;           ;;;;;;;;;;;;;;;;;;;;;;;;;;;;;;;;;;;


save, Filename = output_dir+output_filename+'_pixelarea.sav', pixelarea
save, Filename = output_dir+output_filename+'_verticalpixelsize.sav', VLp
save, Filename = output_dir+output_filename+'_horizontalpixelsize.sav', HLp


stop
END
```

Appendix F Thermal Quantitative Analysis

Below is the IDL code to calculate the thermal properties of a lava surface (lakes or flows) from surface kinetic temperature and emissivity

```
PRO THERMAL_QUANT_ANALYSIS

;James Thompson
;University of Pittsburgh
;2020

;This code calculates the thermal properties of a lava surface (lakes or flows) from surface
    kinetic temperature and emissivity.
;Some additional geometric and atmospheric parameters and properties are also required.

;       ;;;;;;;;;;;;;;;;;;;;;;;;;;;;;;;;

;close all variables
close, /all
;set up colour plotting
device, decomposed=0
loadct, 4

;       ;;;;;;;;;;;;;;;;;;;;;;;;;;;;;;;;
;constants
;       ;;;;;;;;;;;;;;;;;;;;;;;;;;;;;;;;

;Stefan-boltzmann constant
SBC = !const.sigma
```

```
;       ;;;;;;;;;;;;;;;;;;;;;;;;;;;;;;;;
;; select  and input datasets
;       ;;;;;;;;;;;;;;;;;;;;;;;;;;;;;;;;

; select  and input area of  pixel
pixel_area_data  =  dialog_pickfile (path='Z:\jthompson\FLIR\pixelsize\', FILTER='*.sav', Title
    ='Select area of pixel file')
restore ,  pixel_area_data

; select  and input air  properties  and parameters
airlookup = read_csv('Z:\jthompson\IDL\airlookup.csv', header=lookupheader, n_table_header
    =3, table_header=lookuptableheader)

;get  a  user  defined  ambient temperature for time of analysis
ambient_air_temp = TextBox(Title='Provide ambient air temperature...', Label='Temperaure (
    Kelvin): ', Cancel=cancelled, XSize=200, Value='299.0')
Ta = float(ambient_air_temp)

;get  a  user  defined  country rock temperature
country_rock_temp = TextBox(Title='Provide country rock temperature...', Label='Temperaure
    (Kelvin): ', Cancel=cancelled, XSize=200, Value='295.0')
Tcr = float(country_rock_temp)

;get  a  user  defined  wind speed at time of  analysis
windspeed = TextBox(Title='Provide Wind Speed...', Label='Wind Speed (m/s): ', Cancel=
    cancelled, XSize=200, Value='2.6')
WS = float(windspeed)

;get  a  user  defined  thickness  of  the  layer  of  hot  air  overlying  lava
thickness_hot_air  = TextBox(Title='Thickness of the layer of hot air overlying lava ... ' ,
    Label='Thickness (m): ', Cancel=cancelled, XSize=200, Value='1.5')
H = float( thickness_hot_air )
```

```
;get a user defined width of lava over which the wind blows
width_lava = TextBox(Title='Width of lava over which the wind blows ...', Label='Width(m): '
    , Cancel=cancelled, XSize=200, Value='5.0')
L = float(width_lava)

;is this lava lake data
mess8 = 'Is this lava lake data?.'
lavalakeq = dialog_message(mess8, /CENTER, Title='Is this lava lake data?', /question)

;select working directory
input_dir = dialog_pickfile(/directory, path='z:\jthompson\Hawaii 2018\LavaLake', FILTER=
    '*.sav', Title='Select directory containing all the processed files')

;;read and input filenames
filenames_in = input_dir+'filenames3.txt'
OPENR, lun, filenames_in, /GET_LUN
; Read one line at a time, saving the result into array
filenames = ''
line = ''
WHILE NOT EOF(lun) DO BEGIN & $
READF, lun, line & $
filenames = [filenames, line] & $
ENDWHILE
; Close the file and free the file unit
FREE_LUN, lun
filenames = filenames(1:*)
 n_files  = n_elements(filenames)

;       ;;;;;;;;;;;;;;;;;;;;;;;;;;;;;;;
;Define and select ROI from last data
;       ;;;;;;;;;;;;;;;;;;;;;;;;;;;;;;;
```

```
ex_filename = filenames( n_files -1)
ex_data_dir = input_dir + ex_filename+'\Outputs\Atm_TES\'

;ex_radiance
 ex_surf_atm_radiance_file  = ex_data_dir+'surf_atm_radiance.sav'
restore,  ex_surf_atm_radiance_file

example_image = surf_atm_radiance(*,*,0,0)
XROI, example_image, Regions_Out=ROI, /Block
ROImask = ROI -> ComputeMask(Dimensions=Size(example_image, /Dimensions), Mask_Rule
    =2)
Obj_Destroy, ROI
;apply to all data sets
roiexampleimage = example_image * (ROImask GT 0)

;start big loop for calculating thermal parameters
for nf=0, n_files -1 do begin

;select filename for each loop
filename = filenames(nf)
data_dir = input_dir + filename+'\Outputs\Atm_TES\'

;restore surface radiance data
 surf_atm_radiance_file  = data_dir+'surf_atm_radiance.sav'
restore,  surf_atm_radiance_file

;determine data dimensions
data_dimensions = size(surf_atm_radiance, /L64, /DIMENSIONS)
sensorx = data_dimensions(0)
sensory = data_dimensions(1)
bands = data_dimensions(2)
```

```
p_n_cycles = data_dimensions(3)

;average surface radiance
avg_surf_atm_radiance = avg(surf_atm_radiance,2)

;Input TES emissivity and average 6-point
TESemi_s_file = data_dir + 'TESemi_s.sav'
restore, TESemi_s_file
avgTESemi_s = avg(TESemi_s,2)

;;Input TES temperature and average 6-point
LST_s_file = data_dir + 'TESLST_s.sav'
restore, LST_s_file
Ts = TESLST_s

;define output directory
output_dir = data_dir+'TQA\'
file_mkdir, output_dir

;     ;;;;;;;;;;;;;;;;;;;;;;;;
;heat flux calculations
;     ;;;;;;;;;;;;;;;;;;;;;;;;

;define arrays
Tmax = fltarr(sensorx,sensory,p_n_cycles)
Tmin = fltarr(sensorx,sensory,p_n_cycles)
fm = fltarr(sensorx,sensory,p_n_cycles)

;define fraction of melt
for k=0, p_n_cycles-1 do begin
c_min = min(Ts(*,*,k), /NAN)
for i=0, sensorx-1 do begin
```

```
for j=0, sensory-1 do begin

Tmax = 1500.0
Tmin = c_min

;fraction of melt
fm(i,j,k) = (Ts(i,j,k)-tmin) / (tmax-Tmin)
if fm(i,j,k) GE 1.0 then fm(i,j,k)=1.0

endfor
endfor
endfor

;radiative heat flux density
Mrad = avgTESemi_s * !const.sigma * ( (Ts^4) - (Ta^4) )
;Mrad = avgNEMemi * !const.sigma * ( (Ts^4) - (Ta^4) )

;radiative heat flux
Orad = fltarr(sensorx,sensory,p_n_cycles)
for k=0, p_n_cycles-1 do begin
Orad(*,*,k) = Mrad(*,*,k) * pixelarea
endfor

;       ;;;;;;;;;;;;;;;;;;;;;;;;;
;Heat transfer coefficent
;       ;;;;;;;;;;;;;;;;;;;;;;;;;

;temperature of boundary layer above lava
Tbound = (Ts + Ta)/2

roiTbound = fltarr(sensorx,sensory,p_n_cycles)
for k=0, p_n_cycles-1 do begin
```

```
roiTbound(*,*,k) = Tbound(*,*,k) * (ROImask GT 0)
endfor

roiTbound[WHERE(roiTbound EQ 0, /NULL)] = !VALUES.F_NAN
Tboundavg = avg(roiTbound, /nan)

;determine air values using lookup table
lookup_temp =  nearest_element(Tboundavg, airlookup.field1, lookup_index)
vair  = airlookup.field5(lookup_index)
aair  = airlookup.field7(lookup_index)
kair  = airlookup.field6(lookup_index)

if WS EQ 0.0 then begin
;free convection (windless)
; B is bouyancy
B = 1.0/Ts

; Grashof # = ratio buoyancy to viscosity
; vair is air viscosity
Gr = ( (!const.gn * B ) * (Ts-Ta) * (H^3)) / (vair^2)
;     ;;;;;;;;;;;;;;;;;;     check brackets      ;;;;;;;;;;;;;;;;;;;;;;;;

; Prandtl #
; vair is air viscosity  ;aair is thermal diffusivity
Pr = vair / aair

;rayleigh number
Ra = Gr * Pr

;
Nu = 0.16 * (Ra^(1/3))
```

```
;heat transfer coefficent
; kair is thermal conductivity of air ;H is layer of hot air
hc = (kair * Nu)/H

endif else begin

;Reynolds # = ratio of inertial to viscous forces
;W is wind speed and L is length ; vair is air viscosity
Re = (WS * L) / vair

; Prandtl #
; vair is air viscosity ;aair is thermal diffusivity
Pr = vair / aair

RePr = Re * Pr

if (RePr GT 100.0) then begin

Nu = ( 0.3387 * (Prˆ(0.3)) * (Reˆ(0.5)) ) / ( ( 1 + ((0.0468 / Pr)ˆ(0.67)) )ˆ(0.25) )

endif else begin

Nu = 0.332 * (Prˆ(0.3)) * (Reˆ(0.5))
endelse


;heat transfer coefficent
;kair is thermal conductivity of air ;H is layer of hot air
hc = (kair * Nu)/H

endelse
```

```
;      ;;;;;;;;;;;;;;;;;;;;

;convection heat flux density
Mconv = fltarr(sensorx,sensory,p_n_cycles)
Oconv = fltarr(sensorx,sensory,p_n_cycles)
OcondB = fltarr(sensorx,sensory,p_n_cycles)
for k=0, p_n_cycles-1 do begin
Mconv(*,*,k) = Hc * (Ts(*,*,k)-Ta)
Oconv(*,*,k) = Mconv(*,*,k) * pixelarea
endfor

if lavalakeq EQ 'No' then begin

;      ;;;;;;;;;;;;;;;;;;;;
;conductive heat flux density (basal)

;rock thermal diffusivity
;k is thermal conductivity, p is denisty, cp is specific heat capacity
basalpha = ( k / p ) * Cp

;bask is thermal conductivity
bask = 1.5
time=2.0
;basalpha is rock thermal diffusivity , t is time (secs)
deltah = sqrt(basalpha * !const.pi * time)
deltaTemp = Ts-Tcr

;conductive heat flux density (basal)
McondB = -bask *(deltaTemp / deltah)

Oconv = fltarr(sensorx,sensory,p_n_cycles)
for k=0, p_n_cycles-1 do begin
```

```
OcondB(*,*,k) = McondB(*,*,k) * pixelarea
endfor

;     ;;;;;;;;;;;;;;;;;;;;
;total heat flux density
Mtot = McondB + Mconv + Mrad

;total heat flux
Otot = OcondB + Oconv + Orad

endif else begin
;     ;;;;;;;;;;;;;;;;;;;;
;conductive heat flux density (surface)

;     ;;;;;;;;;;;;;;;;;;;;
;total heat flux density
Mtot = Mconv + Mrad

;total heat flux
Otot = Oconv + Orad

endelse

;          ;;;;;;;;;;;;;;;;;;;;;;;;;;;;;;;;;;;;;;;;;;;;;;;;;;;;;;;;;;;
;OUTPUT
;          ;;;;;;;;;;;;;;;;;;;;;;;;;;;;;;;;;;;;;;;;;;;;;;;;;;;;;;;;;;;

;build arrays for ROI values to fill

roifm = fltarr(sensorx,sensory,p_n_cycles)
roiMrad = fltarr(sensorx,sensory,p_n_cycles)
roiOrad = fltarr(sensorx,sensory,p_n_cycles)
```

```
roiMconv = fltarr(sensorx,sensory, p_n_cycles)
roiOconv = fltarr(sensorx,sensory, p_n_cycles)
roiMtot = fltarr(sensorx,sensory, p_n_cycles)
roiOtot = fltarr(sensorx,sensory, p_n_cycles)
roiTESemi_s = fltarr(sensorx,sensory,6, p_n_cycles)
roiavgTESemi_s = fltarr(sensorx,sensory,p_n_cycles)
roiTESemi = fltarr(sensorx,sensory,6, p_n_cycles)
roiavgTESemi = fltarr(sensorx,sensory,p_n_cycles)
roiNEMemi = fltarr(sensorx,sensory,6,p_n_cycles)
roiavgNEMemi = fltarr(sensorx,sensory,p_n_cycles)
roiTESLST_s = fltarr(sensorx,sensory,p_n_cycles)
roiTESLST = fltarr(sensorx,sensory,p_n_cycles)
roiNEMtemp = fltarr(sensorx,sensory,p_n_cycles)
roisurfatmradiance = fltarr(sensorx,sensory,6, p_n_cycles)
roiavgsurfatmradiance = fltarr(sensorx,sensory, p_n_cycles)
roipixelarea = fltarr(sensorx,sensory, p_n_cycles)

; fill  ROI arrays
for k=0, p_n_cycles-1 do begin
roifm(*,*,k) = fm(*,*,k) * (ROImask GT 0)
roiMrad(*,*,k) = mrad(*,*,k) * (ROImask GT 0);  ;;;;;;;;;;;;;;;;;;;;
roiOrad(*,*,k) = orad(*,*,k) * (ROImask GT 0);  ;;;;;;;;;;;;;;;;;;;;
roiMconv(*,*,k) = Mconv(*,*,k) * (ROImask GT 0); ;;;;;;;;;;;;;
roiOconv(*,*,k) = oconv(*,*,k) * (ROImask GT 0); ;;;;;;;;;;;;;
roiMtot(*,*,k) = Mtot(*,*,k) * (ROImask GT 0); ;;;;;;;;;;;;;;;
roiOtot(*,*,k) = otot(*,*,k) * (ROImask GT 0); ;;;;;;;;;;;;;
roiavgTESemi_s(*,*,k) = avgTESemi_s(*,*,k) * (ROImask GT 0);;;;;;;;;;;;;;;
roiavgTESemi(*,*,k) = avgTESemi(*,*,k) * (ROImask GT 0);;;;;;;;;;;;;;;
roiavgNEMemi(*,*,k) = avgNEMemi(*,*,k) * (ROImask GT 0);;;;;;;;;;;;;;;
roiTESLST_s(*,*,k) = TESLST_s(*,*,k) * (ROImask GT 0)
roiTESLST(*,*,k) = TESLST(*,*,k) * (ROImask GT 0)
roiNEMtemp(*,*,k) = NEMtemp(*,*,k) * (ROImask GT 0)
```

```
roipixelarea (*,*,k) = pixelarea(*,*) * (ROImask GT 0)
;roiLSTavg(*,*,k) = all_avgtemp(*,*,k) * (ROImask GT 0)
roiavgsurfatmradiance(*,*,k) = avg_surf_atm_radiance(*,*,k) * (ROImask GT 0)
for p=0, 5 do begin
roiTESemi_s(*,*,p,k) = TESemi_s(*,*,p,k) * (ROImask GT 0)
roiTESemi(*,*,p,k) = TESemi(*,*,p,k) * (ROImask GT 0)
roiNEMemi(*,*,p,k) = NEMemi(*,*,p,k) * (ROImask GT 0)
roisurfatmradiance(*,*,p,k) = surf_atm_radiance(*,*,p,k) * (ROImask GT 0)

endfor
endfor

;save outputs
file_mkdir, output_dir+'ROI\'
save, Filename = output_dir+'ROI\'+filenames(nf)+'_ROIfm.sav', ROIfm
save, Filename = output_dir+'ROI\'+filenames(nf)+'_ROITESemi_s.sav', ROITESemi_s
save, Filename = output_dir+'ROI\'+filenames(nf)+'_ROITESemi.sav', ROITESemi
save, Filename = output_dir+'ROI\'+filenames(nf)+'_ROINEMemi.sav', ROINEMemi
save, Filename = output_dir+'ROI\'+filenames(nf)+'_ROIavgTESemi_s.sav', ROIavgTESemi_s
save, Filename = output_dir+'ROI\'+filenames(nf)+'_ROIavgTESemi.sav', ROIavgTESemi
save, Filename = output_dir+'ROI\'+filenames(nf)+'_ROIavgNEMemi.sav', ROIavgNEMemi
save, Filename = output_dir+'ROI\'+filenames(nf)+'_ROITESLST_s.sav', ROITESLST_s
save, Filename = output_dir+'ROI\'+filenames(nf)+'_ROITESLST.sav', ROITESLST
save, Filename = output_dir+'ROI\'+filenames(nf)+'_ROINEMtemp.sav', ROINEMtemp
save, Filename = output_dir+'ROI\'+filenames(nf)+'_roipixelarea.sav', roipixelarea
save, Filename = output_dir+'ROI\'+filenames(nf)+'_ROIsurfatmradiance.sav',
    roisurfatmradiance
save, Filename = output_dir+'ROI\'+filenames(nf)+'_ROIavgsurfatmradiance.sav',
    roiavgsurfatmradiance
save, Filename = output_dir+'ROI\'+filenames(nf)+'_ROIMrad.sav', roiMrad
save, Filename = output_dir+'ROI\'+filenames(nf)+'_ROIOrad.sav', roiOrad
save, Filename = output_dir+'ROI\'+filenames(nf)+'_ROIMconv.sav', roiMconv
```

```
save, Filename = output_dir+'ROI\'+filenames(nf)+'_ROIOconv.sav', roiOconv
save, Filename = output_dir+'ROI\'+filenames(nf)+'_ROIMtot.sav', roiMtot
save, Filename = output_dir+'ROI\'+filenames(nf)+'_ROIOtot.sav', roiOtot

;calculate averages
avgroiMrad = avg(avg(roiMrad, 0), 0)
avgroiOrad = avg(avg(roiOrad, 0), 0)
avgroiMconv = avg(avg(roiMconv, 0), 0)
avgroiOconv = avg(avg(roiOconv, 0), 0)
avgroiMtot = avg(avg(roiMtot, 0), 0)
avgroiOtot = avg(avg(roiOtot, 0), 0)
avgROITESLST_s = avg(avg(ROITESLST_s, 0), 0)
avgROITESLST = avg(avg(ROITESLST, 0), 0)
avgROINEMtemp = avg(avg(ROINEMtemp, 0), 0)
avgROIfm = avg(avg(ROIfm, 0), 0)
avgroiavgsurfatmradiance = avg(avg(roiavgsurfatmradiance, 0), 0)
avgroisurfatmradiance = avg(avg(roisurfatmradiance, 0), 0)

file_mkdir, output_dir+'AVG\'
save, Filename = output_dir+'AVG\'+filenames(nf)+'_avgROIMrad.sav', avgroiMrad
save, Filename = output_dir+'AVG\'+filenames(nf)+'_avgROIOrad.sav', avgroiOrad
save, Filename = output_dir+'AVG\'+filenames(nf)+'_avgROIMconv.sav', avgroiMconv
save, Filename = output_dir+'AVG\'+filenames(nf)+'_avgROIOconv.sav', avgroiOconv
save, Filename = output_dir+'AVG\'+filenames(nf)+'_avgROIMtot.sav', avgroiMtot
save, Filename = output_dir+'AVG\'+filenames(nf)+'_avgROIOtot.sav', avgroiOtot
save, Filename = output_dir+'AVG\'+filenames(nf)+'_avgROIavgsurfatmradiance.sav',
    avgroiavgsurfatmradiance
save, Filename = output_dir+'AVG\'+filenames(nf)+'_avgROIsurfatmradiance.sav',
    avgroisurfatmradiance
save, Filename = output_dir+'AVG\'+filenames(nf)+'_avgROITESLST_s.sav',
    avgROITESLST_s
save, Filename = output_dir+'AVG\'+filenames(nf)+'_avgROITESLST.sav', avgROITESLST
```

```
save, Filename = output_dir+'AVG\'+filenames(nf)+'_avgROINEMtemp.sav', avgROINEMtemp
save, Filename = output_dir+'AVG\'+filenames(nf)+'_avgROIfm.sav', avgROIfm

;save to bsq files
;       ;;;;;;;;;;;;;;;;;;;;;;;;;;;;;;;;
;; save TQA to bsq file to open in ENVI (including associated header file) for all filters (if
    aporpriate)

; ;; radiative heat flux density
; ;Mrad

; create directories
dir_bsq = output_dir+'Mrad\'
file_mkdir, dir_bsq

save, Filename = dir_bsq+filenames(nf)+'_Mrad.sav', Mrad

;Header file template
harris = 'ENVI'
desc = 'description = {radiative heat flux density (plus)}'
samples = 'samples = '+strtrim(string(sensorx),1)
lines = 'lines = '+strtrim(string(sensory),1)
bands = 'bands = 1'
head_off = 'header offset = 0'
f_type = 'file type = ENVI Standard'
d_type = 'data type = 4'
inter = 'interleave = bsq'
s_type = 'sensor type = Unknown'
b_ord = 'byte order = 0'
wave_unit = 'wavelength units = Micrometers'

; create and output packets and header files
```

```
for i=0, p_n_cycles-1 do begin
output_filename = dir_bsq+filenames(nf)+'_Mrad_'+strtrim(string(i+1), 1)+'.bsq'
output_header_filename = dir_bsq+filenames(nf)+'_Mrad_'+strtrim(string(i+1), 1)+'.hdr'
packet = reverse(reform(Mrad(*,*,i)), 2)
openw, unit, output_filename, /get_lun
writeu, unit, packet
free_lun, unit

openw, unit, output_header_filename, /get_lun
printf, unit, harris
printf, unit, desc
printf, unit, samples
printf, unit, lines
printf, unit, bands
printf, unit, head_off
printf, unit, f_type
printf, unit, d_type
printf, unit, inter
printf, unit, s_type
printf, unit, b_ord
printf, unit, wave_unit
free_lun, unit
close, /all
end

save, Filename = dir_bsq+filenames(nf)+'_roiMrad.sav', roiMrad
save, Filename = dir_bsq+filenames(nf)+'_avgroiMrad.sav', avgroiMrad

; Header file template
harris = 'ENVI'
desc = 'description = { radiative heat flux density (plus) (roi) }'
samples = 'samples = '+strtrim(string(sensorx),1)
```

```
lines = 'lines = '+strtrim(string(sensory),1)
bands = 'bands = 1'
head_off = 'header offset = 0'
f_type = ' file type = ENVI Standard'
d_type = 'data type = 4'
inter = 'interleave = bsq'
s_type = 'sensor type = Unknown'
b_ord = 'byte order = 0'
wave_unit = 'wavelength units = Micrometers'

; create and output packets and header files
for i=0, p_n_cycles-1 do begin
output_filename = dir_bsq+filenames(nf)+'_roiMrad_'+strtrim(string(i+1), 1)+'.bsq'
output_header_filename = dir_bsq+filenames(nf)+'_roiMrad_'+strtrim(string(i+1), 1)+'.hdr'
packet = reverse(reform(roiMrad(*,*,i)), 2)
openw, unit, output_filename, /get_lun
writeu, unit, packet
free_lun, unit

openw, unit, output_header_filename, /get_lun
printf, unit, harris
printf, unit, desc
printf, unit, samples
printf, unit, lines
printf, unit, bands
printf, unit, head_off
printf, unit, f_type
printf, unit, d_type
printf, unit, inter
printf, unit, s_type
printf, unit, b_ord
printf, unit, wave_unit
```

```
free_lun, unit
close, /all
end

;   ;;;;;;;;;;;
;;;; radiative heat flux
;;Orad
;
; create directories
dir_bsq = output_dir+'Orad\'
file_mkdir, dir_bsq

save, Filename = dir_bsq+filenames(nf)+'_Orad.sav', Orad

; Header file template
harris = 'ENVI'
desc = 'description = {radiative heat flux (plus)}'
samples = 'samples = '+strtrim(string(sensorx),1)
lines = 'lines = '+strtrim(string(sensory),1)
bands = 'bands = 1'
head_off = 'header offset = 0'
f_type = 'file type = ENVI Standard'
d_type = 'data type = 4'
inter = 'interleave = bsq'
s_type = 'sensor type = Unknown'
b_ord = 'byte order = 0'
wave_unit = 'wavelength units = Micrometers'

; create and output packets and header files
for i=0, p_n_cycles-1 do begin
output_filename = dir_bsq+filenames(nf)+'_Orad_'+strtrim(string(i+1), 1)+'.bsq'
output_header_filename = dir_bsq+filenames(nf)+'_Orad_'+strtrim(string(i+1), 1)+'.hdr'
```

```
packet = reverse(reform(Orad(*,*,i)), 2)
openw, unit, output_filename, /get_lun
writeu, unit, packet
free_lun, unit

openw, unit, output_header_filename, /get_lun
printf, unit, harris
printf, unit, desc
printf, unit, samples
printf, unit, lines
printf, unit, bands
printf, unit, head_off
printf, unit, f_type
printf, unit, d_type
printf, unit, inter
printf, unit, s_type
printf, unit, b_ord
printf, unit, wave_unit
free_lun, unit
close, /all
end

save, Filename = dir_bsq+filenames(nf)+'_roiOrad.sav', roiOrad
save, Filename = dir_bsq+filenames(nf)+'_avgroiOrad.sav', avgroiOrad

; Header file template
harris = 'ENVI'
desc = 'description = {radiative heat flux (plus) (roi) }'
samples = 'samples = '+strtrim(string(sensorx),1)
lines = 'lines = '+strtrim(string(sensory),1)
bands = 'bands = 1'
head_off = 'header offset = 0'
```

```
f_type = 'file type = ENVI Standard'
d_type = 'data type = 4'
inter = 'interleave = bsq'
s_type = 'sensor type = Unknown'
b_ord = 'byte order = 0'
wave_unit = 'wavelength units = Micrometers'

; create and output packets and header files
for i=0, p_n_cycles-1 do begin
output_filename = dir_bsq+filenames(nf)+'_roiOrad_'+strtrim(string(i+1), 1)+'.bsq'
output_header_filename = dir_bsq+filenames(nf)+'_roiOrad_'+strtrim(string(i+1), 1)+'.hdr'
packet = reverse(reform(roiOrad(*,*,i)), 2)
openw, unit, output_filename, /get_lun
writeu, unit, packet
free_lun, unit

openw, unit, output_header_filename, /get_lun
printf, unit, harris
printf, unit, desc
printf, unit, samples
printf, unit, lines
printf, unit, bands
printf, unit, head_off
printf, unit, f_type
printf, unit, d_type
printf, unit, inter
printf, unit, s_type
printf, unit, b_ord
printf, unit, wave_unit
free_lun, unit
close, /all
end
```

```
;   ;;;;;;;;;;;
; ;;; Melt fraction
; ;fm
;
; create directories
dir_bsq = output_dir+'fm\'
file_mkdir, dir_bsq

save, Filename = dir_bsq+filenames(nf)+'_fm.sav', fm

; Header file template
harris = 'ENVI'
desc = 'description = {Melt fraction (plus)}'
samples = 'samples = '+strtrim(string(sensorx),1)
lines = 'lines = '+strtrim(string(sensory),1)
bands = 'bands = 1'
head_off = 'header offset = 0'
f_type = ' file type = ENVI Standard'
d_type = 'data type = 4'
inter = 'interleave = bsq'
s_type = 'sensor type = Unknown'
b_ord = 'byte order = 0'
wave_unit = 'wavelength units = Micrometers'

; create and output packets and header files
for i=0, p_n_cycles-1 do begin
output_filename = dir_bsq+filenames(nf)+'_fm_'+strtrim(string(i+1), 1)+'.bsq'
output_header_filename = dir_bsq+filenames(nf)+'_fm_'+strtrim(string(i+1), 1)+'.hdr'
packet = reverse(reform(fm(*,*,i)), 2)
openw, unit, output_filename, /get_lun
writeu, unit, packet
```

```
free_lun, unit

openw, unit, output_header_filename, /get_lun
printf, unit, harris
printf, unit, desc
printf, unit, samples
printf, unit, lines
printf, unit, bands
printf, unit, head_off
printf, unit, f_type
printf, unit, d_type
printf, unit, inter
printf, unit, s_type
printf, unit, b_ord
printf, unit, wave_unit
free_lun, unit
close, /all
end

save, Filename = dir_bsq+filenames(nf)+'_roifm.sav', roifm

; Header file template
harris = 'ENVI'
desc = 'description = {Melt fraction (plus) (roi)}'
samples = 'samples = '+strtrim(string(sensorx),1)
lines = 'lines = '+strtrim(string(sensory),1)
bands = 'bands = 1'
head_off = 'header offset = 0'
f_type = 'file type = ENVI Standard'
d_type = 'data type = 4'
inter = 'interleave = bsq'
s_type = 'sensor type = Unknown'
```

```
b_ord = 'byte_order_=_0'
wave_unit = 'wavelength_units_=_Micrometers'

; create and output packets and header files
for i=0, p_n_cycles-1 do begin
output_filename = dir_bsq+filenames(nf)+'_roifm_'+strtrim(string(i+1), 1)+'.bsq'
output_header_filename = dir_bsq+filenames(nf)+'_roifm_'+strtrim(string(i+1), 1)+'.hdr'
packet = reverse(reform(roifm(*,*,i)), 2)
openw, unit, output_filename, /get_lun
writeu, unit, packet
free_lun, unit

openw, unit, output_header_filename, /get_lun
printf, unit, harris
printf, unit, desc
printf, unit, samples
printf, unit, lines
printf, unit, bands
printf, unit, head_off
printf, unit, f_type
printf, unit, d_type
printf, unit, inter
printf, unit, s_type
printf, unit, b_ord
printf, unit, wave_unit
free_lun, unit
close, /all
end

;;;convection flux density
;;Mconv
```

```
; create directories
dir_bsq = output_dir+'Mconv\'
file_mkdir, dir_bsq

save, Filename = dir_bsq+filenames(nf)+'_Mconv.sav', Mconv
save, Filename = dir_bsq+filenames(nf)+'_Mconv.sav', Mconv

; Header file template
harris = 'ENVI'
desc = 'description = { convection heat flux density (plus) }'
samples = 'samples = '+strtrim(string(sensorx),1)
lines = 'lines = '+strtrim(string(sensory),1)
bands = 'bands = 1'
head_off = 'header offset = 0'
f_type = ' file type = ENVI Standard'
d_type = 'data type = 4'
inter = 'interleave = bsq'
s_type = 'sensor type = Unknown'
b_ord = 'byte order = 0'
wave_unit = 'wavelength units = Micrometers'

; create and output packets and header files
for i=0, p_n_cycles-1 do begin
output_filename = dir_bsq+filenames(nf)+'_Mconv_'+strtrim(string(i+1), 1)+'.bsq'
output_header_filename = dir_bsq+filenames(nf)+'_Mconv_'+strtrim(string(i+1), 1)+'.hdr'
packet = reverse(reform(Mconv(*,*,i)), 2)
openw, unit, output_filename, /get_lun
writeu, unit, packet
free_lun, unit

openw, unit, output_header_filename, /get_lun
printf, unit, harris
```

```
printf, unit, desc
printf, unit, samples
printf, unit, lines
printf, unit, bands
printf, unit, head_off
printf, unit, f_type
printf, unit, d_type
printf, unit, inter
printf, unit, s_type
printf, unit, b_ord
printf, unit, wave_unit
free_lun, unit
close, /all
end

save, Filename = dir_bsq+filenames(nf)+'_roiMconv.sav', roiMconv
save, Filename = dir_bsq+filenames(nf)+'_avgroiMconv.sav', avgroiMconv

; Header file template
harris = 'ENVI'
desc = 'description = {convection heat flux density (plus) (roi)}'
samples = 'samples = '+strtrim(string(sensorx),1)
lines = 'lines = '+strtrim(string(sensory),1)
bands = 'bands = 1'
head_off = 'header offset = 0'
f_type = 'file type = ENVI Standard'
d_type = 'data type = 4'
inter = 'interleave = bsq'
s_type = 'sensor type = Unknown'
b_ord = 'byte order = 0'
wave_unit = 'wavelength units = Micrometers'
```

```
; create and output packets and header files
for i=0, p_n_cycles-1 do begin
output_filename = dir_bsq+filenames(nf)+'_roiMconv_'+strtrim(string(i+1), 1)+'.bsq'
output_header_filename = dir_bsq+filenames(nf)+'_roiMconv_'+strtrim(string(i+1), 1)+'.hdr'
packet = reverse(reform(roiMconv(*,*,i)), 2)
openw, unit, output_filename, /get_lun
writeu, unit, packet
free_lun, unit

openw, unit, output_header_filename, /get_lun
printf, unit, harris
printf, unit, desc
printf, unit, samples
printf, unit, lines
printf, unit, bands
printf, unit, head_off
printf, unit, f_type
printf, unit, d_type
printf, unit, inter
printf, unit, s_type
printf, unit, b_ord
printf, unit, wave_unit
free_lun, unit
close, /all
end

;  ;;;;;;;;;;;
; ;;; convection heat flux
;;Oconv
;
; create directories
dir_bsq = output_dir+'Oconv\'
```

```
file_mkdir, dir_bsq

save, Filename = dir_bsq+filenames(nf)+'_Oconv.sav', Oconv

; Header file template
harris = 'ENVI'
desc = 'description = {convection heat flux (plus)}'
samples = 'samples = '+strtrim(string(sensorx),1)
lines = 'lines = '+strtrim(string(sensory),1)
bands = 'bands = 1'
head_off = 'header offset = 0'
f_type = 'file type = ENVI Standard'
d_type = 'data type = 4'
inter = 'interleave = bsq'
s_type = 'sensor type = Unknown'
b_ord = 'byte order = 0'
wave_unit = 'wavelength units = Micrometers'

; create and output packets and header files
for i=0, p_n_cycles-1 do begin
output_filename = dir_bsq+filenames(nf)+'_Oconv_'+strtrim(string(i+1), 1)+'.bsq'
output_header_filename = dir_bsq+filenames(nf)+'_Oconv_'+strtrim(string(i+1), 1)+'.hdr'
packet = reverse(reform(Oconv(*,*,i)), 2)
openw, unit, output_filename, /get_lun
writeu, unit, packet
free_lun, unit

openw, unit, output_header_filename, /get_lun
printf, unit, harris
printf, unit, desc
printf, unit, samples
printf, unit, lines
```

```
printf, unit, bands
printf, unit, head_off
printf, unit, f_type
printf, unit, d_type
printf, unit, inter
printf, unit, s_type
printf, unit, b_ord
printf, unit, wave_unit
free_lun, unit
close, /all
end

save, Filename = dir_bsq+filenames(nf)+'_roiOconv.sav', roiOconv
save, Filename = dir_bsq+filenames(nf)+'_avgroiOconv.sav', avgroiOconv

; Header file template
harris = 'ENVI'
desc = 'description = {convection heat flux (plus) (roi)}'
samples = 'samples = '+strtrim(string(sensorx),1)
lines = 'lines = '+strtrim(string(sensory),1)
bands = 'bands = 1'
head_off = 'header offset = 0'
f_type = ' file type = ENVI Standard'
d_type = 'data type = 4'
inter = 'interleave = bsq'
s_type = 'sensor type = Unknown'
b_ord = 'byte order = 0'
wave_unit = 'wavelength units = Micrometers'

; create and output packets and header files
for i=0, p_n_cycles-1 do begin
output_filename = dir_bsq+filenames(nf)+'_roiOconv_'+strtrim(string(i+1), 1)+'.bsq'
```

```
output_header_filename = dir_bsq+filenames(nf)+'_roiOconv_'+strtrim(string(i+1), 1)+'.hdr'
packet = reverse(reform(roiOconv(*,*,i)), 2)
openw, unit, output_filename, /get_lun
writeu, unit, packet
free_lun, unit

openw, unit, output_header_filename, /get_lun
printf, unit, harris
printf, unit, desc
printf, unit, samples
printf, unit, lines
printf, unit, bands
printf, unit, head_off
printf, unit, f_type
printf, unit, d_type
printf, unit, inter
printf, unit, s_type
printf, unit, b_ord
printf, unit, wave_unit
free_lun, unit
close, /all
end

;;; total flux density
;;Mtot

; create directories
dir_bsq = output_dir+'Mtot\'
file_mkdir, dir_bsq

save, Filename = dir_bsq+filenames(nf)+'_Mctot.sav', Mtot
```

```
; Header file template
harris = 'ENVI'
desc = 'description = { Total heat flux density (plus) }'
samples = 'samples = '+strtrim(string(sensorx),1)
lines = 'lines = '+strtrim(string(sensory),1)
bands = 'bands = 1'
head_off = 'header offset = 0'
f_type = ' file type = ENVI Standard'
d_type = 'data type = 4'
inter = 'interleave = bsq'
s_type = 'sensor type = Unknown'
b_ord = 'byte order = 0'
wave_unit = 'wavelength units = Micrometers'

; create and output packets and header files
for i=0, p_n_cycles-1 do begin
output_filename = dir_bsq+filenames(nf)+'_Mtot_'+strtrim(string(i+1), 1)+'.bsq'
output_header_filename = dir_bsq+filenames(nf)+'_Mtot_'+strtrim(string(i+1), 1)+'.hdr'
packet = reverse(reform(Mtot(*,*,i)), 2)
openw, unit, output_filename, /get_lun
writeu, unit, packet
free_lun, unit

openw, unit, output_header_filename, /get_lun
printf, unit, harris
printf, unit, desc
printf, unit, samples
printf, unit, lines
printf, unit, bands
printf, unit, head_off
printf, unit, f_type
printf, unit, d_type
```

```
printf, unit, inter
printf, unit, s_type
printf, unit, b_ord
printf, unit, wave_unit
free_lun, unit
close, /all
end

save, Filename = dir_bsq+filenames(nf)+'_roiMtot.sav', roiMtot
save, Filename = dir_bsq+filenames(nf)+'_avgroiMtot.sav', avgroiMtot

; Header file template
harris = 'ENVI'
desc = 'description = { Total heat flux density  (plus) (roi) }'
samples = 'samples = '+strtrim(string(sensorx),1)
lines = 'lines = '+strtrim(string(sensory),1)
bands = 'bands = 1'
head_off = 'header offset = 0'
f_type = ' file type = ENVI Standard'
d_type = 'data type = 4'
inter = 'interleave = bsq'
s_type = 'sensor type = Unknown'
b_ord = 'byte order = 0'
wave_unit = 'wavelength units = Micrometers'

; create and output packets and header files
for i=0, p_n_cycles-1 do begin
output_filename = dir_bsq+filenames(nf)+'_roiMtot_'+strtrim(string(i+1), 1)+'.bsq'
output_header_filename = dir_bsq+filenames(nf)+'_roiMtot_'+strtrim(string(i+1), 1)+'.hdr'
packet = reverse(reform(roiMtot(*,*,i)), 2)
openw, unit, output_filename, /get_lun
writeu, unit, packet
```

```
free_lun , unit

openw, unit, output_header_filename, /get_lun
printf, unit, harris
printf, unit, desc
printf, unit, samples
printf, unit, lines
printf, unit, bands
printf, unit, head_off
printf, unit, f_type
printf, unit, d_type
printf, unit, inter
printf, unit, s_type
printf, unit, b_ord
printf, unit, wave_unit
free_lun , unit
close , /all
end

;   ;;;;;;;;;;;;
; ;;; total heat flux
;;Otot
;
; create directories
dir_bsq = output_dir+'Otot\'
file_mkdir , dir_bsq

save, Filename = dir_bsq+filenames(nf)+'_Otot.sav', Otot

; Header file template
harris = 'ENVI'
desc = 'description = { Total heat flux (plus) }'
```

```
samples = 'samples = '+strtrim(string(sensorx),1)
lines   = 'lines = '+strtrim(string(sensory),1)
bands = 'bands = 1'
head_off  = 'header offset = 0'
f_type  = ' file type = ENVI Standard'
d_type = 'data type = 4'
inter  = 'interleave = bsq'
s_type  = 'sensor type = Unknown'
b_ord = 'byte order = 0'
wave_unit = 'wavelength units = Micrometers'

; create and output packets and header files
for i=0, p_n_cycles-1 do begin
output_filename = dir_bsq+filenames(nf)+'_Otot_'+strtrim(string(i+1), 1)+'.bsq'
output_header_filename = dir_bsq+filenames(nf)+'_Otot_'+strtrim(string(i+1), 1)+'.hdr'
packet = reverse(reform(Otot(*,*,i)), 2)
openw, unit, output_filename, /get_lun
writeu, unit, packet
free_lun, unit

openw, unit, output_header_filename, /get_lun
printf, unit, harris
printf, unit, desc
printf, unit, samples
printf, unit, lines
printf, unit, bands
printf, unit, head_off
printf, unit, f_type
printf, unit, d_type
printf, unit, inter
printf, unit, s_type
printf, unit, b_ord
```

```
printf, unit, wave_unit
free_lun, unit
close, /all
end

save, Filename = dir_bsq+filenames(nf)+'_roiOtot.sav', roiOtot
save, Filename = dir_bsq+filenames(nf)+'_avgroiOtot.sav', avgroiOtot

; Header file template
harris = 'ENVI'
desc = 'description = { Total heat flux (plus) (roi) }'
samples = 'samples = '+strtrim(string(sensorx),1)
lines = 'lines = '+strtrim(string(sensory),1)
bands = 'bands = 1'
head_off = 'header offset = 0'
f_type = ' file type = ENVI Standard'
d_type = 'data type = 4'
inter = 'interleave = bsq'
s_type = 'sensor type = Unknown'
b_ord = 'byte order = 0'
wave_unit = 'wavelength units = Micrometers'

; create and output packets and header files
for i=0, p_n_cycles-1 do begin
output_filename = dir_bsq+filenames(nf)+'_roiOtot_'+strtrim(string(i+1), 1)+'.bsq'
output_header_filename = dir_bsq+filenames(nf)+'_roiOtot_'+strtrim(string(i+1), 1)+'.hdr'
packet = reverse(reform(roiOtot(*,*,i)), 2)
openw, unit, output_filename, /get_lun
writeu, unit, packet
free_lun, unit

openw, unit, output_header_filename, /get_lun
```

```
printf, unit, harris
printf, unit, desc
printf, unit, samples
printf, unit, lines
printf, unit, bands
printf, unit, head_off
printf, unit, f_type
printf, unit, d_type
printf, unit, inter
printf, unit, s_type
printf, unit, b_ord
printf, unit, wave_unit
free_lun, unit
close, /all
end

print, 'done ' +strtrim(string(nf+1),1)+' / '+strtrim(string( n_files ),1)
endfor
;close mega loop
stop
END
```

Bibliography

Abrams, M. J. (2000), 'The Advanced Spaceborne Thermal Emission and Reflection Radiometer (ASTER): Data products for the high spatial resolution imager on NASA's Terra platform', *International Journal of Remote Sensing* **21**(5), 847–859.

Abrams, M. J. and Hook, S. J. (2013), 'NASA's Hyperspectral Infrared Imager (HyspIRI)', *In: Kuenzer C., Dech S. (eds) Thermal Infrared Remote Sensing. Remote Sensing and Digital Image Processing* **17**, 117–130.
URL: *http://link.springer.com/10.1007/978-94-007-6639-6*

Abtahi, A. A., Kahle, A. B., Abbott, E. A., Gillespie, A. R., Sabol, D., Yamada, G. and Pieri, D. C. (2002), 'Emissivity changes in basalt cooling after eruption from Puu Oo, Kilauea, Hawaii [abs.]', *Eos, Transactions, American Geophysical Union supp.* **v. 83**(no. 47), F1442.

Andover Corporation (2017), Optical Coating & Filters, Technical report.
URL: *http://www.thinkgate.com/why-choose-us%5Cninternal-pdf://818/why-choose-us.html*

Averbuch, A. and Keller, Y. (2002), 'FFT based image registration', *ICASSP, IEEE International Conference on Acoustics, Speech and Signal Processing - Proceedings* **4**, 3608–3611.

Avolio, M. V., Crisci, G. M., Di Gregorio, S., Rongo, R., Spataro, W. and Trunfio, G. A. (2006), 'SCIARA γ2: An improved cellular automata model for lava flows and applications to the 2002 Etnean crisis', *Computers and Geosciences* **32**(7), 876–889.

Ball, M. and Pinkerton, H. (2006), 'Factors affecting the accuracy of thermal imaging cameras in volcanology', *Journal of Geophysical Research: Solid Earth* **111**(11), 1–14.

Bilotta, G., Cappello, A., Hérault, A., Vicari, A., Russo, G. and Del Negro, C. (2012), 'Sensitivity analysis of the MAGFLOW Cellular Automaton model for lava flow simulation', *Environmental Modelling & Software* **35**, 122–131.
URL: *http://linkinghub.elsevier.com/retrieve/pii/S1364815212000631*

Birnie, R. W. (1973), 'Infrared radiation thermometry of Guatemalan volcanoes', *Bulletin Volcanologique* **37**(1), 1–36.

Brothelande, E., Lénat, J. F., Chaput, M., Gailler, L., Finizola, A., Dumont, S., Peltier, A., Bachèlery, P., Barde-Cabusson, S., Byrdina, S., Menny, P., Colonge, J., Douillet, G. A., Letort, J., Letourneur, L., Merle, O., Di Gangi, F., Nakedau, D. and Garaebiti, E. (2016), 'Structure and evolution of an active resurgent dome evidenced by geophysical investigations: The Yenkahe dome-Yasur volcano system (Siwi caldera, Vanuatu)', *Journal of Volcanology and Geothermal Research* **322**, 241–262.

Bullard, F. M. (1947), 'Studies on parícutin volcano, Michoacan, Mexico', *Bulletin of the Geological Society of America* **58**(5), 433–450.

Byrnes, J. M., Ramsey, M. S. and Crown, D. A. (2004), 'Surface unit characterization of the Mauna Ulu flow field, Kilauea Volcano, Hawai'i, using integrated field and remote sensing analyses', *Journal of Volcanology and Geothermal Research* **135**(1-2), 169–193.

Calkins, J., Oppenheimer, C. and Kyle, P. R. (2008), 'Ground-based thermal imaging of lava lakes at Erebus volcano, Antarctica', *Journal of Volcanology and Geothermal Research* **177**(3), 695–704.

Calvari, S., Lodato, L., Steffke, A., Cristaldi, A., Harris, A. J. L., Spampinato, L. and Boschi, E. (2010), 'The 2007 stromboli eruption: Event chronology and effusion rates using thermal infrared data', *Journal of Geophysical Research: Solid Earth* **115**(4), 1–20.

Calvari, S., Spampinato, L., Lodato, L., Harris, A. J. L., Patrick, M. R., Dehn, J., Burton, M. R. and Andronico, D. (2005), 'Chronology and complex volcanic processes during the 2002-2003 flank eruption at Stromboli volcano (Italy) reconstructed from direct observations and surveys with a handheld thermal camera', *Journal of Geophysical Research B: Solid Earth* **110**(2), 1–23.

Cappello, A., Ganci, G., Bilotta, G., Hérault, A., Zago, V. and Negro, C. D. (2019), 'Satellite-driven modeling approach for monitoring lava flow hazards during the 2017 etna eruption', *Annals of Geophysics* **62**(2 Special Issue).

Carter, A. J., Ramsey, M. S., Durant, A. J., Skilling, I. P. and Wolfe, A. (2009), 'Micron-scale roughness of volcanic surfaces from thermal infrared spectroscopy and scanning electron microscopy', *Journal of Geophysical Research: Solid Earth* **114**(2), 1–13.

Cashman, K. V., Stephen, R. and Sparks, R. S. J. (2013), 'How volcanoes work: A 25 year perspective', *Bulletin of the Geological Society of America* **125**(5-6), 664–690.

Cashman, K. V., Thornber, C. and Kauahikaua, J. P. (1999), 'Cooling and crystallization of lava in open channels, and the transition of pahoehoe lava to 'a'a"', *Bulletin of Volcanology* **62**(4-5), 362–364.

Chevrel, M. O., Labroquère, J., Harris, A. J. and Rowland, S. K. (2018), 'PyFLOWGO: An open-source platform for simulation of channelized lava thermo-rheological properties', *Computers and Geosciences* **111**, 167–180.
URL: *https://doi.org/10.1016/j.cageo.2017.11.009*

Cordonnier, B., Lev, E. and Garel, F. (2016), 'Benchmarking lava-flow models', *Geological Society, London, Special Publications* **426**(1), 425–445.
URL: *http://sp.lyellcollection.org/lookup/doi/10.1144/SP426.7*

Crisci, G. M., Rongo, R., Di Gregorio, S. and Spataro, W. (2004), 'The simulation model SCIARA: The 1991 and 2001 lava flows at Mount Etna', *Journal of Volcanology and Geothermal Research* **132**(2-3), 253–267.

Davies, A. G., Calkins, J., Scharenbroich, L., Vaughan, R. G., Wright, R., Kyle, P., Castańo, R., Chien, S. and Tran, D. (2008), 'Multi-instrument remote and in situ observations of the Erebus Volcano (Antarctica) lava lake in 2005: A comparison with the Pele lava lake on the jovian moon Io', *Journal of Volcanology and Geothermal Research* **177**, 705–724.

Dietterich, H. R., Poland, M. P., Schmidt, D. A., Cashman, K. V., Sherrod, D. R. and Espinosa, A. T. (2012), 'Tracking lava flow emplacement on the east rift zone of Kīlauea, Hawai'i, with synthetic aperture radar coherence', *Geochemistry Geophysics Geosystems* **13**(5), Q05001.
URL: *http://doi.wiley.com/10.1029/2011GC004016*

Dozier, J. (1981), 'A method for satellite identification of surface temperature fields of subpixel resolution', *Remote Sensing of Environment* **11**(C), 221–229.

Dragoni, M. and Tallarico, A. (1994), 'The effect of crystallization on the rheology and dynamics of lava flows', *Journal of Volcanology and Geothermal Research* **59**(3), 241–252.
URL: *https://linkinghub.elsevier.com/retrieve/pii/0377027394900981*

Favalli, M., Pareschi, M. T., Neri, A. and Isola, I. (2005), 'Forecasting lava flow paths by a stochastic approach', *Geophysical Research Letters* **32**(3), L03305.
URL: *http://doi.wiley.com/10.1029/2004GL021718*

FLIR Systems (2014), 'User's Manual - FLIR Ax5 Series'.

Flynn, L. P., Harris, A. J. L. and Wright, R. (2001), 'Improved identification of volcanic features using Landsat 7 ETM+', *Remote Sensing of Environment* **78**(1-2), 180–193.

Flynn, L. P. and Mouginis-Mark, P. J. (1994), 'Temperature of an active lava channel from spectral measurements, Kilauea Volcano, Hawaii', *Bulletin of Volcanology* **56**(4), 297–301.

Gaddis, L. R., Mouginis-Mark, P. J. and Hayashi, J. N. (1990), 'Lava flow surface textures: SIR-B radar image texture, field observations, and terrain measurements', *Photogrammetric Engineering and Remote Sensing* **56**(2), 211–224.

Ganci, G., Bilotta, G., Cappello, A., Corradino, C., Zago, V. and Del Negro, C. (2019), 'Synergy of optical and infrared satellite data to forecast lava flow hazards during the Christmas 2018 Etna eruption', *Geophysical Research Abstracts* **21**, 1.

GATS (2019), 'SpectralCalc.com: High-resolution spectral modeling'.

Gillespie, A., Rokugawa, S., Matsunaga, T., Steven Cothern, J., Hook, S. J. and Kahle, A. B. (1998), 'A temperature and emissivity separation algorithm for advanced spaceborne thermal emission and reflection radiometer (ASTER) images', *IEEE Transactions on Geoscience and Remote Sensing* **36**(4), 1113–1126.

Giordano, D., Russell, J. K. and Dingwell, D. B. (2008), 'Viscosity of magmatic liquids: A model', *Earth and Planetary Science Letters* **271**(1-4), 123–134.

Global Volcanism Program (2018), Report on Kilauea (United States), *in* A. E. Crafford and E. Venzke, eds, 'Bulletin of the Global Volcanism Network', Vol. 43:10, Smithsonian Institution.

Gregg, T. K. and Fink, J. H. (2000), 'A laboratory investigation into the effects of slope on lava flow morphology', *Journal of Volcanology and Geothermal Research* **96**(3-4), 145–159.

Guanter, L., Brell, M., Chan, J. C., Giardino, C., Gomez-Dans, J., Mielke, C., Morsdorf, F., Segl, K. and Yokoya, N. (2019), 'Synergies of Spaceborne Imaging Spectroscopy with Other Remote

Sensing Approaches', *Surveys in Geophysics* **40**(3), 657–687.
URL: *https://doi.org/10.1007/s10712-018-9485-z*

Hall, J. L., Boucher, R. H., Buckland, K. N., Gutierrez, D. J., Hackwell, J. A., Johnson, B. R., Keim, E. R., Moreno, N. M., Ramsey, M. S., Sivjee, M. G., Tratt, D. M., Warren, D. W. and Young, S. J. (2015), 'MAGI: A New High-Performance Airborne Thermal-Infrared Imaging Spectrometer for Earth Science Applications', *IEEE Transactions on Geoscience and Remote Sensing* **53**(10), 5447–5457.

Handcock, R. N., Gillespie, A. R., Cherkauer, K. A., Kay, J. E., Burges, S. J. and Kampf, S. K. (2006), 'Accuracy and uncertainty of thermal-infrared remote sensing of stream temperatures at multiple spatial scales', *Remote Sensing of Environment* **100**(4), 427–440.

Harris, A., Dehn, J., Patrick, M., Calvari, S., Ripepe, M. and Lodato, L. (2005), 'Lava effusion rates from hand-held thermal infrared imagery: An example from the June 2003 effusive activity at Stromboli', *Bulletin of Volcanology* **68**(2), 107–117.

Harris, A. J., Favalli, M., Wright, R. and Garbeil, H. (2011), 'Hazard assessment at Mount Etna using a hybrid lava flow inundation model and satellite-based land classification', *Natural Hazards* **58**(3), 1001–1027.

Harris, A. J., Flynn, L. P., Keszthelyi, L., Mouginis-Mark, P. J., Rowland, S. K. and Resing, J. A. (1998), 'Calculation of lava effusion rates from Landstat TM data', *Bulletin of Volcanology* .

Harris, A. J. L. (2008), 'Modeling lava lake heat loss, rheology, and convection', *Geophysical Research Letters* **35**(7), 1–6.

Harris, A. J. L. (2013), *Thermal Remote Sensing of Active Volcanoes: A User's Manual*, first edn, Cambridge University Press, New York, USA.

Harris, A. J. L., Dehn, J. and Calvari, S. (2007), 'Lava effusion rate definition and measurement: A review', *Bulletin of Volcanology* **70**(1), 1–22.

Harris, A. J. L., Favalli, M., Steffke, A., Fornaciai, A. and Boschi, E. (2010), 'A relation between lava discharge rate, thermal insulation, and flow area set using lidar data', *Geophysical Research Letters* **37**(20), 1–6.

Harris, A. J. L. and Rowland, S. K. (2001), 'FLOWGO : a kinematic thermo-rheological model for lava flowing in a channel', *Bulletin of Volcanology* **63**, 20–44.

Harris, A. J. and Rowland, S. K. (2015), 'Flowgo 2012: An updated framework for thermorheological simulations of channel-contained lava', *Geophysical Monograph Series* **208**, 457–481.

Heliker, C. and Mattox, T. N. (2003), 'The first two decades of the Pu' u 'Ō'ō-Kūpaianaha eruption: Chronology and selected bibliography', *US Geological Survey Professional Paper* (1676), 1–20.

Herault, A., Vicari, A., Ciraudo, A. and Del Negro, C. (2009), 'Forecasting lava flow hazards during the 2006 Etna eruption: Using the MAGFLOW cellular automata model', *Computers and Geosciences* **35**(5), 1050–1060.
URL: *http://dx.doi.org/10.1016/j.cageo.2007.10.008*

Holcomb, R. T. (1987), 'Eruptive history and long-term behavior of Kilauea Volcano (Hawaii).'.

Holman, J. P. (1992), *Heat Transfer*, 2 edn, McGraw Hill, London.

Hook, S. J., Myers, J. J., Thome, K. J., Fitzgerald, M. and Kahle, A. B. (2001), 'The MODIS-/ASTER airborne simulator (MASTER) - A new instrument for earth science studies', *Remote Sensing of Environment* **76**(1), 93–102.

Hulley, G., Hook, S., Fisher, J. and Lee, C. (2017), ECOSTRESS, A NASA Earth-Ventures Instrument for studying links between the water cycle and plant health over the diurnal cycle, *in* 'International Geoscience and Remote Sensing Symposium (IGARSS)', Vol. 2017-July, pp. 5494–5496.

Huntingdon, A. T. and Sato, M. (1973), 'Mount Etna and the 1971 eruption - The collection and analysis of volcanic gases from Mount Etna', *Philosophical Transactions of the Royal Society of London. Series A, Mathematical and Physical Sciences* **274**(1238), 119–128.

Johnson, W. R., Hook, S. J., Mouroulis, P., Wilson, D. W., Gunapala, S. D., Realmuto, V., Lamborn, A., Paine, C., Mumolo, J. M. and Eng, B. T. (2011), 'HyTES: Thermal imaging spectrometer development', *IEEE Aerospace Conference Proceedings* **91109**(818), 1–9.

Karson, J. A. and Wysocki, R. J. (2012), 'Do-it-yourself lava flows: Science, art and education in the Syracuse University LavaProject', *Earth* **57**(9), 38–41.

Kauahikaua, J., Sherrod, D. R., Cashman, K. V., Heliker, C., Hon, K., Mattox, T. N. and Johnson, J. A. (2003), 'Hawaiian lava-flow dynamics during the Pu'u 'Ō'ō-Kū paianaha eruption: A tale of two decades', *US Geological Survey Professional Paper* (1676), 63–87.
URL: *http://www.scopus.com/inward/record.url?eid=2-s2.0-10844293568&partnerID=tZOtx3y1*

Kerr, R. C. and Lyman, A. W. (2007), 'Importance of surface crust strength during the flow of the 1988-1990 andesite lava of Lonquimay Volcano, Chile', *Journal of Geophysical Research: Solid Earth* **112**(3), 1–8.

Koeppen, W. C., Patrick, M., Orr, T., Sutton, A. J., Dow, D. and Wright, R. (2013), 'Constraints on the partitioning of Kīlauea's lavas between surface and tube flows, estimated from infrared satellite data, sulfur dioxide emission rates, and field observations', *Bulletin of Volcanology* **75**(5), 1–18.

Lee, C. T. A., Luffi, P., Plank, T., Dalton, H. and Leeman, W. P. (2009), 'Constraints on the depths and temperatures of basaltic magma generation on Earth and other terrestrial planets using new thermobarometers for mafic magmas', *Earth and Planetary Science Letters* **279**(1-2), 20–33.

Lee, R. J., Ramsey, M. S. and King, P. L. (2013), 'Development of a new laboratory technique for high-temperature thermal emission spectroscopy of silicate melts', *Journal of Geophysical Research: Solid Earth* **118**(5), 1968–1983.

Lodato, L., Spampinato, L., Harris, A., Calvari, S., Dehn, J. and Patrick, M. (2007), 'The morphology and evolution of the Stromboli 2002-2003 lava flow field: An example of a basaltic flow field emplaced on a steep slope', *Bulletin of Volcanology* **69**(6), 661–679.

Lombardo, V. and Buongiorno, M. F. (2006), 'Lava flow thermal analysis using three infrared bands of remote-sensing imagery: A study case from Mount Etna 2001 eruption', *Remote Sensing of Environment* **101**(2), 141–149.

MacDonald, G. A. (1972), *Volcanoes*, Prentice Hall, Englewood Cliffs, New Jersy.

Matson, M. and Dozier, J. (1981), 'Identification of subresolution high temperature sources using a thermal IR sensor.', *Photogrammetric Engineering and Remote Sensing* **47**(9), 1311–1318.

Melnik, O. and Sparks, R. S. (2002), 'Dynamics of magma ascent and lava extrusion at Soufrière Hills Volcano, Montserrat', *Geological Society Memoir* **21**(1), 153–171.

Minitti, M. E., Weitz, C. M., Lane, M. D. and Bishop, J. L. (2007), 'Morphology, chemistry, and spectral properties of Hawaiian rock coatings and implications for Mars', *Journal of Geophysical Research E: Planets* **112**(5), 1–24.

Miyamoto, H. and Crown, D. A. (2006), 'A simplified two-component model for the lateral growth of pahoehoe lobes', *Journal of Volcanology and Geothermal Research* **157**(4), 331–342.

Miyamoto, H. and Papp, K. R. (2004), 'Rheology and topography control the path of a lava flow: Insight from numerical simulations over a preexisting topography', *Geophysical Research Letters* **31**(16), 2–5.

Miyamoto, H. and Sasaki, S. (1997), 'Simulating lava flows by an improved celluar automata method', *Computers and Geosciences* **23**(3), 283–292.

Miyamoto, H. and Sasaki, S. (1998), 'Numerical simulations of flood basalt lava flows: Roles of parameters on lava flow morphologies', *Journal of Geophysical Research: Solid Earth* **103**(B11), 27489–27502.

Moore, H. J. (1987), 'Preliminary estimates of the rheological properties of 1984 Mauna Loa lava (Hawaii).', *US Geological Survey Professional Paper* **1350**(2), 1569–1588.

Mossoux, S., Saey, M., Bartolini, S., Poppe, S., Canters, F. and Kervyn, M. (2016), 'Q-LAVHA: A flexible GIS plugin to simulate lava flows', *Computers and Geosciences* **97**, 98–109.

Murphy, S. W., Wright, R., Oppenheimer, C. and Filho, C. R. (2013), 'MODIS and ASTER synergy for characterizing thermal volcanic activity', *Remote Sensing of Environment* **131**, 195–205.
URL: *http://dx.doi.org/10.1016/j.rse.2012.12.005*

National Academies of Sciences and Medicine, E. (2018), *Thriving on Our Changing Planet: A Decadal Strategy for Earth Observation from Space*, The National Academies Press, Washington, DC, USA.
URL: *https://www.nap.edu/catalog/24938/thriving-on-our-changing-planet-a-decadal-strategy-for-earth*

National Oceanic and Atmospheric Administration (2007), *Digital Elevation Models (DEMs) for the main 8 Hawaiian Islands*, 1st edn, OAA's National Ocean Service (NOS), National Centers for Coastal Ocean Science (NCCOS), Silver Spring, MD.

Neal, C. A., Brantley, S. R., Antolik, L., Babb, J. L. and Etc (2019), 'The 2018 rift eruption and summit collapse of Kīlauea Volcano', *Science* **363**(January), 367–374.

Negro, C., Fortuna, L., Herault, A. and Vicari, A. (2008), 'Simulations of the 2004 lava flow at Etna volcano using the magflow cellular automata model', *Bulletin of Volcanology* **70**(7), 805–812.

Orr, T. R., Heliker, C. and Patrick, M. R. (2013), 'The ongoing Pu'u 'O'o eruption of KIlauea Volcano, Hawai'i—30 years of eruptive activity', *U.S. Geological Survey Fact Sheet 2012-3127* **2012-3127**(January), 6 p.

Park, S. and Iversen, J. D. (1984), 'Dynamics of lava flow: Thickness growth characteristics of steady two-dimensional flow', *Geophysical Research Letters* **11**(7), 641–644.

Patrick, M., Orr, T., Fisher, G., Trusdell, F. and Kauahikaua, J. (2017), 'Thermal mapping of a pāhoehoe lava flow, Kīlauea Volcano', *Journal of Volcanology and Geothermal Research* **332**, 71–87.

Patrick, M., Orr, T., Sutton, A., Elias, T. and Swanson, D. (2013), 'The First Five Years of Kīlauea's Summit Eruption in Halema'uma'u Crater 2008–2013', *U.S. Geological Survey Fact Sheet* **2013-3116**, 1–4.
URL: *http://dx.doi.org/10.3133/fs20133116*

Patrick, M. R., Dietterich, H. R., Lyons, J. J., Diefenbach, A. K., Parcheta, C., Anderson, K. R., Namiki, A., Sumita, I., Shiro, B. and Kauahikaua, J. P. (2019), 'Cyclic lava effusion during the 2018 eruption of Kīlauea Volcano', *Science* **366**(6470).

Patrick, M. R., Orr, T. R., Swanson, D. A., Elias, T. and Shiro, B. (2018), 'Lava lake activity at the summit of Kīlauea Volcano in 2016', *U.S. Geological Survey Scientific Investigations Report 2018–5008* p. 58.
URL: *https://doi.org/10.3133/sir20185008*

Perret, F. A. (1913), 'The circulatory system in the Halemaumau lava lake during the summer of 1911', *American Journal of Science* **s4-35**(208), 337–349.

Pinkerton, H. and Wilson, L. (1994), 'Factors controlling the lengths of channel-fed lava flows', *Bulletin of Volcanology* **56**(2), 108–120.

Planck, M. (1901), 'Ueber das Gesetz der Energieverteilung im Normalspectrum', *Annalen der Physik* **309**(3), 553–563.

Poland, M. P. (2014), 'Time-averaged discharge rate of subaerial lava at Kīlauea Volcano, Hawai'i, measured from TanDEM-X interferometry: Implications for magma supply and storage during 2011-2013', *Journal of Geophysical Research: Solid Earth* **119**(7), 5464–5481.

Prata, A. J. and Bernardo, C. (2009), 'Retrieval of volcanic ash particle size, mass and optical depth from a ground-based thermal infrared camera', *Journal of Volcanology and Geothermal Research* **186**(1-2), 91–107.
URL: *http://dx.doi.org/10.1016/j.jvolgeores.2009.02.007*

Putirka, K. (1997), 'Magma transport at Hawaii: Inferences based on igneous thermobarometry', *Geology* **25**(1), 69–72.

Ramsey, M. S., Chevrel, M. O., Coppola, D. and Harris, A. J. (2019), 'The influence of emissivity on the thermo-rheological modeling of the channelized lava flows at tolbachik volcano', *Annals of Geophysics* **62**(2 Special Issue).
URL: *https://www.annalsofgeophysics.eu/index.php/annals/article/view/8077*

Ramsey, M. S. and Christensen, P. R. (1998), 'Mineral abundance determination Quantitative deconvolution of thermal emission spectra', *JOURNAL OF GEOPHYSICAL RESEARCH* **103**(10), 577–596.

Ramsey, M. S. and Fink, J. H. (1999), 'Estimating silicic lava vesicularity with thermal remote sensing: A new technique for volcanic mapping and monitoring', *Bulletin of Volcanology* **61**(1-2), 32–39.

Ramsey, M. S. and Harris, A. J. (2013), 'Volcanology 2020: How will thermal remote sensing of volcanic surface activity evolve over the next decade?', *Journal of Volcanology and Geothermal Research* **249**, 217–233.
URL: *http://dx.doi.org/10.1016/j.jvolgeores.2012.05.011*

Ramsey, M. S. and Harris, A. J. L. (2016), 'Modelling the thermal and infrared spectral properties of active vents: Comparing basaltic lava flows of Tolbachik, Russia to Arsia Mons, Mars', *AGU Fall Meeting 2016* .

Ramsey, M. S., Harris, A. J. L. and Crown, D. A. (2016), 'What can thermal infrared remote sensing of terrestrial volcanoes tell us about processes past and present on Mars?', *Journal of Volcanology and Geothermal Research* **311**, 198–216.
URL: *http://dx.doi.org/10.1016/j.jvolgeores.2016.01.012*

Ramsey, M. S. and Wessels, R. (2007), 'Monitoring changing eruption styles of Kilauea Volcano over the summer of 2007 with spaceborne infrared data [abs.]', *Eos, Transactions, American Geophysical Union supp.* **88**(52), abstract no. V51H–07.
URL: *http://www.agu.org*

Realmuto, V. J. (1990), Separating the effects of temperature and emissivity: Emissivity spectrum normalization, *in* 'Proceedings of the Second International Airborne Remote Sensing Conference', pp. 31–35.

Riker, J. M., Cashman, K. V., Kauahikaua, J. P. and Montierth, C. M. (2009), 'The length of channelized lava flows: Insight from the 1859 eruption of Mauna Loa Volcano, Hawai'i', *Journal of Volcanology and Geothermal Research* **183**(3-4), 139–156.

Roberts, D. A., Quattrochi, D. A., Hulley, G. C., Hook, S. J. and Green, R. O. (2012), 'Synergies between VSWIR and TIR data for the urban environment: An evaluation of the potential for the Hyperspectral Infrared Imager (HyspIRI) Decadal Survey mission', *Remote Sensing of Environment* **117**(2012), 83–101.

Rose, S. R., Watson, I. M., Ramsey, M. S. and Hughes, C. G. (2014), 'Thermal deconvolution: Accurate retrieval of multispectral infrared emissivity from thermally-mixed volcanic surfaces', *Remote Sensing of Environment* **140**, 690–703.

Rothman, L. S., Gordon, I. E., Babikov, Y., Barbe, A., Chris Benner, D., Bernath, P. F., Birk, M., Bizzocchi, L., Boudon, V., Brown, L. R., Campargue, A., Chance, K., Cohen, E. A., Coudert, L. H., Devi, V. M., Drouin, B. J., Fayt, A., Flaud, J. M., Gamache, R. R., Harrison, J. J., Hartmann, J. M., Hill, C., Hodges, J. T., Jacquemart, D., Jolly, A., Lamouroux, J., Le Roy, R. J., Li, G., Long, D. A., Lyulin, O. M., Mackie, C. J., Massie, S. T., Mikhailenko, S., Müller, H. S., Naumenko, O. V., Nikitin, A. V., Orphal, J., Perevalov, V., Perrin, A., Polovtseva, E. R., Richard, C., Smith, M. A., Starikova, E., Sung, K., Tashkun, S., Tennyson, J., Toon, G. C., Tyuterev, V. G. and Wagner, G. (2013), 'The HITRAN2012 molecular spectroscopic database', *Journal of Quantitative Spectroscopy and Radiative Transfer* **130**, 4–50.
URL: *https://linkinghub.elsevier.com/retrieve/pii/S0022407313002859*

Ruff, S. W., Christensen, P. R., Barbera, P. W. and Anderson, D. L. (1997), 'Quantitative thermal emission spectroscopy of minerals: A laboratory technique for measurement and calibration', *Journal of Geophysical Research: Solid Earth* **102**(B7), 14899–14913.
URL: *http://doi.wiley.com/10.1029/97JB00593*

Ryerson, F. J., Weed, H. C. and Piwinskii, A. J. (1988), 'Rheology of subliquidus magmas. 1. Picritic compositions', *Journal of Geophysical Research* **93**(B4), 3421–3436.

Sahetapy-Engel, S. T. and Harris, A. J. (2009), 'Thermal structure and heat loss at the summit crater of an active lava dome', *Bulletin of Volcanology* **71**(1), 15–28.

Shaw, H. R. (1972), 'Viscosities of magmatic silicate liquids; an empirical method of prediction'.
URL: *http://www.ajsonline.org/content/272/9/870.abstract*

Shimozuru, D. (1971), 'Observation of volcanic eruption by an infrared radiation meter'.

Simurda, C. M., Ramsey, M. S. and Crown, D. A. (2019), 'The Unusual Thermophysical and Surface Properties of the Daedalia Planum Lava Flows', *Journal of Geophysical Research: Planets* **124**(7), 1945–1959.

Soldati, A., Harris, A. J., Gurioli, L., Villeneuve, N., Rhéty, M., Gomez, F. and Whittington, A. (2018), 'Textural, thermal, and topographic constraints on lava flow system structure: the December 2010 eruption of Piton de la Fournaise', *Bulletin of Volcanology* **80**(10).

Soule, S. A. and Cashman, K. V. (2005), 'Shear rate dependence of the pāhoehoe-to-'a 'ā transition: Analog experiments', *Geology* **33**(5), 361–364.

Spampinato, L., Calvari, S., Oppenheimer, C. and Boschi, E. (2011), 'Volcano surveillance using infrared cameras', *Earth-Science Reviews* **106**(1-2), 63–91.

Spampinato, L., Oppenheimer, C., Calvari, S., Cannata, A. and Montalto, P. (2008), 'Lava lake surface characterization by thermal imaging: Erta 'ale volcano (Ethiopia)', *Geochemistry, Geophysics, Geosystems* **9**(12).

Stovall, W. K., Houghton, B. F., Harris, A. J. and Swanson, D. A. (2009), 'Features of lava lake filling and draining and their implications for eruption dynamics', *Bulletin of Volcanology* **71**(7), 767–780.

Thompson, J. O. and Ramsey, M. S. (2017), Thermal infrared data of active lava surfaces using a newly-developed camera system, *in* 'AGU Fall Meeting'.

Thompson, J. O. and Ramsey, M. S. (2018), Thermal infrared measurements of active lava surfaces: Implications for improved flow modeling and future instrument development, *in* 'Asia Oceania Geoscience Society Annual Meeting.'.

Thompson, J. O. and Ramsey, M. S. (2020), 'Uncertainty analysis of remotely-acquired thermal infrared data to extract the thermal properties of active lava surfaces', *Remote Sensing* **12**(1), 193.

Thompson, J. O., Ramsey, M. S. and Hall, J. L. (2019), 'MMT-Cam: A New Miniature Multispectral Thermal Infrared Camera System for Capturing Dynamic Earth Processes', *IEEE Transactions on Geoscience and Remote Sensing* **57**(10), 7438–7446.

Tonooka, H. (2001), 'An atmospheric correction algorithm for thermal infrared multispectral data over land-a water-vapor scaling method', *IEEE Transactions on Geoscience and Remote Sensing* **39**(3), 682–692.
URL: *http://ieeexplore.ieee.org/lpdocs/epic03/wrapper.htm?arnumber=911125*

U.S. Geological Survey (2018), *Thermal map of fissure system: 04 June 2018, 12:30 pm.*
URL: *https://volcanoes.usgs.gov/observatories/hvo/maps_uploads/image-468.jpg*

USGS (2018), 'Preliminary summary of Kīlauea Volcano's 2018 lower East Rift Zone eruption and summit collapse', *USGS Fact Sheet* **June**(September), 1–2.

Vicari, A., Ciraudo, A., Del Negro, C., Herault, A. and Fortuna, L. (2009), 'Lava flow simulations using discharge rates from thermal infrared satellite imagery during the 2006 Etna eruption', *Natural Hazards* **50**(3), 539–550.

Vicari, A., Ganci, G., Behncke, B., Cappello, A., Neri, M. and Del Negro, C. (2011), 'Near-real-time forecasting of lava flow hazards during the 12-13 January 2011 Etna eruption', *Geophysical Research Letters* **38**(13), 1–7.

Walker, G. P. L. (1993), 'Basaltic-volcano systems', *Geological Society, London, Special Publications* **76**(1), 3–38.

Wantim, M. N., Kervyn, M., Ernst, G. G., del Marmol, M. A., Suh, C. E. and Jacobs, P. (2013), 'Numerical experiments on the dynamics of channelised lava flows at Mount Cameroon volcano with the FLOWGO thermo-rheological model', *Journal of Volcanology and Geothermal Research* **253**, 35–53.

Western, L. M., Watson, M. I. and Francis, P. N. (2015), 'Uncertainty in two-channel infrared remote sensing retrievals of a well-characterised volcanic ash cloud', *Bulletin of Volcanology* **77**(8).

Williams, D. B., Ramsey, M. S., Wickens, D. J. and Karimi, B. (2019), 'Identifying eruptive sources of drifting volcanic ash clouds using back-trajectory modeling of spaceborne thermal infrared data', *Bulletin of Volcanology* **81**(9).

Wolfe, E. W., Garcia, M. O., Jackson, D. B., Koyanagi, R. Y., Neal, C. A. and Okamura, A. T. (1987), 'The Puu Oo eruption of Kilauea Volcano, episodes 1-20, January 3, 1983, to June 8, 1984 (Hawaii).', *US Geological Survey Professional Paper* **1350**(1), 471–508.

Worden, A., Dehn, J., Ripepe, M. and Donne, D. D. (2014), 'Frequency based detection and monitoring of small scale explosive activity by comparing satellite and ground based infrared observations at Stromboli Volcano, Italy', *Journal of Volcanology and Geothermal Research* **283**, 159–171.
URL: *http://linkinghub.elsevier.com/retrieve/pii/S0377027314002182*

Wright, R. and Flynn, L. P. (2003), 'On the retrieval of lava-flow surface temperatures from infrared satellite data', *Geology* **31**(10), 893–896.

Wright, R., Garbeil, H. and Harris, A. J. L. (2008), 'Using infrared satellite data to drive a thermorheological/stochastic lava flow emplacement model: A method for near-real-time volcanic hazard assessment', *Geophysical Research Letters* **35**(19), 1–5.

Yamaguchi, Y., Kahle, A. B., Tsu, H., Kawakami, T. and Pniel, M. (1998), 'Overview of advanced spaceborne thermal emission and reflection radiometer (ASTER)', *IEEE Transactions on Geoscience and Remote Sensing* **36**(4), 1062–1071.

Young, S. J., Johnson, B. R. and Hackwell, J. A. (2002), 'An in-scene method for atmospheric compensation of thermal hyperspectral data', *Journal of Geophysical Research Atmospheres* **107**(24), 1–20.

Zies, E. G. (1937), 'The volcanic dome of Santa Maria, Guatemala', *Eos, Transactions American Geophysical Union* **18**(1), 262–263.
URL: *http://doi.wiley.com/10.1029/TR018i001p00262*